FLORIDA STATE UNIVERSITY

COLLEGE OF ARTS AND SCIENCES

A STUDY OF 3π PRODUCTION IN $\gamma p \to n\pi^+\pi^+\pi^-$ AND $\gamma p \to \Delta^{++}\pi^+\pi^-\pi^-$ WITH CLAS AT JEFFERSON LAB

By

ARISTEIDIS TSARIS

A Dissertation submitted to the
Department of Physics
in partial fulfillment of the
requirements for the degree of
Doctor of Philosophy

2016

Aristeidis Tsaris defended this dissertation on February 22, 2016.
The members of the supervisory committee were:

Paul Eugenio

Professor Directing Dissertation

Tomek Plewa

University Representative

Volker Crede

Committee Member

Simon Capstick

Committee Member

Joseph Owens

Committee Member

The Graduate School has verified and approved the above-named committee members, and certifies that the dissertation has been approved in accordance with university requirements.

This dissertation is dedicated to my wife Antigoni. To our home with the true meaning and to the life that we will spend together.

ACKNOWLEDGMENTS

First I want to thank all the scientists, staff members and people who made the CLAS-g12 experiment at Jefferson Lab possible. This analysis could definitely not be done without all those beautiful facilities in place and without the hard work and the amazing ideas that follow the particle physics experiments. We acknowledge the outstanding efforts of the staff of the Accelerator and the Physics Divisions at Jefferson Lab that made this experiment possible. This material is based upon work supported by the U.S. Department of Energy, Office of Science, Office of Nuclear Physics under contract DE-FG02-92ER40735. Also I want to thank all the people that were part of the g12-group throughout the years, setting up the software infrastructures and the analysis frameworks that I used.

This analysis and my professional progress in the world of science could not have been done without my adviser, Dr. Paul Eugenio. He has been very generous with me, helping me at my rough first years in graduate school and motivating me throughout the Ph.D., sending me to conferences and guiding me to do research. He gave me all the necessary assets and more for a successful doctoral study. He trusted me with different projects and he was always showing me his kind support, teaching me his deep knowledge in various aspects of software and hardware issues and above all setting an example for how a Scientist does research and a Professor is teaching. Thank you for all the aforementioned Paul and for the good times at Jefferson Lab.

I want to gratefully thank Dr. Alexander Ostrovidov for all the generous help he offered me, his patience to my overmuch questions and the tremendous help in making this dissertation possible. With all the discussions that we had I broaden my horizons in hadron spectroscopy and in physics. Thank you Sasha for teaching me physics and for the support that you showed me when I needed it.

I also want to thank my good collaborator Mukesh Saini for the help and his advise during the first years of the program and the boost that this had in my research experience. Also, I want to thank my good friend and collaborator Hussein Al Ghoul for all the talks that we had, for all the rides at JLab, for gently sharing his hardware techniques with me and for all the nice times that we spend together. Also I want to thank my old office mates Priyashree Roy and Brad Cannon for the interesting conversations that we had.

The achievement of the thesis could not be done without the collaborate advises from the committee members. The always interesting conversions with Dr. Volker Crede, trusting my work and motivating me to take over GlueX related projects is something that helped me both professionally and in a personal level. Dr. Simon Capstick for his generous advise and the encouragement that he showed me especially the first years of the graduate school. Also I want to thank Dr. Tomasz Plewa and Dr. Joseph F. Owens for advising my thesis.

I also want to thank Dr. Efstratios Manousakis and Dr. Jorge Piekarewicz for teaching me my courses and for showing me the broader picture of how and what the graduate school is about. Also I want to thank them for their warm support and concern that showed to me and my wife.

Special thanks go to all my GlueX collaborators. Getting involved in various projects for the GlueX experiment took almost half of my PhD time and it was totally worth it. Since my involvement in those projects is not part of this thesis I want just to list some of them: construction and commissioning the time-of-flight detector, writing code for online monitoring the TOF, acceptance and background studies using Monte-Carlo simulations and participating in software data challenge. I met great scientists by participating in those projects and apart from being exposed to state of the art tools for hardware and software, I got involved in the best collaborative environment I have met in the science community. A big thanks to Dr. Mark Ito for his help making the projects I was involved possible and his patience for answering all of my questions. I also want to thank him for the support and the recommendation letters he gave me in pursing a career in physics. I also want to thank Dr. Elton Smith for his advise and his help during the Time-of-Flight detector commissioning. I also want to thank Michael Staib, Justin Stevens, Paul Mattione and Alexander Barnes for all the help with the GlueX software code and all the nice times in the collaboration meetings and the workshops.

To my undergraduate adviser Dr. Michael Kokkoris which made it possible for me crossing the "big river" and coming to the United States and pursuing my PhD. I could not have made it here without him. He and Dr. Anastasios Lagoyannis introduced me to the fascinating area of research by performing nuclear experiments in the National Center of Scientific Research Demokritos. I also want to thank my friend and excellent scientist Georgios Laskaris for all the vital help all those years and for his support.

This work is dedicated to my wife, Antigoni Georgiadou, who has been the most wonderful thing that happened to me. She helped me like no other getting my PhD and the patience that she showed is admirable. To our home with the true meaning and to the life that we will spend together.

I also want to thank my lovely parents, Christos Tsaris and Christina Stuliou. Thank you for raising me to look the world in the eyes and the moral values you taught me if I want to be called human. They were the constant source of stability and strength in my life through dark and sunny days. Kosta thank you for being the best brother for me, and for all the talks that we had. I also want to thank my grandparents who spent so much time with me in my early years, thank you Dimitra Stuliou, and my Uncle Kostas.

Last but not least to all the people that shared their knowledge and their hard work with the rest of the world.

> No man is an Iland, intire of itselfe; every man is a peece of the Continent, a part of the maine; if a Clod bee washed away by the Sea, Europe is the lesse, as well as if a Promontorie were, as well as if a Manor of thy friends or of thine owne were; any mans death diminishes me, because I am involved in Mankinde; And therefore never send to know for whom the bell tolls; It tolls for thee.
>
> ---
>
> John Donne

TABLE OF CONTENTS

LIST OF TABLES

LIST OF FIGURES

ABSTRACT

Apart from the mesons that the constituent quark model predicts, QCD allows for additional states beyond the $q\bar{q}$ system. Previous experiments have performed partial wave analysis on pion-production data and claim observation of an exotic $J^{PC} = 1^{-+}$ state decaying via $\rho\pi$. The g12 experiment took place at Jefferson Lab using the CLAS spectrometer, a liquid hydrogen target was used and a tagged photon beam. By studying the reactions $\gamma p \to n\pi^+\pi^+\pi^-$ and $\gamma p \to \Delta^{++}\pi^+\pi^-\pi^-$, the photoproduction of mesons decaying to 3π was studied using two different but complimentary channels. Events are selected with low four-momentum transfer to the baryon, in order to enhance one pion exchange production. For both 3π systems the data exhibit two intermediate decays, $\rho\pi$ and $f_2\pi$. For the $\gamma p \to n\pi^+\pi^+\pi^-$ reaction over 600k events were acquired resulting in the largest 3 photoproduction dataset to date. The exotic $J^{PC} = 1^{-+}$ partial wave does not show resonant behavior and more so it is strongly consistent with a non-resonant non-interfering wave relative to a resonant $\pi_2(1670)$. Furthermore, the partial wave analysis shows production of the $a_2(1320)$ and $\pi_2(1670)$ mesons. For the first time we report observation of a photoproduced $a_1(1260)$ meson. For the $\gamma p \to \Delta^{++}\pi^+\pi^-\pi^-$ reaction nearly 350k events were analyzed. A partial wave analysis was performed for the first time on this channel. The $a_1(1260)$, $a_2(1320)$, and the $\pi_2(1670)$ mesons were observed. Observation of the $a_1(1260)$ confirms the result first reported in $\gamma p \to n\pi^+\pi^+\pi^-$ reaction.

CHAPTER 1

INTRODUCTION

One of the most desirable achievements in physics is the discovery of the fundamental particles, matter is composed of. The tools physicists use to explore it, can be considered as a really intelligent microscope. From Rutherford's experiment where alpha particles where scattered off of a gold foil, until the recent experiments at CERN, scattering and collision of particles is the key for such an achievement.

The world of particle physics, it is known today, is made of three kinds of elementary particles: leptons, quarks and mediators. There are six leptons (e, ν_e, μ, ν_μ, τ, ν_τ) in total and six anti-leptons. Leptons are classified according to their charge, electron number, muon number and tau number. The quarks come in six flavors, and are classified according to charge, strangeness, charm, bottomness, topness, upness and downness. The six quarks (d, u, s, c, b, t) come in three colors. The particles interact with each other by exchanging bosons or mediators. Bosons have integer spins, in units $\hbar$, and they follow the Bose - Einstein statistics. The photon is the mediator for the electromagnetic force and the two W's and Z bosons are the mediators for the weak force. In Yukawa's original theory (1934) the pion was believed to be the mediator for the strong force, but with the discovery that nucleons could exchange heavier mesons than pions, this simple picture could not stand. In order for the strong force to be studied in a fundamental level, the interaction between the quarks was necessary to be understood. Today we know that the exchange particle between two quarks is the gluon. The gluon, like the quarks, carries color and therefore it should not exists as an isolated particle.

1.1 Quantum Chromodynamics and the Quark Model

Based on our knowledge there are four fundamental forces in nature: strong, electromagnetic, weak and gravitational. To each of these forces belongs a physical theory, for example for the electromagnetic force there is the Quantum Electrodynamics (QED). For the strong force there is the Quantum Chromodynamics (QCD). The color in the QCD plays a similar role of the charge

for the QED, though there are some fundamental differences between the two. There are three kinds of colors (and their corresponding anticolors) and only two kinds of electric charges (positive and negative). Also, gluons can carry themselves color (where photons are electrically neutral) and so they can couple directly to other gluons. The gauge symmetry of the strong interaction is the SU(3), which is more complex than the U(1) group of QED. The SU(3) is an exact symmetry and so the color charges is absolutely conserved.

Another major difference between QCD and QED is the size of the coupling constant. In QED each vertex introduces a factor of $\frac{1}{137}$ and we would only need to consider Feynman diagrams with a small number of vertices. On the other hand, experimentally has been found that the QCD coupling constant a_s, for example between two protons, is bigger than 1. It was also found that the a_s is a running coupling constant, in a sense that it depends to the momentum transfer Q^2 (see Figure 1.1).

$$a_s(Q^2) \approx \frac{1}{\beta_0 \ \ln Q^2/\Lambda^2} \tag{1.1}$$

where β_0 is a constant and Λ is the QCD scale which was experimentally observed to be around 220 MeV. The "Lambda-QCD" is important because it separates two energy regimes. For energy values close or below Λ, the QCD coupling constant becomes large and the perturbation QCD (pQCD) can not be applied. This is called the confinement regime. On the other hand, when the two quarks are very close, and so the momentum transfer is large, the QCD coupling constant becomes extremely small. In that region the quarks can be seen as quasi-free or weakly bound particles. Due to the small values of a_s in that region the pQCD can be applied and it shows good agreement with the experimental data.

By 1960s the number of strong interacting particles had grown large and those particles were divided into two great families, the baryons and the mesons. The members of each family were distinguished by charge, strangeness and mass, but beyond that there was no reason to it at all. In 1964, G. Zweig at CERN and M. Gell-Mann in the USA independently proposed that the hadrons are made up by quarks [5]. Quarks are strongly interacting fermions with spin 1/2 and positive parity (antiquarks have negative parity). They are related to the charge Q through the generalized Gell-Mann-Nishijima formula

$$Q = I_z + \frac{Y}{2} \tag{1.2}$$

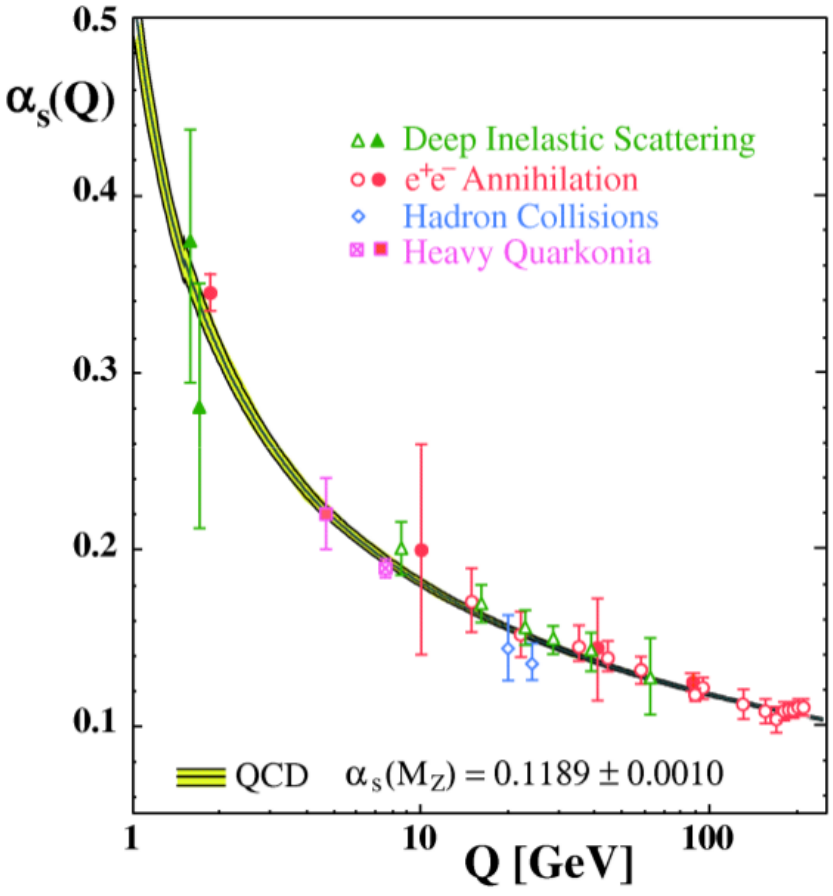

Figure 1.1: World average of a_s from [1]

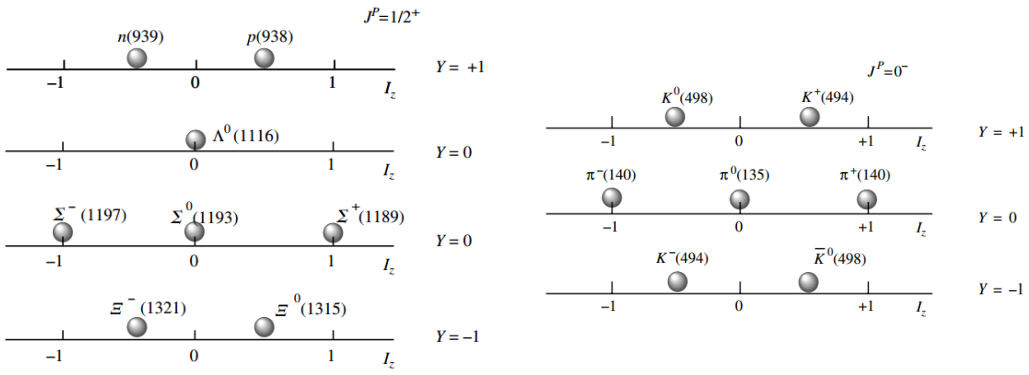

Figure 1.2: Isospin multiplets, where in parenthesis is the approximately value of mass. The **left** plot shows the isospin multiplets for $J^P = 1/2^+$ baryons. The **right** plot shows the isospin multiplet for $J^P = 0^-$ mesons. (Image source [2]).

where Y is the hypercharge which is defined as Y=$\mathcal{B}$+S+C+B+T and I_z is the z-component of the isospin. $\mathcal{B}$ is the baryon number, S is the strangeness, C is the charm, B is the bottomness and T is the topness. The convention that has been used here is that the flavor of a quark has the same sign as its charge Q. A well known symmetry property of the nuclear forces is that they are charge independent, i.e. two nuclear states with the same spin and parity have approximately the same energy (for example a proton and a neutron). In 1932 W. Heisenberg introduced the concept of isospin to describe that property. For example proton and neutron are considered two states of the same particle, with isospin I=1/2, and they differ only by the z-component of the isospin. The number of different particles, that can be thought as different charge states of the same particle is 2I+1 and the group is called isotropic multiplet.

The isotropic symmetry is broken, since the masses are not identical for particles in the same state (for example $m_n - m_p \approx 1.3$ MeV). The same effect is in the quark level, were the mass of the d quark is a few MeV larger than that of the u. Furthermore the electromagnetic interaction does not conserve isospin, only its third component. The isospin invariance can be described by the SU(2) group and so quarks and hadrons can be described as SU(2) multiplets. Figure 1.2 shows the isospin multiplets for the $J^P = 1/2^+$ baryons and $J^P = 0^-$ mesons. All the members of the multiplet have the same hypercharge.

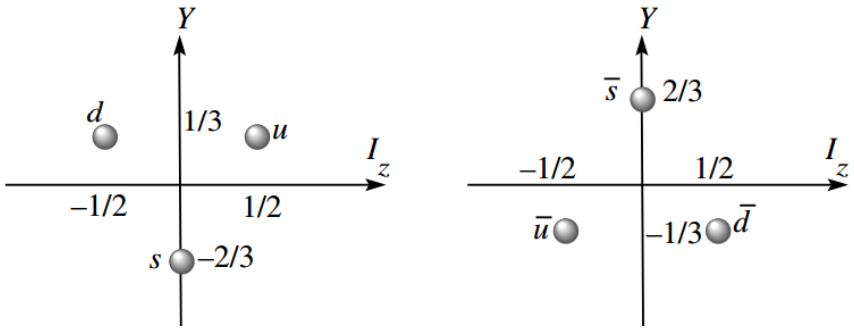

Figure 1.3: The **3** and $\bar{\mathbf{3}}$ representations. (Image source [2]).

With the quark representation in place, the scheme extends from the isospin internal symmetry, SU(2), to SU(3). The two quarks present in the normal matter, u and d, form an isospin doublet. The z-component of the isospin, I_z, can be considered as the flavor of each of the two. The flavor of the s is the strangeness and it is negative, i.e. S=-1. The flavor of c quark is C=+1, of the b quark is B=-1 and of the t quark T=+1. Instead of the one-dimensional representation of the SU(2), the SU(3) has to be represented in two dimensions, by having the hypercharge in the Y-axis. Figure 1.3 shows the two fundamental representations, **3** and $\bar{\mathbf{3}}$, for the quarks and the antiquarks respectively. Both representations contain an SU(2) doublet and an SU(2) singlet.

Mesons and baryons, as described by the constituent quark model, are composed from a quark and an antiquark for the former and three quarks for the latter. Even though the constituent quark model provides with a natural handle for structure, decays and an easy way to classify mesons, it is not perfect. It does not provide explanation for the confinement and the role of gluons is not obvious. Also, it does not make any absolute mass predictions and no absolute rate predictions for decays. An obvious way for someone to see its limitations, is the $\Delta^{++}(1232)$ baryon. It consists of three u quarks with parallel spins, all in an S-wave. Since quarks are fermions and in order for the Pauli principle not to be violated, these quarks can not be identical. The solution was an additional quark property, the color, to ensure antisymmetry of the baryon wave function. In quantum chromodynamics the color became a source of gluonic fields and resumed a decisive dynamical role. QCD allows for a much richer spectrum, where the three quarks determining the

spectroscopy are called 'valence' quarks. There is the 'sea' of quarks and antiquarks, which contains $q\bar{q}$ pairs of all flavors, with decreasing probability for increasing quark masses. Also, QCD allows for valence gluons, where the gluon field contributes to the observed quantum numbers, such as hybrids.

1.2 Light Meson Spectroscopy

The area of light-quark meson spectroscopy deals with mesons made up from u, d and s quarks. Usually, these systems have masses below 2.5 GeV/c^2. We want to express the meson system in J^{PC} quantum numbers and along with the amplitude analysis formalism that will be used, these quantum numbers can be identified experimentally. Mesons are built up from a fermion-antifermion pair and so the two intrinsic parities are opposite, i.e. $P = (-1)^{l+1}$, where l is the orbital angular momentum. On the other hand, for two mesons with the same intrinsic parity, $P = (-1)^l$. If the two mesons are spinless, such as pions, the orbital angular momentum is equal to the total momentum J. The next quantum number is the charge conjugation, C, where it does change the particle into its antiparticle. As one can imagine, only neutral particles are eigenstates of C. The charge conjugation for fermion-antifermion states is $C = (-1)^{l+S}$, since C exchanges position and spin. S is the total spin of the system. On the other hand, the charge conjugation of a meson and antimeson with zero spin (for example two pions) is going to be, $C = (-1)^l$. Another useful quantity that is usually defined is the G-parity. Even though it is not a fundamental quantum number, it is useful for pion systems. G is defined as C followed by a 180^o rotation around the y-axis in isotropic space, i.e. $G = exp(-i\pi I_y)C$. All charge pion states are eigenstates with negative eigenvalue, $G|\pi\rangle = -|\pi\rangle$. Also for a system of n pions we have $G = (-1)^n$.

Furthermore, since mesons, in the constituent quark model, are described as a $q\bar{q}$ system they must be a product of $\mathbf{3}$ by $\bar{\mathbf{3}}$, i.e.

$$\mathbf{3} \otimes \bar{\mathbf{3}} = \mathbf{1} \oplus \mathbf{8} \tag{1.3}$$

which describes exactly the meson nonet. Figure 1.4 shows an octet and a singlet in the isospin and hypercharge representation. At the "center" of the octet there are two states, one with I=1 and one with I=0, but both with $I_z = Y = 0$.

Considering now the spin-parity of the mesons, an S-wave will be the ground state, i.e. a $J^{PC} = 0^{-+}$ (pseudoscalar mesons) and $J^{PC} = 1^{--}$ (vector mesons). The SU(3) representation

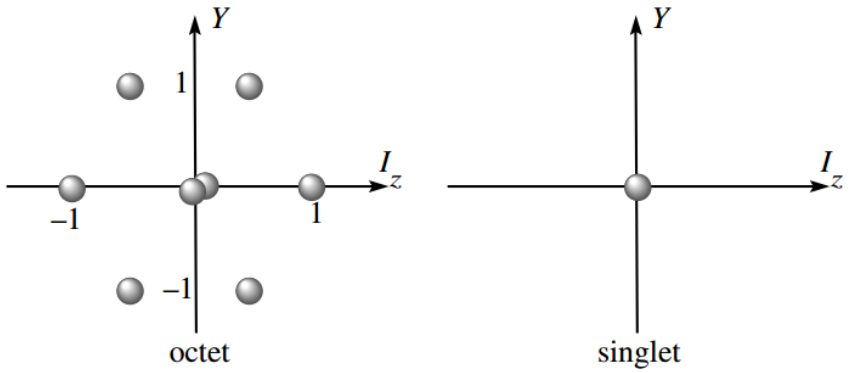

Figure 1.4: The octet and the singlet (Image source [2]).

of both are shown in Figure 1.5. One thing to notice here, is the isotopic singlet and the iso-singlet of the octet. The former is a complete symmetric state $|\eta_1\rangle = |\mathbf{1},\mathbf{1}\rangle = \frac{1}{\sqrt{3}}|u\bar{u} + d\bar{d} + s\bar{s}\rangle$ and the latter is given by $|\eta_8\rangle = |\mathbf{8},\mathbf{1}\rangle = \frac{1}{\sqrt{3}}|\bar{u}u + \bar{d}d - 2\bar{s}s\rangle$. Since SU(3) flavor symmetry is already broken (the particles in the mutliplets do not have the same mass) the $|\eta_1\rangle$ and $|\eta_8\rangle$ are not necessarily the physical states η and η'. For a correct description of these complicated mixtures of quarks-antiquarks pairs and gluons, can only be given by the QCD theory. Using the mentioned relationships, there are many other spin-parity states that can be constructed from $q\bar{q}$ mesons (apart from the pseudoscalar and vector mesons), such as $J^{PC} = 1^{+-}, 0^{++}, 1^{++}, 2^{++}, 2^{-+}, etc.$ By looking carefully at those states we can see that there is a sequence of J^{PC} states that is not allowed, i.e.

$$J^{PC} = 0^{--}, 0^{+-}, 1^{-+}, 2^{+-}, ... \tag{1.4}$$

The latter states are called exotics and by measuring one of these would mean that there must be a $non - q\bar{q}$ meson. As it was discussed before the quark model has no confinement and the gluons are not even needed in the picture. On the other hand, QCD-inspired models or lattice QCD say that glue has an extremely important role in Quantum Chromodynamics. When any model with glue makes predictions, gluonic excitation emerges and apart from the $q\bar{q}$ spectrum, additional states are predicted which directly involves the gluons. One state with only gluons is called glueball, while others involve gluonic excitations and are known as hybrids. Not all hybrids have exotic quantum

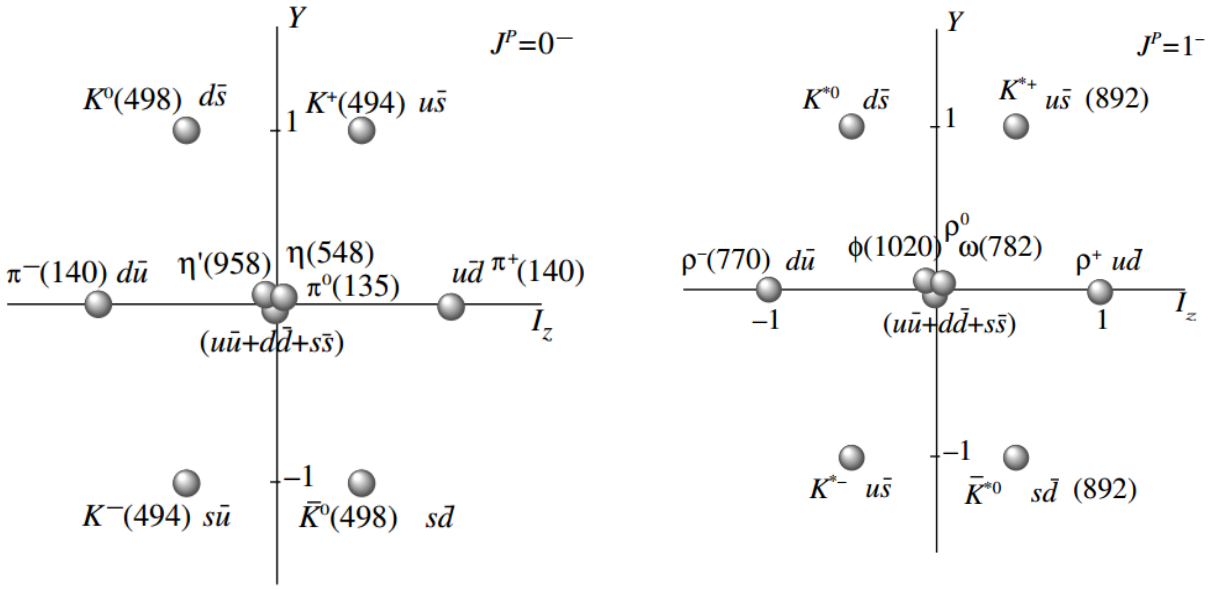

Figure 1.5: Two mesons nonet. The **left** picture shows the pseudoscalar mesons nonet and the **right** picture shows the vector mesons nonet. In parenthesis is an approximate value of their masses in MeV. (Image source [2]).

numbers and in fact one can write mesons as,

$$|meson\rangle = |q\bar{q}\rangle + |q\bar{q}g\rangle + |gg\rangle + ... \tag{1.5}$$

Since gluonic excitations can contribute to non-exotic mesons, such as ρ meson for example, the easiest way to find a gluonic excitation would be with quantum numbers that do not contain the $q\bar{q}$ component. These are the exotic hybrid mesons and the one that potentially could have access to, with the 3π final state and for CLAS energies, is the $J^{PC} = 1^{-+}$.

New models and concepts had to be invented in order to include some of the QCD properties, such as the bag and the flux tube model. The M.I.T. bag model [6] describes the hadrons in a compound system, consisting of quarks and gluonic field variables within a fixed volume. The model considers the states as linear combination of quark-gluon and gluon self interactions, with the lowest one to be a color singlet. It gives more precise predictions from the quark model for the non-exotic spectrum [7]. The lowest quark mode has $J^P = 1/2^+$ and the lowest gluon mode has

$J^{PC} = 1^{+-}$ and so it predicts four gluonic hybrids,

$$J^{PC} = (0^{-+}, 1^{--}) \otimes 1^{+-} = 1^{--}, 0^{-+}, 1^{-+}, 2^{-+} \tag{1.6}$$

The mass for the exotic $J^{PC} = 1^{-+}$ hybrid was predicted to be from 1.4 to 1.6 GeV [8], [9]. Another useful model is the flux-tube model [10]. In this model fixed endpoints are connected by a linear potential on which point like masses are stringed. The system can be treated as a quantum oscillator with transverse excitation modes. The flux-tube is permitted to vibrate, and its vibration modes give the measured quantum numbers. When the flux-tube is left in its ground state the ordinary meson spectrum, as predicted by the quark model, can be reproduced. In its first excited state, coupling one unit of orbital angular momentum of the excited string with the spin and orbital angular momentum of the $q\bar{q}$ system results to eight hybrid nonets (72 new mesons). The hybrids in this model are just $q\bar{q}$ excitations by considering the orbital radial and the gluonic excitations as natural degrees of freedom. From those new states, three do have exotic J^{PC} quantum numbers, $0^{+-}, 2^{+-}$ and 1^{-+}. The flux tube model predicts that the eight hybrid nonets are degenerate in mass at 1.9 GeV, though lattice QCD calculations show that the exotic 1^{-+} nonet is likely to be the lightest.

Undoubtedly the most famous tool for QCD predictions is lattice QCD (LQCD) calculations. In most recent medium energy experimental proposals LQCD predictions play a major role, especially for the non-pertrubative regime of QCD. Instead of a continuous space-time, QCD is formulated on a discrete space-time using increasingly large lattices, while also decreases lattice spacing, α. Discretization in the LQCD is obtained by defining quark field variables on the sides of a hypercubic space-time lattice. In the limit of $\alpha \to 0$, it transforms to a continuum field theory. Quarks and antiquarks do exist on the points of the lattice and the gluons represent the links between the lattice points. Even with modern developed clusters lattice calculations are computationally expensive and for results in a manageable amount of time unphysical large values of the quark masses and lattice spacing are being used. Since the results need to be extrapolated into the real world and the behavior of QCD with physical quark masses in unknown, usually the relative position of states is more reliable to be considered. Figure 1.6 shows recent lattice calculations [3] for isoscalar and isovector spectrum. Most of the known resonances can be identified, and in addition to the $q\bar{q}$ states, a hybrid super multiplet has been identified with $J^{PC} = 0^{-+}, 1^{-+}, 2^{-+}, 1^{--}$ quantum numbers.

Figure 1.6: Spectrum of isoscalar and isovector mesons obtained by LQCD. The candidate states for the lightest hybrid meson supermultiplet are indicated by the blue boxes and stars.(Image source [3])

Remarkably, those states have been predicted before by the bag and flux-tube model which makes those models still competitive with lattice calculations, thirty years after their first introduction.

Experimentally the reactions that are under study in this analysis are $\gamma p \to \pi^-\pi^-\pi^+\Delta^{++}$ and $\gamma p \to n\pi^+\pi^+\pi^-$. Both processes are considered to be diffractive dissociation (certain selection criteria enhance this), i.e. a peripheral high-energetic reaction via the strong interaction. The incoming high energetic photon, interacts with the cloud of virtual mesons of the proton, and forms an intermediate state X that decays into three pions. Since this is a strong interaction, parity and isospin is conserved and by performing partial wave analysis the contribution from different J^{PC} states can be studied. As it was discussed before, of particular importance is the $J^{PC} = 1^{-+}$ state, since LQCD calculations [3] predict it to be the lightest exotic hybrid meson. Several experiments have made observations of this exotic state, but the results are not without controversy.

There are three experimental candidates for the 1^{-+} exotic hybrid, the $\pi_1(1400)$, the $\pi_1(1600)$ and the $\pi_1(2000)$. The $\pi_1(1400)$ was observed by E852 [11], VES [12] and by Crystal Barrel [13]. The best experimental candidate of the three is the $\pi_1(1600)$, where it has been observed

decaying into $\rho\pi$ [14, 15, 16], $\eta'\pi$ [17, 18], $f_1(1285)\pi$ [12, 19] and $b_1(1235)\pi$ [12, 20]. The third 1^{-+} exotic candidate, the $\pi_1(2000)$, decaying into $f_1(1285)\pi$ and $b_1(1235)\pi$ has been observed by only one collaboration [19, 20]. For the current analysis, the three pion final state will potentially give us access to study the $\rho\pi$ mode of the 1^{-+} spin-parity exotic state. Though the $\pi_1(1600)$ is studied before by different experiments, the results are puzzled and there is controversy about the experimental findings. Even though the E852 [14] collaboration showed a clear peak of the 1^{-+} state at 1.6 GeV, recent results from some members of E852 collaboration, mostly from Indiana University, [21], including a higher number of waves on an extended data-set, decided not to claim the 1^{-+} as a resonance. Furthermore, the VES collaboration observed a spin-parity exotic state at 1.6 GeV [15] (it is worth mentioning that the $\eta'\pi$ is the cleanest and strongest evidence of the 1^{-+} state) it shows a much broader structure than the one found in the E852 analysis. Finally, the COMPASS collaboration claimed to see a resonant structure at 1.66 GeV for the 1^{-+} exotic state [16].

Most of the experiments that have searched for exotic hybrids, so far, have used pseudoscalar probes such as pion beams. Theoretical work by Close and Page [22] has shown that photoproduction can strengthen the production of gluonic hybrids. Furthermore, Szczepaniak and Swat concluded [23] that in protoproduction the $\pi_1(1600)$ exotic meson can be produced in equal amounts as the a_2 meson, where in pion production it will be suppressed by a factor of 10. Also in flux-tube model, excited flux-tubes can have ${}_{flux-tube}J^{PC} = 1^{+-} or 1^{-+}$ [24]. Using then a pion beam and coupling the quark degrees of freedom with an excited flux-tube will result to $J^{PC} = 1^{--}, 1^{++}$. On the other hand, using a real photon beam, and by considering the photon as vector meson, an analogous coupling will result $J^{PC} = 0^{-+}, 1^{-+}, 2^{-+}, 0^{+-}, 1^{+-}, 2^{+-}$. Consequently with a vector probe, the flux-tube model predicts exotic quantum numbers. Photoproduction area is considered unexplored until today, since there is very little photoproduced data world wide and even fewer with enough statistics for a partial wave analysis to be performed.

Based on those arguments the HyCLAS experiment was proposed in 2004 and the CLAS-g12 experiment took data in June 2008 at Jefferson Lab. The present analysis is using these data. In 2001 a large photoproduced 3π data sample was analyzed to search for the $\pi_1(1600)$ exotic. The experiment was completed in 2001 as part of the CLAS g6c run group at Jefferson Lab and a partial wave analysis was performed on 83K $\gamma p \to n\pi^+\pi^+\pi^-$ events [25]. No clear resonant structure

was observed in the partial wave intensity of the 1^{-+} exotic partial wave but the production of $\pi_1(1600)$ could not be ruled out as the partial wave phases were not observed. It is interesting to note here that the $\pi_1(1600)$ exotic meson has been observed in pion beam experiments in neutral exchange t-channel reactions. The two channels under study as well as the CLAS-g6c analysis are photoproduced charge 3π states.

Apart from the $\pi_1(1600)$ exotic meson, which is the major motivation for analyzing the two channels, other states do show particular interest as well. As it was said before, photoproduction is basically an unexplored area and mesons that have been observed with pion produced 3π system have not been observed in charge-exchange photoproduction. The $a_1(1260)$ and $a_1(1700)$ mesons are such examples. The former is constantly present in diffractive processes with pion beams, but its strength and decay width show some variations ($\Gamma = 250 - 600$ MeV/c^2 [26]). Also due to its large decay width, new models needed to explain it, such as a production process by a non-resonant 3π final state. This model was introduced by Deck [27], and further studies showed [28, 29] that the Deck effect is not a negligible effect for this resonance. Until now the mass, the width and the underlying process of the $a_1(1260)$ meson is not well understood [30]. Finally, the $\pi_2(1670)$ meson was discovered [31] in a partial wave intensity $J^{PC} = 2^{-+}$. A few years later a second resonance was observed [32, 33] with the same quantum numbers at 1.88 GeV. Various models try to explain this variation in mass of the $\pi_2(1670)$ either as a Deck-like resonance [34], or as a hybrid [35, 3].

1.3 The Rest of This Document

In order to further investigate this very interesting area of the 3π final state topology, an analysis of a 3π photoproduced data-set was performed. The data were obtained in 2008 using the CEBAF Large Acceptance Spectrometer (CLAS) at Jefferson Lab (JLab). The specifics of the CLAS spectrometer are described in Chapter 2 as well as the specific conditions for the CLAS-g12 run. 25B events were reconstructed for various topologies from this run. Initial selection criteria applied to both reaction channels are described in Chapter 3. For the $\gamma p \to \pi^-\pi^-\pi^+\Delta^{++}$ reaction 100M events were collected and certain selection criteria were applied (discussed in Chapter 4). In Chapter 5 the selection criteria for the $\gamma p \to n\pi^+\pi^+\pi^-$ reaction are described for the 700M events collected. Partial wave analysis is applied to both data samples and the formalism of it is described

in Chapter 6. The PWA results for the $\gamma p \to \pi^-\pi^-\pi^+\Delta^{++}$ reaction are described in Chapter 8, and in Chapter 9 the results for the $\gamma p \to n\pi^+\pi^+\pi^-$ reaction are discussed.

CHAPTER 2

THE CLAS DETECTOR AT JLAB AND THE G12 EXPERIMENT

The data analyzed in this work were collected during the g12 run period from the CEBAF Large Acceptance Spectrometer (CLAS) using the Continuous Electron Beam Accelerator Facility (CEBAF), located at Thomas Jefferson National Accelerator Facility (JLab). JLab, is located in Newport News, Virginia and it is one of the 17 national laboratories funded by the U.S. Department of Energy. The g12 experiment collected over 126 TB of raw data in 44 days of beam time from April to June 2008. By that time, JLab had three Halls, A, B and C and the CEBAF Accelerator was able to deliver a continuous-wave electron beam of up to 6 GeV (shown in Figure 2.1). The capabilities and the configurations that are discussed in this Chapter refer to the conditions of the lab for the period that the data were acquired (around 2008). Currently, the JLab site houses four Halls (the three previous Halls and in addition Hall D) and the CEBAF Accelerator can provide, eventually, up to 12 GeV electron beam.

For the g12 run three CLAS proposals (04-005 [36], 04-017 [37] and 08-003 [38]) defined the experimental and theoretical basis of the data taken. The 04-005 experiment, also called HyCLAS, focused on meson spectroscopy with multiple charged final states particles. The primary difference with other CLAS experiments was that the target was pulled up-stream in order to have better acceptance for the forward going particles and so to favor meson spectroscopy.

2.1 CEBAF Accelerator

The CEBAF accelerator is able to deliver up to 6 GeV electron beam with 75% polarization. The cluster of electrons, in the continues-wave beam is separated by 2 ns. Typical intensities for the beam current in Hall B is 10-100 nA, in contrast with Hall A and C which are 10-100 μA.

Electron's journey begins in the injector, where electrons are produced by shooting pulse laser to a GaAs photo-cathode. The laser pulses are fixed that way so that each Hall is able to receive electrons every 2 ns. From the injector the beam is traveling to the main accelerator where a

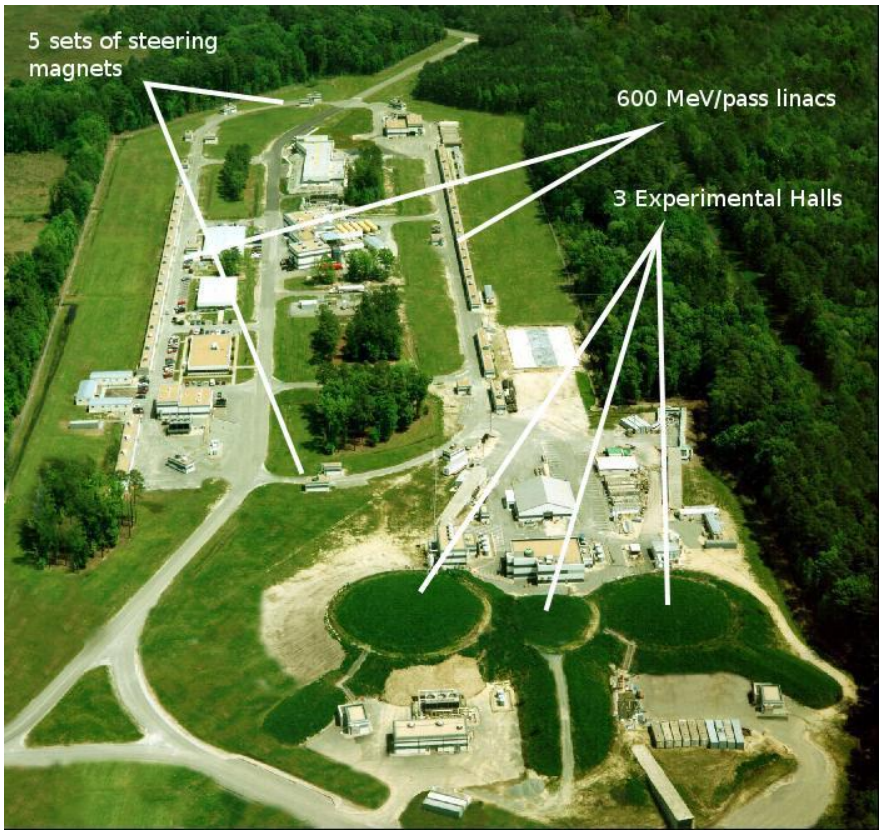

Figure 2.1: Aerial view of the Jefferson Lab (JLab) facing east. (Image source: [4])

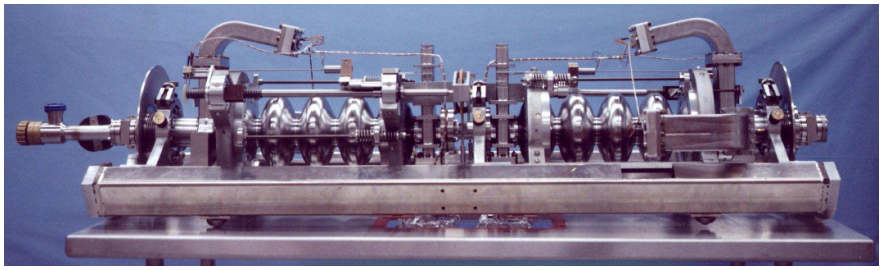

Figure 2.2: A superconducting niobium cavity pair with its support hardware. Its length is mechanically adjusted for specific resonances. (Image source: [4])

chopping system of superconducting radio-frequency (SRF) cavities accelerates further the beam. In normal conditions, three beams were produced in the injector with a frequency of 499 MHz and 120 degrees phase separation. This is to allow for all the three Halls to operate simultaneously.

The main accelerator consists of a pair of linear accelerators (LINACs) which consist of twenty cryomodules each containing eight superconducting niobium cavities as shown in Figure 2.2. The LINACs are connected by two sets of 180^o magnetic-dipole bending arcs with a radius of 80 meters (shown in Figure 2.3). After the first trip through linac, electrons are passing through a different set of magnets according to their momentum. These electrons are getting 1.2 GeV per pass and usually they travel up to five times around, before being delivered to each Hall. Each of the first four passes can deliver beam to only one hall at a time, however the fifth and final pass can sent beam to all three halls almost simultaneously (separated by 2.004 ns).

2.2 Radiator and Electron Tagger

CLAS has been used for experiments using electron beam and photon beam. The g12 experiment was a photon run. The accelerator delivers to the tagger Hall, a 5.7 GeV electron beam, and considering the detection system in the tagger Hall, this translated to a photon energy range of 1.2 to 5.4 GeV.

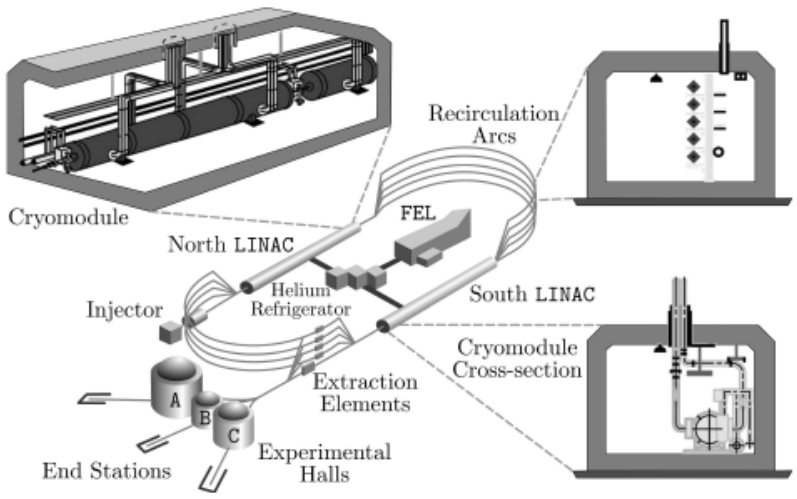

Figure 2.3: The Continuous Electron Beam Accelerator Facility (CEBAF) components. The picture shows the linear accelerator (LINAC), the three Halls, the Free Electron Laser (FEL) and the helium refrigerator (FEL).(Image source: [4])

In order to produce real photons the electrons passed through the radiator, a gold foil 10^{-4} radiation lengths thick. Then the electrons were decelerated, interacting with the radiator, and produced a bremsstrahlung photon. The scattered electrons were bended using a dipole magnet. The photons passed through a 6.2 mm diameter collimator before they entered the target which had a radius of 2 cm. Thin radiator was used to ensure a singe electron is correlated with a singe photon.

In order to get energy and timing information of the photon beam, the scattered electrons needed to be detected. Specifically, two arrays of scintillators were used, the E-counters and the T-counters (shown in Figure 2.4). The first layer is the E-counters, consisting of 384 scintillators. With a known generated magnetic field from the dipole and by knowing the position of the scattered electron in the E-counter, the energy of the electron can be measured (and so of the photon). The second layer of scintillators (61 in number) are the T-counters and are responsible for timing information of the scattered electrons. This time combined with timing information from the CEBAF and the timing information from the Start Counter will tell us which beam bucket caused the event to occur.

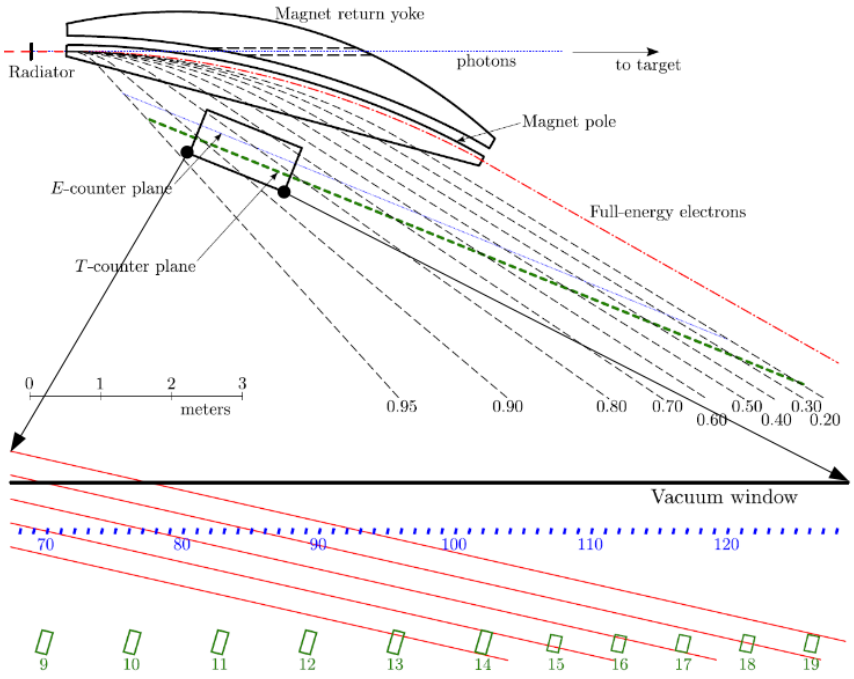

Figure 2.4: Scale drawing of the photon tagger system. The blue dot-dashed line represents the E-counters and the green dot-dashed line represents the T-counters. The dashed red line shows scattered electrons that have not lost any energy. The black dashed lines are scattered electrons, which they have produced a bremsstrahlung photon and now carry the labeled fractional energies.(Image source: [4])

Figure 2.5: The 40 cm long cylindrical Kapton target cell used for the g12 run. (Image source: [4])

2.3 Hydrogen Target

The target that was used for the g12 experiment was a cylindrical liquid hydrogen (H2) cell made of Kapton 40 cm in length (shown in Figure 2.5). The cell was 2 cm in radius while the photon beam had a radial size of approximately 1.5 cm as it exited the target. The typical position of the target for CLAS experiments was at its center. This is a well defined point inside region one of the drift-chambers. This setup is ideal for energies below 4 GeV and optimizes detection for large angle tracks. For the g12 experiment, the target was placed 90 cm upstream of CLAS center which yielded a geometric acceptance starting at approximately 6^o from the beam-line (compared with 8^o with the previous configuration). Also by moving the target upstream, CLAS was optimized for small angle track detection. The drawback, from this different configuration, was that the acceptance for large angle tracks was reduced from 140^o to 100^o in the lab frame. Furthermore, the drift-chamber resolution was decreased due to the oblique angle the tracks made with the detector planes and the geometric acceptances at large angles decreased in the same way for each subsystem.

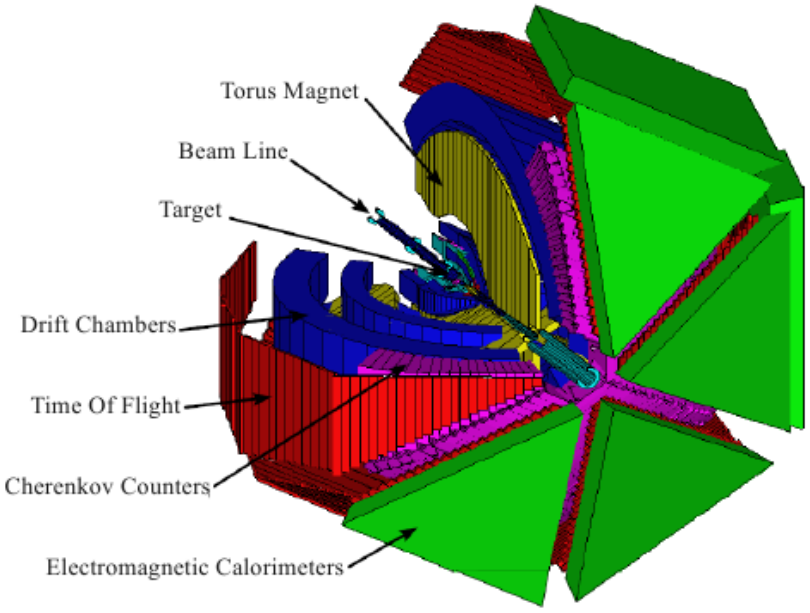

Figure 2.6: 3D schematic picture of the CLAS detector, looking upstream and the beam is coming from the upper left.(Image source: [4])

2.4 The CLAS spectrometer

The CEBAF Large Acceptance Spectrometer (CLAS) consists of six segments in ϕ (angle about the beam line), called sectors (as shown in Figures 2.6, 2.7). Each of those sectors covers approximately $\frac{3}{4}\pi$ radians in θ (angle from the beam line). Each segment consists of a scintillator start counter (ST), three layers of drift chambers (DC), a gas Cerenkov counter (CC), a series of scintillator time-of-flight (TOF) counters and an electromagnetic calorimeter (EC). There is a toroidal magnetic field concentrated in the middle DC layer which bends negative charged particles towards the beam line and positive charged particles away from the beam line. Most of the subsystems provide ADC and TDC information and the total number of electronic channels recorded by the data acquisition system from all the subsystems is up to 40,000.

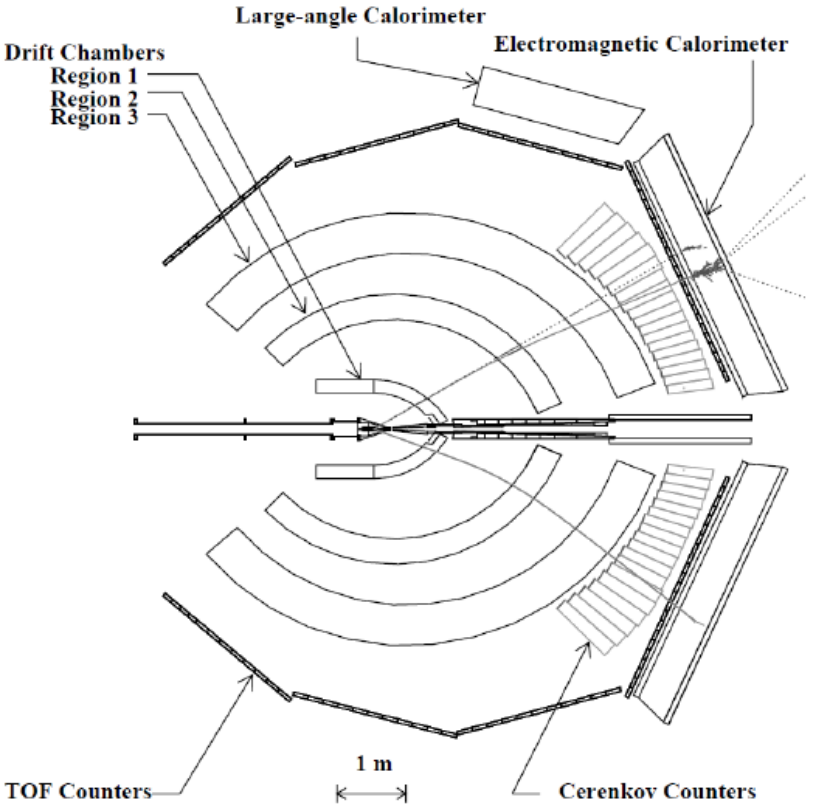

Figure 2.7: Cross section of the CLAS detector showing an event with a photon, electron and a proton track.

2.4.1 Start Counter

After the photons interact with the target the first detector that the produced particles encounter is the start counter (ST), as shown in Figures 2.8, 2.9. The ST consists of 24 scintillator paddles which surrounds the 40 cm target hermetically. Even though the read out gives both ADC and TDC information, in the reconstruction process only the timing information was used in order to identify the hit in the tagger associated with the event. The ST is capable of 350 ps timing resolution.

Once there is an event, it will have multiple tracks in the drift chambers. For each of those tracks, most likely, a hit will be registered in the ST and the TOF. Having the path length from the drift chambers and the difference in time between the TOF and the ST, the velocity can be derived. So the ST plays a crucial role for the Particle Identification (PID). Also working backwards, the track can be propagated from the ST to the event vertex and find the time that the event occur. For events with multiple tracks, there are going to be multiple times that the event occur, so the average of them has been taken and compared with a list of hits in the tagger in order to select the in time photon. Finally, the ST was also used in the triggering scheme for the g12 runs.

2.4.2 Drift Chambers and the Superconducting Toroidal Magnet

The primary subsystem of the CLAS detector is the drift chambers (DC). Each of the six sectors of CLAS, consists of three layers of drift chambers, as shown in Figure 2.7. Each region of the DC consists of two superlayers, which consists of 20-m diameter gold-plated tungsten sense wires (sense wires) and 140-m diameter gold-plated aluminum field wires (field wires). The field wires were kept at high negative voltage and the sense wires were kept at moderate positive voltage. The gas that was used in the DC for ionization is a mixture of 90% argon and 10% carbon-dioxide. Finally the DC was only able to give TDC information and no ADC. As a consequence, the energy loss of particles passing through the DC had to be measured using other subsystems, such as the TOF.

Furthermore the toroidal magnetic field in CLAS was created by six iron-free superconducting coils (as shown in Figure 2.10) and made the charged particles to bend away or towards the beamline. Figure 2.11 shows the cross section of the toroidal magnetic field. The magnetic field in region 2 is relative stronger compared to regions 1 and 3. Tracks entering this field are bend only in polar angle (except near the coils, see Figure 2.12) and thus they keep their azimuthal angle along

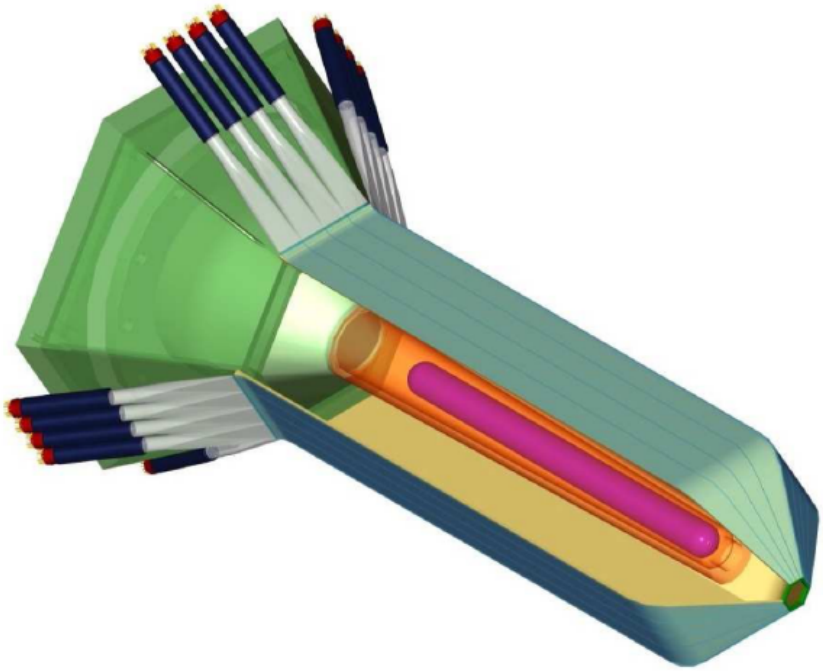

Figure 2.8: Schematic picture of the start counter with the 40 cm long target cell inside. The beam enters from the upper left. (Image source: [4])

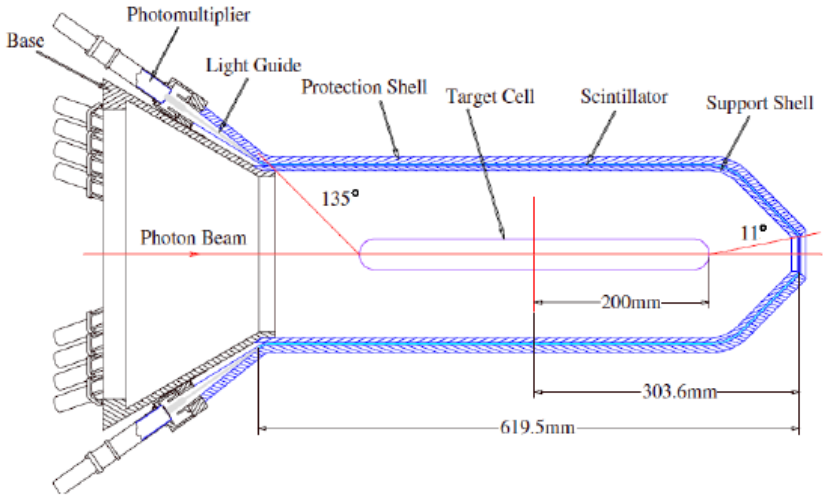

Figure 2.9: Diagram of the cross section of the start counter along the beam line.(Image source: [4])

their trajectory and they rarely travel between sectors. This configuration simplifies the tracking algorithm, but negative charged particles that bend back towards the beamline will not be detected. The charge and momenta of the particles are determined by measuring the deflection angle of the tracks.

2.4.3 Cherenkov Counter

The Cherenkov Counters (CC) are placed between the DC and the TOF detector. They are divided into 18 segments in the polar angle away from the beam line (shown in Figures 2.13 and 2.14). It follows the CLAS geometry, and so it has been divided into six segments. The CC covers a polar angle from 8^o to 45^o for events that occurred from the center of CLAS. Since the target for the g12 runs was 90 cm upstream, the angle coverage is moving from 6^o to 35^o. The gas that was used in the CC is perfluorobutane (C_4F_{10}) with an index of refraction of 1.00153. It primary purpose is lepton-pion separation since the threshold for kaons and protons is much higher than the maximum beam energy for the CLAS-g12 run.

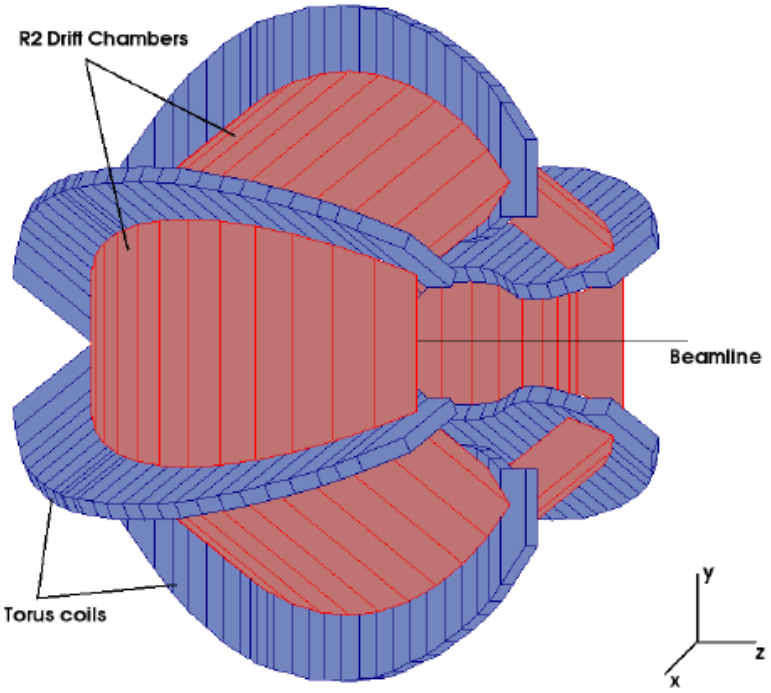

Figure 2.10: A GEANT geometry drawing of the torus magnets and the R2 drift chambers. (Image source: [4])

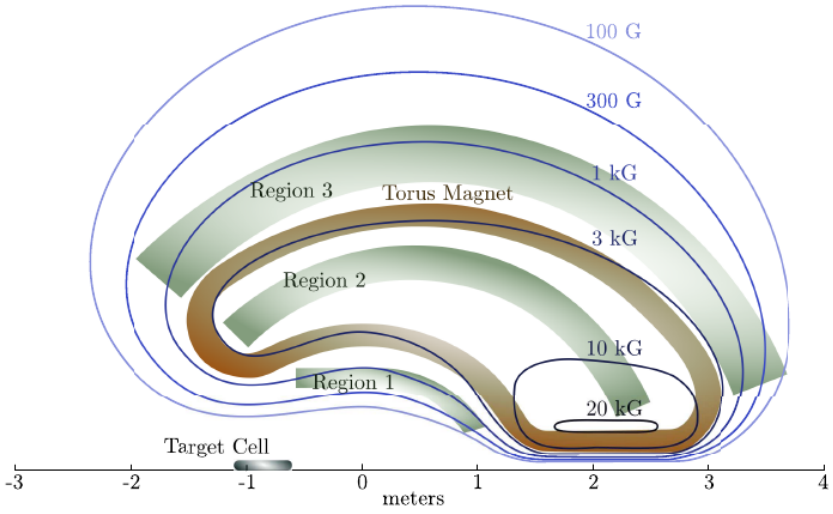

Figure 2.11: Schematic picture of the cross section of the toroidal magnetic field. For the g12 run the magnets operated at half capacity current (1930 A) giving the maximum magnetic field at 20 KG. The Region 2, which has the strongest magnetic field, is located inside the torus magnets (see Figure 2.12).(Image source: [4])

2.4.4 Time-of-Flight Detector

The TOF detector follows the CLAS geometry and it was divided into six shells, in the outside of the CC detector. One of the shells is shown in Figure 2.15 and it is made of 57 scintillator paddles. The paddles are all 5.08 cm thick and their length varies. Also each of the paddles has two photomultiplier tubes attached in each end and it gives both ADC and TDC information. The timing resolution of the TOF is 150-200 ps and one of its primarily usage is PID. Also due to its fast response time it was used in the level 1 trigger. The ADC signals from the TOF were primarily used for calibration purposes, but it is also possible to perform rudimentary particle identification by examining the energy deposited by tracks passing through the TOF.

2.4.5 Electromagnetic Calorimeters

The final layer of the CLAS detector is the Electromagnetic Calorimeter (EC). The EC was essential for experiments that used electron beam where in conjunction with the CC, scattered beam electrons can be detected. Also another usage of EC is the reconstruction of high energy

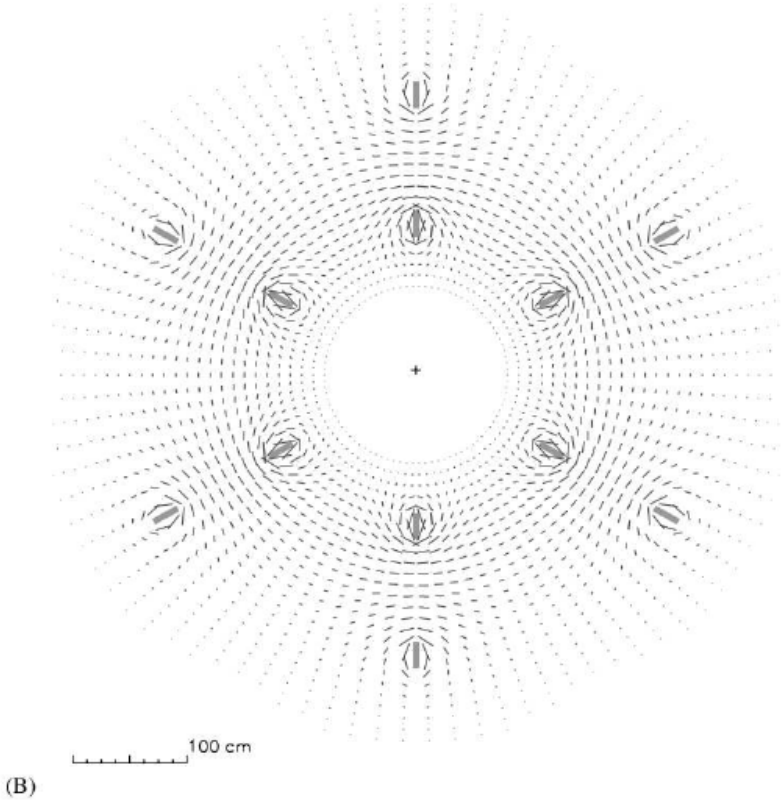

Figure 2.12: The CLAS toroidal magnetic field line diagram looking downstream. The length of each line segment is proportional to the field.(Image source: [4])

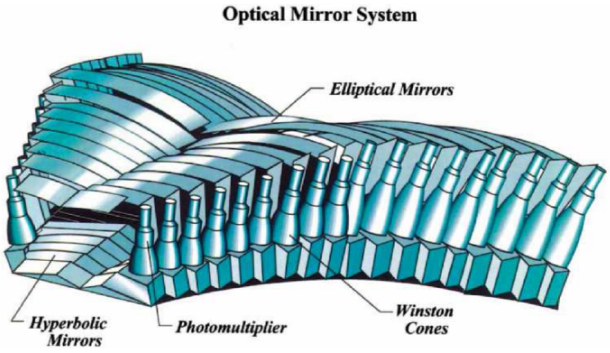

Figure 2.13: 3D schematic picture of the Cherenkov counters. It shows the 18 symmetrical mirrored segments of the CLAS CC.(Image source: [4])

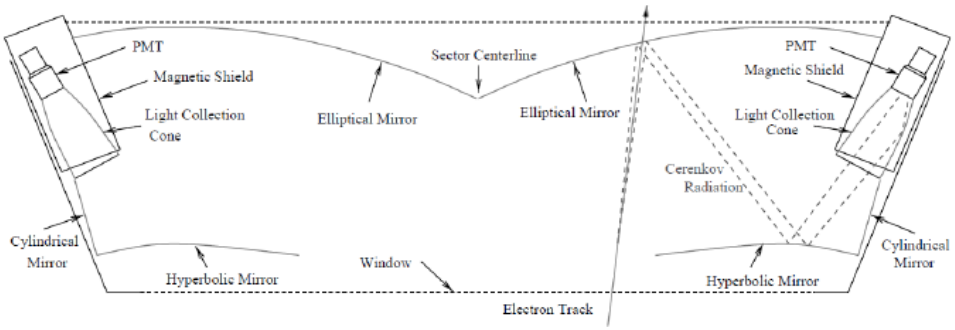

Figure 2.14: The picture shows one segment of the Cherenkov counters with an electron entering from the bottom.(Image source: [4])

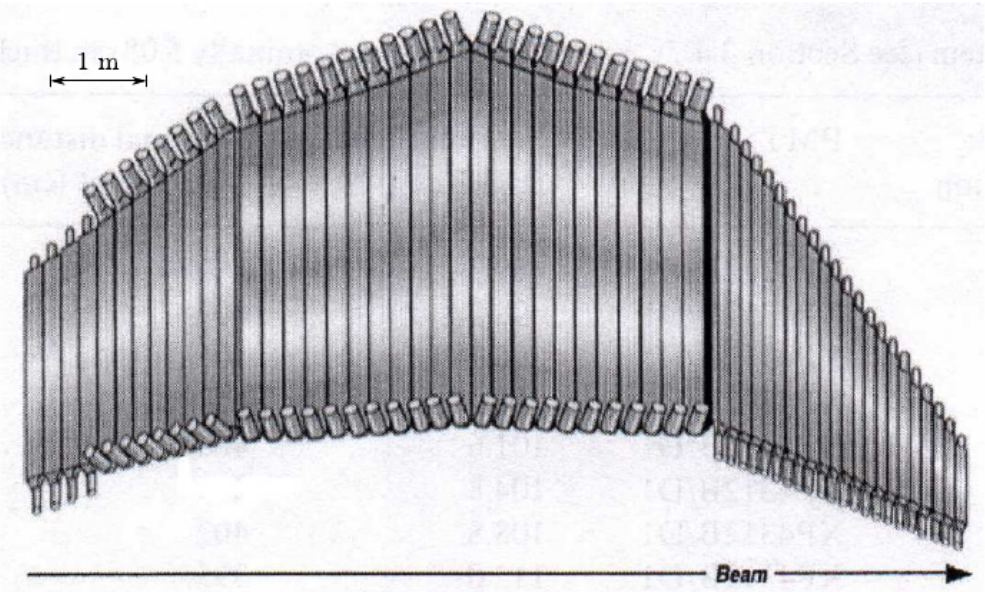

Figure 2.15: The picture shows the arrangement of the time-of-flight paddles for one sector. There are 57 scintillator paddles covering the entire acceptance region of the drift chambers for each sector.(Image source: [4])

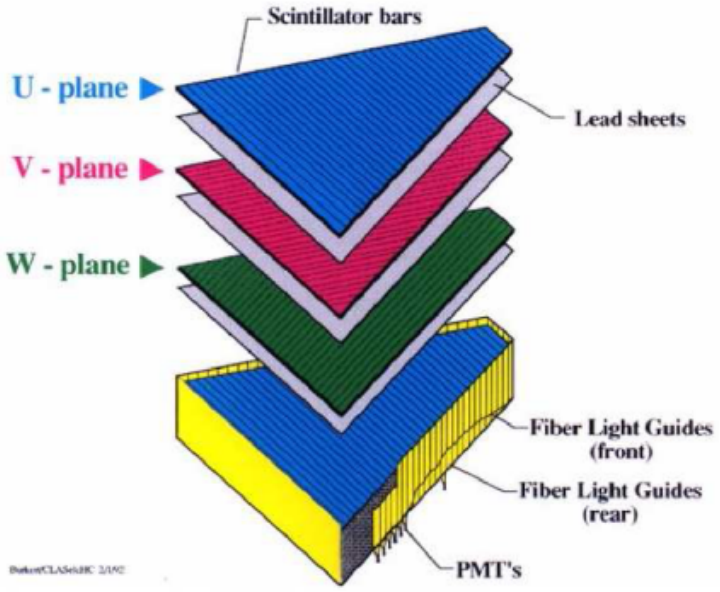

Figure 2.16: Schematic view of the Electromagnetic calorimeter for one sector. The picture shows the three planes (u, v, w) of scintillator-lead pairs which make up one of the 13 logical layers. (Image source: [4])

neutral particles, such as photons. The structure of the EC is an equilateral triangle and each layer of scintillator consists of 36 strips (shown in Figure 2.16). It is divided into an inner and outer layer. The inner section consists of 8 logical layers of lead and scintillator, each of them is made of three scintillator-lead layer pairs, labeled as u, v and w. The outer section consists of 5 logical layers. There are a total of 39 scintillator-lead layer pairs in each sector of the EC. Finally, since the EC can provide energy loss information, it can be used in the PID as well.

2.5 g12 Data Acquisition System and Trigger Configuration

When an event occurs, hundrents of hits will take place in various detector subsystems and ADC and TDC signals are generated. The data acquisition system (DAQ) of CLAS consists of several layers of electronics. The total number of channels in the CLAS detector is 40K composed of all the individual detector elements. Most of the subsystems, in the CLAS detector, have ADC and TDC counters. Thus when a signal is generated, above some particular threshold, information

is recorded. Since the total storage and the bandwidth to mass storage have their limitations, certain criteria must be given to the system. Certain sets of these signals are used in the trigger to determine if an event does meet those criteria to be recorded. Then all the signals, for that particular event, are sent to the event builder and recorded as a signal event.

The main production trigger for g12 run was a tagged photon above 4.4 GeV (first 19 paddles of the tagger) and at the same time a coincidence of two charged tracks in different sectors. The tracks were identified at the trigger level by a coincidence of a start counter hit and a time-of-flight hit in the same sector. Figure 2.17 shows the $''ST \times TOF''$. The DC was not used in the (L1) trigger, due to its slow time response (compared to the ST and TOF). Since the TOF and the ST can give only six signals (one for each sector), the triggering on two tracks in the same sector was not possible. The DC was possible to be used in the trigger by a second lower level (L2) mode which would require a track reconstruction of the event. Other noticeable triggers were, three charged track events with any beam energy photon and the lepton trigger (EC and CC coincidence above a certain threshold).

The DAQ rates for the g12 run reached 8KHz. At the end, 622 good runs were recorded with approximately 50 million triggers in each. A total of 26B events were written to tape, occupying 121 terabytes of disk space on the Jefferson Lab mass storage system.

2.6 Raw Data Reconstruction

The reconstruction process starts by reconstructing the tracks and their subsequent identification by using the a1c program. Data is recorded to disk in finite intervals of time, in an event based format. The first step is the hit-based tracking where the timing of the hits was not taken into account. The DC hits were created by particles passing through the DC detector. The triggered wires were filtered for noise, isolated hits were not selected, and the remaining hits were grouped into clusters for each superlayer. The hits in each cluster were linked together and then the track segments were linked from superlayer to superlayer. From the track candidates the midpoint and the local angle was recorded for each superlayer and compared with the prlink table. This table was created by simulating tracks from a random sampling to travel through the CLAS magnetic field. Various momenta and vertex positions were linked that way.

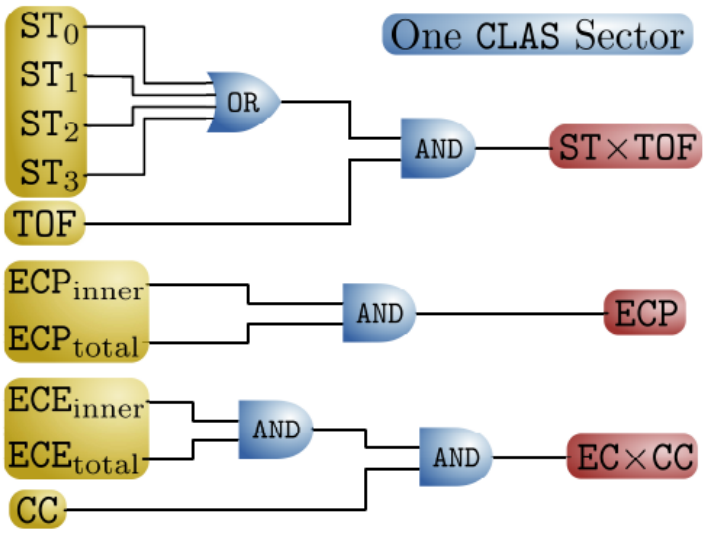

Figure 2.17: Trigger logic for one of the six sectors of CLAS. The $''ST \times TOF''$ signal is a coincidence between any of the four start counter TDC signals (numbered from 0 to 3) and any of the 57 TOF TDC signals. The ECE_{inner} and ECE_{total} are the electron-threshold EC signals for the energy deposited in the inner layer and in all layers. These are combined with a CC signal to produce the $''EC \times CC''$ trigger for this sector. The ECP trigger signal is the photon-threshold EC signal.

Since there is no timing information yet for those tracks, the PID is still ambiguous. Each of the hit based tracks is then associated with a hit in the TOF detector. This reduces the clusters in the DC from multiple hit based tracks to one time based track. The tracks then refitted up to two more times in order to get the final momentum and event vertex measurements. Finally the tracks are matched with the ST, EC and CC when those subsystems have an in-time hit.

Finally the reconstruction algorithm will do the PID for each track, assigned well known states to them. Experimentally, the mass of the particles can be calculated for each track and based on this measurement the mass from the PDG tables can be assigned. The speed of each particle can be calculated as:

$$\beta_{ST-TOF} = \frac{l_{ST-TOF}}{ct_{TOF} - t_{ST}} \tag{2.1}$$

where the difference of the times from the time-of-flight (t_{TOF}) and the start counter (t_{ST}) was used, along with the path length from the ST to the TOF (l_{ST-TOF}). In case where the ST hit was not in time with the track, β was calculated with the RF-corrected tagger vertex time ($t_{VTX}(TAG_{RF})$:

$$\beta_{VTX-TOF} = \frac{t_{TOF} - t_{VTX}(TAG_{RF})}{cl_{TOF}} \tag{2.2}$$

Having the β from the PID detectors and the momentum (p) from the DC (with the help from TOF and ST as well), the mass of the particle can be calculated from the following equation:

$$m = \frac{p\sqrt{1-\beta^2}}{\beta} \tag{2.3}$$

The initial identification considered only pions, kaons, protons and deuterons. Electrons and muons were identified using the EC and CC information in a later stage. The following thresholds were used before the mass from the PDG tables (m_{PDG}) was assigned:

$$\text{Particle ID} = \begin{cases} \pi & \text{if } m < 0.3 \text{ GeV} \\ K & \text{if } 0.35 < m < 0.65 \text{ GeV} \\ p & \text{if } 0.8 < m < 1.2 \text{ GeV} \\ d & \text{if } 1.75 < m < 2.2 \text{ GeV} \end{cases}$$

In order to have all four momentum components of the particle, the last remaining is its energy. By knowing the momentum and the mass of the particle it can be calculated from the following equation: $E^2 = m_{PDG}^2 c^4 + |\vec{p}^2| c^2$

CHAPTER 3

INITIAL SELECTION CRITERIA APPLIED TO BOTH $\gamma p \to \pi^-\pi^-\pi^+\Delta^{++}$ AND $\gamma p \to n\pi^+\pi^+\pi^-$ REACTION CHANNELS

The data-set from the CLAS-g12 experiment consists of 622 runs with approximately 50M events in each run. After processing these events through the CLAS event reconstruction software, the first step of this analysis was to select events with two positive and two negative detected charged pions for the $\gamma p \to \pi^-\pi^-\pi^+\Delta^{++}$ reaction and two positive and one negative detected charged pions for the $\gamma p \to n\pi^+\pi^+\pi^-$ reaction. In addition, the missing mass (determined through energy and momentum conservation) was required to be consistent with that of the missing proton for the former reaction and a missing neutron for the latter.

After the reconstructed data have been selected according to the desired topology, corrections and specific selection criteria were applied in order to improve the quality of the final data sample. In this Chapter the selection cuts applied to both reaction channels are described.

3.1 Kinematic Corrections to the Reconstructed Four-Vectors

Three post-processing corrections were applied to the reconstructed data. The first correction was to account for the energy loss of the detected charged particles due to their interactions with materials in the detector. Specifically, the standard CLAS ELOSS [39] package was used to account for the energy loss in the hydrogen target and the start counter. Without such correction, the momentum of the track reconstructed in the drift chambers will be less than its true momentum at the production vertex.

The next correction applied was the beam energy correction. Due to the tagger magnet hysteresis, a systematic run-dependent effect was introduced in the calculation of the momentum of the recoil beam electron through its bend in the tagger magnet field, leading to a small shift of the calculated photon beam energy [40]. This particular correction is important for inclusive events, where one of the final state particles is being identified via energy and momentum conservation.

The last correction applied to the reconstructed four-vectors is the momentum correction. It was found that the momentum of each track, provided by the drift chambers, has a systematic shift within each sector depending on the azimuthial angles ϕ of this track [40]. This effect is due to limited knowledge of the deviations of the real magnetic field of CLAS torus from the magnetic field map used in the reconstruction software.

3.2 Event Vertex Selections

The location of the event vertex is estimated by extrapolating the tracks back to the target. A fraction of the photon beam can interact with the target walls and its support structures instead of the target hydrogen. These cuts are designed to eliminate events originating from the interactions outside of the hydrogen volume. To achieve this, the geometry of the target needs to be considered as well as the positional resolution of the tracks reconstructed in the drift chambers. The target was centered at 90 cm upstream of the geometrical center of the detector, and it was 40 cm in length. Also, the hydrogen cell of the target was 2 cm in radius while the photon beam had radial size of approximately 1.5 cm. Consequently, the requirement was imposed that that the Z-component of the event vertex is located from -110 cm to -70 cm along the beam line. This cut eliminates less than 5% of the original event statistics for the $\gamma p \to \pi^-\pi^-\pi^+\Delta^{++}$ reaction and around 7% for the $\gamma p \to n\pi^+\pi^+\pi^-$ reaction. Taking into account the resolution of the vertex reconstruction in the transverse direction, events were chosen beyond the geometrical radius of the target but not beyond the start counter. Specifically, event vertex radius was chosen to be smaller than 10.0 cm (the distance from the beam axis to the closest point of the start counter is 10.35 cm). With the applied cut, 7% of the events were rejected for the $\gamma p \to \pi^-\pi^-\pi^+\Delta^{++}$ reaction and 10% for the $\gamma p \to n\pi^+\pi^+\pi^-$ reaction. Note that if one to chose this cut to be strictly at the 2 cm radius of the target then a loss of 33% of the events would occur for the $\gamma p \to \pi^-\pi^-\pi^+\Delta^{++}$ reaction. Figure 3.1 shows the distribution of the event vertex components for the reconstructed events.

3.3 Timing Selections

CEBAF delivers electron beam in short bunches with 2.004 ns period. In order to do time-of-flight based particle identification, the exact RF bunch of the beam photon which caused the event needs to be determined. The accelerator provides very accurate RF timing of each electron

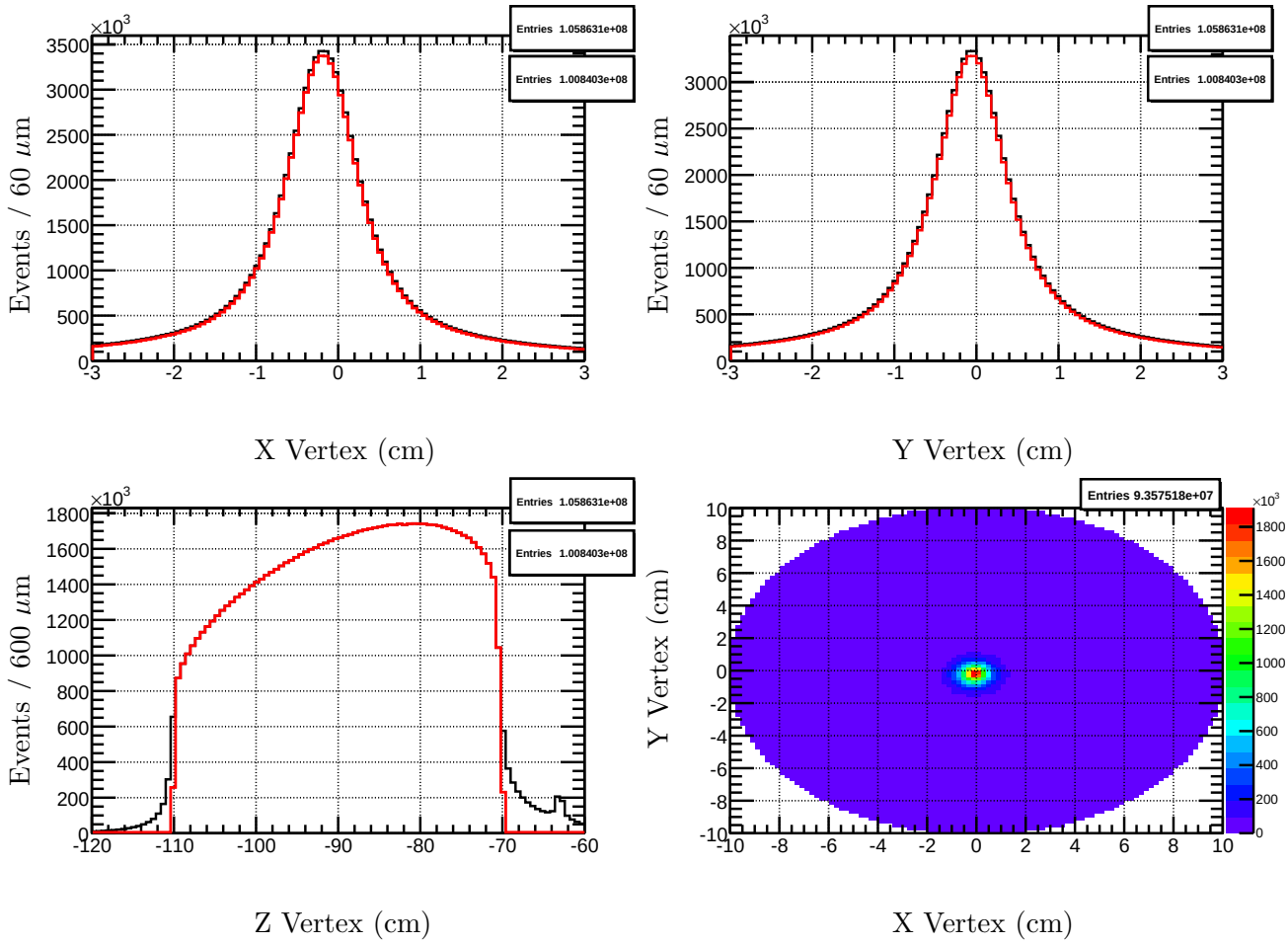

Figure 3.1: $\gamma p \rightarrow \pi^-\pi^-\pi^+\Delta^{++}$: X, Y and Z vertex components of the selected $p\pi^-\pi^-\pi^+\pi^+$ events. The red histograms show the effect of the z selection, where the radius vertex plot has additionally $r < 10$ cm selection.

beam bunch entering the tagger hall. This time can be propagated to the radiator location. Simultaneously, time of the hits from a recoil beam electron in the tagger counters is measured as was discussed in Chapter 2. By matching this tagger time with RF time at the radiator, the correct photon beam bucket can be determined for each beam photon whose energy was deduced from the tagger measurements. Such photons will be referred to as in-time photons. By propagating their timing further from the radiator to the event vertex, the "RF vertex time" is defined.

Another quantity that is used for PID is the detector vertex time. This is defined as the time of a hit in this detector minus the propagation time along the path from the vertex to the detector. The most useful time for the identification of the beam photon which caused the interaction in the target is the start counter time. Because of its proximity to the target, the propagation time from the vertex to the start counter (including variations of this time due to track angles and particle type) is smaller than the period of RF bunches. This allows to match the event recorded in the start counter with a proper in-time beam photon.

To that end, the Δt_{tvx} is defined as the difference between the RF vertex time, $t_{vtx}(TAG)$, and the start counter vertex time, $t_{vtx}(ST)$. Figure 3.2 shows the Δt_{tvx} distribution. Events were selected to be within $\pm$ 1.002 ns of Δt_{tvx} value of zero.

3.4 Beta Selections

The quantity $\beta = \frac{v}{c}$, where v is the velocity of the track and c is the speed of light, can be obtained in two different ways. First, it can be derived from the TOF detector. By combining the time of the TOF hit, the event RF corrected start time and the length of the trajectory from the vertex to the TOF, the β_{TOF} is calculated. Second, β for a particle of a particular mass can be derived from the momentum of the track obtained from the curvature of its trajectory through the drift chambers in the known magnetic field:

$$\beta^2_{p/m} = \frac{p^2}{m^2_{PDG} + p^2}, \tag{3.1}$$

where p is the momentum of the particle, and m_{PDG} is the mass of the particle from the Particle Data Group table, [41]. After making a hypothesis about the particle type, two values of β are matched with each other to select only cases consistent with this particular hypothesis. Figure 3.3 shows the $\delta\beta$ for the $\gamma p \to n\pi^+\pi^+\pi^-$ reaction, with $\delta\beta = \beta_{TOF} - \beta_{p/m}$, which has been fitted with

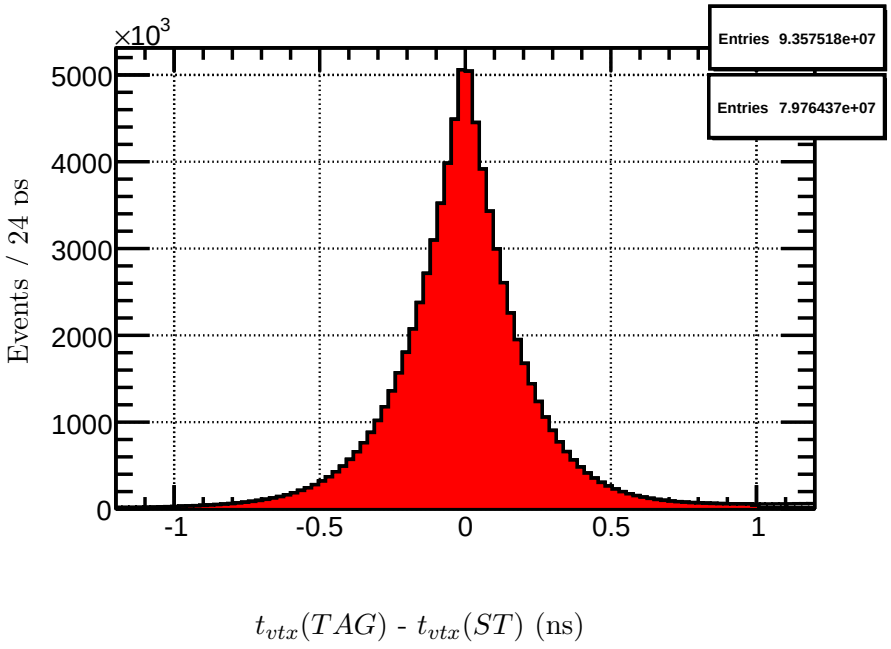

Figure 3.2: $\gamma p \to \pi^-\pi^-\pi^+\Delta^{++}$: Difference between event-vertex time as calculated by the RF-corrected tagger and start counter. The red histogram shows the events that pass the 1.002 ns selection.

a Gaussian distribution. In this analysis for the $\gamma p \to n\pi^+\pi^+\pi^-$ reaction the π^+_{slow} is defined as the positive pion with the smaller magnitude of momentum whereas π^+_{fast} is the positive pion with the larger magnitude of momentum. In the same way for the $\gamma p \to \pi^-\pi^-\pi^+\Delta^{++}$ reaction the π^+_{slow}, π^+_{fast} and π^-_{slow}, π^-_{fast} are defined. Figure 3.4 shows the $\delta\beta$ for the $\gamma p \to \pi^-\pi^-\pi^+\Delta^{++}$ reaction. The fit shows that events with $|\delta\beta| > 0.03$ don't follow a Gaussian distribution.

A useful plot to study the quality of the events with $|\delta\beta| > 0.03$ is the missing mass distribution. Figure 3.5 shows the missing mass distribution for events with at least two charged tracks with $|\delta\beta| > 0.03$ for the $\gamma p \to n\pi^+\pi^+\pi^-$ reaction and the missing mass distribution for events with at least two charged tracks with $|\delta\beta| < 0.03$. Events with $|\delta\beta| > 0.03$ for all three charged tracks have a reasonable missing mass distribution. For the majority of these events, a timing mistake was made for a bad track, i.e., an incorrect TOF TDC hit was selected from an earlier interaction or noise instead of the proper later hit. It appears that there is no good reason to reject such events - they are still well-measured kinematically and the bad track is likely to be a pion anyway (due to dominance of the pion production over Kaon/proton, and good identification of the other pions in the reaction). On the other hand, events with multiple tracks with large β discrepancy are likely caused by an incorrect in-time photon assignment to the event. This may happen if a proper beam photon was not registered by the tagger, and the next best in-time photon is selected. Such photon, being from a different RF bunch, will distort both the PID timing and the missing mass calculations. Such events are needed to be rejected. Having that in mind, for the $\gamma p \to n\pi^+\pi^+\pi^-$ reaction out of three charged tracks, at least two tracks are required to have good $\delta\beta < 0.03$. In the same way, for the $\gamma p \to \pi^-\pi^-\pi^+\Delta^{++}$ reaction events with $|\delta\beta| > 0.03$ for at least three charged tracks are not selected for this analysis. Figure 3.6 shows the missing mass distribution after applying such β selection. By requiring all four tracks to have good $|\delta\beta| < 0.03$ will reject 16% of the statistics, while only 5% is reduced with the applied selection.

Figure 3.7 shows the β_{TOF} against momentum of the pion for events that pass this selection criteria for the $\gamma p \to \pi^-\pi^-\pi^+\Delta^{++}$ reaction and Figure 3.8 is for events that are not selected. In Figure 3.8 the horizontal band around $\beta \sim 1$ at low momenta corresponds to electrons or positrons. Events that form a non-physical band above $\beta > 1$ most likely come either from an incorrectly selected beam photon from some later RF beam bunch, or from an unrelated TDC hit in the

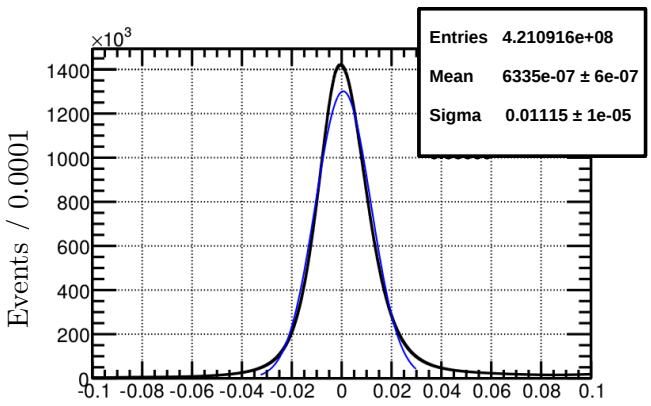

$\beta_{TOF} - \beta_{p/m}$ of π^+_{fast}

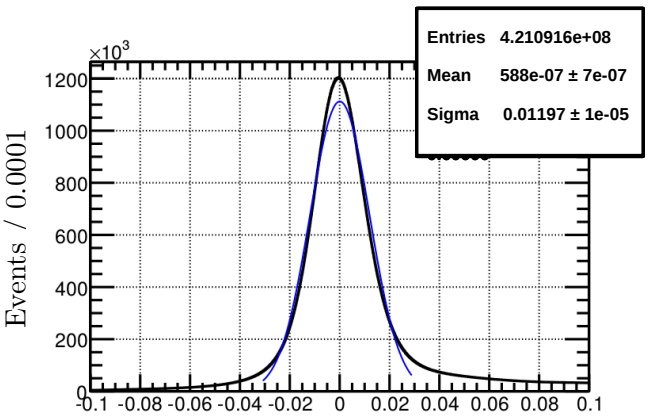

$\beta_{TOF} - \beta_{p/m}$ of π^+_{slow}

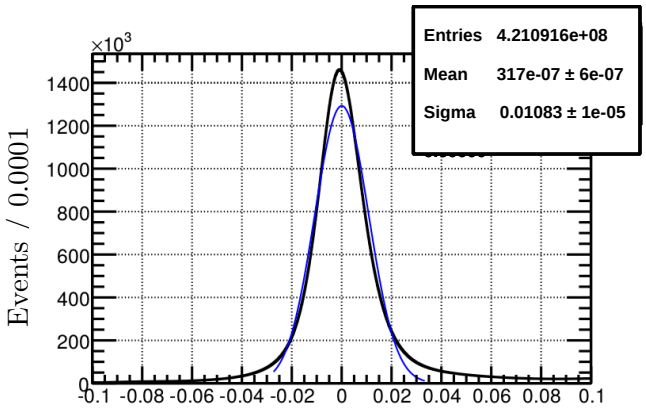

$\beta_{TOF} - \beta_{p/m}$ of π^-

Figure 3.3: $\gamma p \to n\pi^+\pi^+\pi^-$: The $\delta\beta$ distribution for all charged particles. They have been fitted with a Gaussian distribution.

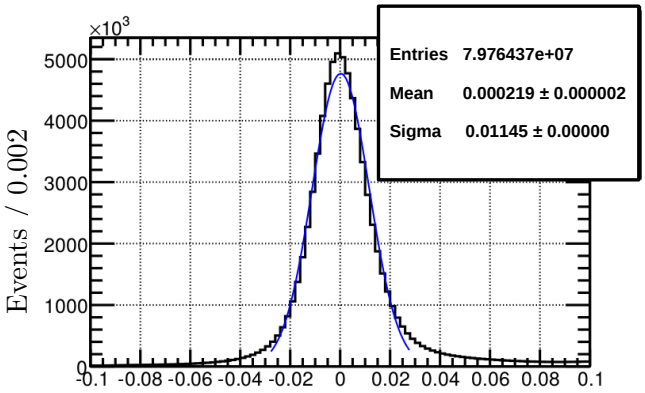

$\beta_{TOF} - \beta_{p/m}$ of π^+_{fast}

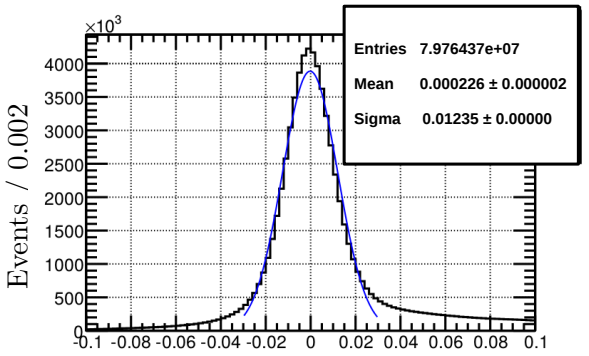

$\beta_{TOF} - \beta_{p/m}$ of π^+_{slow}

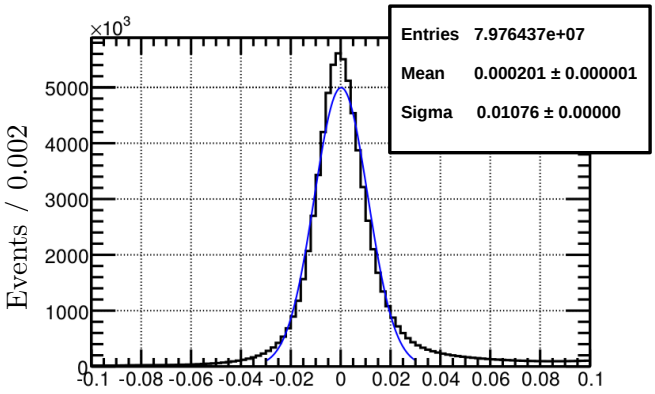

$\beta_{TOF} - \beta_{p/m}$ of π^-_{fast}

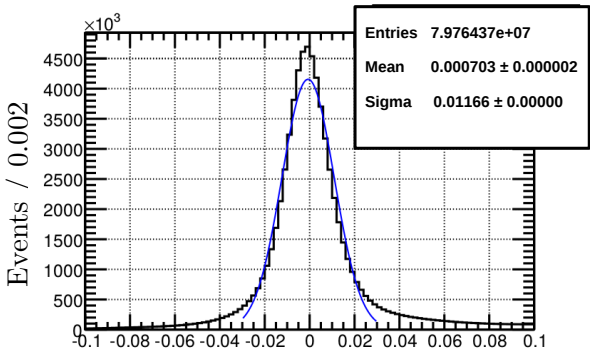

$\beta_{TOF} - \beta_{p/m}$ of π^-_{slow}

Figure 3.4: $\gamma p \to \pi^-\pi^-\pi^+\Delta^{++}$: The $\delta\beta$ distribution for all charged particles. They have been fitted with a Gaussian distribution.

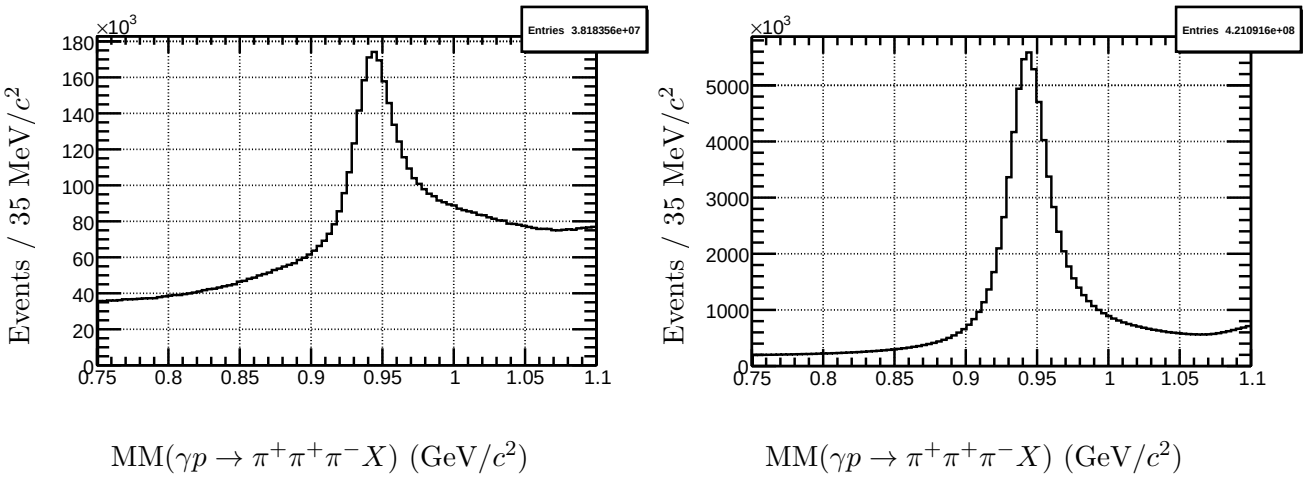

Figure 3.5: $\gamma p \to n\pi^+\pi^+\pi^-$: **Left:** missing mass distribution for events with $\delta\beta > 0.03$ for at least two charge tracks. Those events do not pass the selection criteria for the current analysis. **Right:** missing mass distribution for events with $\delta\beta < 0.03$ for at least two charged tracks.

appropriate channel but from some earlier untriggered interaction. The same features are shown in Figures 3.9, 3.10 for the $\gamma p \to n\pi^+\pi^+\pi^-$ reaction.

3.5 Beam Photon Energy Selection

The goal of this analysis is to study the t-channel photoproduction of the mesons. To achieve this, only the highest energy photons need to be selected to suppress the s-channel contribution. As discussed in Chapter 2, not all t-counters of the tagger have the same geometry. The first 19 counters were chosen for triggering on high energy photons, i.e. on the recoil beam electrons corresponding to the bremsstrahlung photon energies $\geq$ 4.4GeV. This is the range of the photon beam energies which was chosen for this analysis. The s-channel baryon production at these energies should be small in comparison to the t-channel.

Another complication of the analysis is the possibility of multiple breamsstrahlung photons even within a single 2.004 ns CEBAF beam bunch as discussed in Chapter 2. Even after identifying the proper RF bunch based on event timing (as described in the previous section), the problem of figuring out which of the possible multiple beam photons within the proper bunch has caused the recorded interaction in the target remains.

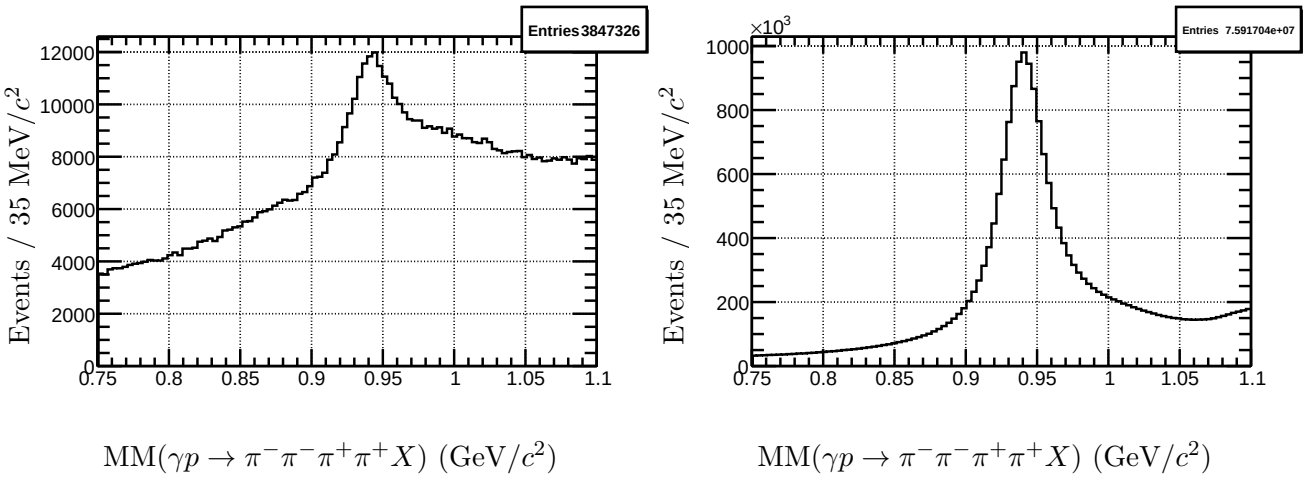

Figure 3.6: $\gamma p \to \pi^-\pi^-\pi^+\Delta^{++}$: **Left**: missing mass distribution for events with $|\delta\beta| > 0.03$ for at least three charged tracks. Those events do not pass the selection criteria for the current analysis. **Right**: missing mass distribution for the remaining events.

We require to have at least one photon above 4.4GeV. If the trigger was caused by another photon with much lower energy, the event will be rejected by the energy/momentum conservation (i.e., missing mass cut). However, if there are 2 high energy photons above 4.4GeV and missing mass resolution is insufficient to choose between them, one of them can be selected randomly. Fortunately, less than 1% [42] of events have 2 or more photons above the $4.4GeV$ threshold in the same RF bunch. We have verified that randomly selecting among these photons or just rejecting such events does not affect the results in any way.

3.6 Kinematic Fitting

To identify the missing particle in the reaction the kinematic fitting procedure was used. Due to detector resolution, the measured quantities may differ from their true values:

$$\vec{y} = \vec{\eta} + \vec{\epsilon} \tag{3.2}$$

where $\vec{y}$ is a set of true values, $\vec{\eta}$ is a set of measured observables and $\vec{\epsilon}$ is a set of values needed to shift the measured values in order get to the true values. During the track reconstruction in CLAS, the covariant matrix is being calculated, based on the resolution uncertainties and the tracking parameters. It is saved in the recorded event together with the measured observables. Later,

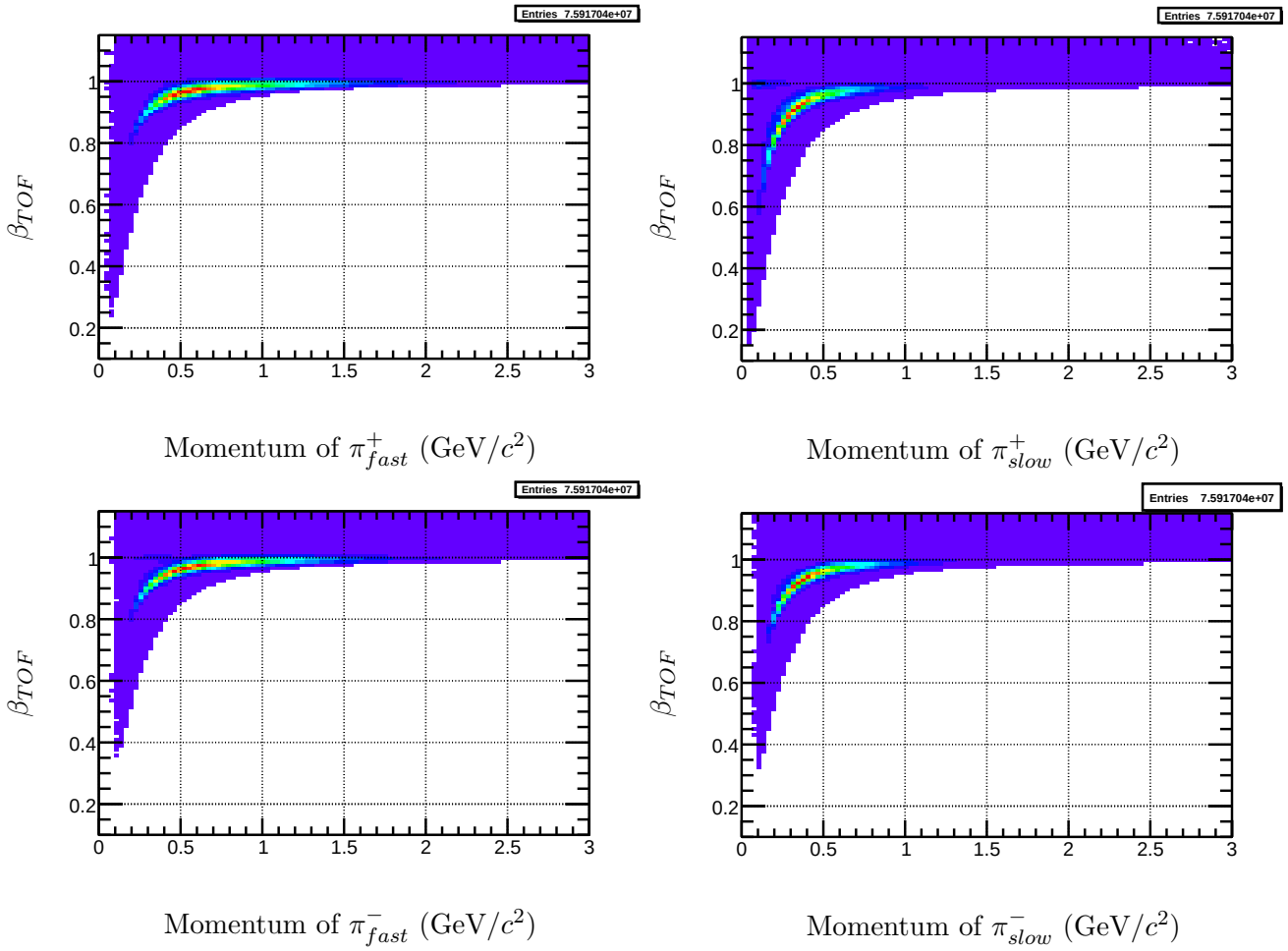

Figure 3.7: $\gamma p \to \pi^-\pi^-\pi^+\Delta^{++}$: The Figure shows for each pion the β as measured from the Time of Flight detector against the momentum of the particle. Events with at least three charged tracks with $\delta\beta > 0.03$ were rejected for the shown plots.

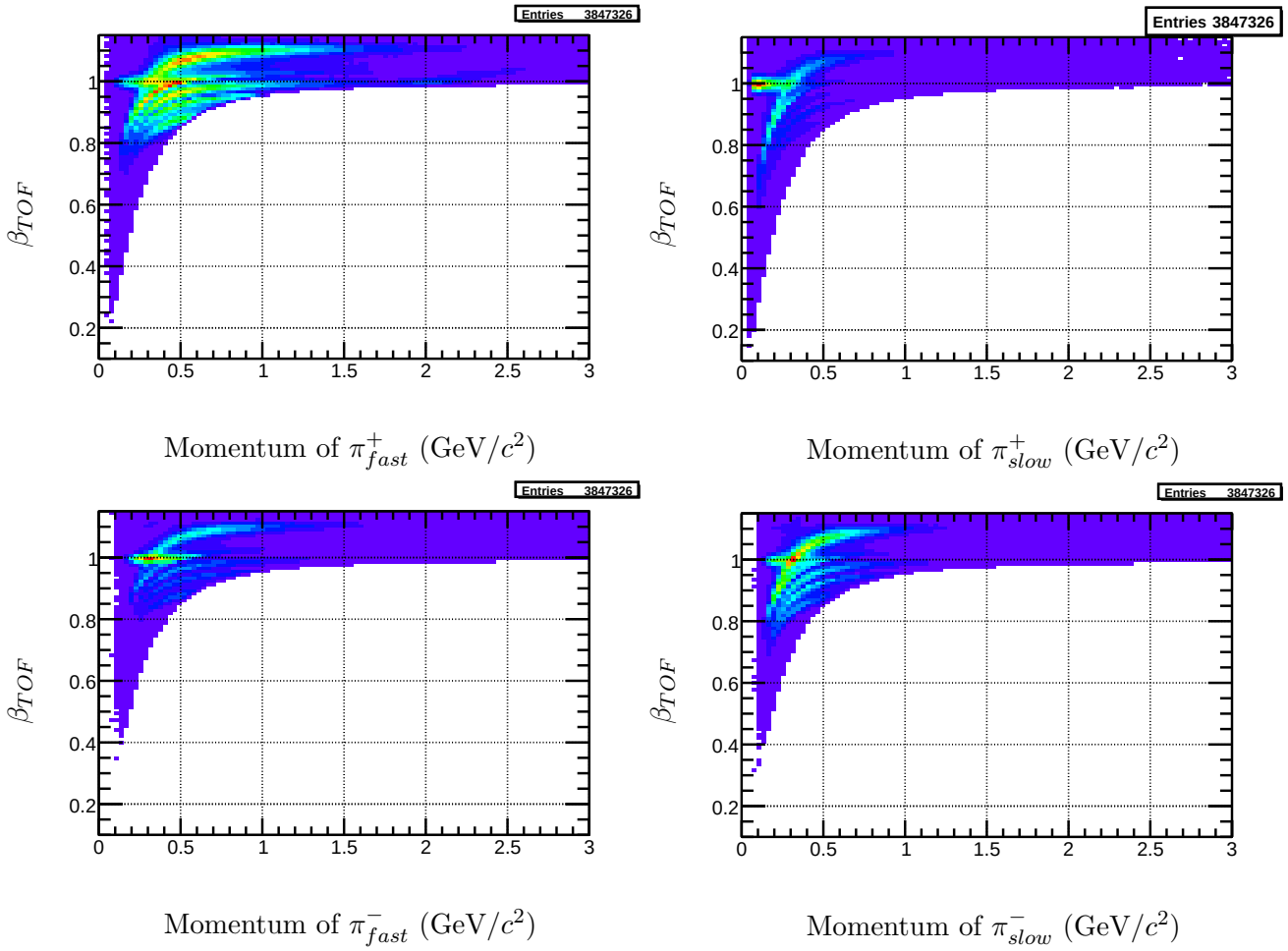

Figure 3.8: $\gamma p \to \pi^-\pi^-\pi^+\Delta^{++}$: The Figure shows for each pion the β as measured from the Time of Flight detector against the momentum of the particle. The events showed have at least three charged tracks with $\delta\beta > 0.03$.

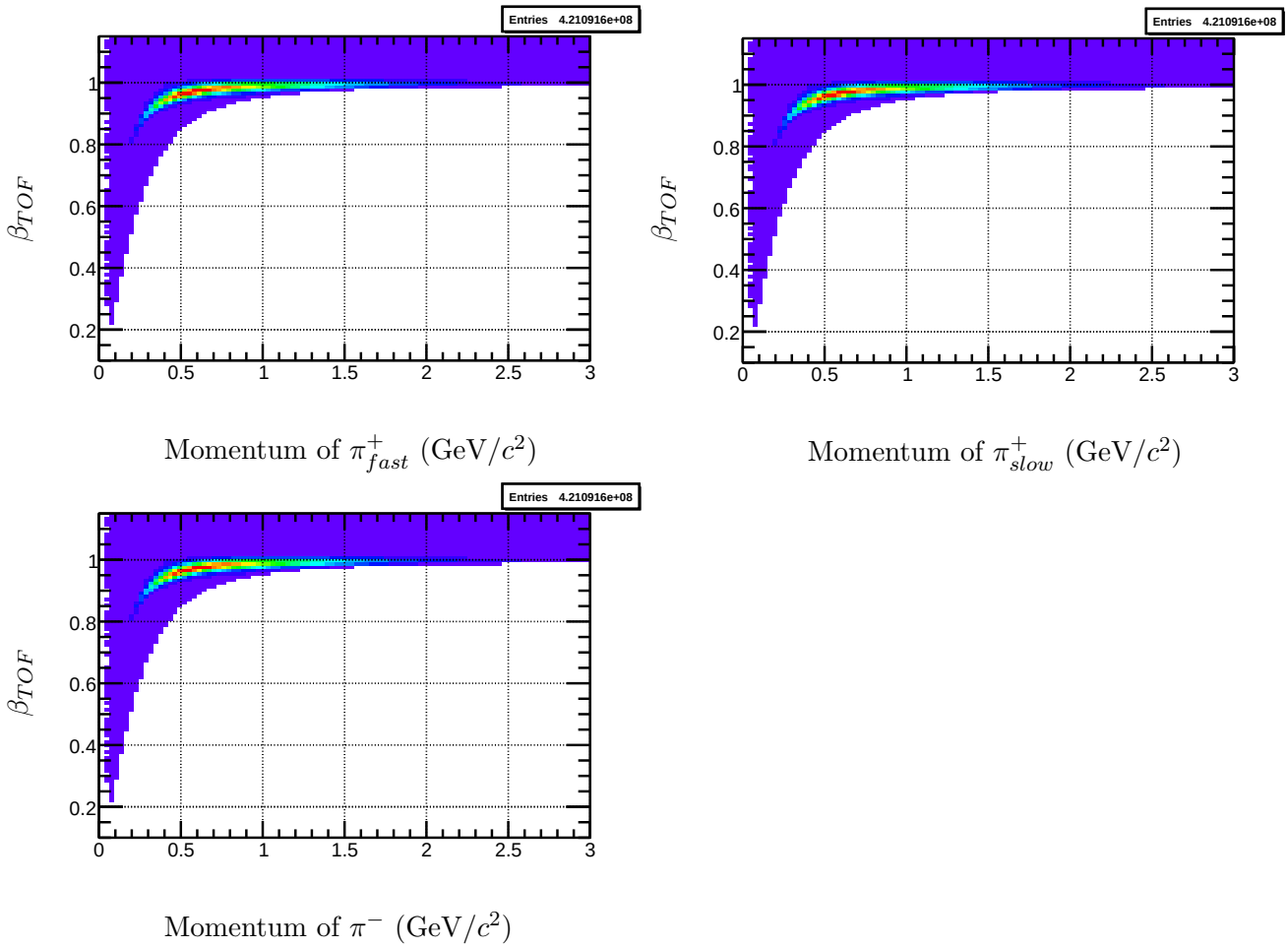

Figure 3.9: $\gamma p \to n\pi^+\pi^+\pi^-$: The Figure shows for each pion the β as measured from the Time of Flight detector against the momentum of the particle. The events showed have at least two charged tracks with $\delta\beta < 0.03$.

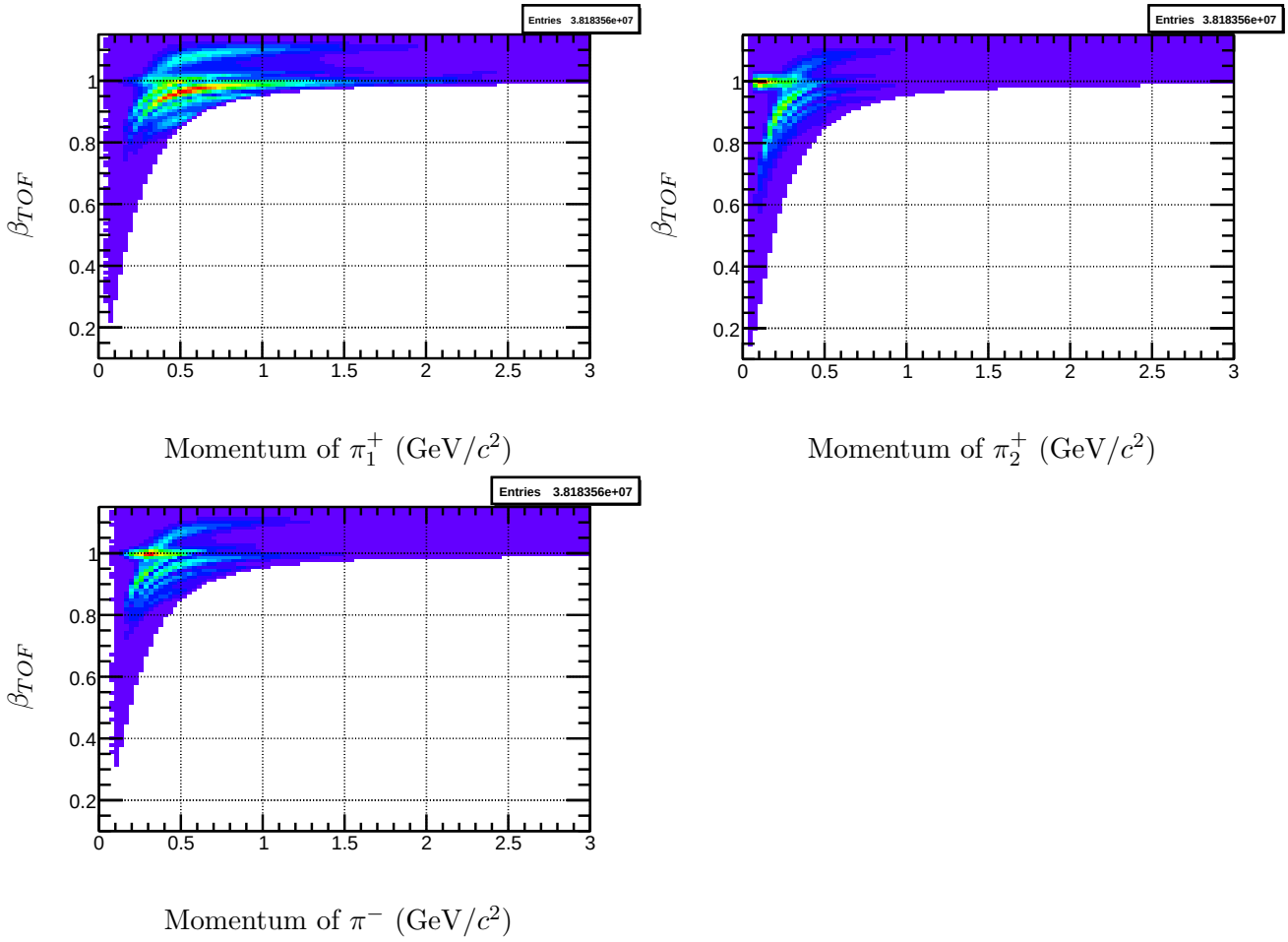

Figure 3.10: $\gamma p \to n\pi^+\pi^+\pi^-$: The Figure shows for each pion the β as measured from the Time of Flight detector against the momentum of the particle. The events showed have at least two charged tracks with $\delta\beta > 0.03$.

the kinematic fitting is used to find such values of shifts which are consistent statistically with the covariant matrix and which bring the true values in agreement with energy and momentum conservation for a particular missing particle hypothesis. The kinematic fitter that was used in this analysis is based on Lagrange multipliers for the constraints and the least squares minimization method. It was developed by Dustin Keller. Further details of the algorithm can be found in Ref. [43].

After the fit is performed, the primary tool to check the agreement between the data and the hypothesis is the confidence level, CL. The latter is defined as

$$CL = \int_{x^2}^{\infty} f(z;n)dz, \tag{3.3}$$

where $f(z;n)$ is the χ^2 probability density function with n degrees of freedom (number of measurements minus the number of unknown parameters). CL measures the probability that the χ^2 for a chosen event is greater than the one found in the fit. In the absence of a background, the CL should follow a flat distribution from 0 to 1. This is expected from the gaussian nature of the resolution errors and the properly determined covariance matrix. Events that do not satisfy the hypothesized constraint equations (background events) will produce a sharp rise near zero. Additional method to check the quality of the kinematic fit is to examine the pull distributions. A pull distribution is defined as the difference between the measured and the final parameter values obtained by the kinematic fitter and normalized by the statistical error of the shift for this parameter. The pull distribution is given by

$$\vec{z} = \frac{\vec{\eta_i} - \vec{\eta_f}}{\sqrt{\sigma^2_{\vec{\eta_i}} - \sigma^2_{\vec{\eta_f}}}}, \tag{3.4}$$

where $\vec{\eta_i}$ and $\vec{\eta_f}$ are the initial and final vector values of the measured quantities and $\sigma^2_{\vec{\eta_i}}$ and $\sigma^2_{\vec{\eta_f}}$ are the corresponding covariant matrix elements. If the covariant matrix errors are correctly estimated the pulls will follow a normal distribution around zero with a unit standard deviation.

Figure 3.11 shows the confidence level (CL) distribution for all events for the $\gamma p \to \pi^-\pi^-\pi^+\Delta^{++}$ reaction. Also, the pull distributions for this reaction are shown in Figure 3.11 for events with greater than 1% CL cut. The flatness of the CL distribution indicates that the data is well described by the hypothesis $\gamma p \to p\pi^-\pi^-\pi^+\pi^+$, where the proton is constrained by the energy and momentum conservation. In the pull distributions, λ is the angle between the track and the $(x-y)_{track}$ plane

Table 3.1: Table with the number of events before and after each selection for the $\gamma p \to \pi^-\pi^-\pi^+\Delta^{++}$ reaction.

Description	**Interval**	**Events In**	**Events Selected**
Vertex within z-extent of target	$-110 < z < -70$ cm	105,863,100	100,840,300
Vertex within target radius	$r < 10.0$ cm	100,840,300	93,575,180
Event vertex timing cut	$\lvert t_{vtx}(TAG) - t_{vtx}(ST)\rvert < 1.002$ ns	93,575,180	79,764,370
Beta selection for particle tracks	$\lvert\beta_{TOF} - \beta_{p/m}\rvert < 0.03$	79,764,370	75,917,040
Photon Energy	$Beam - Photon \geq 4.4$GeV	75,917,040	31,874,591
Confidence level cut	$FOM - kinFit > 1\%$	31,874,591	3,750,040

Table 3.2: Table with the number of events before and after each selection for the $\gamma p \to n\pi^-\pi^-\pi^+$ reaction.

Description	**Interval**	**Events In**	**Events Selected**
Vertex within z-extent of target	$-110 < z < -70$ cm	707,329,219	658,403,589
Vertex within target radius	$r < 10.0$ cm	658,403,589	587,508,335
Event vertex timing cut	$\lvert t_{vtx}(TAG) - t_{vtx}(ST)\rvert < 1.002$ ns	587,508,335	421,091,544
Beta selection for particle tracks	$\lvert\beta_{TOF} - \beta_{p/m}\rvert < 0.03$	421,091,544	382,907,980
Photon Energy	$E_\gamma \geq 4.4$GeV	382,907,980	118,656,025
Confidence level cut	$FOMkinFit > 1\%$	118,656,025	7,424,941

and ϕ is the angle between the track and the beamline. A greater than 1% confidence level cut is applied to the data sample.

Also, in $\gamma p \to n\pi^+\pi^+\pi^-$ reaction the missing neutron is constraint via energy and momentum conservation using kinematic fitting. The confidence level (CL) distribution from the missing neutron hypothesis is shown in Figure 3.12. Also in the same Figure the pull distributions are shown by selecting events with CL greater than 1%. The CL seems to be relatively flat in the 0.1 to 1 range, and the pull distributions seem to follow a Gaussian distribution centered around 0 with the value of sigma close to 1. This reflects the fact that the data are well described by the $\gamma p \to n\pi^+\pi^+\pi^-$ hypothesis where the neutron is constraint by the energy-momentum conservation. A greater than 1% CL cut is applied to the final data sample.

Tables 3.1, 3.2 show the initial selection criteria and the number of events passing each selection for the reactions $\gamma p \to \pi^-\pi^-\pi^+\Delta^{++}$ and $\gamma p \to n\pi^+\pi^+\pi^-$ respectively.

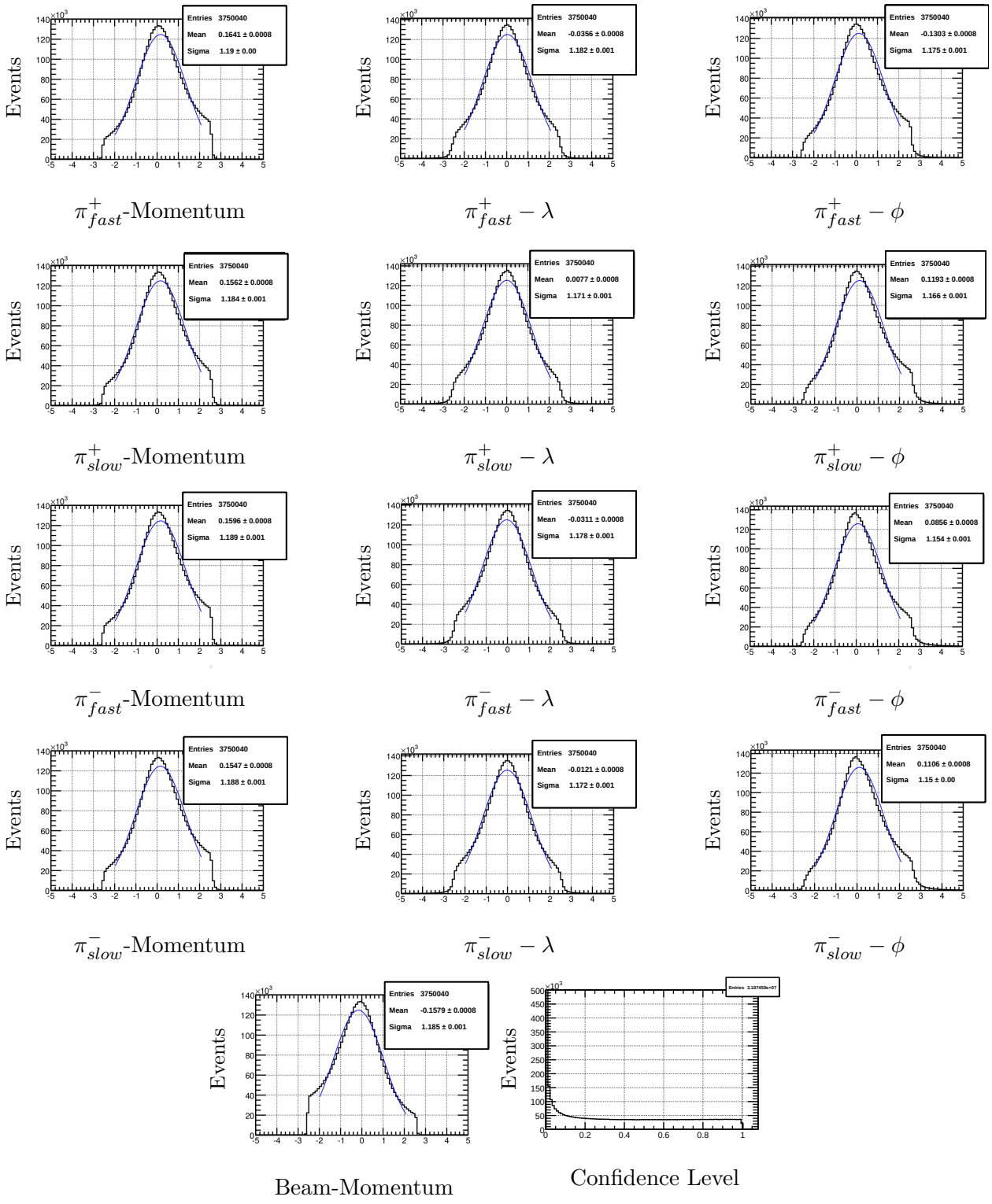

Figure 3.11: Kinematic fit results for high energy photons for the $\gamma p \to \pi^+\pi^-\pi^+\pi^-[p]$ reaction. The pull distributions have 1% confidence level cut and have been fitted with a Gaussian. The last plot is the confidence level of the reaction without the confidence level cut.

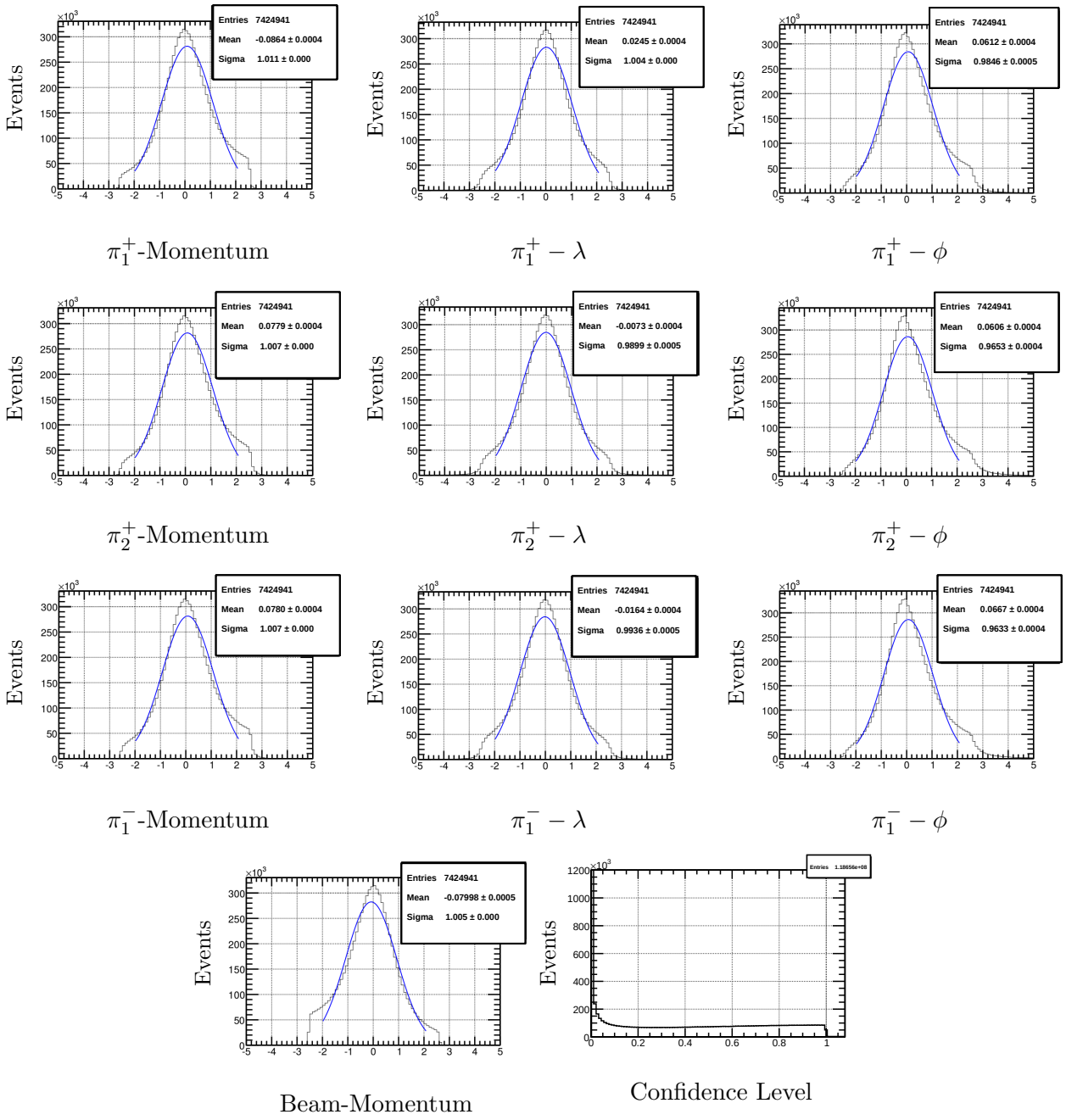

Figure 3.12: Kinematic fit results for high energy photons for the $\gamma p \rightarrow \pi^+\pi^-\pi^+[n]$ reaction. The events in the pull distributions are greater than 1% confidence level and they have been fitted with a Gaussian function. The bottom right plot is the confidence level distribution for a missing neutron hypothesis.

CHAPTER 4

EVENT SELECTIONS FOR THE EXCLUSIVE $\gamma p \to \pi^-\pi^-\pi^+\Delta^{++}$ REACTION

After selecting the desired $\gamma p \to \pi^-\pi^-\pi^+\pi^+p$ topology from the reconstructed data, additional selection criteria were applied in order to enhance the desired reaction with recoil Δ^{++}, i.e. $\gamma p \to \pi^-\pi^-\pi^+\Delta^{++}$. These criteria were chosen as a compromise between improving signal-to-background ratio and preserving as much statistics of the final data sample as possible.

4.1 Selecting the Δ^{++}

The main purpose of the selection cuts that have been applied so far has been the selection of the $\gamma p \to \pi^+\pi^-\pi^+\pi^-p$ events. Because of the short decay life time of the Δ^{++}, this baryon can not be detected by CLAS directly, and certain criteria should be applied for its selection. Other reactions with the same final state topology will also contribute to the recorded data sample. Their relative contributions depend on the cross section of each reaction and the typical acceptance for the reaction's kinematics.

There are two positive pions in the final state, and certain criteria need to be applied in order to kinematically separate the π^+ coming from the meson vertex (the 3π system) from the π^+ coming from the baryon vertex (the Δ^{++}). Figure 4.1 shows the invariant mass distribution of the $p\pi^+$. It shows that it is more likely to associate the π^+_{slow} with the $\Delta^{++}(1230)$ rather than the π^+_{fast}. Even though there is a small Δ^{++} signal around 1.2 GeV in the invariant $p\pi^+_{fast}$ mass distribution, the $p\pi^+_{slow}$ invariant mass distribution shows a much stronger and cleaner Δ^{++} signal. The reason for this is that the pion associated with the recoil baryon will be slower than the pion from the 3π meson system. The Δ^{++} events in the $p\pi^+_{fast}$ invariant mass distribution are treated as baryon contamination which needs to be reduced since the partial wave analysis of the 3π system is based on the assumption that all three pions assigned to the 3π system are indeed coming from the meson vertex and not from the baryon one. It was found that the most effective way to eliminate such contamination is to select events with well separated momenta of the two positively charged pions.

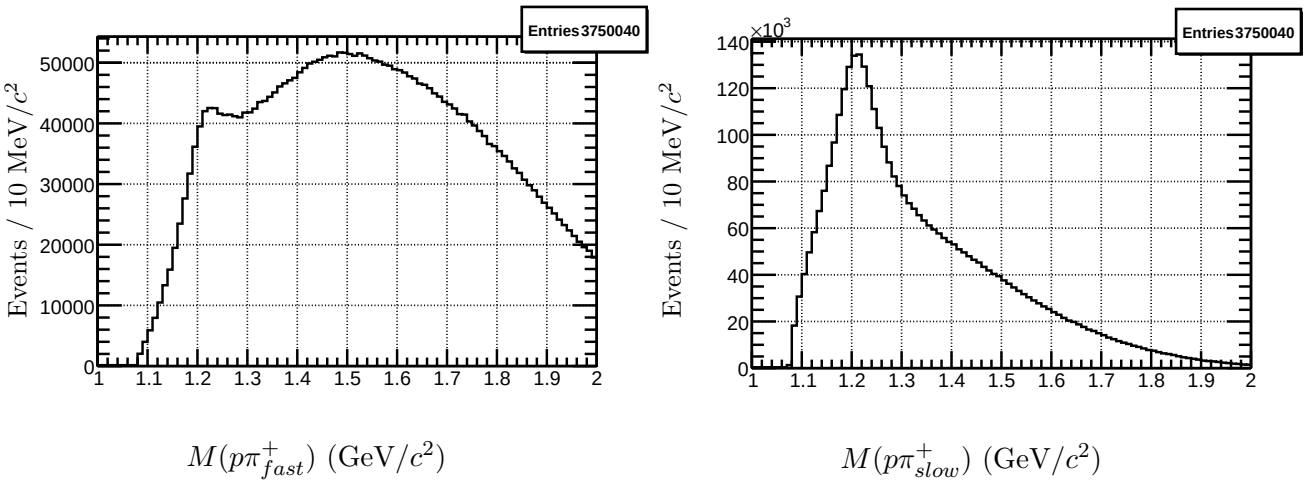

Figure 4.1: $\gamma p \to \pi^-\pi^-\pi^+\Delta^{++}$:**Right**: $p\pi^+_{slow}$ invariant mass distribution. **Left**: $p\pi^+_{fast}$ invariant mass distribution.

Figure 4.2 shows the result for the different values of the $|p_{\vec{\pi^+_{fast}}}| - |p_{\vec{\pi^+_{slow}}}|$. It was determined that $|p_{\vec{\pi^+_{fast}}}| - |p_{\vec{\pi^+_{slow}}}| > 0.35$GeV is the optimal value for such cut. To come to this conclusion, the phase space events were generated and simulated through the CLAS detector in order to understand the acceptance of the main and background reactions. By looking at various distributions of those Monte Carlo events, the background present in the data can be studied (more details on the Monte Carlo simulations can be found at the end of this Chapter). To that end, the bottom right plot in Figure 4.2 shows the $p\pi^+$ invariant mass distribution for MC events, where the π^+ is coming from the 3π meson system. This is the invariant mass distribution which is expected from the measured four-vectors of a clean 3π data sample. By comparing the Monte Carlo distribution with the data, it can be seen that a cut tighter than 0.35 GeV/c does not not reduce the Δ^{++} contamination further. For the small remaining shoulder at 1.2 GeV, we need an additional selection cut which is described below.

The 3π and $\pi\pi$ invariant mass distributions with the difference in momentum selection are shown in Figure 4.3. The peak of the 3π invariant mass at 1.3 GeV agrees with the $a_2(1320)$ meson, as it will be shown later in the analysis. Also, the shoulder above 1.5 GeV is in the 3π mass region where the $\pi_2(1670)$ is expected to be. Furthermore, both $\pi^+\pi^-$ invariant mass distributions show the strong ρ signal, with the $\pi^+\pi^-_{fast}$ spectrum also revealing the $f_2(1270)$ meson.

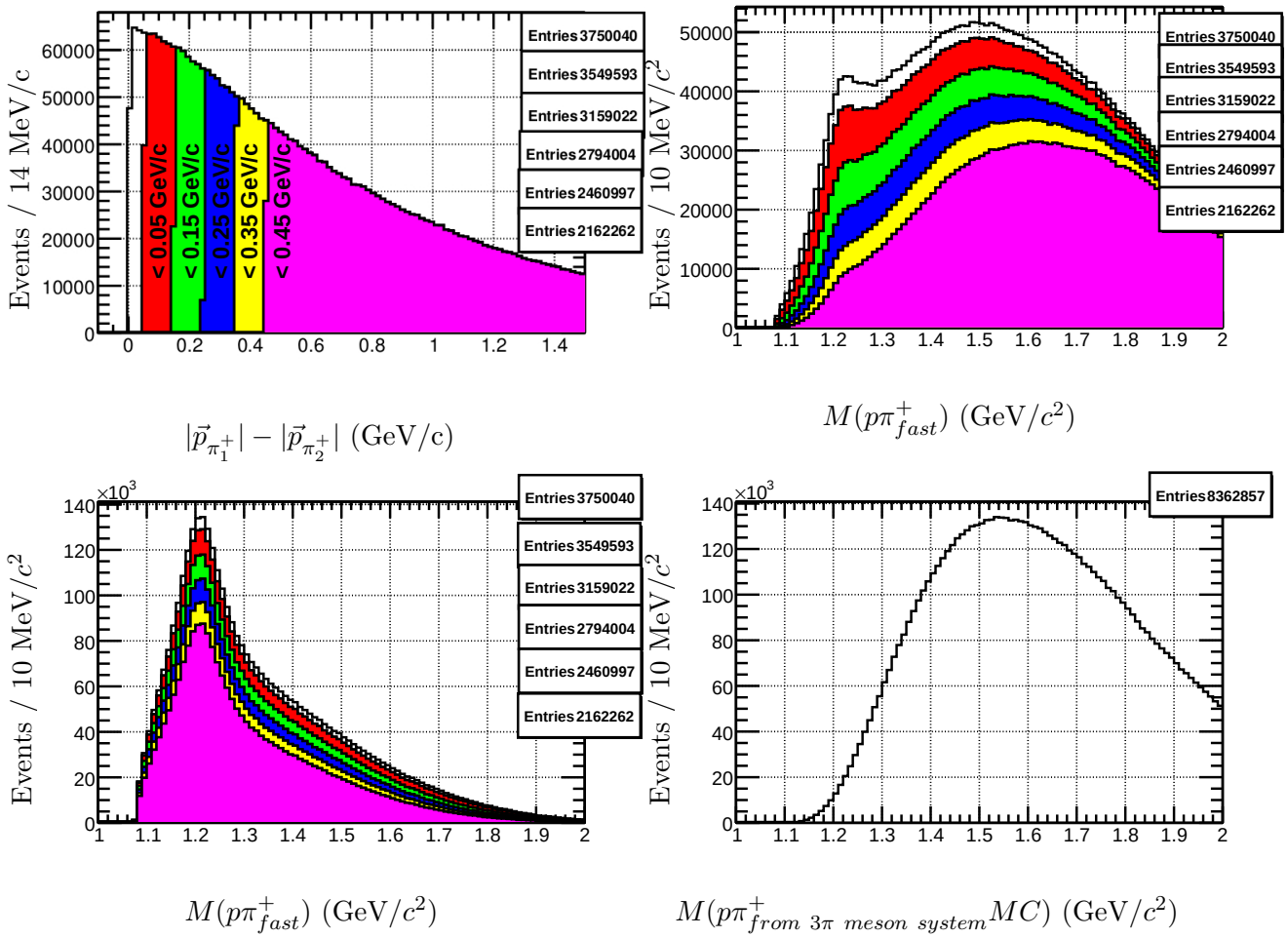

Figure 4.2: **Top Left**: difference in momentum for the two π^+. In this plot, colors represent different selection values and those colors are consistent with the other plots in this Figure. **Top Right**: invariant mass distribution of $p\pi^+_{fast}$ for different momentum selections. **Bottom Left**: invariant mass of $p\pi^+_{slow}$ for different momentum selections. **Bottom Right**: invariant mass of $p\pi^+$ for simulated MC events in which the π^+ is coming from the 3π meson system.

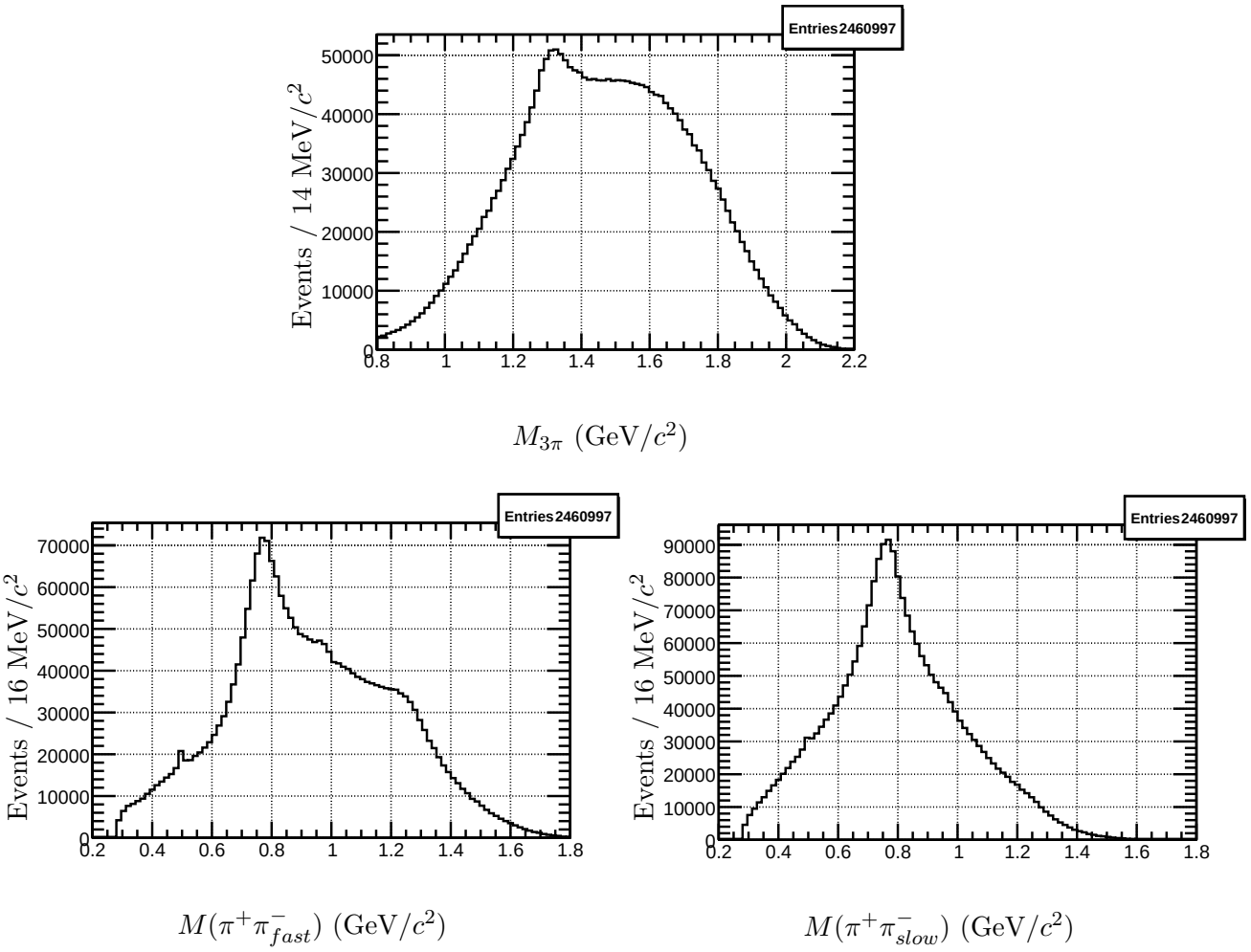

Figure 4.3: Plots of interest for the $\gamma p \to \pi^-\pi^-\pi^+\Delta^{++}$ reaction. Difference in momentum cut has been applied here. **Top**: invariant mass of the 3π system. **Bottom Left**: invariant mass of $\pi^+\pi^-_{fast}$. **Bottom Right**: invariant mass of $\pi^+\pi^-_{slow}$.

4.2 Reduction of Baryon Background

CLAS detector was designed originally for the baryon spectroscopy, which means that it has lower acceptance for the small decay angles in the lab frame. The g12 run was focused on the meson spectroscopy. So, the adjustments were made to optimize the detector acceptance for the forward decay angles of t-channel meson resonances. As discussed in Chapter 2, the main optimization made was the relocation of the hydrogen target further upstream. While improving the ratio of the accepted meson reactions relative to baryon ones, this does not eliminate the excited baryon background in the data, and additional selection criteria had to be applied to the data sample in order to reduce this background. Systematic dependencies of the results due to such selection criteria had been studied.

Another way to deal with the baryon background would be to apply a global partial wave analysis which includes both the meson and baryon reactions. However, the present PWA framework does not support the global description of s-channel and t-channel reactions. Performing such an analysis is beyond the scope of this effort. The approach chosen utilizes kinematic constraints on the data sample and studies the systematic dependencies. The latter is being done primarily by tightening and relaxing the applied selection criteria. In order to enhance the peripheral production of the mesons, a selection is made based on the four-momentum transfer to the Δ^{++} baryon. The Mandelstam t is defined as:

$$t = (p^{\mu}_{\gamma} - p^{\mu}_{X})^2 = (p^{\mu}_{target} - p^{\mu}_{\Delta^{++}}) \tag{4.1}$$

where p^{μ}_{γ} is the four-momentum of the beam photon, p^{μ}_{target} is the four-momentum of the target proton, p^{μ}_{X} is the momentum of the 3π meson system, and $p^{\mu}_{\Delta^{++}}$ is the momentum of the recoil Δ^{++}. Instead of the Mandelstam variable t, the normalized variable t' was used for this selection. The t' is defined as

$$t' = t - t_0 \tag{4.2}$$

$$t_0 = \left[\frac{m^2_{\Delta^{++}} - m^2_X - m^2_{target}}{2\sqrt{s}}\right]^2 - (p^{CM}_{\gamma} - p^{CM}_{X})^2 \tag{4.3}$$

$$s = (p^{\mu}_{\gamma} + p^{\mu}_{target})^2 = (p^{\mu}_{X} + p^{\mu}_{\Delta^{++}})^2 \tag{4.4}$$

where $|t_0|$ is the minimum momentum transfer required to produce a system of mass m_X with the momentum in the overall center of mass frame p_X^{CM}, the target mass is m_{target}, and the recoil nucleon mass is $m_{\Delta^{++}}$. Figure 4.4 shows the t distribution, and the correlation of t and t' with the 3π invariant mass.

The Mandelstam variable t depends on the 3π invariant mass distribution. Therefore, application of a t selection will result in a sliding mass cut, where the higher 3π is increasingly suppressed. This effect can be seen in the bottom plots of Figure 4.4. The high 3π mass region is showing an upturn for the t threshold, while it is flat in the t' case. For the current analysis, events were selected with $t' < 0.4\text{GeV}^2/c^4$.

Since the low t' selection enhances the peripheral production (due to the fact that $\frac{d\sigma}{dt} \sim e^{-b|t|}$), a cleaner 3π signal is expected. Figure 4.5 shows exactly this effect in the invariant mass of $p\pi^+_{fast}$. The shoulder around 1.2 GeV, which is most likely related to Δ^{++} events with the incorrectly assigned positive pion, disappears.

In Figure 4.6, the effect of the low t' selection is shown for the $p\pi^-_{slow}$ invariant mass distribution as well as for its correlation with the $M(\pi^+_{fast}\pi^{-+}_{slow}\pi^-_{fast})$. The narrow peak appearing at 1.1 GeV in the $M(p, \pi^-_{slow})$ is most likely the $\Lambda^0(1115)$ state. Since this is a strange baryon, it is associated with another strange particle in the reaction such as a K^0_S. The low t' selection does reduce the number of $\Lambda's$ present in the data, but some of them still remain. Figure 4.7 shows that the remaining $\Lambda^0(1115)$, seen in the invariant mass of $p\pi^-_{slow}$, are related to the $M(\pi^+_{slow}, \pi^-_{fast})$. A circular cut needs to be made around that region in order to reject the $\Lambda^0(1115)$ events in the final data sample.

Different values for t' selection were studied and 0.4 $(\text{GeV}/c^2)^2$ threshold seemed to be optimal. In appendix F, five different values for the t' selection are tested by performing partial wave analysis. Figure 4.8 shows the invariant mass distributions of $\pi^+_{fast}\pi^-_{fast}$, $\pi^+_{fast}\pi^-_{slow}$ and $\pi^+_{fast}\pi^-_{fast}\pi^-_{slow}$. The red curve shows the effect of the low t' cut on these invariant masses. The main difference is the reduction of the shoulder above 1.5 GeV in the 3π mass distribution.

Figure 4.9 shows the invariant mass distribution of the $p\pi^+_{slow}$. For the present analysis, events are selected with $M(p, \pi^+_{slow}) < 1.35\text{GeV}$ in order to enhance the $\Delta^{++}(1232)$ selection. Figure 4.10 shows the invariant mass distribution of $p\pi^+_{slow}\pi^-_{slow}$, $\pi^+_{slow}\pi^-_{slow}$ and $p\pi^-_{fast}$. The $M(p\pi^+_{slow}\pi^-_{slow})$ and $M(p\pi^-_{fast})$ distributions reach a peak at 1.7 and 1.5 GeV respectively. Most likely, these peaks

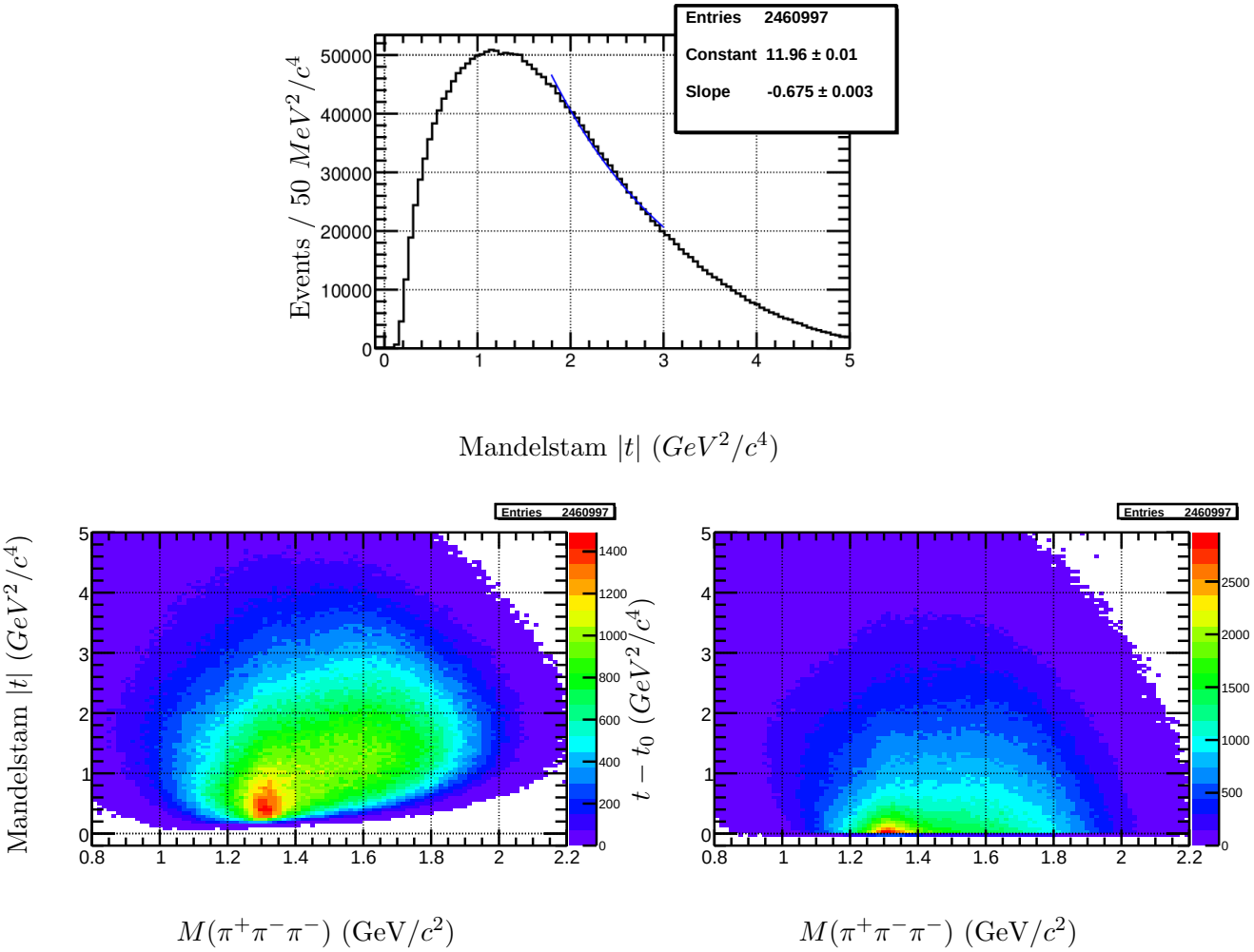

Figure 4.4: $\gamma p \to \pi^-\pi^-\pi^+\Delta^{++}$: The **top** plot shows an exponential fit of the Mandelstam t distribution. The **bottom left** plot shows the t against the 3π invariant mass and the **bottom right** plot shows the normalized t, t', against the 3π invariant mass.

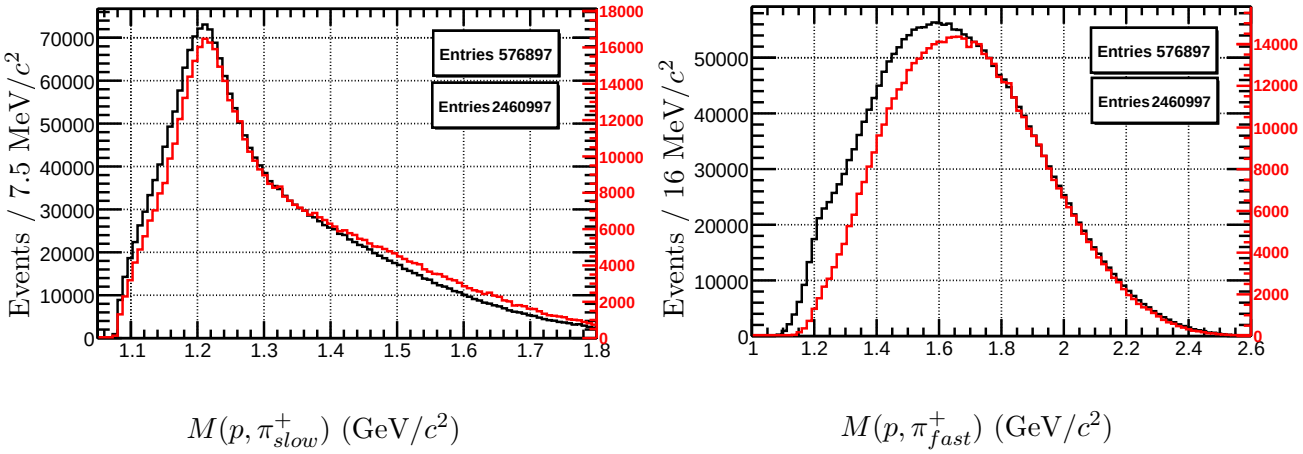

Figure 4.5: $\gamma p \to \pi^-\pi^-\pi^+\Delta^{++}$: **Left**: invariant masses of $p\pi^+_{slow}$ and $p\pi^+_{fast}$ (**right**). The plot shows the effect of the low t' selection in those invariant masses.

are excited nucleon states. By applying the $M(p,\pi^+_{slow}) < 1.35$GeV selection, these structures seem to be reduced. Furthermore, the $M(\pi^+_{slow}\pi^-_{slow})$ distribution shows the $\rho(770)$ meson production which shouldn't be there if two pions belong to different vertices, but the applied selection seems to eliminate such ρ background. Furthermore, a fit of the final $p\pi^+_{slow}$ invariant mass distribution is performed, shown in Figure 4.12 where the details of the fit are discussed at the end of this section. The latter figure shows that the background increases for higher $p\pi^+_{slow}$ mass events, which is an indication that the low $M(p,\pi^+_{slow})$ selection forces a cleaner Δ^{++} signal.

In the appendix A, all the invariant masses and the rest frame angles before and after the baryon background reduction are presented. Also, the phase space Monte Carlo (MC) events are plotted. The latter have been generated with the same t-slope as the data (see the next chapter for a detailed discussion). There is pretty good agreement between MC and data in almost all the plots. Since the MC events are free of the baryon background, big contamination from it in the data is not expected. The only invariant mass plot that seems to show a small structure is the $M(\pi^+_{slow},\pi^-_{fast})$. Figure 4.11 shows this distribution, along with the invariant mass distributions of the $p\pi^+_{fast}$ and $\pi^+_{slow}\pi^-_{fast}\pi^-_{slow}$. A short discussion of this small structure follows.

One possible source of this background can be wrongly assigned π^+ to the top and bottom vertices. Even though this kind of background is not visible in the $M(p,\pi^+)$ plot, it can be seen indirectly in the $M(\pi^+_{slow},\pi^-_{fast})$ plot. The π^+_{slow} in our assumption is associated with the Δ^{++}

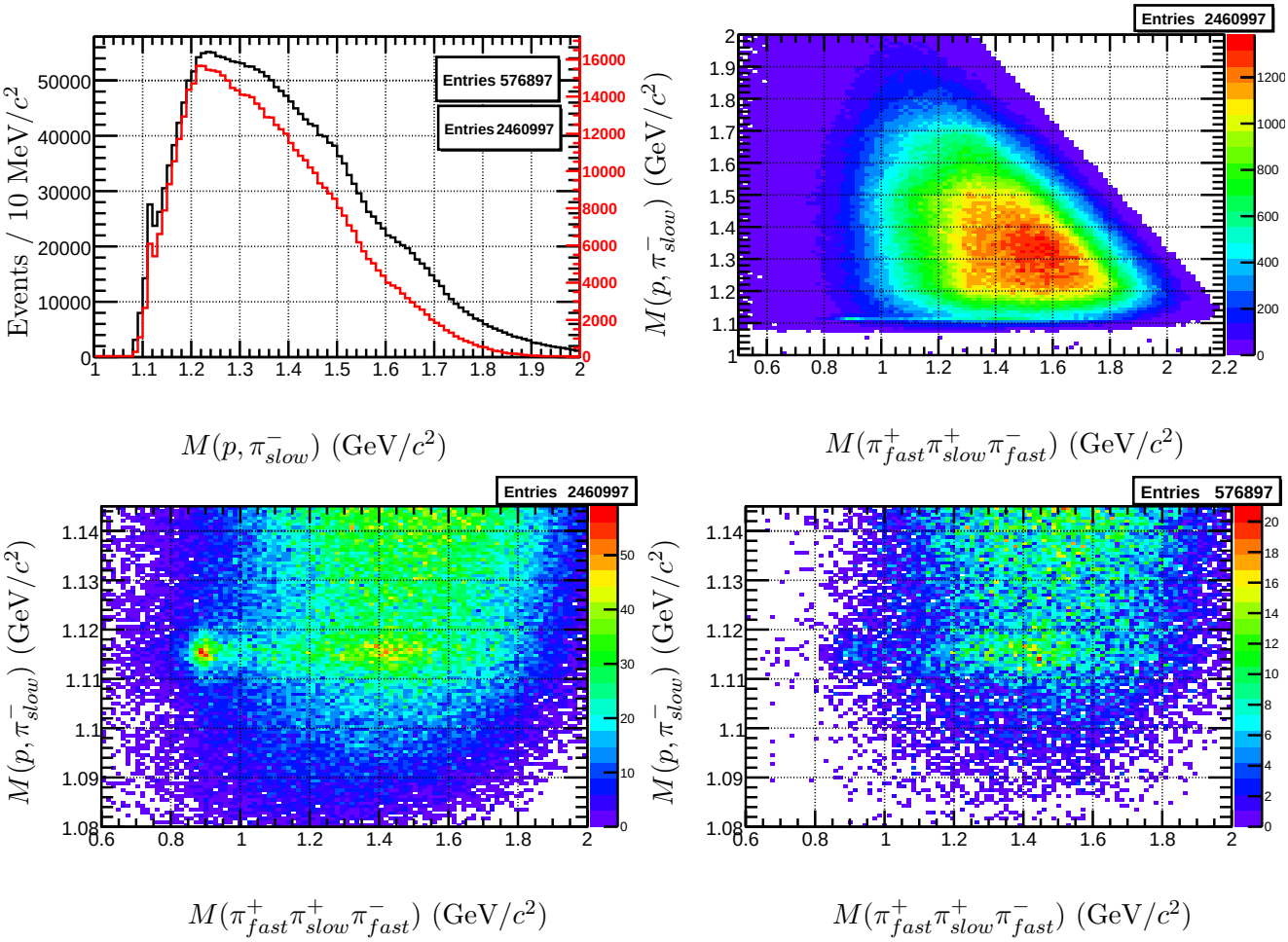

Figure 4.6: $\gamma p \to \pi^-\pi^-\pi^+\Delta^{++}$: **Top left:** Invariant mass of the $p\pi^-_{slow}$, showing the effect of the t'selection. **Top Right:** correlations between the $\pi^+_{fast}\pi^+_{slow}\pi^-_{fast}$ and the $p\pi^-_{slow}$. **Bottom Left:** same as top right plot but zooming into $\Lambda^0(1115)$ region ($M(p,\pi^-_{slow})$ between 1.08 and 1.15 GeV). **Bottom right:** correlations between the $\pi^+_{fast}\pi^+_{slow}\pi^-_{fast}$ and the $p\pi^-_{slow}$ for events with $t' < 0.4GeV^2/c^4$.

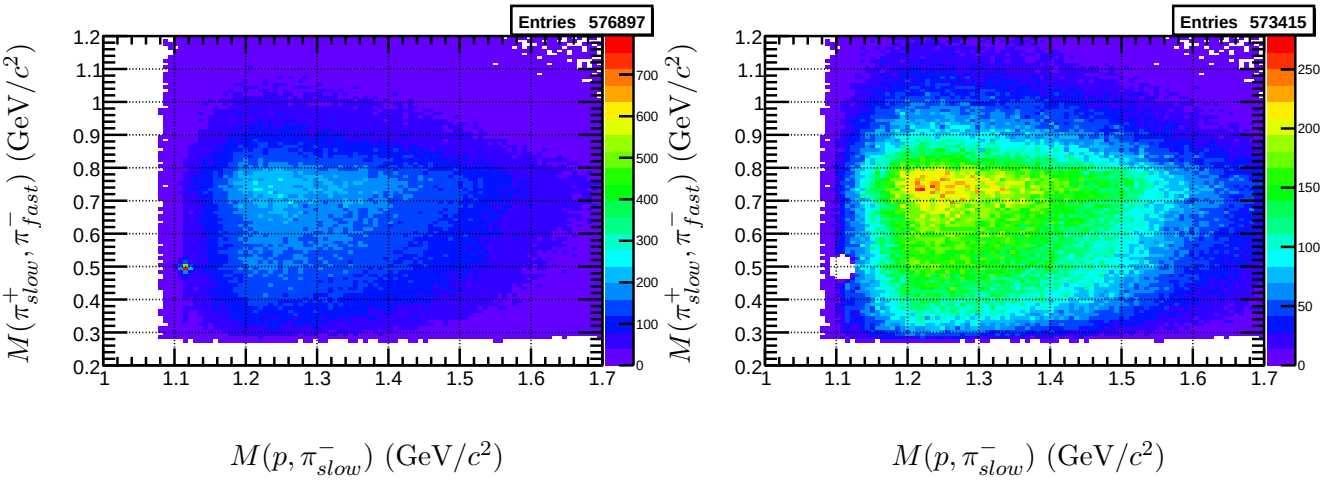

Figure 4.7: $\gamma p \to \pi^-\pi^-\pi^+\Delta^{++}$: **Left:** correlations between the $\pi^+_{slow}\pi^-_{fast}$ and the $p\pi^-_{slow}$. The correlation between the $\Lambda^0(1115)$ and the K^0_S is visible. **Right:** the effect on the left plot of a circular cut: $(M(\pi^+_{slow},\pi^-_{fast})^2 - 0.247009)^2 + (M(p,\pi^-_{slow})^2 - 1.225449)^2 > 0.04472^2$.

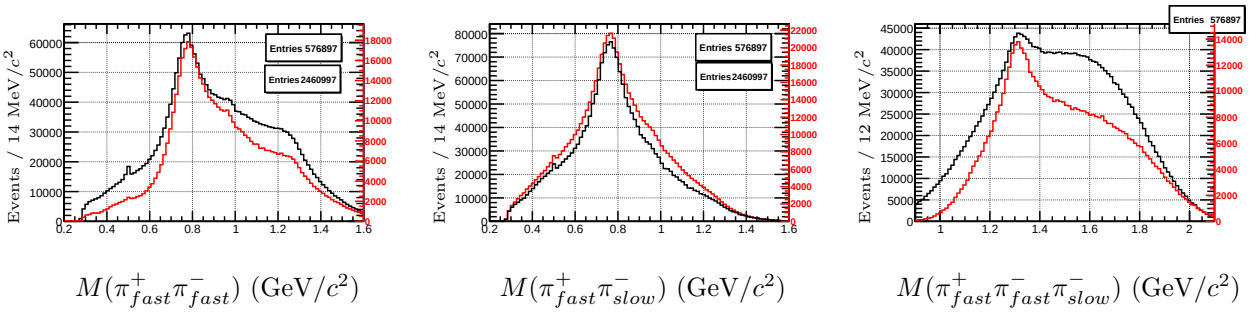

Figure 4.8: $\gamma p \to \pi^-\pi^-\pi^+\Delta^{++}$: Invariant mass for $\pi^+_{fast}\pi^-_{fast}$, $\pi^+_{fast}\pi^-_{slow}$ and $\pi^+_{fast}\pi^-_{fast}\pi^-_{slow}$. The red curve is from events that are passing the t' selection criteria.

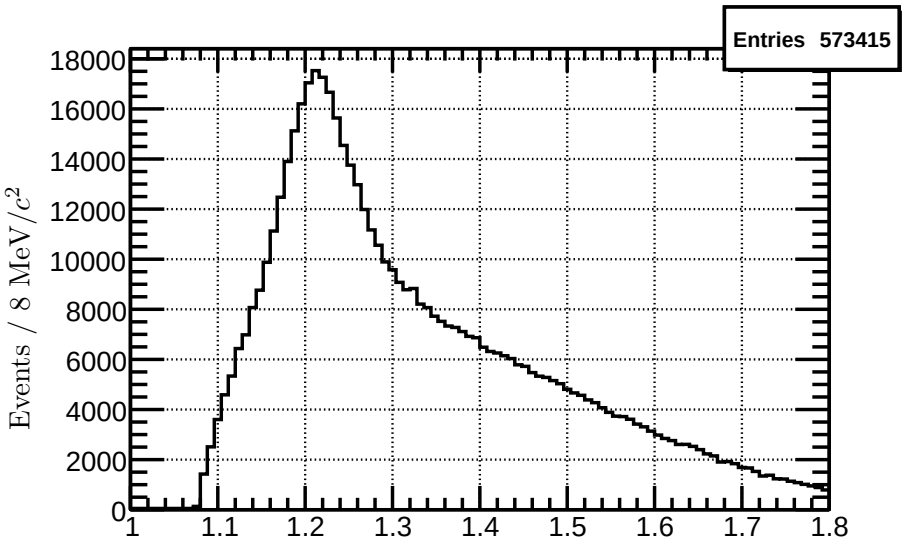

Figure 4.9: $\gamma p \to \pi^-\pi^-\pi^+\Delta^{++}$: Invariant mass distribution of the $p\pi^+_{slow}$.

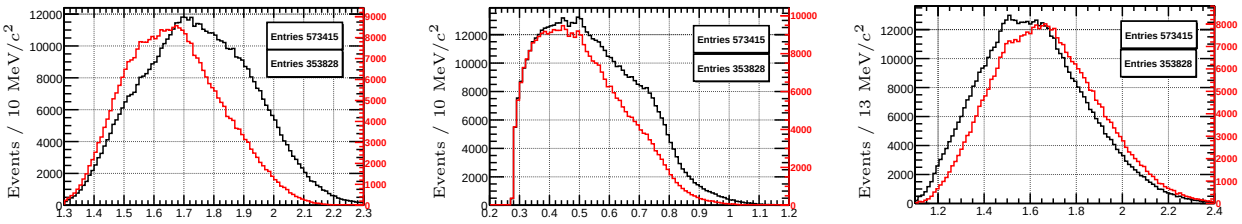

Figure 4.10: $\gamma p \to \pi^-\pi^-\pi^+\Delta^{++}$: Invariant mass for $\pi^+_{fast}\pi^-_{fast}$, $\pi^+_{fast}\pi^-_{slow}$ and $\pi^+_{fast}\pi^-_{fast}\pi^-_{slow}$. The red curve is for events restricted to have $M(p, \pi^+_{slow}) < 1.35\ GeV$.

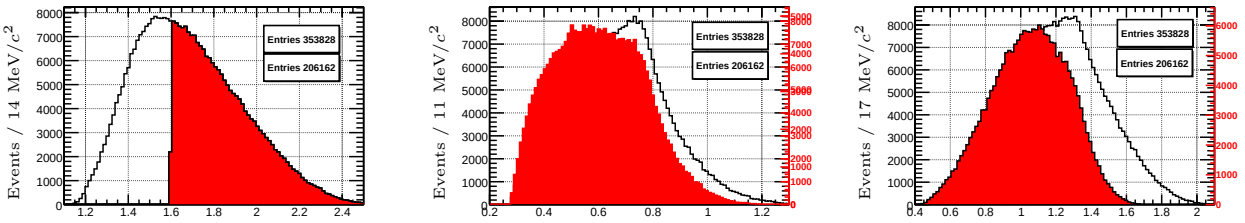

$M(p, \pi^+_{fast})$ (GeV/c^2) $M(\pi^+_{slow}\pi^-_{fast})$ (GeV/c^2) $M(\pi^+_{slow}\pi^-_{fast}\pi^-_{slow})$ (GeV/c^2)

Figure 4.11: $\gamma p \rightarrow \pi^-\pi^-\pi^+\Delta^{++}$: Invariant masses of $p\pi^+_{fast}$, $\pi^+_{slow}\pi^-_{fast}$ and $\pi^+_{slow}\pi^-_{fast}\pi^-_{slow}$. The red histogram is by selecting $M(p, \pi^+_{fast}) > 1.6GeV$.

and the π^-_{fast} is associated with the top meson vertex. In a fraction of the events, these two particles are correlated since they form the apparent $\rho(770)$ meson. The number of events with such correlation is small, compared to the full statistics. In order to remove these events, several approaches have been tried. In all attempted cases, at least 1/3 of the statistics was lost anyway. The two most effective ways seemed to be the low momentum $\pi^+_{slow}\pi^-_{fast}$ events selection and events with $M(p, \pi^+_{fast}) > 1.6$ GeV. Figure 4.11 shows the effect of the latter on the data. While effective in the elimination of the ρ peak, the selection results in a loss half of the data. Further study shows no major change in the meson X rest frame angles with this cut and, therefore, this small background is not expected to change the results of the PWA (most likely, it will contribute to the isotropic background wave). In order to prove this statement, a partial wave analysis was performed for events with $M(p, \pi^+_{fast}) > 1.6$ GeV, and no major changes were observed (see appendix F).

Figure 4.12 shows the Breit Winger (BW) fit of the final invariant mass distribution of $p\pi^+_{slow}$. The function that was used to fit the Δ^{++} distribution is a mass dependent Breit-Wigner (BW) function convoluted with a Gaussian (in order to take into account the resolution), along with the first degree polynomial background function. Apart from the three regular parameters of the BW function, the interaction radius that is used for the centrifugal barrier factors was fitted as a free parameter. A value of 0.2 F was found for this parameter. It is worth mentioning here, that during the partial wave analysis, all calculated amplitudes for the meson states had an interaction radius of 1 F. The polynomial function serves as an approximation of non-Δ^{++} background.

In an additional effort to estimate how many Δ^{++} events are in the data sample, a comparison was made in the Δ^{++} rest frame between the data and the accepted phase space Monte Carlo

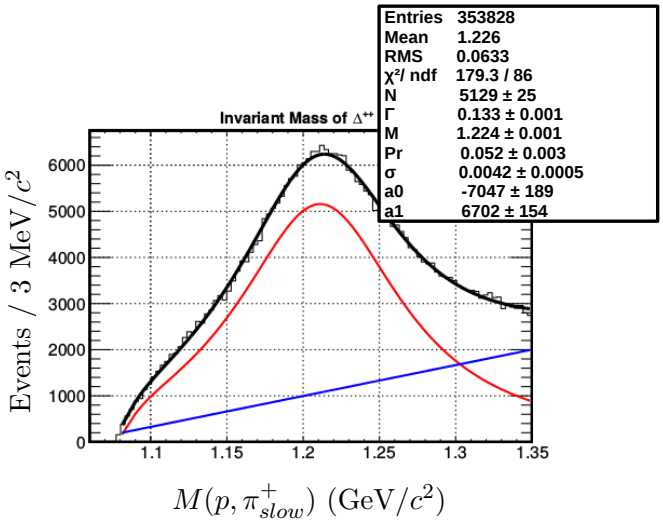

Figure 4.12: $\gamma p \to \pi^-\pi^-\pi^+\Delta^{++}$: Invariant mass of the final $p\pi^+_{slow}$ distribution. It has been fitted with a mass dependent Breit-Wigner function convoluted with a Gaussian along with a first degree polynomial function.

events which have been weighted with Δ^{++} decay amplitudes. Figure 4.13 shows the $cos\theta$ in the Δ^{++} rest frame for the measured four-vectors and for the weighted accepted MC four-vectors. By comparing the bottom plots of Figure 4.13, one can see that the data distribution is consistent with the accepted-weighted MC events with the spin projection M=1/2 (bottom left plot) rather than M=3/2 or the sum of the two projections. This leads to an obvious conclusion: the exchange particle is likely to be spin-less (i.e., a pion rather than a ρ) since it predominantly form states with M=1/2 after combining with spin-1/2 target proton. Also, a "fake" non-existent Δ^{++} incorrectly formed from the unrelated proton and π^+_{slow} particles should exhibit a flat M=0 distribution rather than an observed M=1/2 one. Because there is no obvious structures or discrepancies between the data and pure Δ^{++} MC (apart from a very small mismatch in the bottom left plot of Figure 4.13), it is safe to conclude that non-Δ background in the final sample is rather small and is likely to contribute mostly to an isotropic background wave during PWA.

4.3 Features of the Final $\gamma p \to \pi^-\pi^-\pi^+\Delta^{++}$ Sample

Table 4.1 shows the full selection criteria applied to this channel and the number of events passing each selection. After all listed cuts have been applied, the main features of the data going

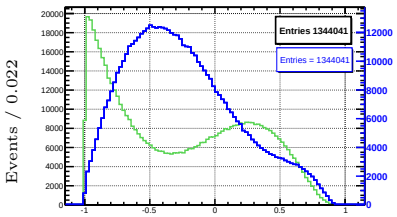

cosθ in the Δ^{++} rest frame for M=1/2, for positive and negative helicity

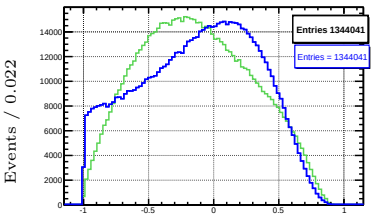

cosθ in the Δ^{++} rest frame for M=3/2, for positive and negative helicity

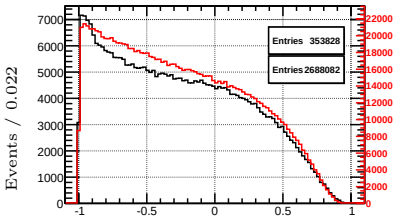

cosθ in the Δ^{++} rest frame for data and summing the helicities for M=1/2

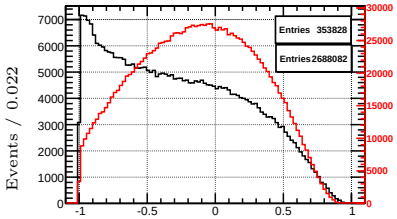

cosθ in the Δ^{++} rest frame for data and summing the helicities for M=3/2

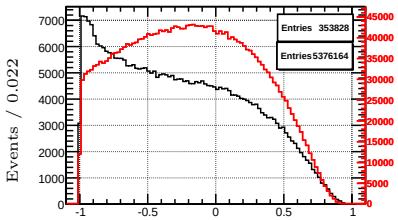

cosθ in the Δ^{++} rest frame for data and summing the helicities and the spin projections

Figure 4.13: $\gamma p \to \pi^-\pi^-\pi^+\Delta^{++}$: The *cosθ* in the Δ^{++} rest frame. **Top:** accepted Monte Carlo four-vectors weighted by the Δ^{++} decay amplitudes for positive (blue) and negative (green) helicities. **Bottom:** the black lines are for the data four-vectors and the red lines are for accepted Monte Carlo weighted by the Δ^{++} amplitudes for different spin projections.

Table 4.1: Table with the number of events before and after each selection for the $\gamma p \to \pi^-\pi^-\pi^+\Delta^{++}$ reaction.

Description	**Interval**	**Events In**	**Events Selected**
Vertex within z-extent of target	$-110 < z < -70$ cm	105,863,100	100,840,300
Vertex within target radius	$r < 10.0$ cm	100,840,300	93,575,180
Event vertex timing cut	$\lvert t_{vtx}(TAG) - t_{vtx}(ST)\rvert < 1.002$ ns	93,575,180	79,764,370
Beta selection for particle tracks	$\lvert\beta_{TOF} - \beta_{p/m}\rvert < 0.03$	79,764,370	75,917,040
Photon Energy	$Beam - Photon \geq 4.4GeV$	75,917,040	31,874,591
Confidence level cut	$FOM - kinFit > 1\%$	31,874,591	3,750,040
Momentum difference	$\lvert\vec{p}_{\pi^+_{fast}}\rvert - \lvert\vec{p}_{\pi^+_{slow}}\rvert > 0.35GeV$	3,750,040	2,460,997
Low momentum transfer	$t' < 0.4$	2,460,997	576,897
Circular cut for K^0_S	see Figure 4.7 for the equation	576,897	573,415
Low mass of $p\pi^+$	$M(p, \pi^+_{slow}) < 1.35GeV$	573,415	353,828

into partial wave analysis are discussed below.

Figure 4.14 shows the 3π and 2π invariant mass distributions for the final sample of events used in the partial wave analysis. Two peaks are visible in the 3π invariant mass distribution, one at 1.3 GeV and another around 1.7 GeV. Figure 4.15 shows the Dalitz plots of $\pi^+\pi^-_{fast}$ and $\pi^+\pi^-_{slow}$ for two different 3π mass regions, i.e. $M_{3\pi} < 1.5$GeV and $M_{3\pi} > 1.5$GeV. The peak at 1.3 GeV of the 3π invariant mass, looking at the Dalitz plot, can be associated with the $\rho(770)\pi$ decay mode. This is consistent with the $a_2(1320)$ meson, which is expected to be dominant in this mass area. The second peak at 1.7 GeV of the 3π invariant mass seems to be associated with two decay modes - the $\rho(770)\pi$ and the $f_2(1270)\pi$. Since this is consistent with the decay modes of the $\pi_2(1670)$ meson, it is evident that these modes need to be included in the partial wave analysis as well. Finally, Figure 4.16 shows the angular distributions in the 3π meson rest frame (defined per the Gottfried-Jackson convention) and in the di-pion rest frame (defined per the helicity convention). Both rest frames are described in detail in Appendix G. The fast and slow in Figure 4.16 are defined as the isobar Y with the larger and smaller magnitude of momentum respectively. The fast $cos\theta$ distribution, in the meson rest frame, populates the forward region and the slow does populate the backward region. In the helicity rest frame, the fast and slow $cos\theta$ distributions appear a little bit differently, mainly due to the small difference in the acceptance, while the azimuthal angles seem to be heavily sculpted by the acceptance.

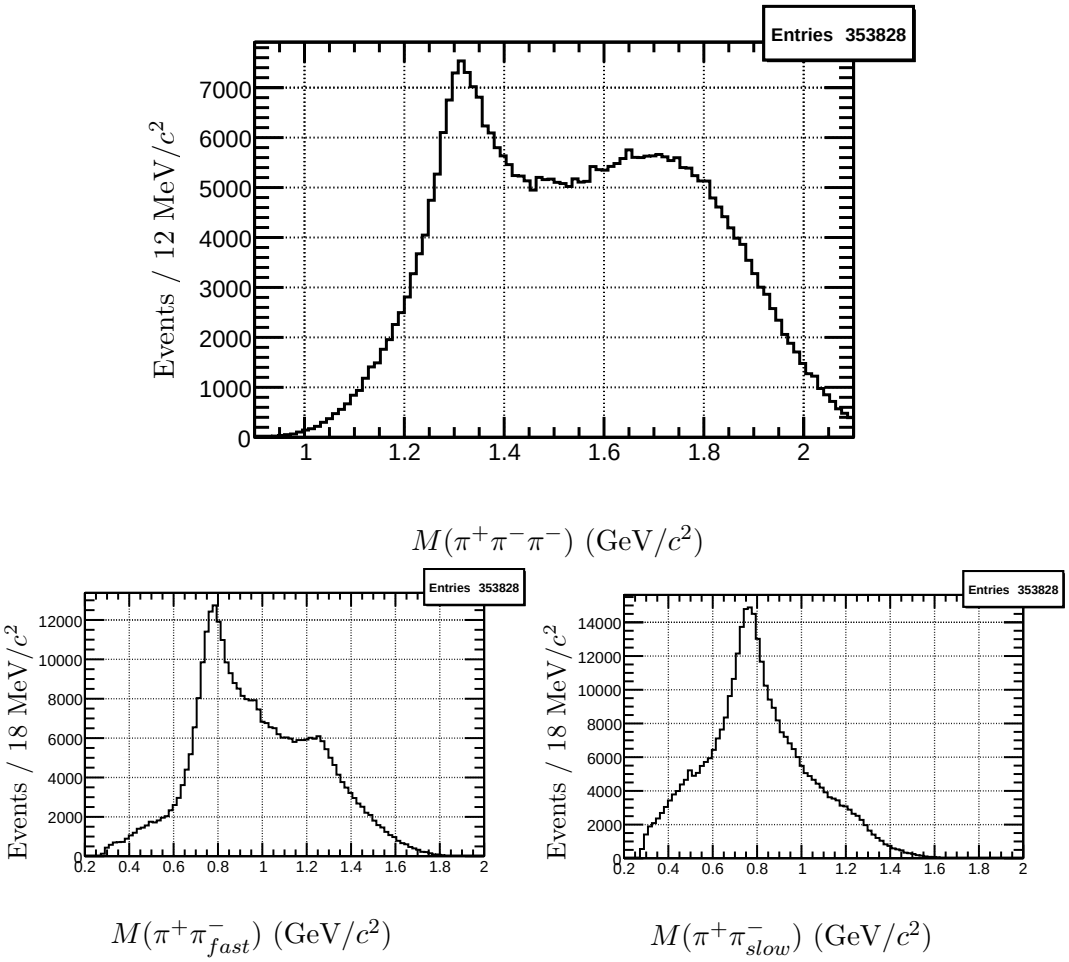

Figure 4.14: $\gamma p \to \pi^-\pi^-\pi^+\Delta^{++}$: The **top** plot shows the invariant 3π mass distribution for the final number of events that were used in the PWA. The **bottom** plots are the $\pi\pi$ invariant mass distributions.

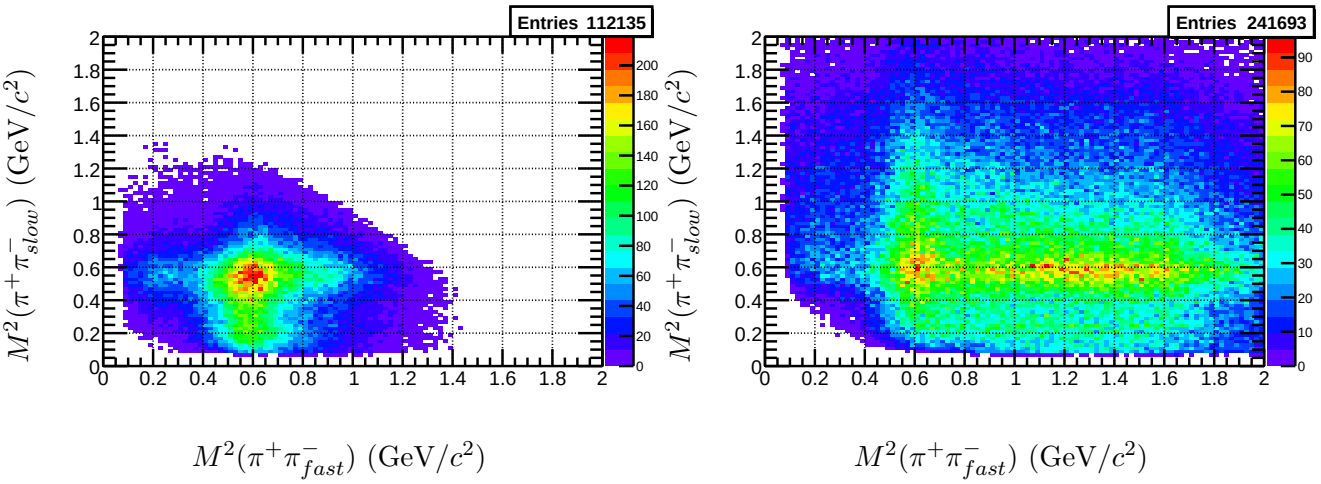

Figure 4.15: $\gamma p \to \pi^-\pi^-\pi^+\Delta^{++}$: Dalitz distributions for the $a_2(1320)$ (**left**) and the $\pi_2(1670)$ (**right**) regions.

4.4 CLAS Detector Acceptance

One of the most important tasks when one is analyzing physics data is to be able to correctly simulate these data. For the current analysis, there are three main reasons why simulation is needed. The first one is understanding of the acceptance for the studied reaction. The second reason is the study of the background that is present in the data sample. By generating three body phase space events and projecting them onto the detector, a one-to-one comparison can be made between the data and the Monte-Carlo (MC). Finally, the MC events were used in the partial wave normalization.

4.4.1 Event Generation

Events were generated isotropically (raw events) in the 3π phase space off of a Δ^{++}; the momentum transfer distribution was also simulated. The range of the photon beam energy used was the same range as for the high energy photons selected in the data. For the Δ^{++}, a relativistic Breit Wigner (BW) function was used, with parameters obtained by fitting the data distribution. At the next stage, the generated events were passed through the CLAS detector simulation and event reconstruction software, and the new four-vectors were collected, i.e., the accepted events.

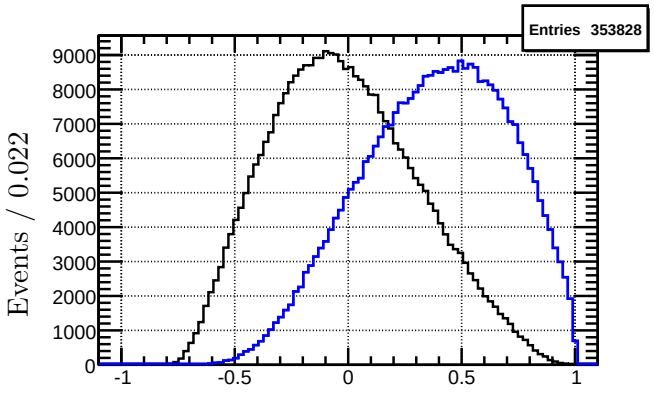

$cos\theta$ (slow Y, fast Y) in the meson rest frame

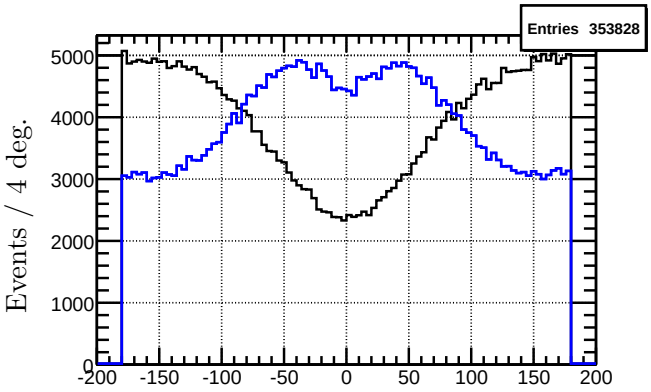

ϕ (slow Y, fast Y) in the meson rest frame

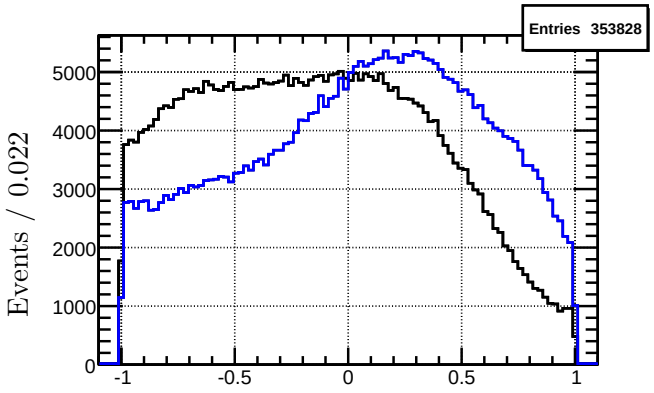

$cos\theta$ (slow Y, fast Y) in the helicity rest frame

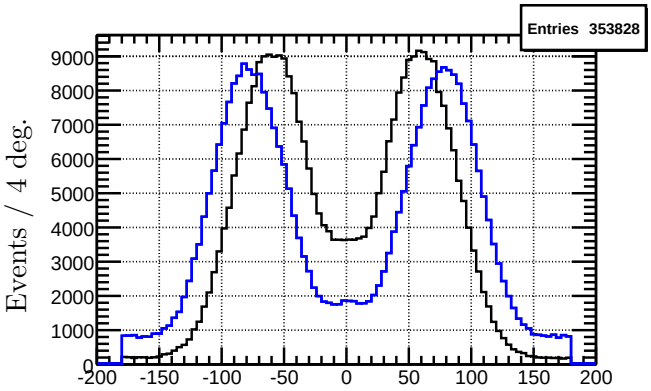

ϕ (fast Y, slow Y) in the helicity rest frame

Figure 4.16: $\gamma p \to \pi^-\pi^-\pi^+\Delta^{++}$: $cos\theta$ and ϕ distributions in the meson rest frame (**top**) and in the helicity rest frame (**bottom**) for the final data sample. **Top left:** for the blue curve the π^-_{fast} was used to form the $\rho - isobar$ and for the black curve the π^-_{slow} was used to form the $\rho - isobar$. **Top right:** ϕ distribution for fast and slow isobar. **Bottom left:** for the blue curve the π^-_{fast} was used as the analyzer and for the black curve the π^-_{slow} was used as the analyzer. **Bottom right:** ϕ distribution for fast and slow analyzer.

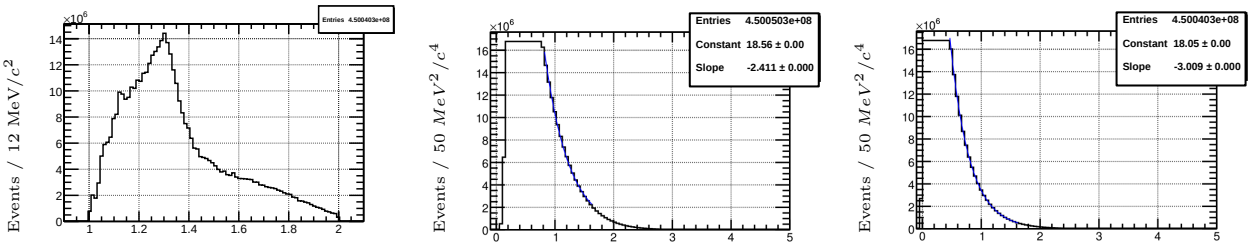

Figure 4.17: $\gamma p \rightarrow \pi^-\pi^-\pi^+\Delta^{++}$: Generated four-vectors distributions. The **left** plot shows the 3π invariant mass distribution, the **center** plot shows the Mandelstam t distribution and the **right** plot shows the t' distribution.

Since a mass independent PWA is applied (i.e., performing the likelihood fit in the narrow 3π mass bins), the MC events were generated in even narrower mass bins than the ones used in the PWA. Specifically, the four-vectors were generated in 5 MeV bins in 3π mass. Also, the 3π invariant mass of the accepted events was constrained to be analogous to the 3π mass of the data. The reason for this was to take into account the bin migration due to the resolution of the detector. Simultaneously, the same procedure was followed for the photon beam energy. The MC events were used for the calculation of the normalization integrals (see Chapter 6 for details). In order to make the MC statistical error negligible in comparison with the statistical error of the data, a much larger number of MC events than the data events were needed. Specifically, events were generated so that the number of accepted events in each mass bin will be ten times the number of data events. Figure 4.17 shows the 3π invariant mass distribution along with the t and t' distributions for the generated four-vectors. The raw four-vectors were generated with the exponential slope b (in the form of $\frac{d\sigma}{dt} \sim e^{-b|t|}$), and several tries were made in order for the t distribution of the accepted events to reproduce the t distribution of the measured events. A total number of 450M events were generated with a t-slope of b=3. Finally, the photon beam energy was generated according to a bremsstrahlung distribution of photon energies between 4.4 GeV and 5.45 GeV.

4.4.2 Modeling the CLAS Detector Response

Following the standard CLAS-g12 procedure for simulating the CLAS detector, the generated events were modeled using the GSIM program. GSIM is based on GEANT3 libraries [44] and is responsible for producing the digitized detector hits in accordance with the generated four-

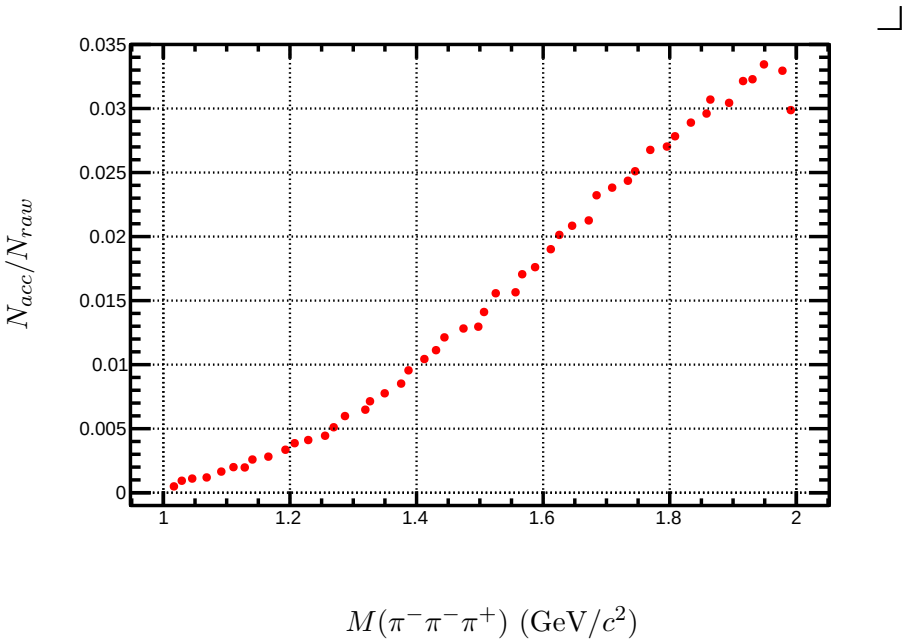

Figure 4.18: $\gamma p \to \pi^-\pi^-\pi^+\Delta^{++}$: The shape of CLAS acceptance as a function of 3π mass.

vectors and event vertex, and taking into account the detector geometry and materials as well as the magnetic field. After the ADC and TDC hits have been generated, the events are smeared according to the CLAS resolution. Also, the dead or inefficient wires and channels from the g12 run are simulated. The GPP program was used for smearing. At the next step, these events are reconstructed back from the detector hits by using the a1c program. Finally, the resulting four-vectors (accepted events) are subjected to the same selection criteria as the real data.

Figure 4.18 shows the acceptance as a function of the 3π invariant mass. As it is expected from the CLAS geometry, the acceptance is low in the very low mass region and varies smoothly over the whole mass range. The 3π and 2π invariant mass distributions are shown in Figure 4.19 for the accepted four-vectors. Figure 4.20 shows the exponential fit of the Mandelstam $|t|$ distribution for the final data events and the final accepted events. Finally, Figure 4.21 shows the angular distributions for the accepted four-vectors in the 3π meson rest frame and in the di-pion rest frame. The same angular distributions for the generated four-vectors are flat, thus, Figure 4.21 shows the effect of the acceptance on the angular distributions from which the physics information about the partial wave quantum numbers is extracted by PWA.

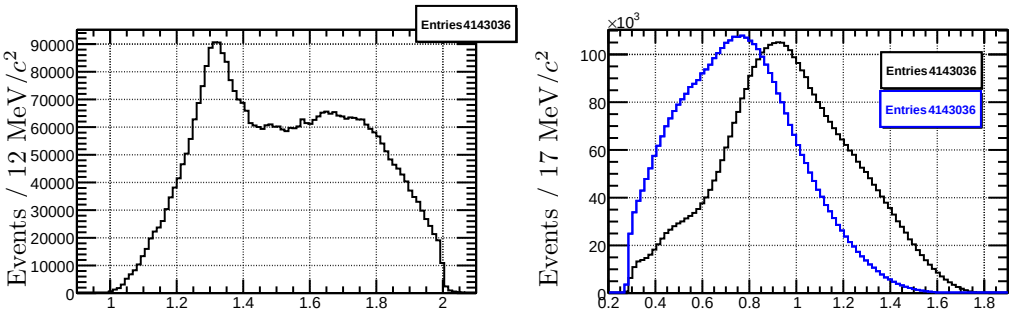

Figure 4.19: $\gamma p \to \pi^-\pi^-\pi^+\Delta^{++}$: The 3π invariant mass distribution is on the **left** plot and on the **right** plots is the $\pi^-\pi^+$ invariant mass distributions. In the right plot the blue curve is formed with the π^+_{slow} and the black curve is formed with the π^+_{fast}.

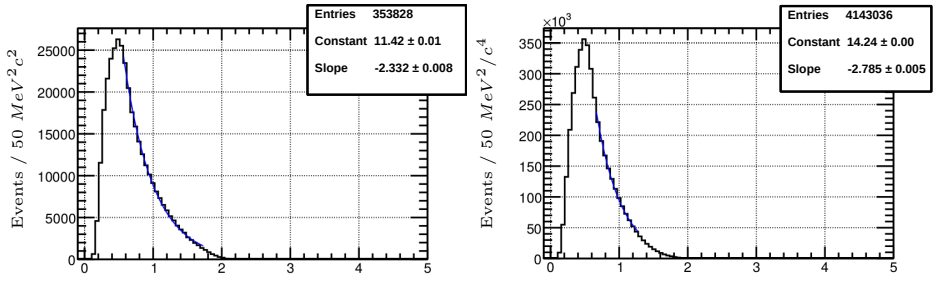

Figure 4.20: $\gamma p \to \pi^-\pi^-\pi^+\Delta^{++}$: The Mandelstam $|t|$ distribution of the final data events (**left**) and for the accepted MC events (**right**).

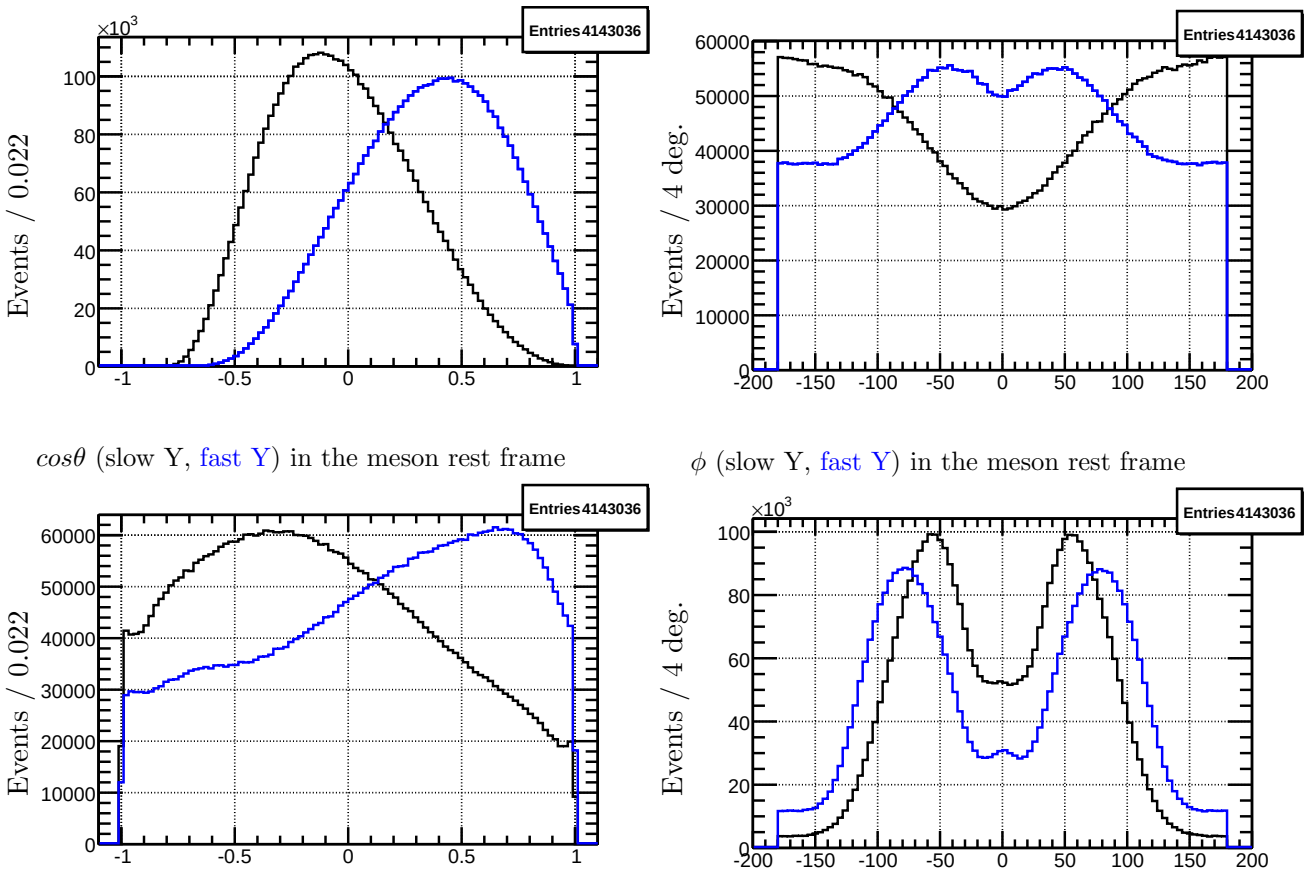

cosθ (slow Y, fast Y) in the meson rest frame

ϕ (slow Y, fast Y) in the meson rest frame

cosθ (slow Y, fast Y) in the helicity rest frame

ϕ (fast Y, slow Y) in the helicity rest frame

Figure 4.21: $\gamma p \to \pi^-\pi^-\pi^+\Delta^{++}$: *cosθ* and ϕ distributions in the meson rest frame (**top**) and in the helicity rest frame (**bottom**) for the accepted four-vectors. **Top left:** for the blue curve the π^-_{fast} was used to form the $\rho - isobar$ and for the black curve the π^-_{slow} was used to form the $\rho - isobar$. **Top right:** ϕ distribution for fast and slow isobar. **Bottom left:** for the blue curve the π^-_{fast} was used as the analyzer and for the black curve the π^-_{slow} was used as the analyzer. **Bottom right:** ϕ distribution for fast and slow analyzer.

4.5 Summary

From the initial sample of 25B events collected and reconstructed during the g12 run, about 100M events have 2 positive and 2 negative detected charged pions. Standard timing and vertex selection criteria were applied, leaving 76M events. 31M events were found to have the high energy beam photon, and a missing proton selection with the kinematic fitting resulted in 3.8M events. Further selection criteria were applied to enhance the peripheral production and to reduce the baryon background. After all the applied cuts, the final event sample size is 350K. PWA was performed on these events. Also, 450M 3π raw phase space events were generated and, after detector simulation, reconstruction and application of the same selection cuts, about 4M accepted events remained. The generated and the accepted four-vectors were used as normalization integrals in the PWA.

CHAPTER 5

EVENT SELECTIONS FOR THE EXCLUSIVE $\gamma p \to n\pi^+\pi^+\pi^-$ REACTION

Another way to analyze charged 3π production is with a recoil neutron. In this channel, the events with three detected charged particles are selected from the CLAS-g12 data-set. The neutron is identified via energy and momentum conservation. Note that these events do not overlap with events selected for the $\gamma p \to \pi^-\pi^-\pi^+\Delta^{++}$ channel, where four detected charged particles were required. The difference in the number of particles in the final state will result in a lower acceptance for the 3π with a recoil Δ^{++}. An extensive analysis for the $\gamma p \to n\pi^+\pi^+\pi^-$ reaction channel was performed earlier by Dr. Craig Bookwalter. However, an error was found later in the parametrization of some partial waves in his analysis. As a result, the channel has been fully reanalyzed using the latest software tools such as a kinematic fitter. One can refer to Chapter 3 for the standard selection criteria applied for this channel. In this Chapter emphasis is going to be given to baryon background reduction and simulation of 3π phase space events for this reaction.

5.1 Reduction of Baryon Background

Figure 5.1 shows the $n\pi$ invariant mass distributions and their correlations with the mass of the 3π. The $n\pi^-$ invariant mass plot shows a peak around the mass of $\Delta(1232)$. The $n\pi^+_{fast}$ invariant mass distributions show enhancements around the mass of $N^*(1520/1535)$ and $N^*(1650/1675/1680)$. Similar enhancements are present in the $n\pi^+_{slow}$ spectrum, along with a shoulder around the mass of $\Delta(1232)$. These baryon resonances can be effectively removed by selecting events with a low squared four-momentum transfer between the incoming photon and the three-pion system. To enhance the peripheral production and to account for the strong dependence of the minimal value of t on the 3-pion mass, the normalized four-momentum transfer t' was used to select events with t' less than 0.1 GeV$^2/c^4$. A discussion of the t' along with its definition can be found in Section 4.2. The top left plot of Figure 5.1 shows the effect of the low t' selection on the 3π invariant mass. The main effect seems to be in the high 3π mass region where the broad enhancement from 1.5 to

Table 5.1: Table with the number of events before and after each selection for the $\gamma p \to n\pi^-\pi^-\pi^+$ reaction.

Description	**Interval**	**Events In**	**Events Selected**
Vertex within z-extent of target	$-110 < z < -70$ cm	707,329,219	658,403,589
Vertex within target radius	$r < 10.0$ cm	658,403,589	587,508,335
Event vertex timing cut	$\lvert t_{vtx}(TAG) - t_{vtx}(ST)\rvert < 1.002$ ns	587,508,335	421,091,544
Beta selection for particle tracks	$\lvert\beta_{TOF} - \beta_{p/m}\rvert < 0.03$	421,091,544	382,907,980
Photon Energy	$E_\gamma \geq 4.4GeV$	382,907,980	118,656,025
Confidence level cut	$FOMkinFit > 1\%$	118,656,025	7,424,941
Low momentum transfer	$t' < 0.1GeV^2$	7,424,941	980,019
Backward lab angle cut	$\theta_{lab}(\pi^+_{slow}) < 25^o$	980,019	600,925

2 GeV/c has been reduced. By looking at the effect of the low t' selection in the correlation plots of Figure 5.1, the reduction of events in the high 3π mass region has an obvious correlation with the reduction of the unwanted baryon resonances.

Figure 5.2 shows the $n\pi^+$ invariant mass distributions, the θ_{lab} of the π^+_{slow} and its correlation with the $n\pi^+$ invariant mass distributions. There are still small structures from the baryon resonances in the data even after the t' cut. To further enhance the 3π meson production relative to the baryonic background, events were chosen with $\theta_{lab}[\pi^+_{slow}] < 25^o$. Pions from the decay of the mesons produced at the top vertex are expected to be boosted more in the forward direction comparing with pions from the isotropic decays of a slow moving excited recoil baryons. Removal of a fraction of the events with large lab angles of the pions helps to reduce the baryon background, especially the structure in the $n\pi^+_{slow}$ invariant mass distribution at 1.5 GeV/c.

Table 5.1 shows the number of events that pass each selection cut for the $\gamma p \to n\pi^+\pi^+\pi^-$ reaction.

5.2 Features of the Final $\gamma p \to n\pi^-\pi^-\pi^+$ Reaction

The main features of the final 3π event sample can now be examined. Figure 5.3 shows the 3π and the $\pi^+\pi^-$ invariant mass distributions. The strong $\rho(770)$ resonance is formed in both $\pi\pi$ distributions as well as the $f_2(1270)$ meson in the $\pi^+_{fast}\pi^-$ combination. The 3π invariant mass distribution for the final sample of events used in the PWA shows a clear peak around the $a_2(1320)$ meson, along with a broad enhancement in 1.5 to 1.7 GeV mass region. Figure 5.4 shows the Dalitz plots for the two different 3π mass regions. The Dalitz plots exhibit ρ and f_2 intermediate $\pi\pi$

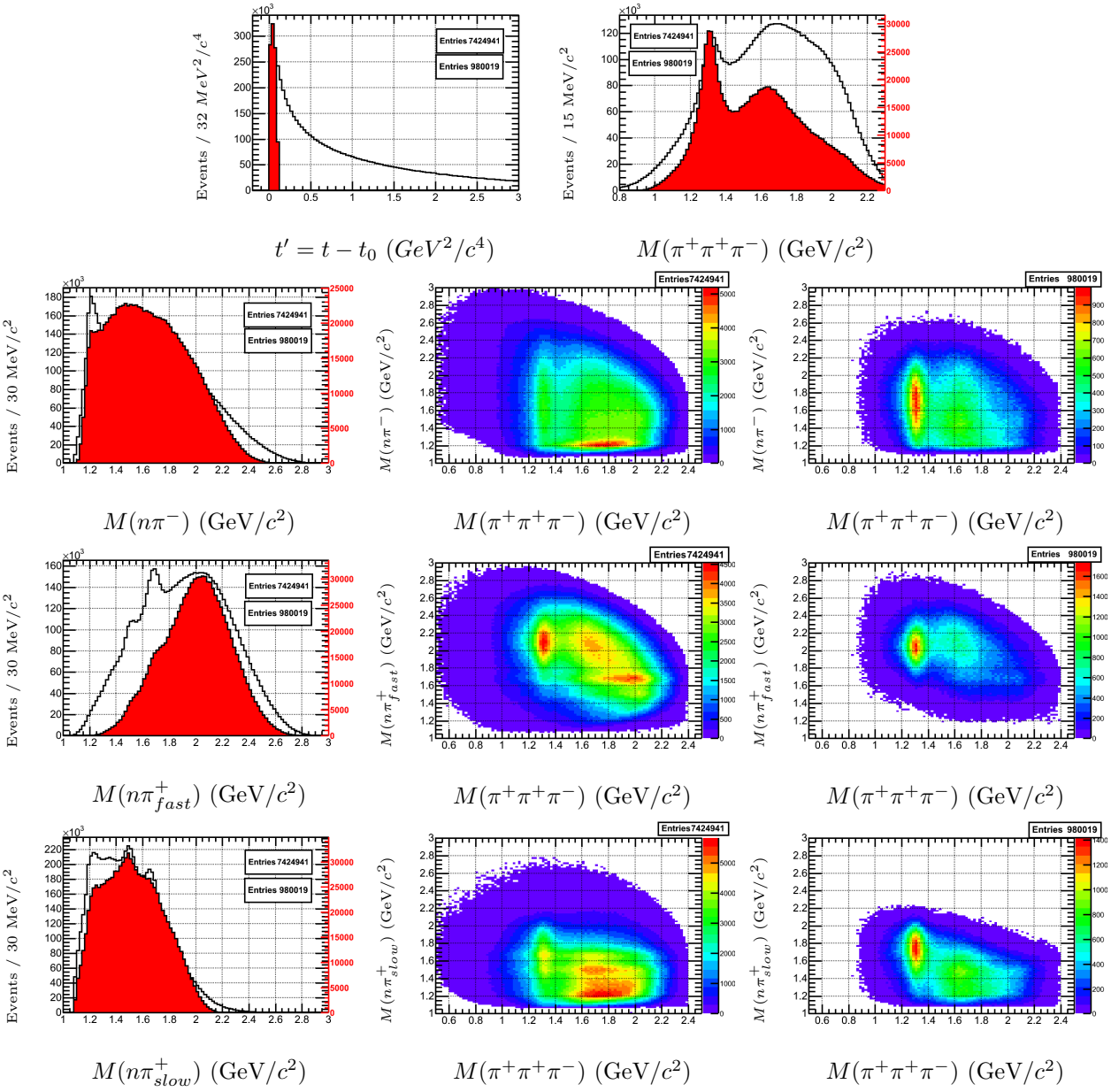

Figure 5.1: $\gamma p \to n\pi^+\pi^+\pi^-$: The top two plots show the t' and the 3π invariant mass distributions. The first column shows the $n\pi$ invariant mass distributions. The second column shows the correlations between the $n\pi$ and 3π invariant mass plots and the third column shows those correlations for events with $t' < 0.1\ GeV^2/c^4$.

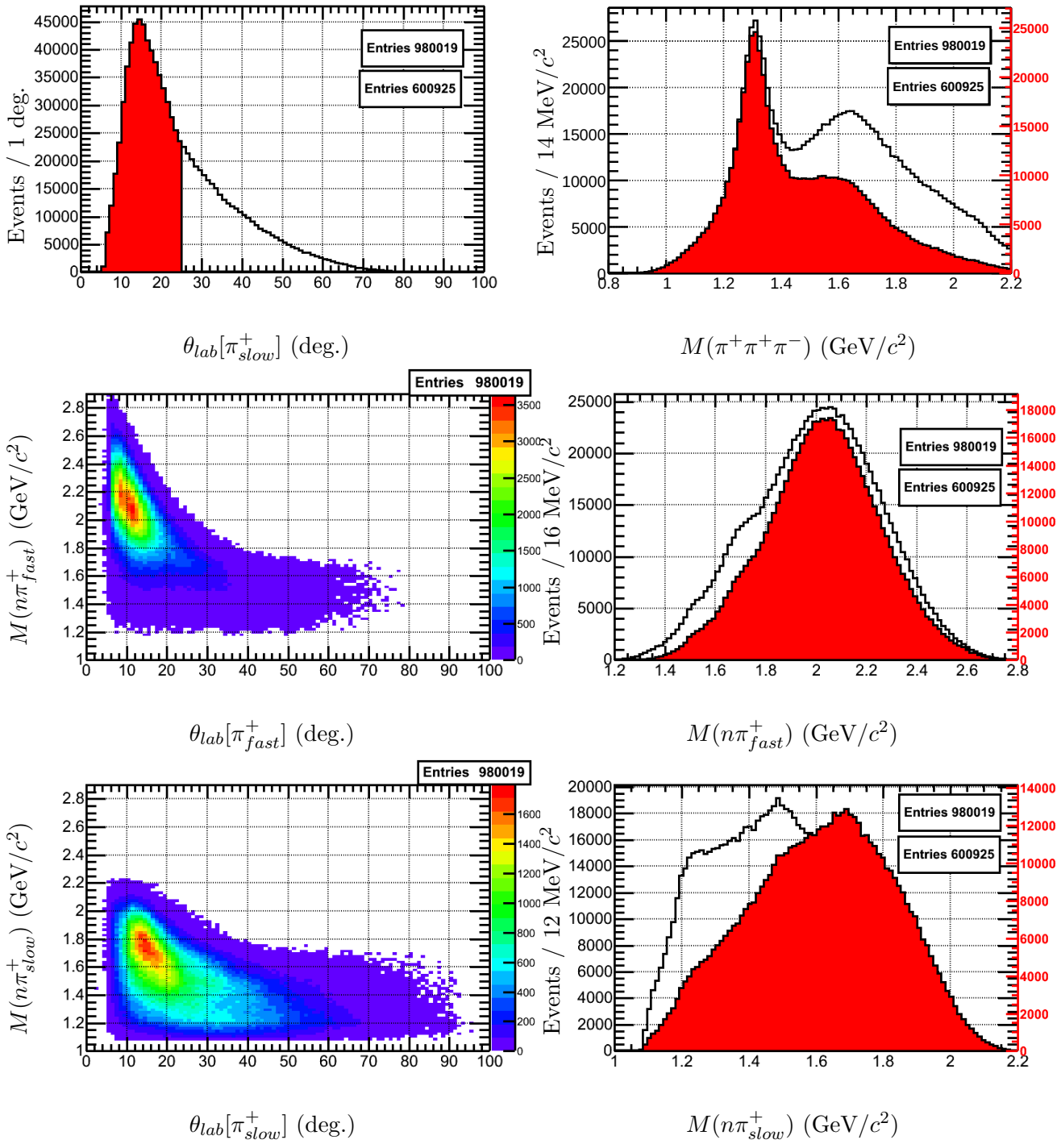

Figure 5.2: $\gamma p \to n\pi^+\pi^+\pi^-$: The first column shows the $\theta_{lab}(\pi^+_{slow})$ distribution and its correlation with the $n\pi^+$ invariant mass. The second column is the 3π and $n\pi^+$ invariant mass distributions. The red histograms have been plotted for events with $\theta_{lab}(\pi^+_{slow}) < 25^o$.

isobar states. In the high 3π mass region the dominant decay mode is the $f_2\pi$ which is consistent with the primary decay mode of the $\pi_2(1670)$. The $\rho\pi$ decay mode is also accessible in the high 3π mass region. This is the secondary decay mode of the $\pi_2(1670)$. Note that the exotic $\pi_1(1600)$ state has being seen previously decaying also in that mode. In the low 3π mass region, the dominant $\rho\pi$ decay mode along with the peak at 1.3 GeV of the 3π invariant mass distribution is a strong indication of the $a_2(1320)$ meson production.

Figure 5.5 shows the $|t|$ distributions for two different 3π mass regions. The $cos\theta$ and ϕ distributions in the Gottfried-Jackson and the helicity frames are shown in Figure 5.6. Both rest frames are described in detail in Appendix G. The θ distributions in the GJ rest frame have both forward and backward angles populated. The θ in the helicity frame is different for fast and slow isobar combinations. Most likely, this is an artifact due to a different acceptance. Details of the acceptance studies follow in the next section.

5.3 CLAS Detector Acceptance

Events were generated isotropically in the 3π phase space off of a neutron with an exponential slope b (in the form of $\frac{d\sigma}{dt} \sim e^{-b|t|}$). The photon beam energy was generated according to a bremsstrahlung distribution for photon energies from 4.4 to 5.45 GeV. The generated four vectors were projected to the CLAS detector using the same software packages as described in the $\gamma p \rightarrow \pi^-\pi^-\pi^+\Delta^{++}$ reaction. The momentum transfer distribution was simulated and several tries were made for the Mandelstam $|t|$ distribution of the accepted four-vectors to reproduce the measured $|t|$ distribution. 540M events were generated in 5 MeV bins in 3π mass with a slope of b=4.37. The accepted 3π mass distribution was constrained to follow the 3π data distribution to account for the bin migration.

The raw events were simulated according to the CLAS detector and the same selection cuts as with the real data were applied, leaving 5.8M events at the end (which is more than ten times the statistics of the data). Figure 5.7 shows the 3π and the $\pi\pi$ invariant mass distributions for the accepted four-vectors. A comparison between the momentum transfer distribution of the data and the accepted four-vectors is shown in Figure 5.8. Figure 5.9 shows the acceptance as a function of the 3π invariant mass, which varies smoothly over the whole mass range. Finally, Figure 5.10 shows the $cos\theta$ and ϕ distributions in the Gottfried-Jackson and the helicity rest frames. The

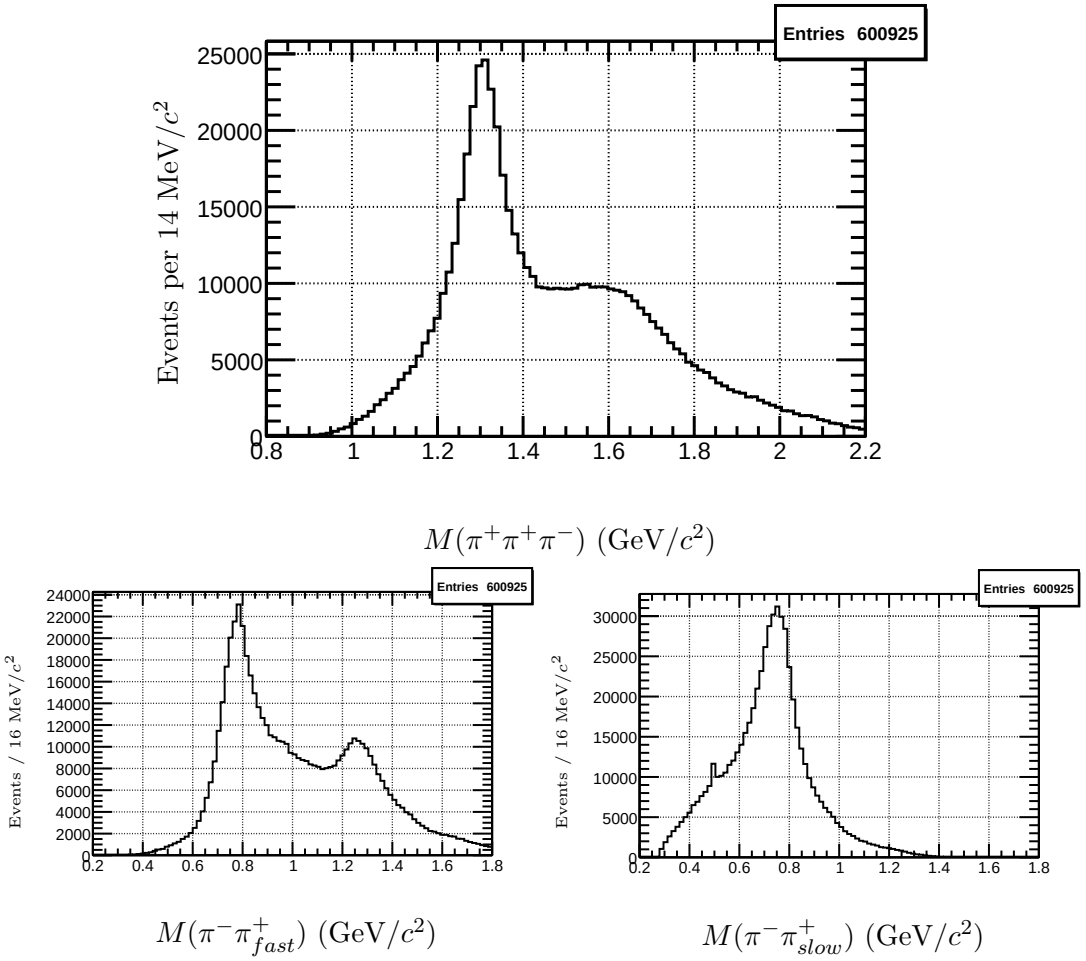

Figure 5.3: $\gamma p \to n\pi^+\pi^+\pi^-$: The invariant 3π mass distribution for the final sample of events used in the PWA and the $\pi^+\pi^-$ invariant mass distributions.

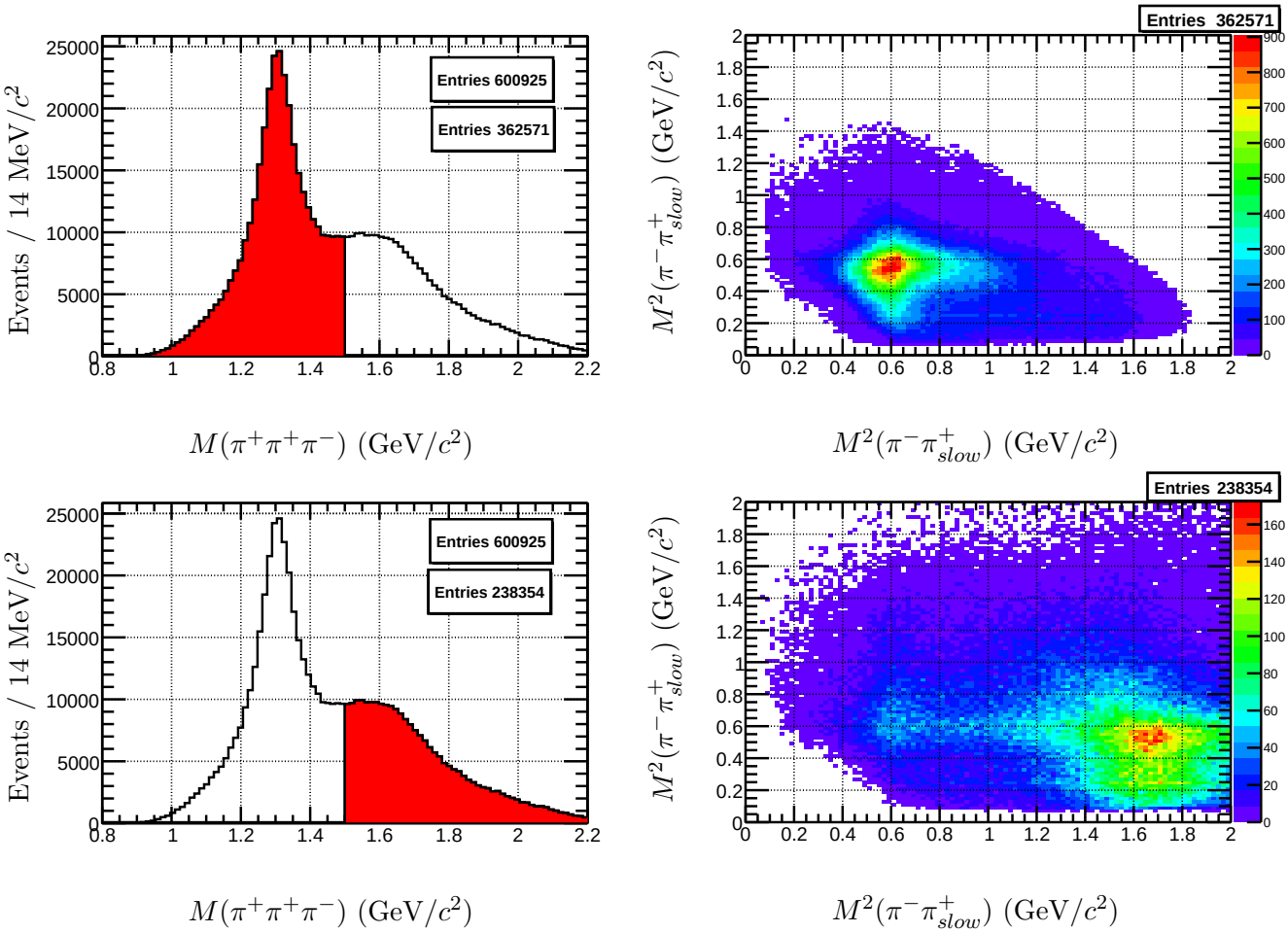

Figure 5.4: $\gamma p \rightarrow n\pi^+\pi^+\pi^-$: The **top right** plot shows the Dalitz plot for $M_{3\pi} < 1.5 GeV/c$ (low mass region). The **bottom right** plot shows the Dalitz plot for $M_{3\pi} > 1.5 GeV/c$ (high mass region).

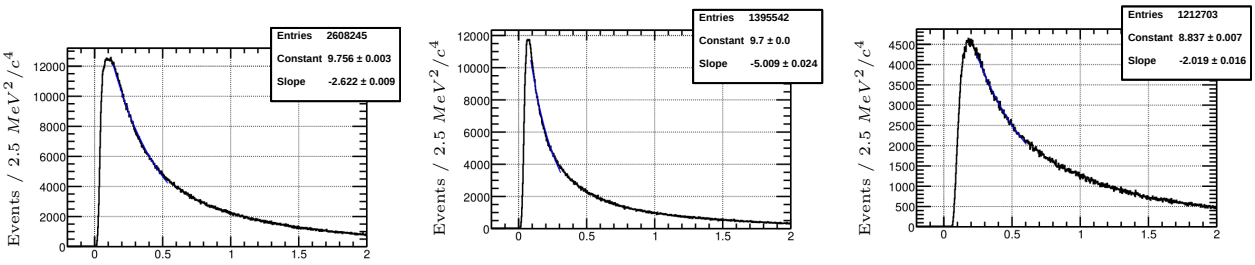

Mandelstam $|t|$ (GeV^2/c^4)

Mandelstam $|t|$ in the $a_2(1320)$ region (GeV^2/c^4)

Mandelstam $|t|$ in the $\pi_2(1670)$ region (GeV^2/c^4)

Figure 5.5: $\gamma p \to n\pi^+\pi^+\pi^-$: Exponential fits to the $|t|$ distribution for the full 3π mass range (**left plot**), for the low 3π mass region (**center plot**) and for the high 3π mass region (**right plot**). The events showed have the θ_{lab} cut but not the low t' selection.

acceptance seems to vary smoothly in the Gottfried-Jackson frame, while the helicity angles are heavily sculptured by the acceptance.

5.4 Summary

From the initial sample of 25B events reconstructed from the g12 run, about 700M events have 3 detected charged pions. Standard timing and vertex selection criteria were applied, leaving 380M events. Among them, 110M events were found with the high energy beam photon. A missing neutron was selected though the kinematic fitting, leaving 7.4M events. Further selection criteria were applied to enhance peripheral production and to reduce the baryon background. After all the applied cuts, the final event sample has 600K events. The PWA was performed to this events. Also, 540M 3π phase space events were generated. After projecting them through the CLAS detector, doing the kinematic fitting and applying the selection cuts, about 5.8M accepted Monte Carlo events have remained. The generated and the accepted four-vectors were used as normalization integrals in the PWA.

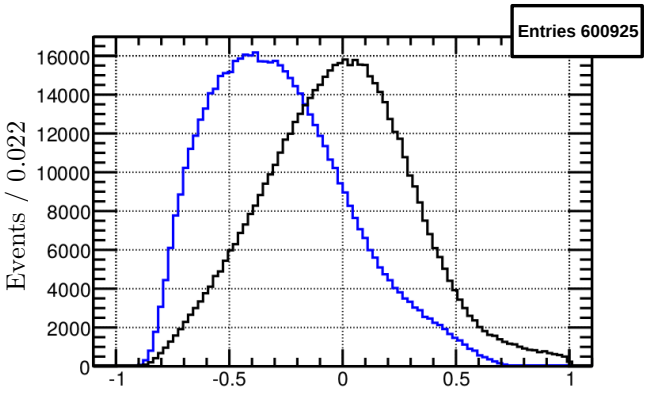

$cos\theta$ (fast Y, slow Y) in the meson rest frame

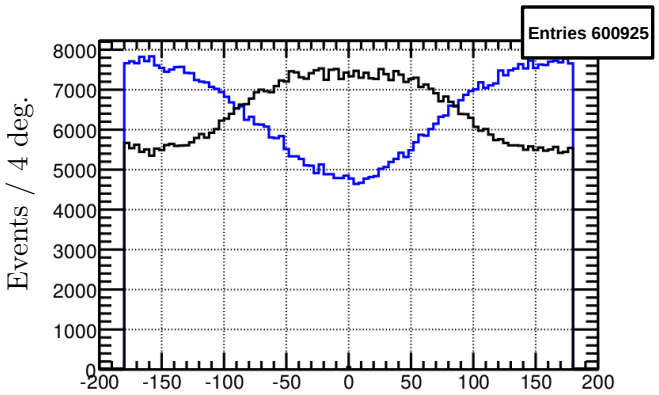

ϕ (fast Y, slow Y) in the meson rest frame

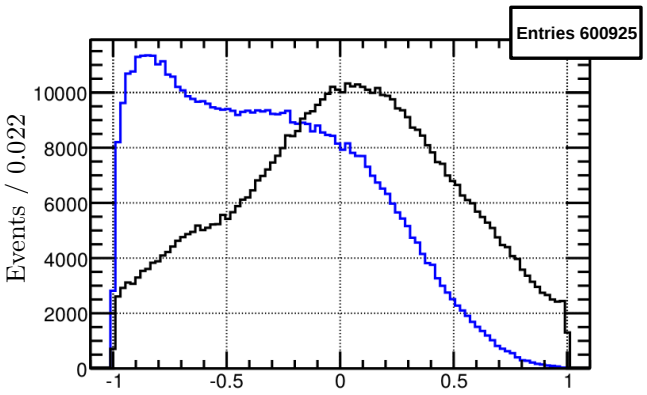

$cos\theta$ (fast Y, slow Y) in the helicity rest frame

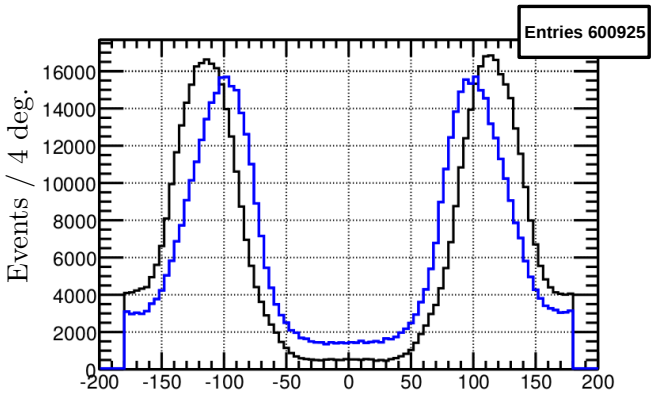

ϕ (fast Y, slow Y) in the helicity rest frame

Figure 5.6: $\gamma p \to n\pi^+\pi^+\pi^-$: $cos\theta$ and ϕ distributions in the meson rest frame (**top**) and in the helicity rest frame (**bottom**) for the final data sample. **Top left:** for the blue curve the π^-_{slow} was used to form the $\rho - isobar$ and for the black curve the π^-_{fast} was used to form the $\rho - isobar$. **Top right:** ϕ distribution for fast and slow isobar. **Bottom left:** for the blue curve the π^-_{slow} was used as the analyzer and for the black curve the π^-_{fast} was used as the analyzer. **Bottom right:** ϕ distribution for fast and slow analyzer.

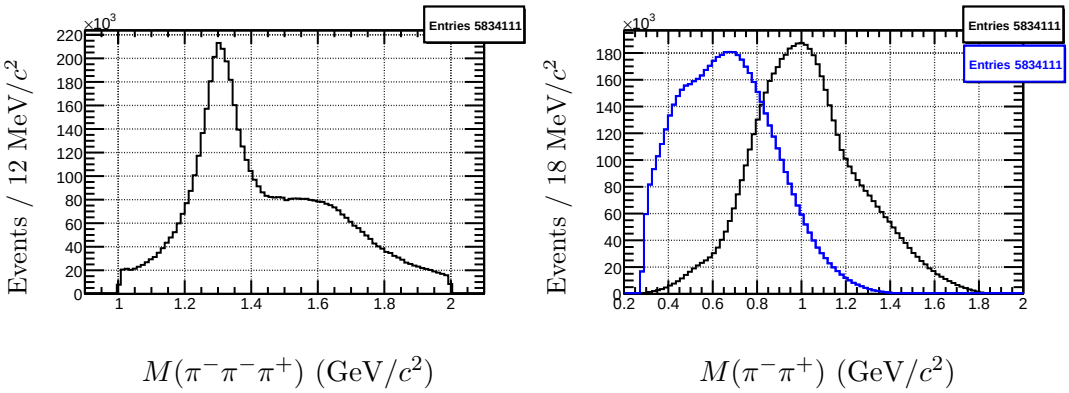

Figure 5.7: $\gamma p \to n\pi^+\pi^+\pi^-$: The **left** plot is the invariant 3π mass distribution and the **right** plot is the $\pi^-\pi^+$ invariant mass distribution for the final number of accepted events. In the left plot: the blue curve is plotted with the π^+_{slow}, while the black curve is plotted with the π^+_{fast}. All the selection cuts that are applied to the data, are also applied to those MC events.

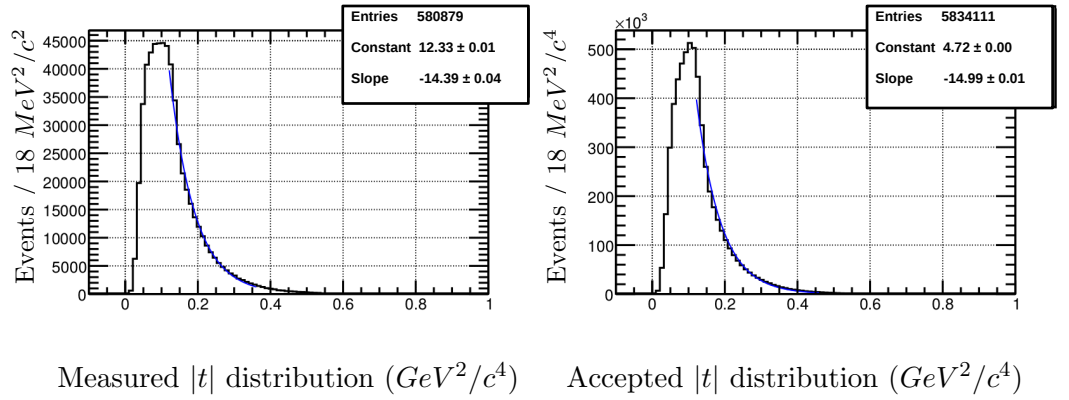

Figure 5.8: $\gamma p \to n\pi^+\pi^+\pi^-$: The Mandelstam $|t|$ distribution of the final data events (**left**) and for the accepted MC events (**right**). Since the MC events were generated from 1 to 2 GeV the measured events in the left plot are also constrained in the same mass region.

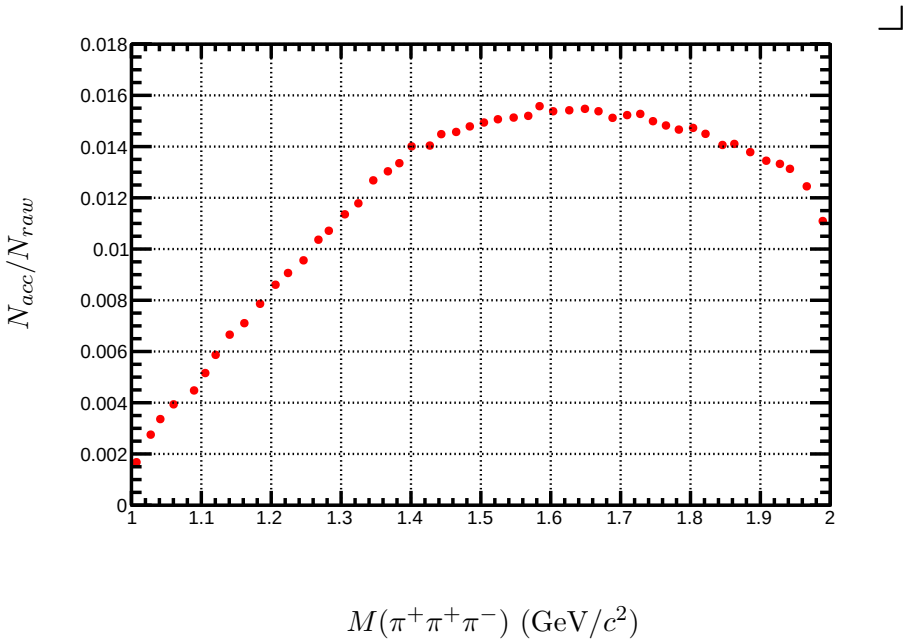

Figure 5.9: $\gamma p \to n\pi^+\pi^+\pi^-$: The shape of CLAS acceptance as a function of 3π mass with all the selection cuts been applied.

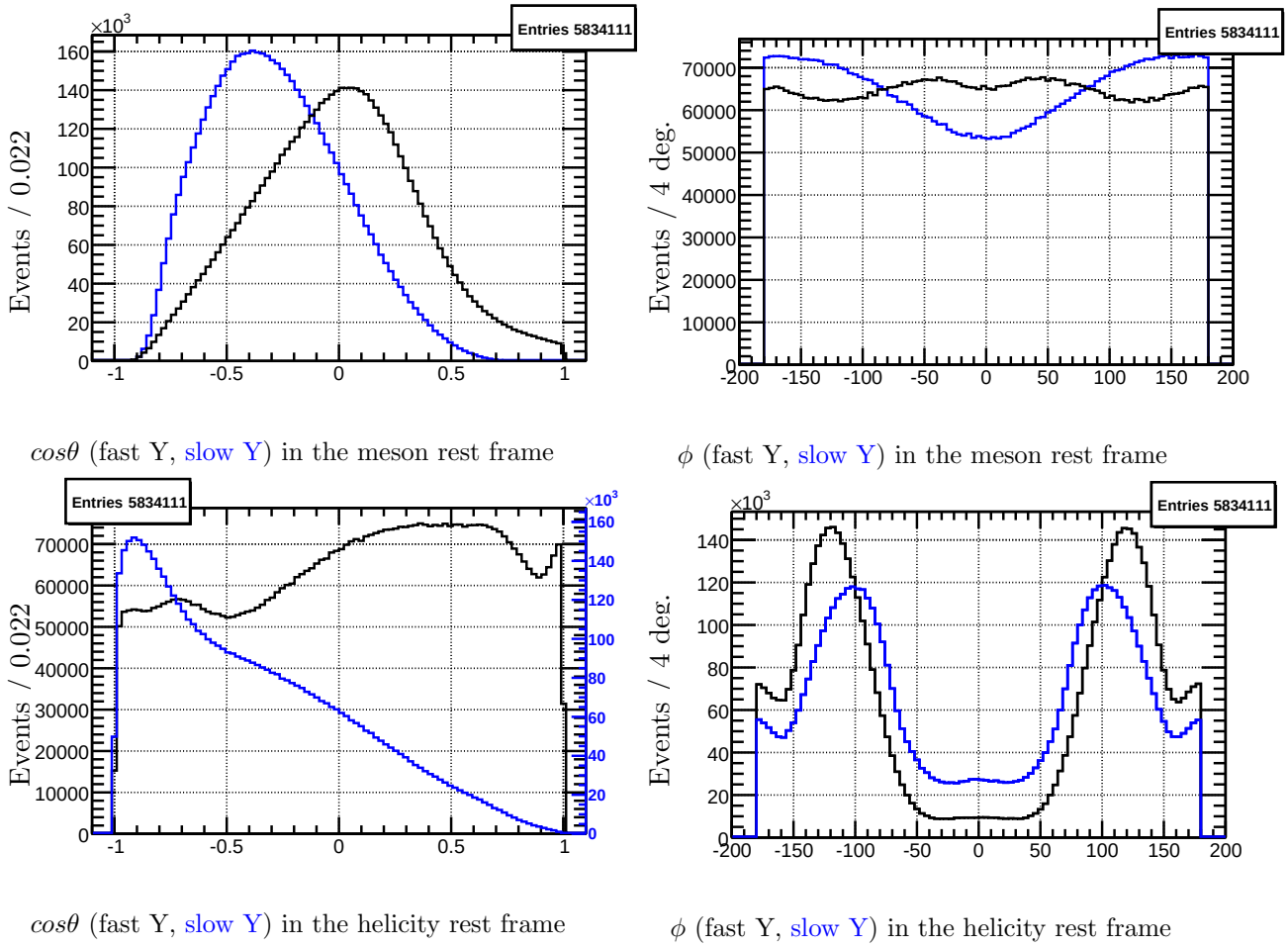

cosθ (fast Y, slow Y) in the meson rest frame

ϕ (fast Y, slow Y) in the meson rest frame

cosθ (fast Y, slow Y) in the helicity rest frame

ϕ (fast Y, slow Y) in the helicity rest frame

Figure 5.10: $\gamma p \to n\pi^+\pi^+\pi^-$: *cosθ* and ϕ distributions in the meson rest frame (**top**) and in the helicity rest frame (**bottom**) for the accepted four-vectors. **Top left:** for the blue curve the π^-_{slow} was used to form the $\rho - isobar$ and for the black curve the π^-_{fast} was used to form the $\rho - isobar$. **Top right:** ϕ distribution for fast and slow isobar. **Bottom left:** for the blue curve the π^-_{slow} was used as the analyzer and for the black curve the π^-_{fast} was used as the analyzer. **Bottom right:** ϕ distribution for fast and slow analyzer.

CHAPTER 6

PARTIAL WAVE ANALYSIS FORMALISM

In the previous two chapters, events were selected which fulfill certain kinematic criteria for a diffractive dissociation. The next step is to analyze the dynamics of the intensity distributions, using amplitude analysis. The goal of partial wave analysis (PWA) is to identify the various spin-parity states by disentangle the intensity spectrum. In this chapter the PWA formalism is described, and the last two chapters of this work are dedicated to the PWA results for the two reaction channels.

6.1 Introduction

This analysis is concentrated in multiparticle final states, produced by an unpolarized real photon, which is generated from electron inelastic scattering. We want to find strong interacting mesonic resonances and to identify their quantum numbers. Also, the photon is considered to be composed of vector mesons ($\rho, \omega, \phi, ...$) according to vector dominance model (VMD) [45]. Furthermore, both of the reactions subject to PWA are multi-final state channels, and so the isobar model has been used. The latter assumes a two body sequential decay series of the resonance. A schematic for the two reaction channels can be seen in Figure 6.1. Also the majority of the formulas described here is based on PWA analysis in Brookhaven National Laboratory [46] and JLab [47].

To begin with, we consider the following reaction:

$$\gamma p \to XN', \quad X \to \pi\pi\pi \tag{6.1}$$

where the N' is the recoil baryon. Using the Fermi's golden rule the differential cross section is given by:

$$\frac{d\sigma}{dtds} = \sum_{ext.spins} \int |\mathcal{M}|^2 d\rho(\tau) \tag{6.2}$$

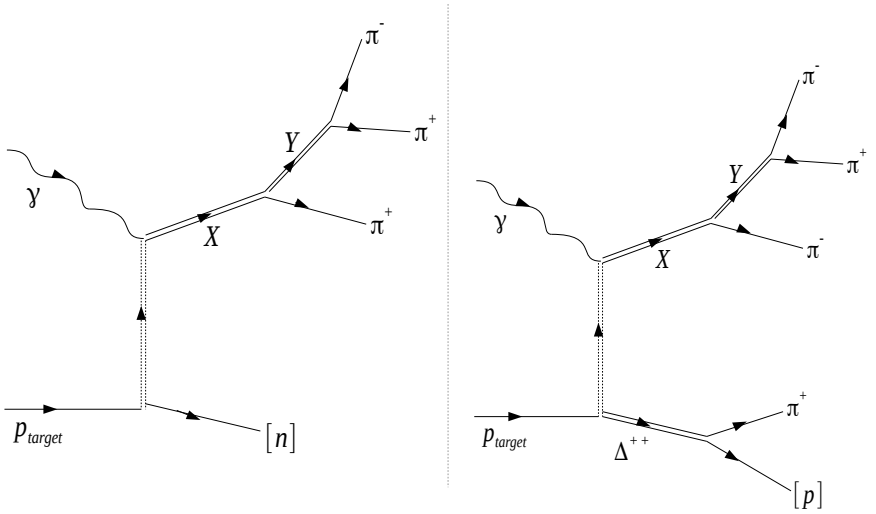

Figure 6.1: The two diagrams show a diffractive reaction in the isobar model. The **left** shows a $\gamma p \to n\pi^+\pi^+\pi^-$ reaction and the **right** plot shows a $\gamma p \to \pi^-\pi^-\pi^+\Delta^{++}$ reaction.

where τ is the complete set of variables needed to describe the decay of the resonance. In our case:

$$\tau = \{\Omega, \Omega_h, w\} \tag{6.3}$$

$$d\tau = d\Omega \; d\Omega_h \; dw \tag{6.4}$$

$$= d\Phi \; dcos\Theta \; d\phi \; dcos\theta \; dw \tag{6.5}$$

$\Omega = (\Theta, \Phi)$ are the polar and azimuthal angles, describing the isobar orientation $\vec{p}$ in the meson X rest frame. The z-axis is chosen to be parallel to the beam momentum in the X rest frame and the y axis is along the production normal to $\vec{beam} \times \vec{X}$ defined in the overall center of mass frame (CM). The $\Omega_h = (\theta, \phi)$ are the polar and azimuthal angles, that describe the orientation $\vec{q}$ of one of the decay products of the isobar in the helicity frame. The axes are defined as $\hat{z_h} = \hat{p}$ and $\hat{y_h} = \hat{z} \times \hat{p}$ where the z-axis is the one in the X-rest frame. W is the mass of the resonance X, w is the mass of the isobar Y, t is the mandelstam variable, $d\rho(\tau)$ is the Lorentz invariant phase space element (LIPS) and $\mathcal{M}$ is the Lorentz invariant transition amplitude. We can then write:

$$d\rho(\tau) \propto p_{CM} \; dW \; d\tau \tag{6.6}$$

where p_{CM} is the center-of-mass momentum. Assuming that the cross section does not change for the CM energies the analysis is referring to, we can write:

$$\frac{d\sigma}{dt \; dW} \propto \sum_{ext.spins} \int |\mathcal{M}|^2 d\tau \tag{6.7}$$

By considering small bins on W and because we simulate the t distribution, the $\mathcal{M}$ will only depend on τ and we can define the intensity, $I(\tau)$, as:

$$I(\tau) \equiv \sum_{ext.spins} |\mathcal{M}|^2 \tag{6.8}$$

then

$$\frac{d\sigma}{dt \; dW} \propto \int I(\tau) d\tau \tag{6.9}$$

The intensity represents the probability for having a particle scattered into the angular distribution specified by τ in the $\Delta W \; \Delta t$ kinematical range. Also using the transition operator, $\hat{T}$, we can express the transition amplitude as $\mathcal{M} = \langle out|\hat{T}|in\rangle$ and then we can write:

$$I(\tau) = \sum_{ext.spins} \langle out|\hat{T}|in\rangle \langle in|\hat{T^\dagger}|out\rangle \tag{6.10}$$

Also we can define the initial spin density matrix operator as $\hat{\rho_{in}} \equiv |in\rangle\langle in|$. For polarized photon beam and target we can express the polarized state as a linear combination of two pure polarized states, such as:

$$\hat{\rho_{in}} = \sum_{i,j} \rho_{i,j} = \sum_{i,j=1}^{2} |i\rangle\langle j| \tag{6.11}$$

The transition operator can be factorized into two parts: the production of X and the decay operator of X. Then,

$$I(\tau) \propto \sum_{ext.spins} \sum_{i,j} \langle out|^i\hat{T}_{decay}{}^i\hat{T}_{production}\rho_{ij}{}^j\hat{T}^{\dagger}_{production}{}^j\hat{T}^{\dagger}_{decay}|out\rangle \tag{6.12}$$

Here in the ext. spins we excluded the beam and the target spins, since they are described by the initial state spin density matrix. Furthermore, we can include a complete set of orthogonal states, called partial waves, such that $\sum_X |X\rangle\langle X| = 1$ and by inserting it in the previous equation we have:

$$I(\tau) \propto \sum_{ext.spins} \sum_{i,j} \sum_{X,X'} \langle out|^i\hat{T}_d|X\rangle\langle X|^i\hat{T}_p\rho_{i,j}{}^j\hat{T}^{\dagger}_p|X'\rangle\langle X'|^j\hat{T}^{\dagger}_d|out\rangle \tag{6.13}$$

Each of these states can be described by a set of quantum numbers and we are going to call them b. The decay amplitude can then be defined as ${}^iA_b(\tau) = \langle out|^i\hat{T}_d|X\rangle$ for a given partial wave b. We can also define the production amplitudes ${}^iV^k_b$ for the external spins k as:

$$\langle X|^i\hat{T}_p\hat{\rho_{in}}{}^j\hat{T}^{\dagger}_p|X'\rangle = {}^iV^k_b\rho_{i,j}{}^jV^{k*}_{b'} \tag{6.14}$$

then

$$I(\tau) = \sum_k \sum_{i,j} \sum_{b,b'} {}^iA_b(\tau){}^iV^k_b\rho_{i,j}{}^jV^{k*}_{b'}\ {}^jA^*_{b'}(\tau) \tag{6.15}$$

and the resonance spin density matrix is

$${}^{i,j}\rho_{b,b'} = \sum_{k}^{K} {}^iV^k_b\rho_{ij}{}^jV^{k*}_{b'} \tag{6.16}$$

where K represents the rank of the spin density matrix of resonance X. For the g12 run an unpolirized target and photon beam was used. That means that the photon beam is going to be an equal mixture of positive and negative states and for that reason we are taking the average of the two and so disregarding the ρ_{ij} term.

6.2 Decay Amplitudes

The calculation of the decay amplitudes has been done recursively, using the isobar model. The resonance X is considered to decay into an intermediate unstable particle (isobar) and a stable particle (bachelor). The bachelor will be among the final state particles that are being detected. Then the decay amplitude of X decaying into the final state is the amplitude of X decaying into the isobar and the bachelor times the amplitude of the isobar decaying to its children. The decay of X into its children is calculated in the X rest frame (or Gottfried Jackson frame, GJ). We define this rest frame by taking the z axis in the direction of the beam and the y axis perpendicular to the production plane. We can then write the total amplitude as:

$$A_b(\tau) \propto \widetilde{J}\widetilde{s}\sum_{\lambda} D^{J}_{m\lambda}{}^{*}(\Phi,\Theta,0)D^{s}_{\lambda 0}{}^{*}(\phi,\theta,0)f_{\alpha\lambda}(w) \tag{6.17}$$

where

$$\widetilde{J} = \sqrt{(2J+1)}, \qquad \widetilde{s} = \sqrt{(2s+1)} \tag{6.18}$$

we have defined the following sets of quantum numbers $\alpha = \{l, s, J^P(u)\}$ and $b = \{a, m\}$. u is for the isobar, s is its spin and l is the orbital angular momentum between the isobar and the bachelor particle. J is the total spin, m is its z-component and P is the intrinsic parity given by $P = (-1)^{l+s+1}$. The D in the previous equation corresponds to the matrix elements of the rotation operator and they can be calculated analytically with the Winger-d functions. The expressions in the parenthesis represent Clebsch-Gordan coefficients. Also, λ is the helicity of the isobar and $f_{\alpha\lambda}(w)$ is the helicity coupling constant. The later can be expressed as:

$$f_{\alpha\lambda}(w) \propto \frac{\widetilde{l}}{\widetilde{J}}(l0s\lambda|J\lambda)Q^{u}_{ls}(w)g_a \tag{6.19}$$

where g_a is the l-s coupling constant and it will be absorbed into the production amplitudes. The production amplitudes are complex numbers that we are getting by minimizing the likelihood function. The Q factor refers to the isobar of mass w,

$$Q^{u}_{ls}(w) = F_l(p)F_s(q)\Delta_u(w) \tag{6.20}$$

where the functions F are the Blatt-Weisskopf centrifugal barrier factors, which they do depend on the angular momentum of the isobars as well as the breakup momentum p. Full description

of those functions can be found in von Hippel and Quigg paper [48]. The Δ function is the mass dependent Breit-Winger for the isobar u,

$$\Delta_u(w) = \frac{w_0\Gamma_0}{w_0^2 - w^2 - iw_0\Gamma_u(w)} \tag{6.21}$$

with

$$\Gamma_u(w) = \Gamma_0 \frac{w_0}{w}\frac{q}{q_0}\frac{F_s^2(q)}{F_s^2(q_0)} \tag{6.22}$$

where w_0 and Γ_0 are the mass and the width of the isobar. Now using equations (6.17) and (6.19) we can rewrite the decay amplitude as:

$$A_b(\tau) = E_m^{Jls\ *}(\Omega, \Omega_h) Q_{ls}^u(w) \tag{6.23}$$

where

$$E_m^{Jls\ *}(\Omega, \Omega_h) = \widetilde{J}\widetilde{s}\sum_\lambda D_{m\lambda}^{J\ *}(\Theta, \Phi, \phi)\ d_{\lambda 0}^s(\theta)\ [\frac{\widetilde{l}}{\widetilde{J}}(l0s\lambda|J\lambda)] \tag{6.24}$$

The function E has no w dependence from the isobar u and it forms a complete orthonormal set defined by the four angles Ω and Ω_h. For J = l = s = m = 0 the E function is one. Also it can be shown that

$$\int d\Omega\ d\Omega_h\ E_m^{Jls\ *}(\Omega, \Omega_h)\ E_{m'}^{J'l's'\ *}(\Omega, \Omega_h) = (4\pi)^2\ \delta_{JJ'}\ \delta_{ll'}\ \delta_{ss'}\ \delta_{mm'} \tag{6.25}$$

The strong interaction conserves parity, i.e. the parity operator commutes with the transition operator. On the other hand, helicity states are not eigenstates of parity. The reason is that parity does change the position and momentum vectors but it does not change the angular momentum. We need to change basis, in order for the parity to be a good quantum number, and this is going to be done via the reflection operator:

$$\hat{\epsilon} = \hat{P}e^{i\pi J_y} \tag{6.26}$$

where $\hat{P}$ is the parity operator and $e^{i\pi J_y}$ is a 180^o rotation through the x-z plane. We can then define the eigenstates as:

$$|\epsilon\alpha m\rangle = [|\alpha m\rangle - \epsilon P(-1)^{J-m}|a - m\rangle]\theta(m) \tag{6.27}$$

where P is the parity of the state α and

$$\theta(m) = \frac{1}{\sqrt{2}}, \quad m > 0 \tag{6.28}$$

$$= \frac{1}{2}, \quad m = 0 \tag{6.29}$$

$$= 0, \quad m < 0 \tag{6.30}$$

Also if $\epsilon = P(-1)^J$ then $|\epsilon\alpha m\rangle = 0$ for m =0. In the reflectivity basis then, the function E becomes:

$$^{\epsilon}E^{Jls\ *}_{m}(\Omega,\Omega_h) = \widetilde{l}\widetilde{s}\sum_{\lambda}{}^{\epsilon}D^{JP\ *}_{m\lambda}(\Phi,\Theta,\phi)\ d^{s}_{\lambda 0}(\theta)\ (l0s\lambda|J\lambda) \tag{6.31}$$

where

$$^{\epsilon}D^{JP\ *}_{m\lambda}(\Phi,\Theta,\phi) = \theta(m)[D^{J\ *}_{m\lambda}(\Phi,\Theta,\phi) - \epsilon P(-1)^{J-m}D^{J\ *}_{-m\lambda}(\Phi,\Theta,\phi)] \tag{6.32}$$

The normalization of the E function in the new basis is given by,

$$\int d\Omega\ d\Omega_h\ {}^{\epsilon}E^{Jls\ *}_{m}(\Omega,\Omega_h)\ {}^{\epsilon'}E^{J'l's'}_{m'}(\Omega,\Omega_h) = (4\pi)^2\delta_{\epsilon\epsilon'}\ \delta_{JJ'}\ \delta_{ll'}\ \delta_{ss'}\ \delta_{mm'} \tag{6.33}$$

The decay amplitude can now be expressed in the new basis as:

$$^{\epsilon}A_b(\tau) = {}^{\epsilon}E^{Jls\ *}_{m}(\Omega,\Omega_h)Q^{u}_{ls}(w) \tag{6.34}$$

Now we can rewrite the intensity equation (6.15) in the new basis and borne in mind that since an un-polirized beam was used, we take the average of the initial polarized states. The intensity is given by:

$$I(\tau) = \sum_{\epsilon bb'}{}^{\epsilon}\rho_{bb'}\ {}^{\epsilon}A_b(\tau)\ {}^{\epsilon}A^{*}_{b'}(\tau) \tag{6.35}$$

where ${}^{\epsilon}\rho_{bb'}$ is the spin density matrix in the new basis given by:

$$^{\epsilon}\rho_{bb'} = \sum_{k}^{K}{}^{\epsilon}V_{bk}{}^{\epsilon}V^{*}_{b'k} \tag{6.36}$$

The spin density matrix is block diagonal, as it can be seen from equation (6.36), since ϵ' does not appear in the equation.

6.3 Production Amplitudes

The production amplitude shows the strength of a particular partial wave in the intensity spectrum. We can not calculate them (in contrast with the decay amplitudes), but they are inserted as parameters by fitting the data. Specifically, the production amplitudes are the results of minimizing an extended likelihood function. In general the maximum likelihood method is the preferred one for finding values of unknown parameters. Its biggest disadvantage is that there is no well defined estimate of the goodness of a fit. We are going to overcome this challenge by looking

the predicted distributions and compare them with the data (details of this method can be found in the next chapter).

Let's assume n number of events and the probability of each event occurring P_i. Then the total probability for the data-set is going to be:

$$P_{data-set} = P_1 \; P_2 \; ... \; P_n \tag{6.37}$$

if the P_i is a function with some fit parameters, we can vary those until we reach the maximum probability of measuring this data-set. We can then construct the likelihood function as:

$$\mathcal{L} \propto \prod_{i=1}^{n} I(\tau_i) \tag{6.38}$$

and by normalizing the likelihood function over all available phase space we would then have:

$$\mathcal{L} = \prod_{i=1}^{n} \frac{I(\tau_i)}{\int I(\tau) d\tau} \tag{6.39}$$

We also need to scale according to the number of events that we have observed. In order to do this, we are going to use the Poisson distribution. For some process that you expect to measure $\overline{n}$ events, the probability that you will actually measure n events is given by:

$$P_n = \frac{\overline{n}^n}{n!} \; e^{-\overline{n}} \tag{6.40}$$

This will give us the definition of the extended maximum likelihood function (EML), i.e. including the probability that we have measured n number of events:

$$\mathcal{L} = \left[\frac{\overline{n}^n}{n!} \; e^{-\overline{n}} \right] \; \prod_{i=1}^{n} \frac{I(\tau_i)}{\int I(\tau) d\tau} \tag{6.41}$$

The first calculation that we need to do (after the decay amplitude calculation) is for the normalization integrals. We are going to do it numerically by using the N generated phase space events, as it was described in the previous chapter. Specifically:

$$\int I(\tau) \; d\tau = \frac{1}{N_{MC}} \sum_{j=1}^{N} I(\tau_j) \tag{6.42}$$

$$\overline{n} = n \int I(\tau) \; d\tau \tag{6.43}$$

and then we can write the EML function as:

$$\mathcal{L} = \left[\frac{1}{n!}\ e^{-\overline{n}}\right]\ \prod_{i=1}^{n} I(\tau_i) \tag{6.44}$$

Since we need to take the product of many numbers less than 1, due to computational precision issues, it is better to take the sum by having log on both sides.

$$ln\mathcal{L}\ =\ ln\left\{\left[\frac{1}{n!}\ e^{-\overline{n}}\right]\ \prod_{i=1}^{n} I(\tau_i)\right\} \tag{6.45}$$

$$= -ln\ n! - \frac{n}{N_{MC}} \sum_{j=1}^{N} I(\tau_j) + \sum_{i=1}^{n} lnI(\tau_i) \tag{6.46}$$

and since we want to maximize this function, we can drop the constants having:

$$ln\mathcal{L} = -\frac{n}{N_{MC}} \sum_{j=1}^{N} I(\tau_j) + \sum_{i=1}^{n} lnI(\tau_i) \tag{6.47}$$

In the definition of the EML function so far we have assumed a detector with 100% acceptance, in a sense that we have not used an acceptance function yet. Since it is not possible to have the acceptance function format, we can use the accepted Monte-Carlo events instead. Then the ELM function is going to be:

$$ln\mathcal{L} \propto -\frac{n}{N_{acc}} \sum_{acc=1}^{N} I(\tau_{acc}) + \sum_{i=1}^{n} lnI(\tau_i) \tag{6.48}$$

We can now go back to the intensity distribution from equation (6.35) and define the following quantities. Board in mind here that whenever we use the decay amplitudes, ${}^{\epsilon}A_b(\tau)$, from now on we have symmetrized for identical particles. For the raw MC sample we have:

$${}^{\epsilon}\Psi_{bb'} = \frac{1}{M} \sum_{i}^{M} {}^{\epsilon}A_b(\tau_i) {}^{\epsilon}A^*_{b'}(\tau_i) \tag{6.49}$$

where M is the number of generated events. For the accepted MC sample:

$${}^{\epsilon}\Psi^{x}_{bb'} = \frac{1}{M_x} \sum_{i}^{M_x} {}^{\epsilon}A_b(\tau_i) {}^{\epsilon}A^*_{b'}(\tau_i) \tag{6.50}$$

where M_x is the number of accepted events. Then by defining $\eta_x = M_x/M$ we can define the accepted normalization integral as:

$$\eta_x\, {}^{\epsilon}\Psi^{x}_{bb'} = \frac{1}{M} \sum_{i}^{M_x} {}^{\epsilon}A_b(\tau_i) {}^{\epsilon}A^*_{b'}(\tau_i) \tag{6.51}$$

The ELM function can have its final format and can be written as:

$$ln\mathcal{L} = \sum_{i}^{n} ln\Big[\sum_{\epsilon bb'} {}^{\epsilon}A_b(\tau_i)\ {}^{\epsilon}\rho_{bb'}\ {}^{\epsilon}A^*_{b'}(\tau_i)\Big] - \eta_x\Big[\sum_{\epsilon bb'}\ {}^{\epsilon}\rho_{bb'}\ {}^{\epsilon}\Psi^x_{bb'}\Big] \tag{6.52}$$

and the production amplitudes are normalized such that

$$\eta_x \sum_{\epsilon bb'} {}^{\epsilon}\rho_{bb'}\ {}^{\epsilon}\Psi^x_{bb'} = n \tag{6.53}$$

The EML function is a positive quantity, and since we are using the minimizer MINUIT for the fit, the negative of the equation (6.52) is going to be used. Also the event yield is given by,

$$Event\ Yield = \sum_{\epsilon bb'} {}^{\epsilon}\rho_{bb'}{}^{\epsilon}\Psi_{bb'} \tag{6.54}$$

6.4 Summary

The observed intensity distribution $I(\tau)$ was derived and it was expanded as a product of production and decay amplitudes. The latter can be calculated analytically where the former is included as parameter by fitting the data. The extended maximum likelihood function was derived and by taking the negative logarithmic of it and by minimizing it we can find the optimal production amplitude parameters that describe the data. Then the event yield and the phase difference between two partial waves is calculated in narrow mass bins and can be plotted as a function of mass to study resonant behaviors.

CHAPTER 7

PARTIAL WAVE ANALYSIS PROCEDURE

In this Chapter the preparation of the 3π event sample is discussed along with the details and the procedure of the minimization process. The method to check the quality of the fit is described at the end of this Chapter.

7.1 Event Sample Preparation

The preparation of the final event data sample starts by binning the data in 3π invariant mass bins. For the main fit results described in the last two Chapters of this work, 20 MeV width mass bin was chosen from 1 to 2 GeV for the $\gamma p \to n\pi^+\pi^+\pi^-$ reaction and 25 MeV wide 3π mass bins was chosen for the $\gamma p \to \pi^-\pi^-\pi^+\Delta^{++}$ reaction. Since a mass independent partial wave analysis was performed, the finer the binning is the more natural the description of the true decay widths of the partial waves are going to be. On the other hand, there must be enough events per bin for the fitter to find the global minimum in the likelihood space and to account for statistical fluctuations. The number of data events in the 1 - 2 GeV 3π mass range is 580K for the $\gamma p \to n\pi^+\pi^+\pi^-$ reaction and 345K for the $\gamma p \to \pi^-\pi^-\pi^+\Delta^{++}$ reaction. The bin with the largest number of events is at 1.3 GeV with 17K events for the $\gamma p \to n\pi^+\pi^+\pi^-$ reaction and 15K for the $\gamma p \to \pi^-\pi^-\pi^+\Delta^{++}$ reaction, where the bin with the lowest number of events has 1300 and 600 events for the two reactions respectively. In appendixes B, F systematic dependencies are studied for different values of the bin width of the two reactions.

The three final samples (data, accepted Monte-Carlo and generated) are sliced into small mass bins and the decay amplitudes were calculated in an event base for all the allowed partial waves (up to J=4). The decay amplitudes for the accepted and generated four-vectors were used for the partial wave normalization. The gamp program [49] was used for the calculation of the decay amplitudes.

7.2 Fitting Procedure

In the next step we find the values of the production amplitudes that best describe the data. The tool to find those values is the extended maximum likelihood method. In order for the likelihood function to be constructed, a hypothesis of the number of partial waves that composed the 3π mass spectrum needs to be made. Hundreds of fits have been performed with different number of partial waves for both reactions and the ones that best describe the data are discussed in the first section of the PWA results Chapter.

7.2.1 Minimization

The software package used to minimize the likelihood function is called MINUIT [50]. Minuit is a collection of numerical minimization routines and it is designed to find the parameters that will minimize a function. The number of parameters depends on the number of partial waves that we choose. Since the production amplitudes are complex numbers and in the special case where no imaginary components are fixed, the parameters will be twice as many as the partial waves.

7.2.2 Fit Quality

For each mass bin a minimization of the likelihood function needs to be performed and the starting values of each parameter can be configured. Since we are dealing with a likelihood space with dozens of parameters, the case of the fitting process stopping in a local minimum rather than the global minimum needs to be considered. In order to study the latter and to look for biases introduced from the choice of the initial set of parameters in the fits, two different approaches were followed.

In the first approach, a fit is performed to the mass bin with the highest number of events, i.e. at 1.3 GeV. The resulting parameters from that particular bin are used as initial starting values for their neighbor bins. This method is called "tracking", and by "tracking up" and "tracking down" the whole 3π mass spectrum is covered. The limitation of this method is that a parallel fitting for all the mass bins is not possible, but the chosen bin width is expected to be broader than the resonance decay width (since strong interactions are studied the resonances will be relative broad anyway) and smooth likelihood function is expected. Indeed this is the picture that we get by performing PWA to the 3π intensity spectrum, resulting to a fast fitting.

The second approach follows the use of random starting values for each mass bin. By taking the highest and lowest parameters found with the tracking method and multiplying by a factor of a 100, the range of the generated random starting values is defined. Then for each mass bin, random starting values were generated, performing 500 fits per bin and the results with the minimum likelihood value were chosen. This method can be done in parallel since those are independent fits and the resulting parameters are not being passed during the fitting process. This is a more time consuming method (depending of course on the available CPUs) due to the multiple number of fits needed. Another reason why this method is slower compared to the tracking method, is that starting values might end up really far from the global minimum of the likelihood function and many iterations would be required until the minimizer is satisfied.

The results given by the two approaches are in a good agreement and the ones presented in this work are obtained by the tracking method where the second approach was mainly used to study the full likelihood space. Also to study any fit dependencies, different values for the number of iterations and the required tolerance on the function value at the minimum were tested for the main wave-set and not change was found in the results.

The maximum likelihood method is the most powerful for finding the values of unknown parameters, but its biggest challenge is that there is no well defined estimate goodness of the fit. In order to test the quality of the fit, comparison needs to be made between the predicted and the data distributions. The predicted distributions were obtained by weighting the accepted monte-carlo events with the production amplitudes obtained from the fitting results. Those weights are calculated using the following equation

$$W_{i,\alpha} = V_{\alpha}^{*} V_{\alpha} A_{i,\alpha}^{*} A_{i,\alpha} \tag{7.1}$$

for each wave α and for each event i. Summing the weights over α for each reflectivity separately and normalizing each weight to the number of 3π data events, one then obtains a weight for each accepted event. Discrepancies between the data and the predicted distributions would be an indication of a poor description of the data.

7.2.3 Wave Selection

As mentioned earlier the number of parameters is related to the number of partial waves used to describe the data. With infinite amount of data all the allowed partial waves should have been

Table 7.1: The allowed spin-parities J^{PC} for charge 3π system in the isobar model. States allowed to decay to $\sigma\pi$ and $f_0(980)\pi$ have been grouped together because the quantum numbers of the σ and f_0 are identical. Exotic J^{PC} states are boxed; Higher-L states for the $f_2(1270)$ and $\rho_3(1690)$ have been omitted because the mass of a parent resonance decaying through such modes would likely be greater than 2 GeV.

L	$\mathbf{f_0\pi}$	$\boldsymbol{\rho\pi}$	$\mathbf{f_2(1270)\pi}$	$\boldsymbol{\rho_3(1690)\pi}$
S	0^{-+}	1^{++}	2^{-+}	3^{++}
P	1^{++}	0^{-+}, $\boxed{1^{-+}}$, 2^{-+}	1^{++}, 2^{++}, 3^{++}	
D	2^{-+}	1^{++}, 2^{++}, 3^{++}	0^{-+}, $\boxed{1^{-+}}$, 2^{-+}, $\boxed{3^{-+}}$, 4^{-+}	
F	3^{++}	2^{-+}, $\boxed{3^{-+}}$, 4^{-+}		
G	4^{-+}	3^{++}, 4^{++}, 5^{++}		

used in the PWA process, but since we are limited in phase space due to the acceptance, due to the limited range of the photon beam energy and due to the kinematic region of interest, the optimal number of partial waves (wave-set) that describes the data needs to be found. An overly extended wave-set can result to an over fitting of the data sample and this can lead to washing out the fit results. An overly small wave-set can lead to adding intensity in amplitudes which have similar angular distributions as the one which would fit best but not included in the fit. The usual way to find the optimal wave-set required to describe the data, is to start with a basic wave-set, expected to be observed for this kind of reaction and to add more partial waves according to some criteria. Some of the partial waves might be so dominant that their intensity can be seen in the invariant mass spectrum. Furthermore, one can also see the correlation distributions of the intensity spectrum that is under PWA, in order to have some idea about the isobars that will be used.

Since we do not want to make any assumptions for the production mechanism we will work backwards and calculate the allowed partial waves from the 3π final state. In table 7.1 one can see a few of the allowed partial waves. Heavier isobars than the ones shown in the table are expected to be suppressed by the lack of the available phase space.

The CLAS-g12 experiment used an un-polarized photon beam and as a $J^P = 1^-$ particle, it is equally likely to have spin helicity projection $M_\gamma = \pm 1$. This means that equal amounts of ± 1 reflectivities are expected and so whenever a partial wave with $M_\epsilon = +1$ is included, a partial wave with $M_\epsilon = -1$ must also be included.

Furthermore, since the beam is mass-less $M_\gamma = 0$ is forbidden. At the same time events with low four-momentum transfer to the nucleon are selected, which strongly enhances one pion exchange. Due to the fact that the incoming particle has $M \neq 0$ and events with one pion exchange are enhanced, no $M = 0$ partial waves are expected. If $M = 0$ partial waves are found, it will most likely be an indication of other exchange mechanism such as the deck effect.

7.3 Summary

The fitting procedure was described in this Chapter along with the fit quality method that chosen and the general wave selection criteria followed for both channels. The next two Chapters describe the specifics of the wave selection criteria as well as the PWA results.

CHAPTER 8

FIT RESULTS FROM PARTIAL WAVE ANALYSIS FOR THE $\gamma p \to \pi^-\pi^-\pi^+\Delta^{++}$ REACTION

In this Chapter the results from the partial wave analysis, performed in the $\gamma p \to \pi^-\pi^-\pi^+\Delta^{++}$ data sample, are described. The Chapter begins by describing the wave selection criteria and it continues with the PWA results. The quality of the fit and interpretation of the results are described in the last two sections.

8.1 Wave Selection for the $\gamma p \to \pi^-\pi^-\pi^+\Delta^{++}$ Reaction

The allowed spin-parity states which can be used to describe the observed 3π meson system are the same for both channels. Table 7.1 shows the most important J^{PC} waves. From the physics point of view, these two channels are expected to have the same production mechanism of the 3π meson system. However, due to different number of the detected particles in the final states, their acceptances are not identical leading to an apparently dissimilar shape of the raw data spectra. The statistics of the $\gamma p \to \pi^-\pi^-\pi^+\Delta^{++}$ reaction is smaller due to lower acceptance and production cross section and requires larger binning in the 3π mass, i.e. 25 MeV bins. Even with such binning, the small number of events per mass bin might result in the statistical fluctuations during the minimization process. Another distinction between two channels is that measurement resolution for an additional detected particle increases the smearing for the whole event. Detector resolution is an effect that can not be corrected for in the current PWA formalism (in contrast with the corrections made for the acceptance), but the effect of the finite resolution is expected to be small. Also, the selection of the Δ^{++} baryon requires kinematic separation of the two pions as described earlier. This cut will decrease the available kinematic phase space for the 3π mesonic system in the reaction with the Δ^{++} recoil. Finally, different sources of the background will contribute to these two channels, and this is accounted for by the variation of the event selection criteria.

Features of the final $\gamma p \to \pi^-\pi^-\pi^+\Delta^{++}$ data sample were discussed in Chapter 4 and a further study of them is necessary in order to finalize the list of partial waves to use. Some features are

similar with the $\gamma p \to n\pi^+\pi^+\pi^-$ reaction, such as the peak of the 3π mass distribution around the $a_2(1320)$ meson and the $f_2\pi$ decay contribution in the high 3π mass region. There are also some differences between two channels, for example, the $\pi^+\pi^-$ forms a broader $\rho(770)$ (shown in Figure 4.14) in comparison with the one from the $\gamma p \to n\pi^+\pi^+\pi^-$ reaction. Also, in the high 3π mass region, the $\rho\pi$ decay mode has stronger presence (shown in Figure 4.15), and the area between the ρ and the f_2 exhibits a broad enhancement. Finally, in the 3π invariant mass plot, the high mass region shows a peak at 1.7 GeV rather than a broad enhancement as is the case in the $\gamma p \to n\pi^+\pi^+\pi^-$ reaction.

Such variations of the features for the two channels do not necessarily infer that a different set of partial waves has to be used. However, all these consideration do indicate that partial waves with the small expected contribution to the overall intensity, such as the $J^{PC} = 1^{-+}$, will be difficult to study in this channel. Hundreds of fits were performed with different sets of partial waves in order to find the ones that make the most significant contribution to the description of the data.

Table 8.1 shows the optimal number of partial waves required for the $\gamma p \to \pi^-\pi^-\pi^+\Delta^{++}$ reaction for $M_{3\pi} < 1.425$ GeV:

Table 8.1: $\gamma p \to \pi^-\pi^-\pi^+\Delta^{++}$: Partial waves required for $M_{3\pi} < 1.425$ GeV

J^{PC}	M^ϵ	L	Y	Number of waves
1^{++}	$1^\pm$	S, D	$\rho(770)$	4
2^{++}	$1^\pm$	D	$\rho(770)$	2
2^{-+}	$1^\pm$	P	$\rho(770)$	2
isotropic background wave				

Also the table 8.2 shows the optimal number of partial waves required for the $\gamma p \to \pi^-\pi^-\pi^+\Delta^{++}$ reaction for $M_{3\pi} > 1.425$ GeV:

The extra partial waves in the high mass region were due to the opening of the $f_2\pi$ mass threshold.

8.2 Fit Results

The results of the partial wave analysis performed on the 3π meson system off of the Δ^{++} baryon are presented in this section. The notation used to describe the partial waves is $J^{PC}M^\epsilon[Y\pi]_L$,

Table 8.2: $\gamma p \to \pi^-\pi^-\pi^+\Delta^{++}$: Partial waves required for $M_{3\pi} > 1.425$ GeV

J^{PC}	M^ϵ	L	Y	Number of waves
1^{++}	$1^\pm$	S, D	$\rho(770)$	4
2^{++}	$1^\pm$	D	$\rho(770)$	2
2^{-+}	$1^\pm$	S, P, D	$f_2(1270)$,$\rho(770)$	6
isotropic background wave				

where J is the angular momentum, P is the parity, C is the C-parity, M is the projection of J on the quantization axis, ϵ is the reflectivity, Y is the intermediate decay isobar with parameters taken from the PDG, and L is the relative orbital angular momentum between Y and π. Often the $J^{PC}[Y\pi]$ notation will be used referring to all J^{PC} states decaying into the same $Y\pi$ isobar.

8.2.1 $2^{++}[\rho(770)\pi]$

Figure 8.1 shows the $2^{++}[\rho(770)\pi]_D$ partial wave intensity for two different reflectivities $M^\epsilon = 1^\pm$. The shape and the scale of these intensity distributions are similar. This is expected for an un-polarized photon beam which contains equal amounts of both photon helicities. The dominant peak of the 3π mass spectrum at 1.3 GeV has been identified as the $J^{PC} = 2^{++}$ partial wave. In all PWA fits performed, the $2^{++}[\rho(770)\pi]_D$ is the most dominant partial wave in the 3π mass spectrum which is consistent with the results of the previous charge-exchange photoproduction analyses [25], [51]. The observed mass and width of the $a_2(1320)$ resonance are close to the expected values.

8.2.2 $1^{++}[\rho(770)\pi]$

Figure 8.2 shows the $1^{++}[\rho(770)\pi]_S$ and $1^{++}[\rho(770)\pi]_D$ partial wave intensities for two different reflectivities. As expected, the S wave is the dominant one among these two waves. The $1^{++}[\rho(770)\pi]_S$ wave shows a stable behavior in different fits while the D wave becomes much less stable when the number of waves included into the fit grows. The appearance of the $1^{++}[\rho(770)\pi]$ waves is consistent with the production of the $a_1(1260)$ meson. This is the first time this state has been observed in the photoproduction of the 3π system with Δ recoil. It was not observed previously in a similar photoproduction analysis at SLAC [52] (the statics of the final data sample was low to perform a mass independent partial wave analysis). Here, we observe the production of this meson in both the S and D waves albeit at different rates. Furthermore, a small enhancement

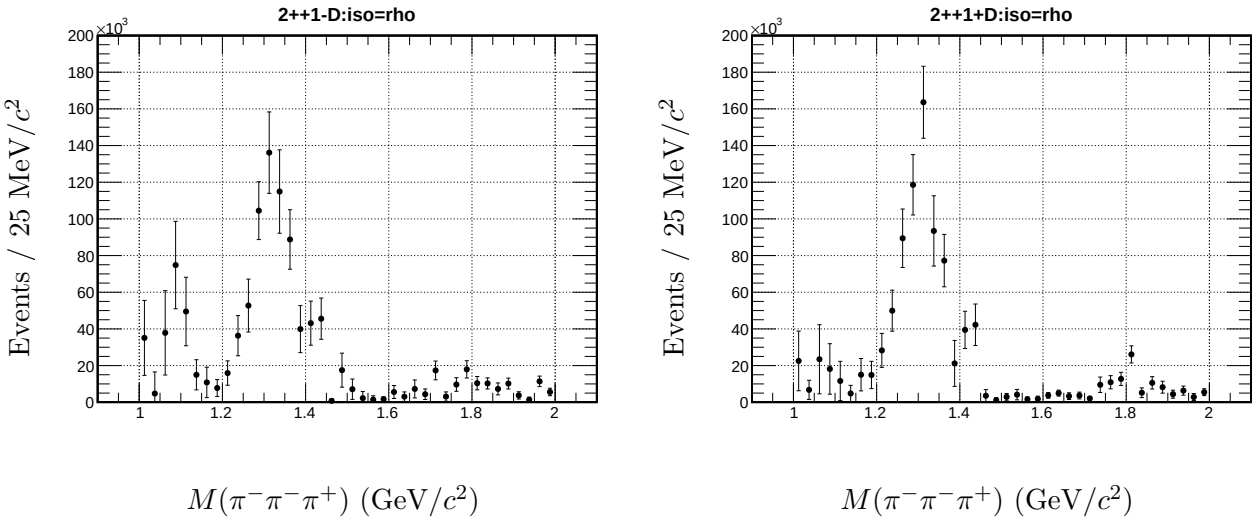

Figure 8.1: $\gamma p \to \pi^-\pi^-\pi^+\Delta^{++}$: The intensity spectrum of the $2^{++}1^-[\rho(770)\pi]_D$ (**left**) and $2^{++}1^+[\rho(770)\pi]_D$ (**right**) partial waves.

at around 1.6 GeV is seen in the $1^{++}[\rho(770)\pi]_D$ partial wave intensities for both reflectivities. The analysis in [53] has observed the evidence for both the $a_1(1260)$ and the $a_1(1700)$ states in the $1^{++}[\rho(770)\pi]_D$ intensity.

8.2.3 Mass Dependent Fit of the $1^{++}1^{\pm}[\rho(770)\pi]_S$ and $2^{++}1^{\pm}[\rho(770)\pi]_D$ partial waves

A coupled mass dependent Breit-Wigner (BW) fit was performed on the $1^{++}[\rho(770)\pi]_S$ and the $2^{++}[\rho(770)\pi]_D$ partial waves, separately for each reflectivity. Both intensities and the phase difference between the partial waves were combined into a single χ^2 fit, which utilized the full error matrix found in the mass independent PWA fit (after the appropriate Jacobian transformation). Results from the fit are shown in Figure 9.4. Similar to the $\gamma p \to n\pi^+\pi^+\pi^-$ reaction, the fit is predominantly driven by the phase difference between the two partial waves rather than by their intensities. The reason for such behavior is the small statistical errors for the phase difference in comparison with the statistical errors for the intensity distributions. To study this a little bit further, many mass independent PWA fits were performed with the random starting values for the fitted production amplitudes. Figure 8.4 shows the difference between the final likelihood values in each mass bin and the minimum value found among them. 500 PWA fits with the random starting values were performed in each mass bin. Clearly, there are many local minimal in the

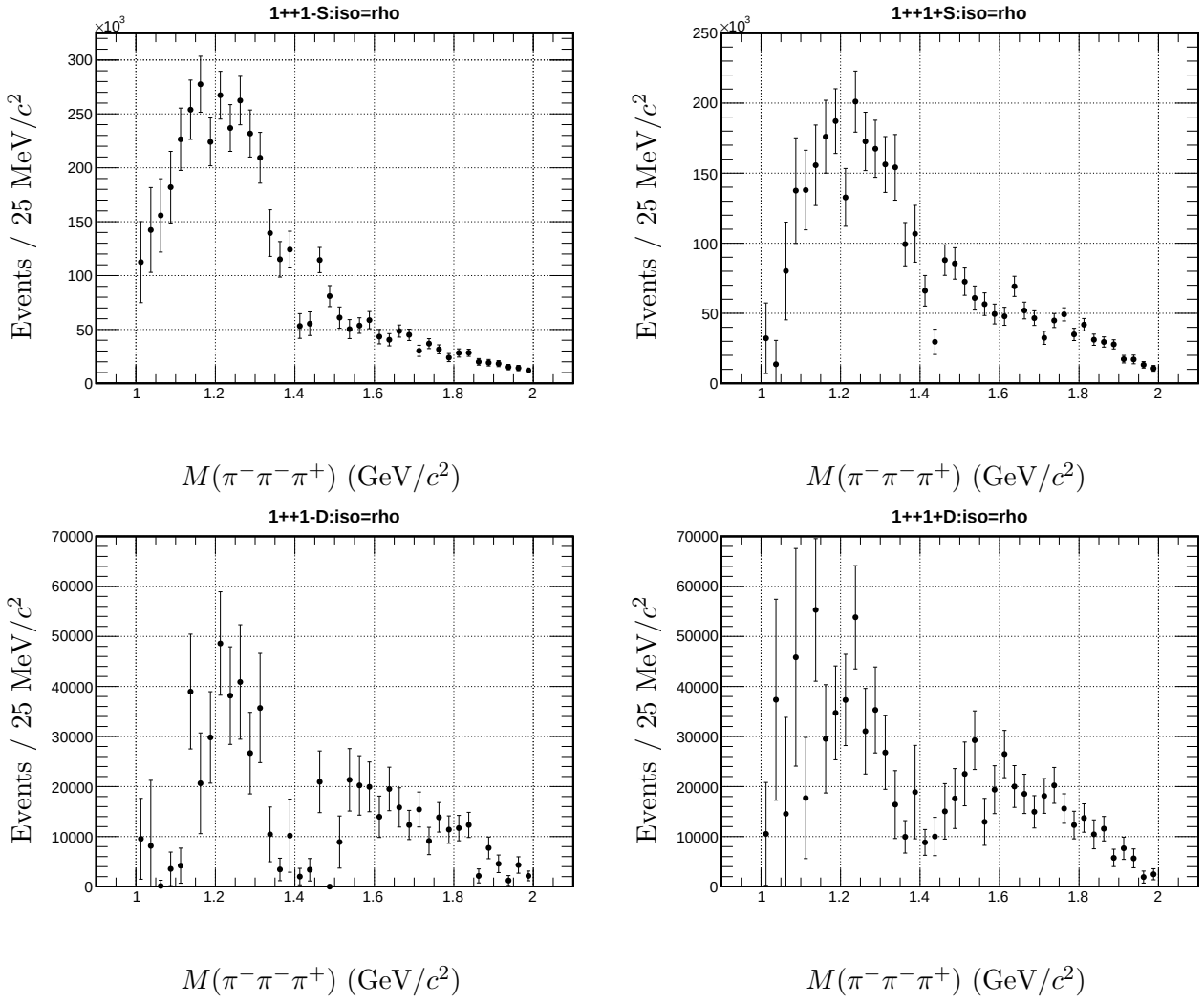

Figure 8.2: $\gamma p \to \pi^-\pi^-\pi^+\Delta^{++}$: The intensity spectrum of the $1^{++}1^-[\rho(770)\pi]_S$ (**top left**), $1^{++}1^+[\rho(770)\pi]_S$ (**top right**), $1^{++}1^-[\rho(770)\pi]_D$ (**bottom left**) and $1^{++}1^+[\rho(770)\pi]_D$ (**bottom right**) partial waves.

likelihood shape which are close statistically to the global minimum. The intensity distributions of the $2^{++}[\rho(770)\pi]_D$ and $1^{++}[\rho(770)\pi]_S$ partial waves, along with their phase difference, are shown in Figure 8.5. This figure includes only such PWA fits from the set of 500 initial random fits that have the final likelihood value differ by no more than 60 counts from the minimum value found.

Since all partial waves in the PWA fit of the 3π system in the low-mass region have the ρ intermediate isobar only, there will be a mathematical ambiguity in the sign of the phase difference between waves. This effect is shown in the phase difference plots in Figure 8.5. Apart from the sign ambiguity, the phase difference plot demonstrates that mass bins above 1.25 GeV have more than one value of such difference found in the random fits, and their spread is significantly larger than a typical statistical error of $\Delta\phi$ found in any single fit. On the other hand, per-bin variations of the intensity distributions are typically less than the statistical errors of a single fit. In other words, the systematic errors of the phase difference are much larger than the statistical ones. The phase-driven effect described above is caused by such underestimation of the total errors. Therefore, a different approach to the mass dependent fit has been tried.

The study of the resonance structures was done by performing at first a mass dependent Breit Wigner (BW) fit to the reflectivity-combined $J^{PC} = 2^{++}$ and, separately, $J^{PC} = 1^{++}$ partial wave intensities. Figure 9.7 shows the intensities of the $2^{++}1^{\pm}[\rho(770)\pi]_D$ and $1^{++}1^{\pm}[\rho(770)\pi]_S$ partial waves along with the results of the fit. The obtained values for the mass of $M = 1.325 \pm 0.004$ GeV and for the width of $\Gamma = 0.098 \pm 0.008$ GeV for the $2^{++}[\rho(770)\pi]_D$ wave are consistent with known values for the $a_2(1320)$ resonance. Fitting the $1^{++}[\rho(770)\pi]_S$ intensity with a mass dependent BW function yields a mass of $M = 1.242 \pm 0.005$ GeV and a width of $\Gamma = 0.28 \pm 0.01$ GeV which are consistent with the known values for the $a_1(1260)$ meson.

At the next step, the masses and widths of both states were fixed, and the difference in phase of the $a_2(1320)$ and the $a_1(1260)$ BW functions were fitted to the phase difference from the PWA fit, with the overall phase offset as the only free parameter. Comparison of the observed and fitted phase differences is shown in the bottom plots of Figure 9.7 for the $M^{\epsilon} = 1^{+}$ and $M^{\epsilon} = 1^{-}$ waves respectively. The red curve is the fitted BW phase difference of the $a_1(1260)$ and $a_2(1320)$. Over the $a_1(1260)$ and $a_2(1320)$ mass range, the observed phase differences are in a good agreement with a BW relative phase. This means that both of these states exhibit proper BW resonance behavior.

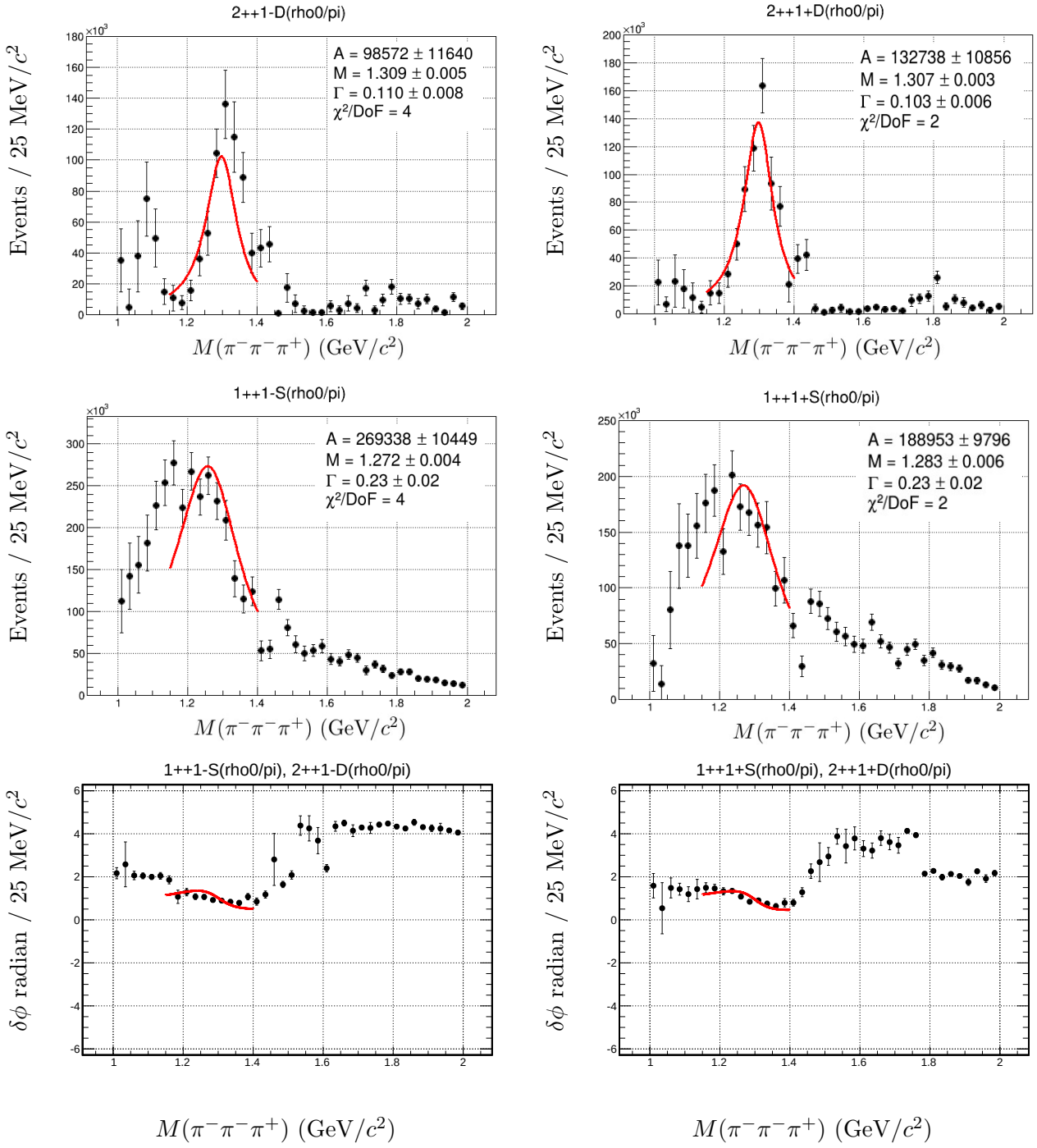

Figure 8.3: $\gamma p \to \pi^-\pi^-\pi^+\Delta^{++}$: A mass dependent fit of the $1^{++}[\rho(770)\pi]_S$ and $2^{++}[\rho(770)\pi]_D$ intensity distributions and their phase difference was performed for each reflectivity separately. The **first column** shows the fit results for $M^\epsilon = 1^-$ and the **second column** for $M^\epsilon = 1^+$.

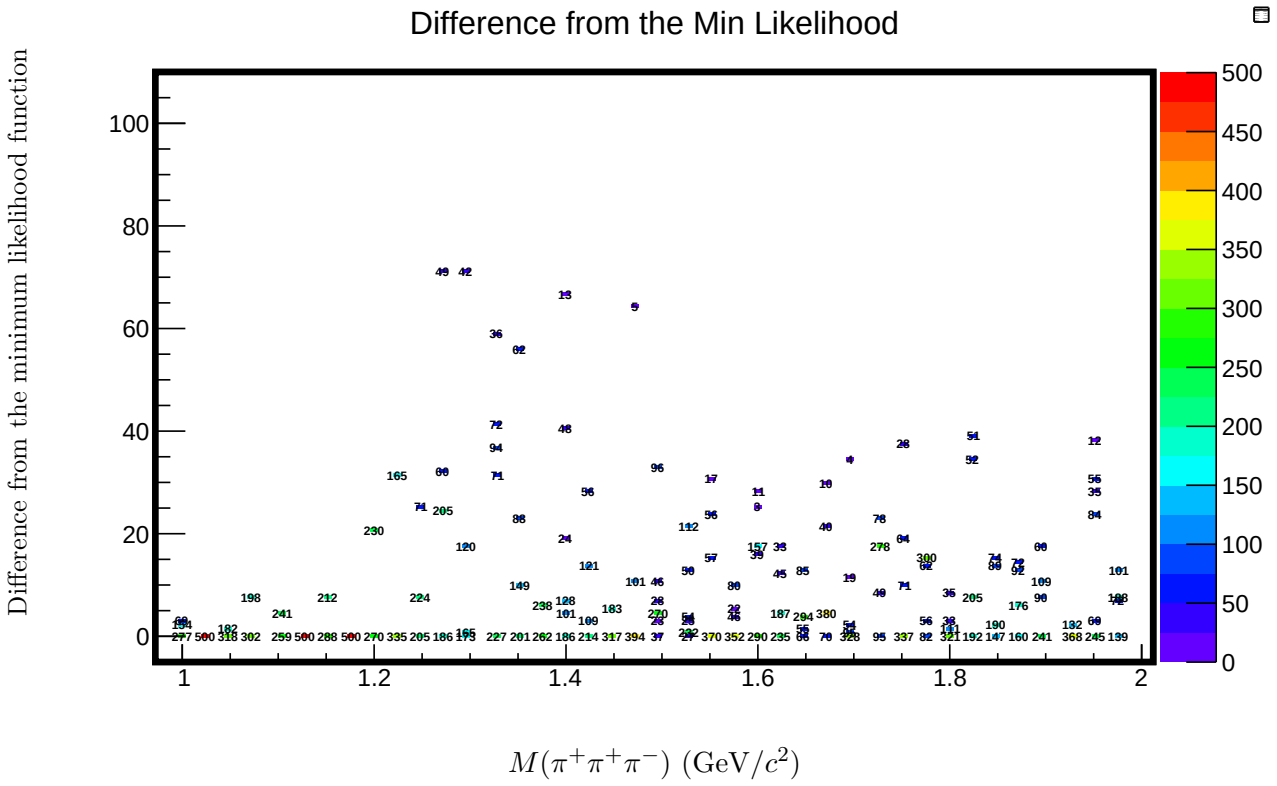

Figure 8.4: $\gamma p \to \pi^-\pi^-\pi^+\Delta^{++}$: Difference between the final likelihood values in each mass bin and the minimum likelihood value seen among them for 500 PWA fits with the random starting values of the fitted parameters.

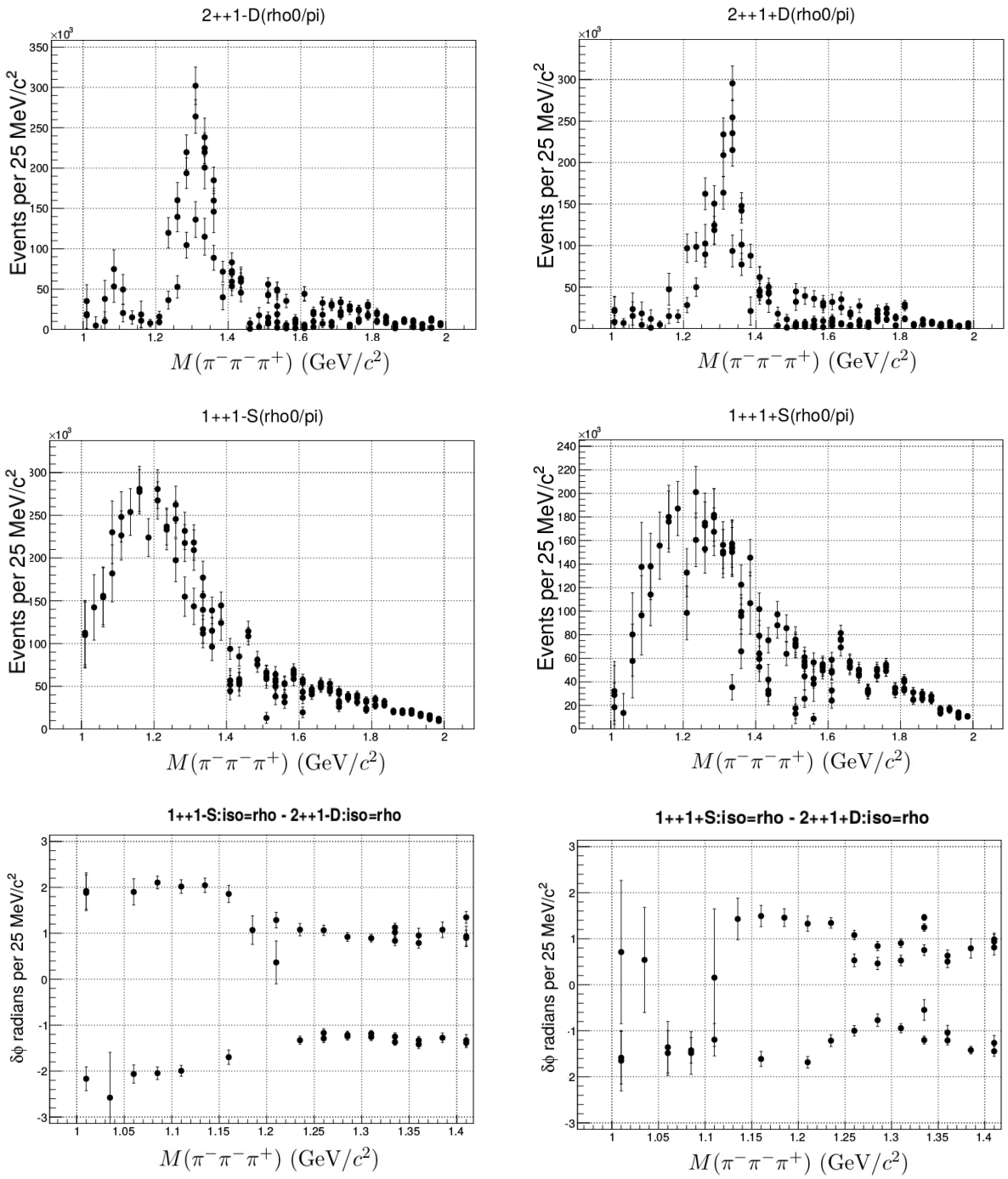

Figure 8.5: $\gamma p \to \pi^-\pi^-\pi^+\Delta^{++}$: Results of multiple random fits after selection of only fits with final likelihood within 60 counts from the minimum value found. The **top and middle** plots show the intensities for the $1^{++}1^{\pm}[\rho(770)\pi]_S$ and $2^{++}1^{\pm}[\rho(770)\pi]_D$ waves. The **bottom left** plot shows the phase difference between the $1^{++}1^{-}[\rho(770)\pi]_S$ and $2^{++}1^{-}[\rho(770)\pi]_D$ wave. The **bottom right** plot shows the phase difference between the $1^{++}1^{+}[\rho(770)\pi]_S$ and $2^{++}1^{+}[\rho(770)\pi]_D$ wave.

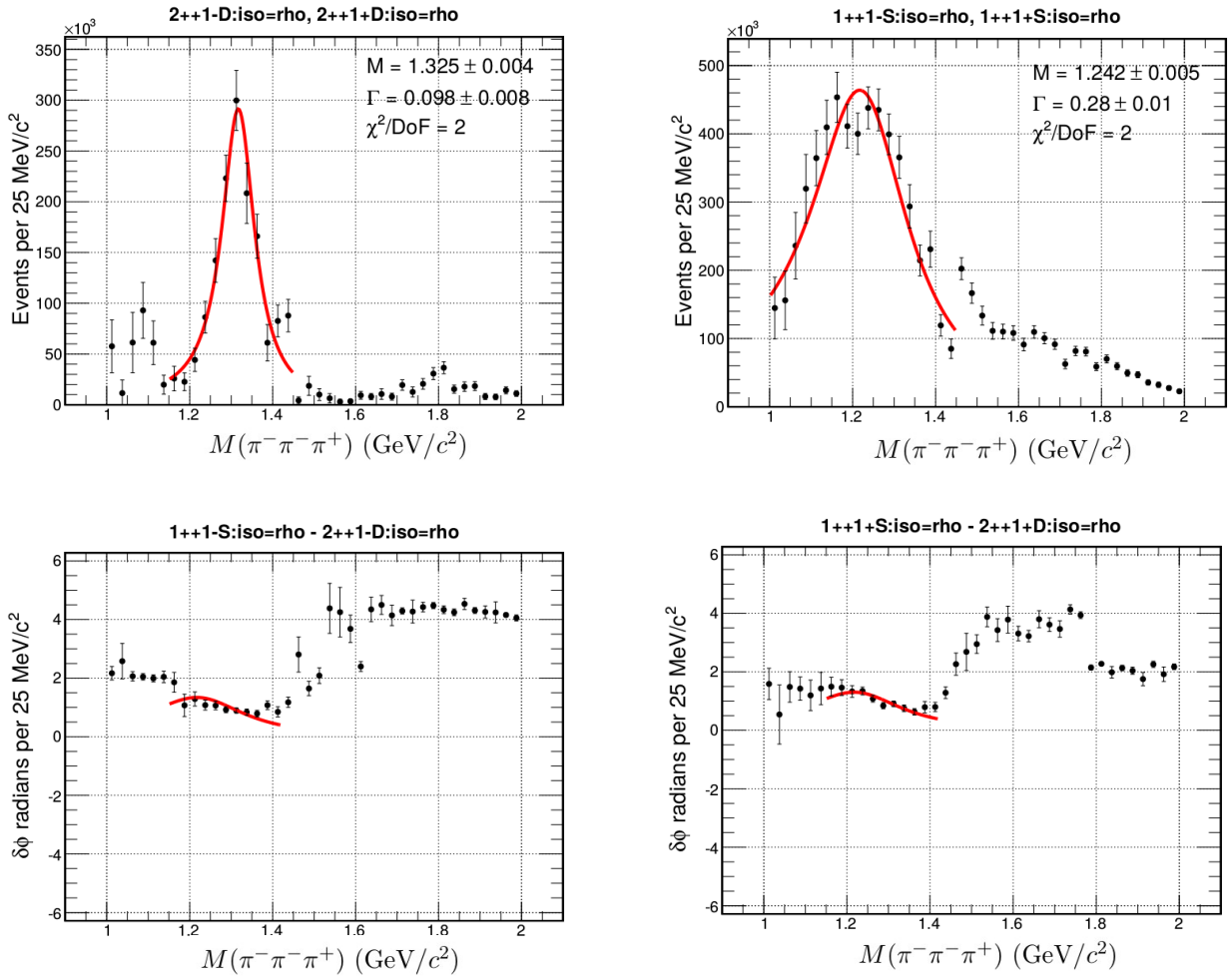

Figure 8.6: For the $\gamma p \to \Delta^{++}\pi^+\pi^-\pi^-$ reaction, the **top row** shows the intensity, combined over two reflectivities $M^\epsilon = 1^\pm$, for the $2^{++}1^\pm[\rho(770)\pi]_D$ and the $1^{++}1^\pm[\rho(770)\pi]_S$ partial waves. The two intensities have been fitted with a mass dependent BW function which is plotted with a red curve along with the obtained parameters. In the **bottom row**, the phase difference of the $2^{++}D$ wave against $1^{++}S$ wave for the two different reflectivities is shown. The red curve is a plot of BW phase difference with the parameters obtained by fitting the intensities.

8.2.4 $2^{-+}[f_2(1270)\pi]$

In the high 3π mass region, the dominant partial wave is the $2^{-+}[f_2(1270)\pi]_S$. The intensity distributions of the $2^{-+}1^{\pm}[f_2(1270)\pi]_S$ and $2^{-+}1^{\pm}[f_2(1270)\pi]_D$ partial waves are shown in Figure 8.7. All waves share a peak at around 1.7 GeV. The detailed shape of the intensity distributions for the partial waves is not in a complete agreement among opposite reflectivities. This might be an indication of a background present in the high mass region, since the variations in the shape of these waves are sensitive to the number of additional $\rho\pi$ partial waves included to accommodate the background. Nevertheless, the results are consistent with the production of the $\pi_2(1670)$ meson. The PDG D-wave/S-wave ratio for the $\pi_2(1670) \to f_2(1270)\pi$ is 0.18 ± 0.06, which is similar to the one observed in this analysis.

8.2.5 $2^{-+}[\rho(770)\pi]$

Figure 8.8 shows the intensities of the $2^{-+}[\rho(770)\pi]$ partial waves. There is an obvious leakage from the strong $a_2(1320)$ state into these waves in the low mass region. In the high 3π mass region, the intensity of the $2^{-+}1^{\pm}[\rho(770)\pi]_P$ wave shows a peak at around 1.8 GeV which also can be interpreted as the $\pi_2(1670)$ meson. Surprisingly, the strength of the $\pi_2(1670)$ peak is similar for both the $2^{-+}[\rho(770)\pi]$ and $2^{-+}[f_2(1270)\pi]$ partial waves. This is not in agreement with the world data - the PDG branching fractions for the $\pi_2(1670)$ decaying into the $f_2(1270)\pi$ and the $\rho(770)\pi$ are 56.3% and 31% respectively. This is an indication that a fraction of the background, not accommodated by an isotropic background wave. prefers to go into the $\rho(770)\pi$ waves rather than the $f_2(1270)\pi$ ones.

8.2.6 Predicted Angular Distributions

The quality of the PWA fits was studied by producing the predicted distributions. The accepted four-vectors were weighted with the obtained production amplitudes from the fit, and various distributions were compared with the data. Specifically, Figure 8.9 shows the $\pi\pi$, $\Delta^{++}\pi$ and $\Delta^{++}\pi\pi$ invariant mass distributions for the predicted and data events. The angular distributions are shown in Figure 8.10 for the GJ rest frame and in Figure 8.11 for the helicity rest frame. Overall, there is good agreement between the data and the predicted distributions.

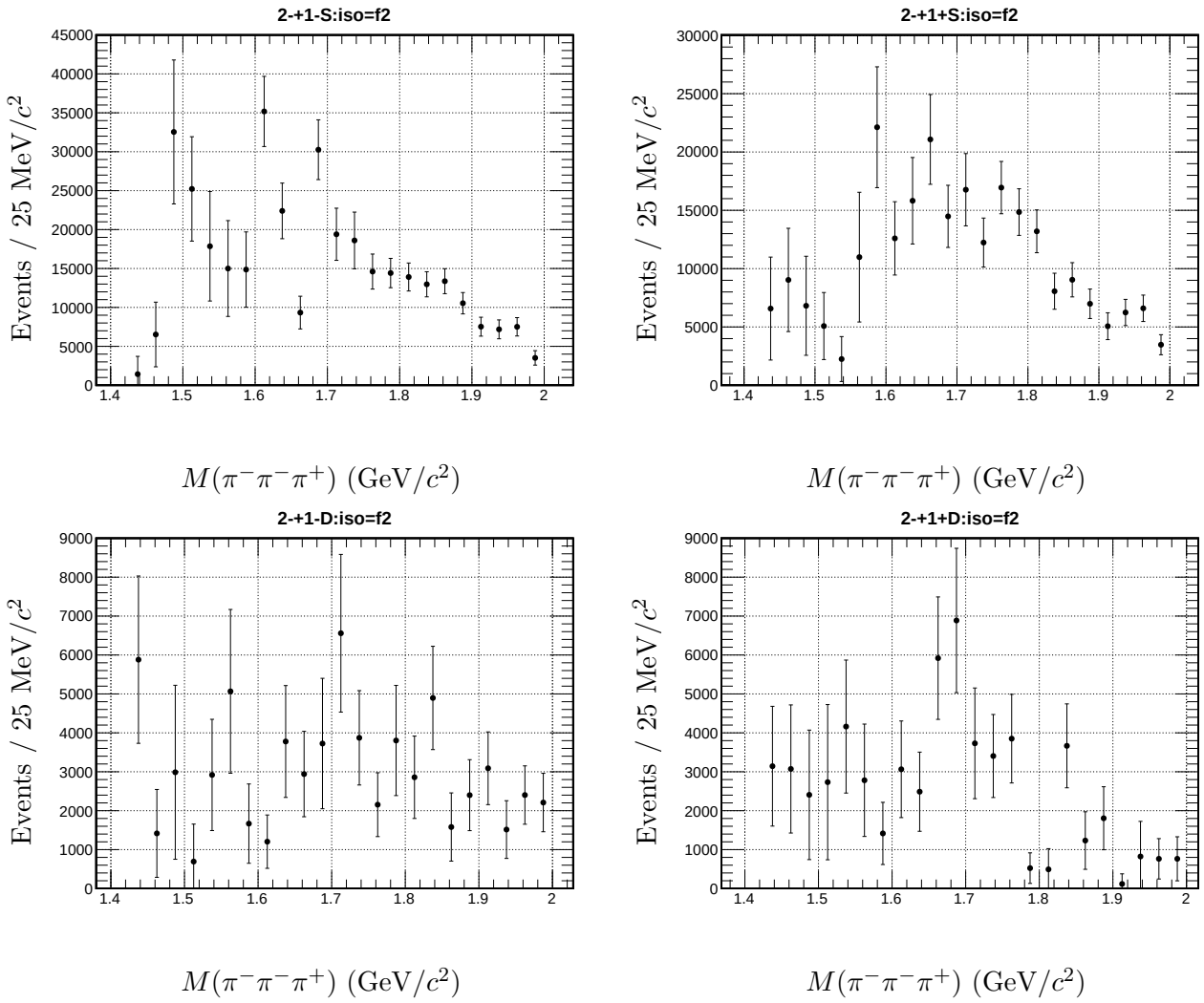

Figure 8.7: $\gamma p \to \pi^-\pi^-\pi^+\Delta^{++}$: The intensity spectrum of the $2^{-+}1^-[f_2(1270)\pi]_S$ (**top left**), $2^{-+}1^+[f_2(1270)\pi]_S$ (**top right**), $2^{-+}1^-[f_2(1270)\pi]_D$ (**bottom left**) and $2^{-+}1^+[f_2(1270)\pi]_D$ (**bottom right**) partial waves.

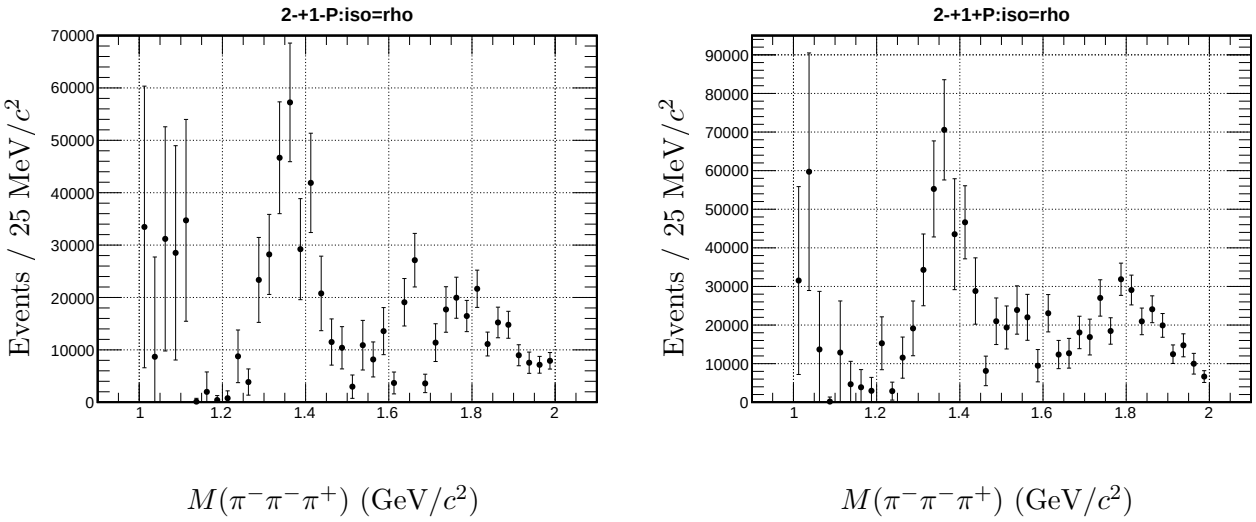

Figure 8.8: $\gamma p \to \pi^-\pi^-\pi^+\Delta^{++}$: The intensity spectrum of the $2^{-+}1^-[\rho(770)\pi]_P$ and $2^{-+}1^+[\rho(770)\pi]_P$ partial waves.

8.2.7 Systematic Dependencies of the Fit Results

In general, the presented results do show stable behavior against different values of the selection criteria and for different bin sizes used the fits. Systematic dependence on the low four-momentum transfer selection was studied for four different values of the t' cut (0.1, 0.2, 0.4 and 1 GeV$^2/c^4$) as well as without any t' selection. Also, the cut on the momentum difference between two π^+ was tested for four different values of 1.0, 0.65, 0.45 and 0.25 GeV/c as well as without such cut. Finally, a fit was done with the nominal fiducial cuts which had been determined in a separate CLAS-g12 analysis [54]. The only significant effect observed was in the smaller partial waves in the high 3π mass region which were less stable when the values of the selection criteria were varied. Also, the isotropic background seems to be rising in the high 3π mass region as the cuts become more relaxed. Finally, the second peak in the $1^{++}S$ wave at 1.6 GeV seems to become more prominent as the cuts become tighter. Meanwhile, the same peak can be seen in the $1^{++}D$ wave even with the the minimum cuts. Finally, the results do not show any dependence on the 3π mass bin size. Detailed comparison for all partial waves intensity distributions is shown in appendix F for different selection cuts, and in appendix E for variations of the mass bin size.

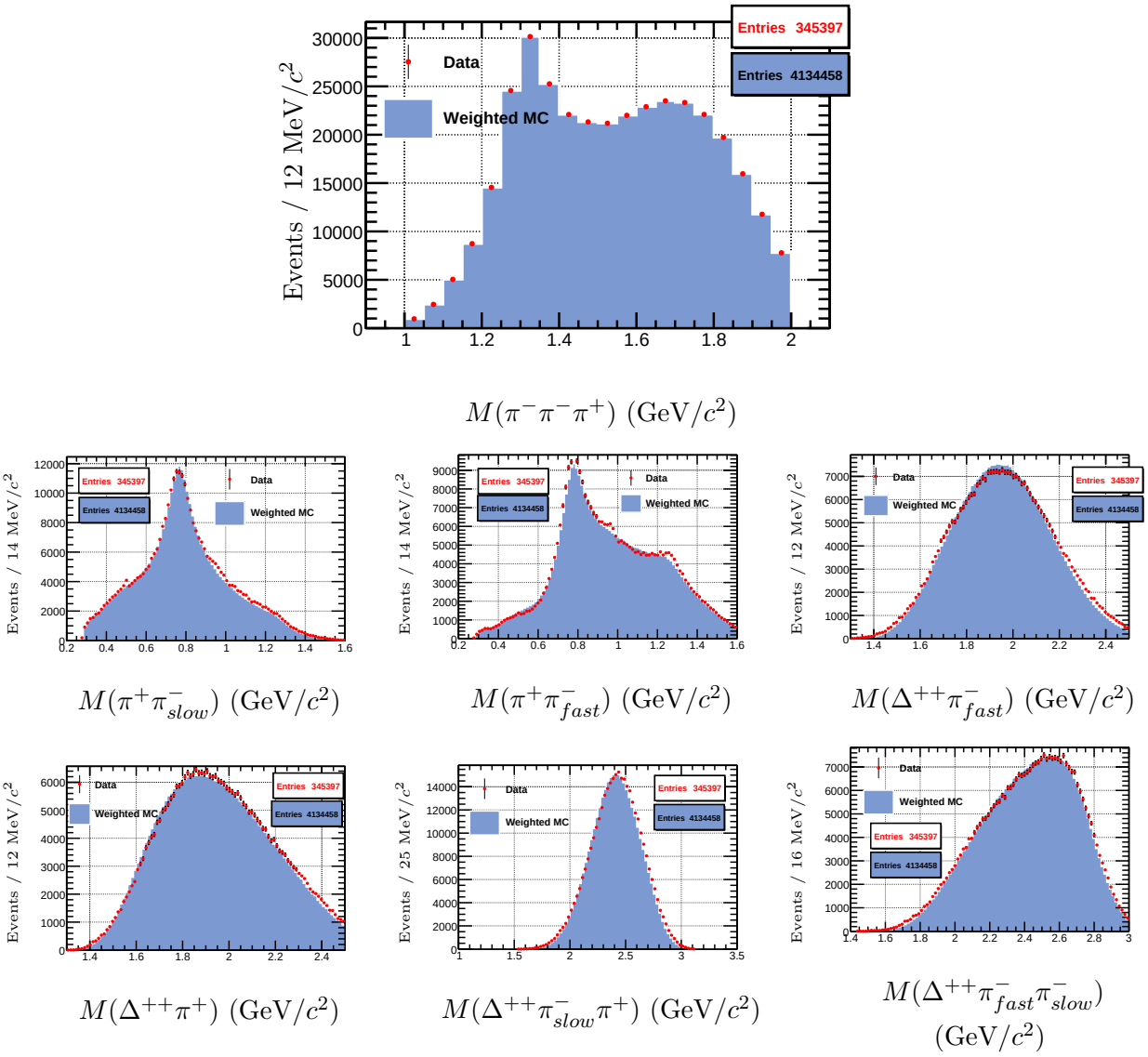

Figure 8.9: $\gamma p \to \pi^-\pi^-\pi^+\Delta^{++}$: Invariant mass distributions for data (points) and predicted (blue histograms) four-vectors.

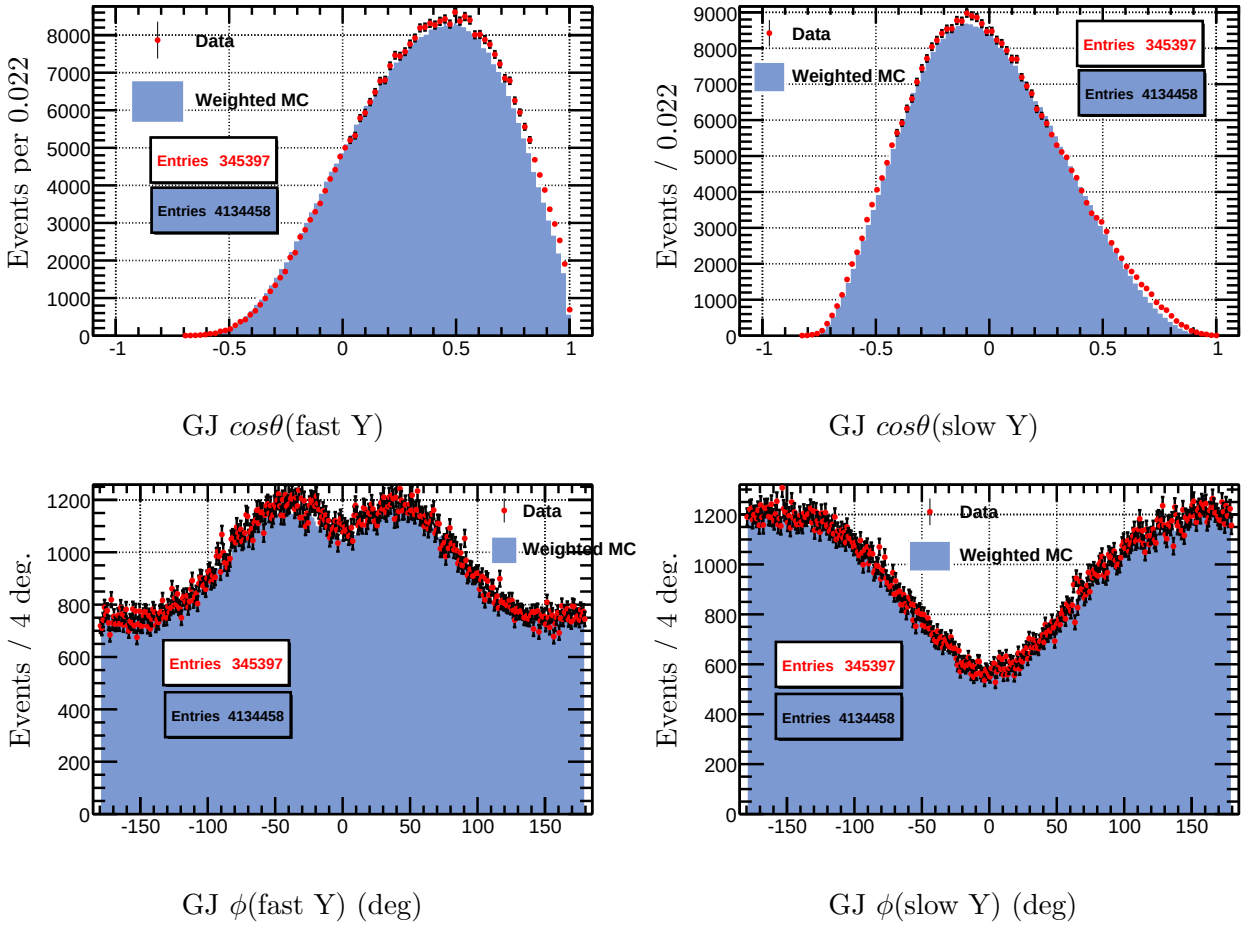

Figure 8.10: $\gamma p \to \pi^-\pi^-\pi^+\Delta^{++}$: Angular distributions in the Gottfried-Jackson rest frame for data (points) and predicted (blue histograms) four-vectors.

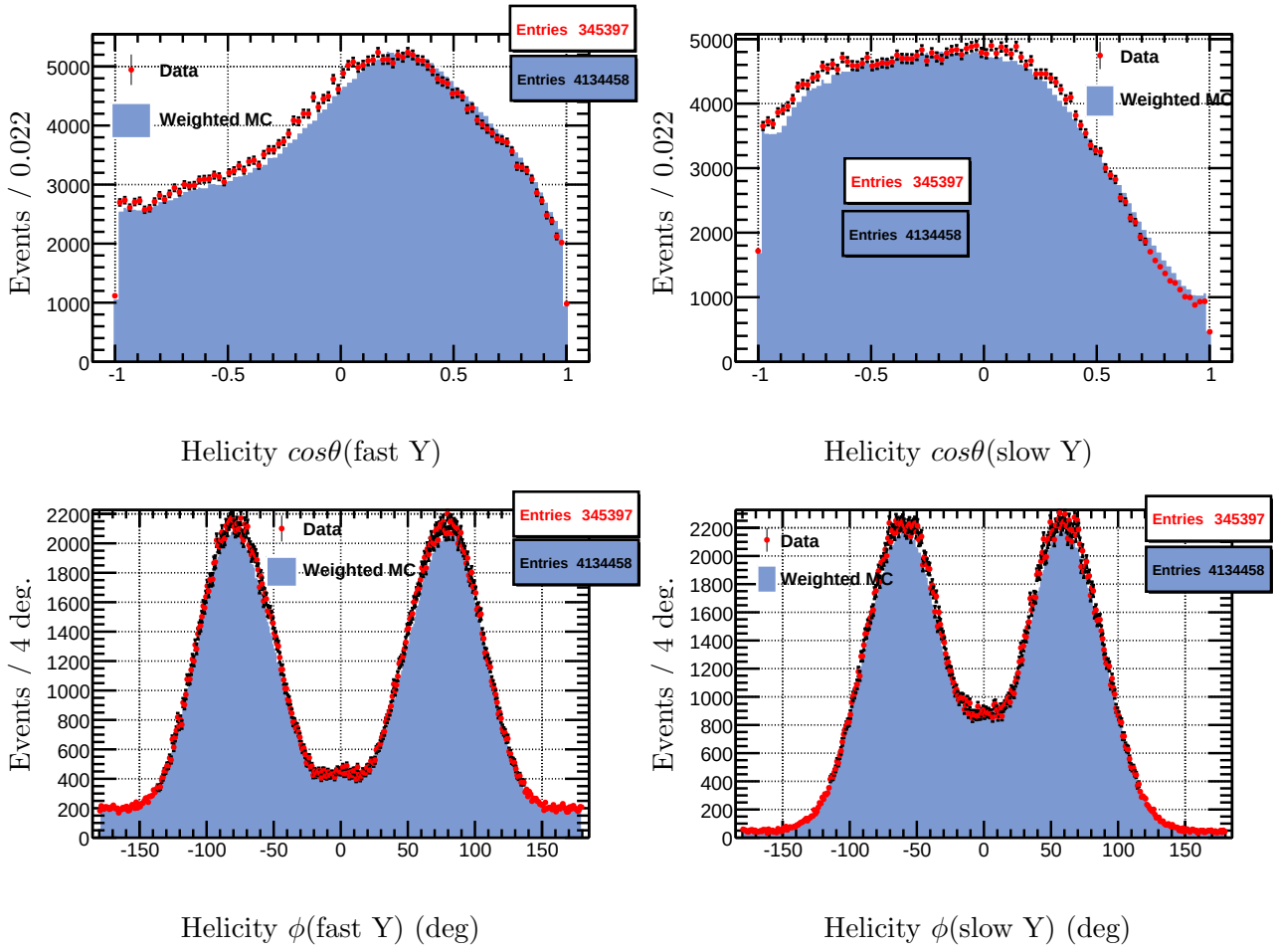

Figure 8.11: $\gamma p \to \pi^-\pi^-\pi^+\Delta^{++}$: Angular distributions in the Helicity rest frame for data (points) and predicted (blue histograms) four-vectors.

8.2.8 Interpretation of the Results and Future Work

A much better understanding of the background can be achieved by comparing the outcomes of multiple partial wave analyses of the $\gamma p \to \pi^-\pi^-\pi^+\Delta^{++}$ reaction. The increase in the number of partial waves mostly affected the stability of the P waves in the fits such as the $2^{-+}P$ wave. We interpret this as an indication that part of the background contamination in the high mass region is an-isotropic and prefers to go into the $\rho\pi$ P waves. The fits become especially unstable if multiple such waves were included such as the exotic $1^{-+}[\rho\pi]_P$ wave together with the expected $2^{-+}[\rho\pi]_P$ decay mode of the $\pi_2(1670)$. Figure 8.12 shows the final likelihood values for 500 fits per mass bin with the random starting values for the case when the $1^{-+}P$ partial waves are added to the mix. By comparing this Figure with the previous Figure 8.4 in the high 3π mass region, one can concluded the the likelihood shape became much more complex and the results of a single fit much more ambiguous in the presence of the $1^{-+}P$ partial waves.

What may be the origin of the background in the high 3π mass region? As was demonstrated earlier, the extensive study was made to reduce the excited baryon background as much as possible, and, indeed, no evidence of it is seen in the $p\pi$, $p2\pi$ or $p3\pi$ invariant mass distributions for the final event sample. Also, Monte Carlo studies indicate that when a excited baryon reaction is treated as our primary reaction with the recoil Δ^{++} formed with the incorrect decay pion, sharp peaks at $Cos(\Theta) = \pm 1$ in GJ frame are created. However, we don't observed such peaks in the final event sample. One can conclude that the source of the remaining background is not due to some other excited baryons but due to the $\gamma p \to p\ 2\pi^-2\pi^+$ reaction when 4-pion states are produced off a recoil proton. Such production channel is not expected to form any structures in the $p\pi$, $p2\pi$ or $p3\pi$ distributions but it may reveal itself in the 4π invariant mass distribution.

In an effort to study this background further, $\gamma p \to p\ 4\pi$ phase space events were generated and projected through the CLAS detector. The same selection cuts were applied to these events as for the data in order to study the fraction of them which do get through the cuts designed to select the recoil Δ^{++} only and, therefore, do contribute to the background of the primary reaction. Figure 8.13 shows the 4π invariant mass distribution of the raw and accepted "background" generated events, as well as for the data. The 3π and $\pi\pi$ invariant mass distributions for the $\gamma p \to p\ 4\pi$ MC events are shown is Figure 8.14. One can see that the accepted 3π spectrum of this background

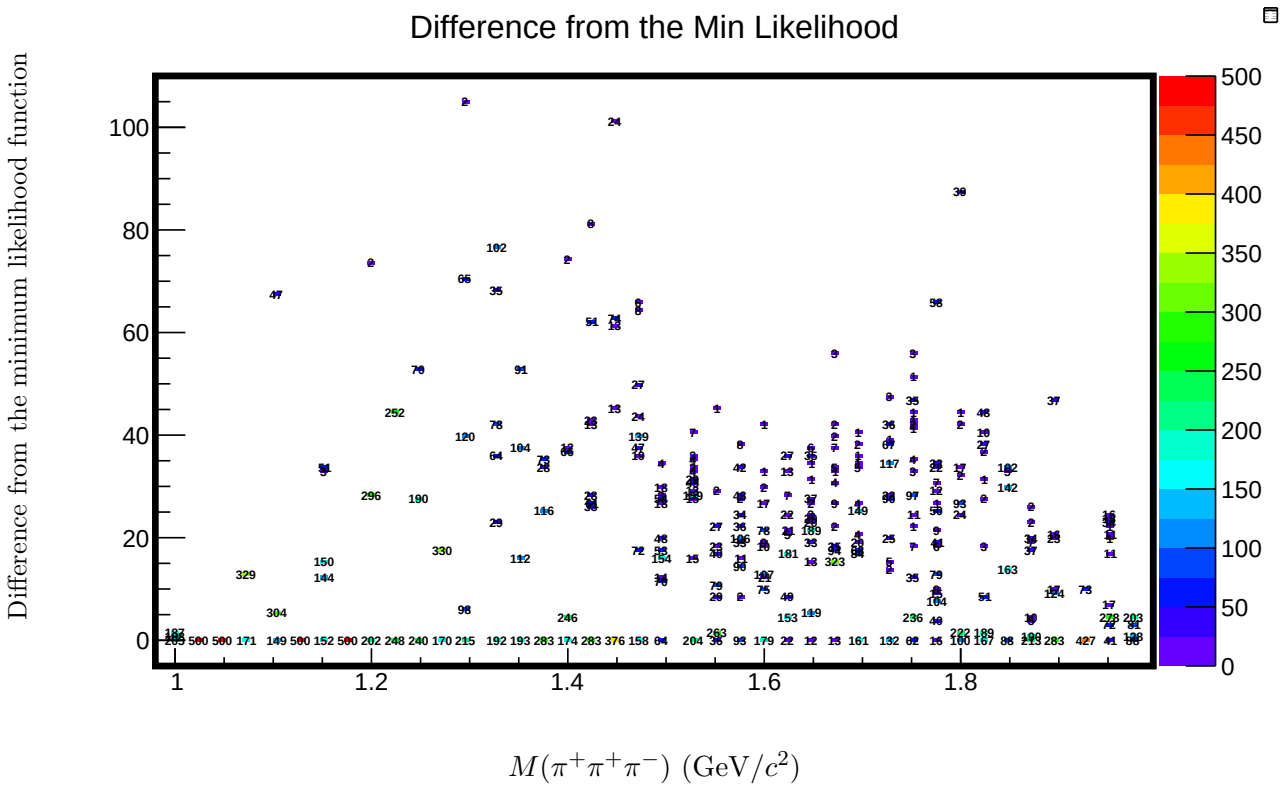

Figure 8.12: $\gamma p \to \pi^-\pi^-\pi^+\Delta^{++}$: Final likelihood values for 500 random fits per mass bin when the $1^{-+}P$ exotic wave is included. The plot shows the difference from the minimum likelihood values found per bin.

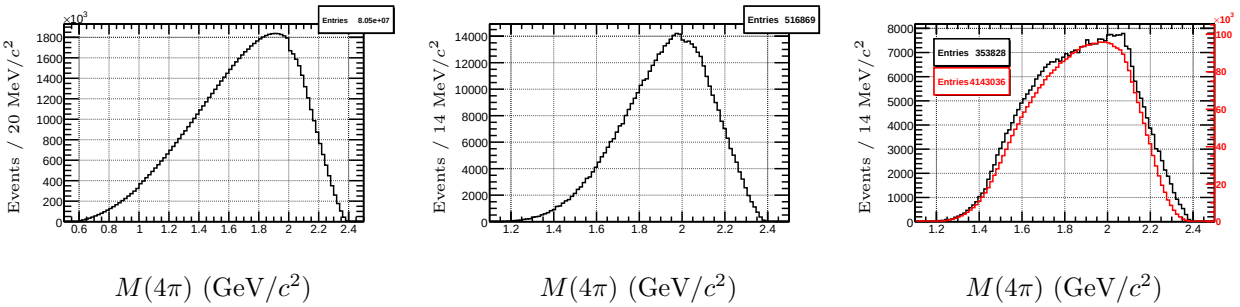

Figure 8.13: $\gamma p \to \pi^-\pi^-\pi^+\Delta^{++}$: Invariant mass of the 4π. The **right** plot is for generated $\gamma p \to p\ 4\pi$ events. The **middle** plot is for accepted $\gamma p \to p\ 4\pi$ events. The **left** plot is for $\gamma p \to \pi^-\pi^-\pi^+\Delta^{++}$ data events.

is concentrated only in the high 3π mass range significantly complicating the interpretation of the PWA results there.

After all selection cuts had been applied, the acceptance for the $\gamma p \to p\ 2\pi^-2\pi^+$ reaction was found to be around 0.6%, compared with the acceptance of 1.4% for the $\gamma p \to \pi^-\pi^-\pi^+\Delta^{++}$ reaction. Considering also the fact that the cross section for the $\gamma p \to p\ 4\pi$ reaction is factor 2.4 higher than for the $\gamma p \to \pi^-\pi^-\pi^+\Delta^{++}$ reaction, the fraction of such background in the high mass region can be up to 40%.

The 4π invariant mass distribution of the data is shown in Figure 8.13. A small structure is visible around 1.7 GeV and 2.1 GeV. These is where two excited ρ states, decaying into 4π, have been seen before. Due to vector dominance, the incoming photon beam can be considered as the virtual ρ beam which make the diffractive photoproduction of such excited ρ states likely.

A possible way to deal with this background is to try to remove it from the data sample. In a similar way with the background reduction of the $\gamma p \to n\pi^+\pi^+\pi^-$ reaction, the θ_{lab} cut has been tried. Figure 8.15 shows the $\theta_{lab}[\pi^+_{slow}]$ for the accepted and generated events for two reactions, i.e., for $\gamma p \to p\ 4\pi$ and $\gamma p \to \pi^-\pi^-\pi^+\Delta^{++}$. As expected, the θ_{lab} plots for the generated four-vectors do look differently for two reactions. However, after the events are passed through the CLAS detector, the θ_{lab} distributions began to resemble each other. The plot with the generated events indicates that a significant reduction of the $\gamma p \to p\ 4\pi$ background could be achieved with a cut on π^+_{slow} lab angle such as $\theta_{lab}[\pi^+_{slow}] > 85^o$). But Figure 8.15 shows that CLAS acceptance drops to zero for such selection. This is due to the fact that the hydrogen target for the g12 run was pulled upstream

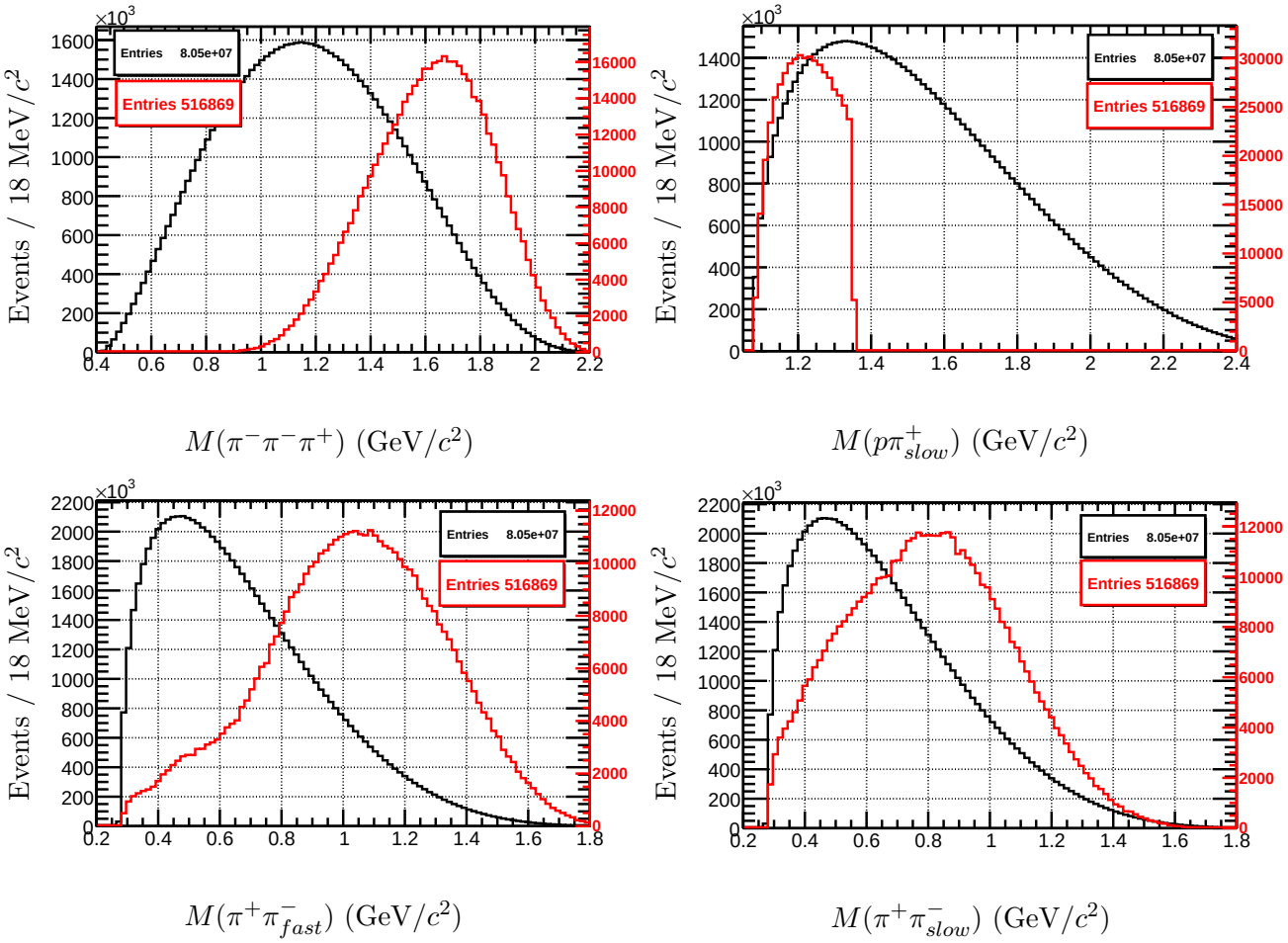

Figure 8.14: Invariant masses for generated $\gamma p \to p\ 4\pi$ events (black line) and accepted $\gamma p \to p\ 4\pi$ events with all the cuts applied (red line).

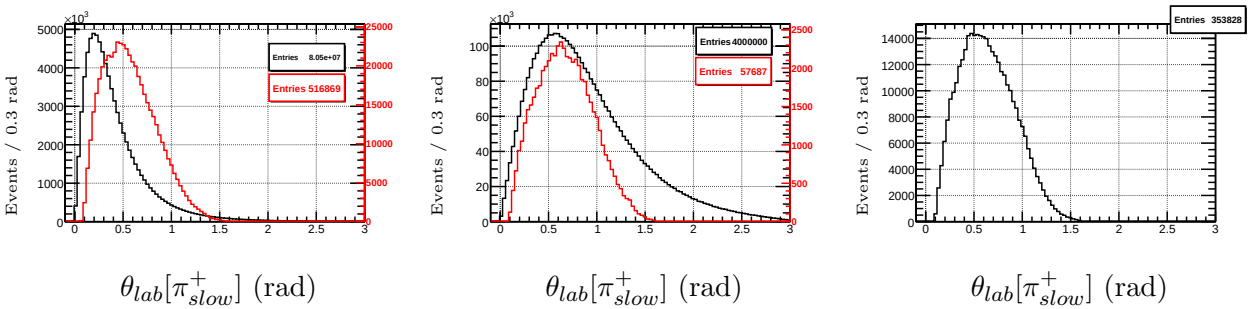

Figure 8.15: **Left:** $\theta_{lab}[\pi^+_{slow}]$ for generated (black like) and accepted (red line) $\gamma p \to p\, 4\pi$ events. **Middle:** $\theta_{lab}[\pi^+_{slow}]$ for generated (black like) and accepted (red line) $\gamma p \to \pi^-\pi^-\pi^+\Delta^{++}$ events. **Right:** $\theta_{lab}[\pi^+_{slow}]$ for $\gamma p \to \pi^-\pi^-\pi^+\Delta^{++}$ data events.

to increase acceptance for forward-going particles but the ability to detect pions for large angles as been lost.

Without finding any acceptable way to eliminate such background contribution, the only remaining way to deal with it properly would be through a global partial wave analysis which combines both the $\Delta 3\pi$ and $p4\pi$ waves (and, therefore, cannot be a mass independent fit in the 3π or 4π mass bins), but this is beyond the scope of this effort.

CHAPTER 9

FIT RESULTS FROM PARTIAL WAVE ANALYSIS FOR THE $\gamma p \to n\pi^+\pi^+\pi^-$ REACTION

In this Chapter the wave selection criteria are described, followed by the PWA fit results. The quality of the PWA fit is briefly discussed at the end of the Chapter along with our conclusions.

9.1 Wave Selection For The $\gamma p \to n\pi^+\pi^+\pi^-$ Reaction

The Figures in section 5.2 show the main features of the $\gamma p \to n\pi^+\pi^+\pi^-$ final data sample. The 3π invariant mass spectrum and the Dalitz plots of the $\pi\pi$ system need to be looked at in order to come up with a list of hypotheses for the partial waves that contribute to the intensity spectrum. The dominant peak around 1.3 GeV along with the $\rho\pi$ decay mode showed in that region, is an indication of the $a_2(1320)$ meson; thus the $J^{PC} = 2^{++}$ partial wave should be included. Also at the same mass region the $a_1(1260)$ meson has seen decaying into $\rho\pi$ and $\sigma\pi$; thus the $J^{PC} = 1^{++}$ partial wave will also be included in both decay modes. In the high mass region the 3π mass spectrum shows an enhancement from 1.5 to 1.7 GeV. The Dalitz plot in that mass region (see Figure 5.4) shows two decay modes, $\rho\pi$ and $f_2\pi$, with the latter being the dominant one. This feature is consistent with a $\pi_2(1670)$ meson where its primary decay mode is the $f_2\pi$. We should then include the 2^{-+} partial wave decaying into $f_2\pi$ and $\rho\pi$. Also, since the $f_2(1270)\pi$ mass threshold opens around 1.4 GeV we will not include this isobar for bins below 1.4 GeV. The main reason for not using this isobar in the low 3π mass region is because minuit does minimizations through a sequence of derivatives and by considering the need of minimization in a dozen of parameter likelihood space, values close to zero can create huge unnecessary spikes for the values of the error matrix. Finally the exotic 1^{-+} partial wave decaying to $\rho\pi$ was included in order to search for the $\pi_1(1600)$ meson.

Table 9.1 shows the optimal number of partial waves required for the $\gamma p \to n\pi^+\pi^+\pi^-$ reaction for $M_{3\pi} < 1.4$GeV:

Also the table 9.2 shows the optimal number of partial waves required for the $\gamma p \to n\pi^+\pi^+\pi^-$ reaction for $M_{3\pi} > 1.4$ GeV:

Table 9.1: $\gamma p \to n\pi^+\pi^+\pi^-$: Partial waves required for $M_{3\pi} < 1.4$ GeV

J^{PC}	M^{ϵ}	L	Y	Number of waves
1^{++}	$1^{\pm}$	S, P, D	$\rho(770), \sigma$	6
1^{-+}	$1^{\pm}$	P	$\rho(770)$	2
2^{++}	$1^{\pm}$	D	$\rho(770)$	2
2^{-+}	$1^{\pm}$	P	$\rho(770)$	2
isotropic background wave				

Table 9.2: $\gamma p \to n\pi^+\pi^+\pi^-$: Partial waves required for $M_{3\pi} > 1.4$ GeV

J^{PC}	M^{ϵ}	L	Y	Number of waves
1^{++}	$1^{\pm}$	S, P, D	$\rho(770), \sigma$	6
1^{-+}	$1^{\pm}$	P	$\rho(770)$	2
2^{++}	$1^{\pm}$	D	$\rho(770)$	2
2^{-+}	$1^{\pm}$	S, P, D	$f_2(1270)$,$\rho(770)$	6
isotropic background wave				

9.2 Fit Results

In this section the results from the PWA performed in the $\gamma p \to n\pi^+\pi^+\pi^-$ data sample are described in details. Hundreds of fits were performed to determine the partial waves which make the most significant contributions of describing the data. It is worth mentioning here that the challenge of the PWA procedure was the search of the optimal set of partial waves that best describes the data. Even though the procedure itself is not time consuming, the comparison and the interpretation of the fit results between different wave-sets can be very challenging. The notation used to describe the partial waves in this work is $J^{PC}M^{\epsilon}[Y\pi]_L$, where J is the angular momentum, P is the parity, C is the C-parity, M is the J projection, ϵ is the reflectivity, Y is the PDG state whose parameters are used for the intermediate isobar and L is the relative orbital angular momentum between Y and π. Often the $J^{PC}[Y\pi]$ notation will be used referring to all J^{PC} states decaying into the same $Y\pi$ isobar.

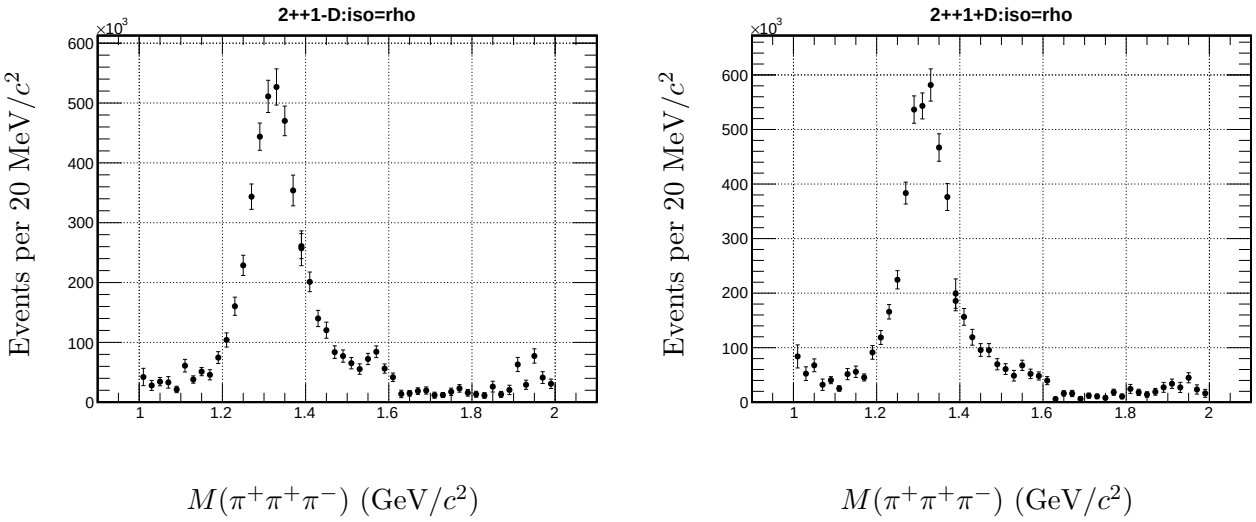

Figure 9.1: $\gamma p \to n\pi^+\pi^+\pi^-$: The partial wave intensity spectra of the $2^{++}1^-[\rho(770)\pi]_D$ (**left**) and $2^{++}1^+[\rho(770)\pi]_D$ (**right**) partial waves.

9.2.1 $2^{++}[\rho(770)\pi]$

The dominant partial wave present in the data is the $2^{++}1^{\pm}[\rho(770)\pi]_D$ and it is consistent in all the performed fits, with various wave-sets. Figure 9.1 shows the $2^{++}1^{\pm}[\rho(770)\pi]_D$ partial wave intensity distribution. This feature is consistent with previous charge exchange photoproduction analysis [55], [25]. The peak at 1.3 GeV that shows up in the 3π mass spectrum has now been identified as a $J^{PC} = 2^{++}$ partial wave decaying into $\rho\pi$. From this we can conclusively say that the $a_2(1320)$ meson was observed.

9.2.2 $1^{++}[\rho(770)\pi]$

The $1^{++}1^{\pm}[\rho(770)\pi]_S$ and $1^{++}1^{\pm}[\rho(770)\pi]_D$ partial waves were included in the fit, with the S wave as expected to be the dominant one. Figure 9.2 shows the $1^{++}[\rho(770)\pi]$ partial wave intensities for the two different reflectivities. The $1^{++}1^{\pm}[\rho(770)\pi]_S$ partial wave remains stable through many different fits and it is consistent with an $a_1(1260)$ meson. The symmetry in the shape of the intensity distributions for opposite reflectivities is consistent with the expectations of an un-polarized photon beam.

The $1^{++}[\rho(770)\pi]_D$ partial waves also show stable behavior for different fits but are less significant. Some leakage seems to be present of the dominant $a_2(1320)$ signal into the $1^{++}[\rho(770)\pi]_D$ wave.

The $a_1(1260)$ has never been seen in charge-exchange photoproduction, including the previous CLAS analysis, [25]. Furthermore the experiment [53] observes both the $a_1(1260)$ and a higher mass $a_1(1700)$ meson. The analysis reported here finds a $1^{++}[\rho(770)\pi]$ wave structure in both S and D partial waves near 1.8 GeV, consistent with the $a_1(1700)$.

9.2.3 $1^{++}[\sigma\pi]$

Figure 9.3 shows the $1^{++}1^{\pm}[Y=\sigma]_P$ partial wave intensities. The shape of the two intensities is similar for both reflectivities and the enhancement shown is around the same mass region as the intensity of the $1^{++}S$ partial wave. Also, by not including those waves in the fit, a significant leakage is introduced from the $a_2(1320)$ into the $1^{++}1^{\pm}[\rho(770)\pi]_S$ partial wave.

9.2.4 Mass Dependent Fit of the $1^{++}1^{\pm}[\rho(770)\pi]_S$ and $2^{++}1^{\pm}[\rho(770)\pi]_D$ partial waves

To study the resonance structures a mass dependent Breit Wigner (BW) fit was performed. In the first approach a simultaneously mass dependent fit was performed of the $1^{++}1^{\pm}[\rho(770)\pi]_S$ and $2^{++}1^{\pm}[\rho(770)\pi]_D$ partial wave intensities along with their phase difference, using the full error matrix. The fit was performed for the two reflectivities separately and results from this fit are shown in Figure 9.4. The latter Figure shows that the fit result does not cleanly go through all the $2^{++}1^{\pm}[\rho(770)\pi]_D$ intensity data points. The small errors in the phase difference (compared to the larger errors in the intensity distributions) are the major reason for this behavior making the fitter biased dominantly by the phase difference.

A mass independent fit was performed with random starting values in an effort to study this behavior further. Figure 9.5 shows the difference from the minimum value of the likelihood for 500 fits in each mass bin with random starting values. The $2^{++}1^{\pm}[\rho(770)\pi]_D$ and $1^{++}1^{\pm}[\rho(770)\pi]_S$ partial wave intensity distributions are shown in Figure 9.6 along with the phase difference between the two waves for values of the likelihood less than 60 from the minimum value of the likelihood for that particular mass bin. The results infer that there is a systematic uncertainty in the errors of the phase difference that is not taken into account. The sign ambiguity that the fit results exhibit

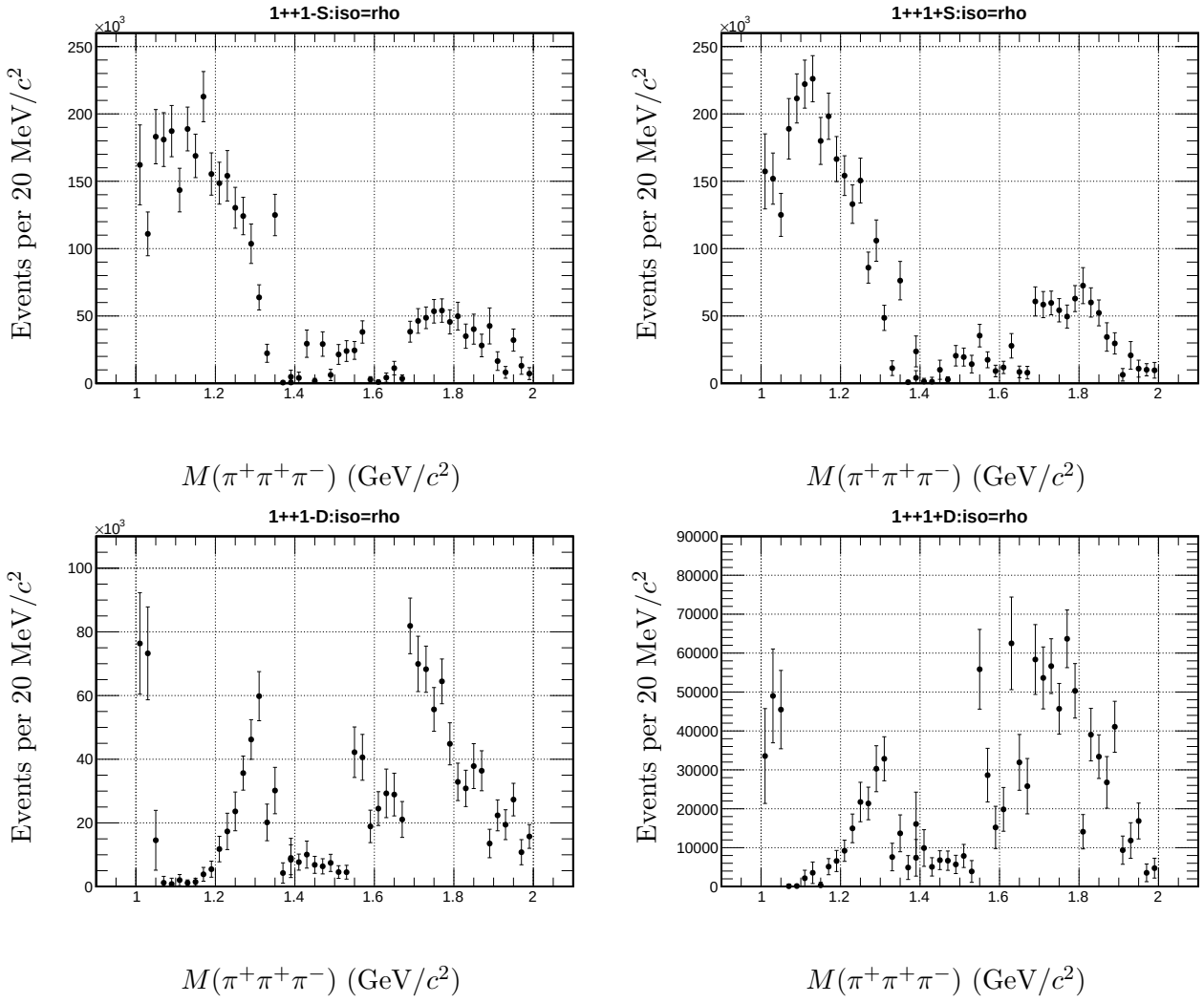

Figure 9.2: $\gamma p \to n\pi^+\pi^+\pi^-$: The partial wave intensity spectra of the $1^{++}1^-[\rho(770)\pi]_S$ (**top left**), $1^{++}1^+[\rho(770)\pi]_S$ (**top right**), $1^{++}1^-[\rho(770)\pi]_D$ (**bottom left**) and $1^{++}1^+[\rho(770)\pi]_D$ (**bottom right**) partial waves.

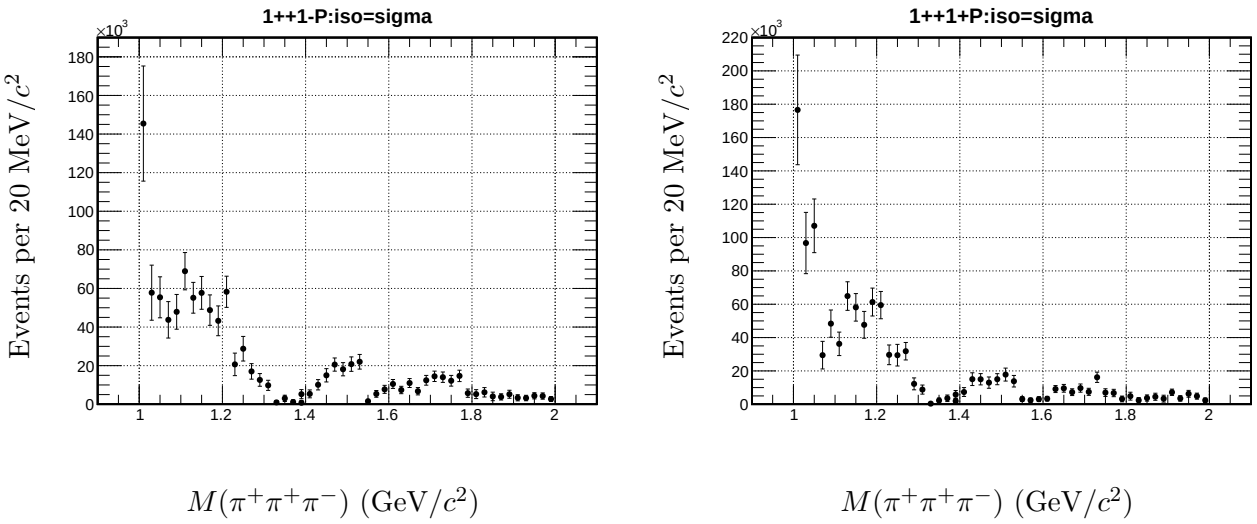

Figure 9.3: The partial wave intensity spectra of the $1^{++}1^-[\sigma\pi]_P$ (**left**) and $1^{++}1^+[\sigma\pi]_P$ (**right**) partial waves.

in the 1.3-1.4 GeV mass region, is the same mass region where the $1^{++}[\sigma\pi]_P$ intensity distribution is dropping to zero. Note that for the low 3π mass region only the $1^{++}[\sigma\pi]_P$ partial wave has other isobar than the $\rho\pi$.

To overcome that the mass dependent fit is dominantly driven by the phase difference between the two partial waves, two approaches were tried. In the first approach PWA fits were performed with difference wave-sets, and the resulting χ^2/DoF from the BW mass dependent fit of the $2^{++}1^{\pm}[\rho(770)\pi]_D$ and $1^{++}1^{\pm}[\rho(770)\pi]_S$ was recorded. By including the $2^{++}2^{\pm}[\rho(770)\pi]_D$ partial waves in the minimum wave-set, the χ^2/DoF value seems to be slightly improved but the PWA fit results were not consistent with previous measured well established resonant structures. Details about this fit can be find in Appendix C.

The second approach, is to study the resonance structures by first performing a mass dependent Breit Wigner (BW) fit to the partial wave intensity distributions. Then the phase difference between the two partial waves can be plotted with the parameters obtained by fitting the partial wave intensities. Figure 9.7 shows the $2^{++}1^{\pm}[\rho(770)\pi]_D$ and the $1^{++}1^{\pm}[\rho(770)\pi]_S$ partial wave intensities along with mass dependent fit results. The $J^{PC} = 2^{++}$ wave yields a mass of $M = 1.331 \pm 0.001$ GeV and a width of $\Gamma = 0.108 \pm 0.002$ GeV. These values are consistent with known PDG values for the $a_2(1320)$ meson. A mass dependent BW fit of the $1^{++}1^{\pm}[\rho(770)\pi]_S$ partial waves intensity yields

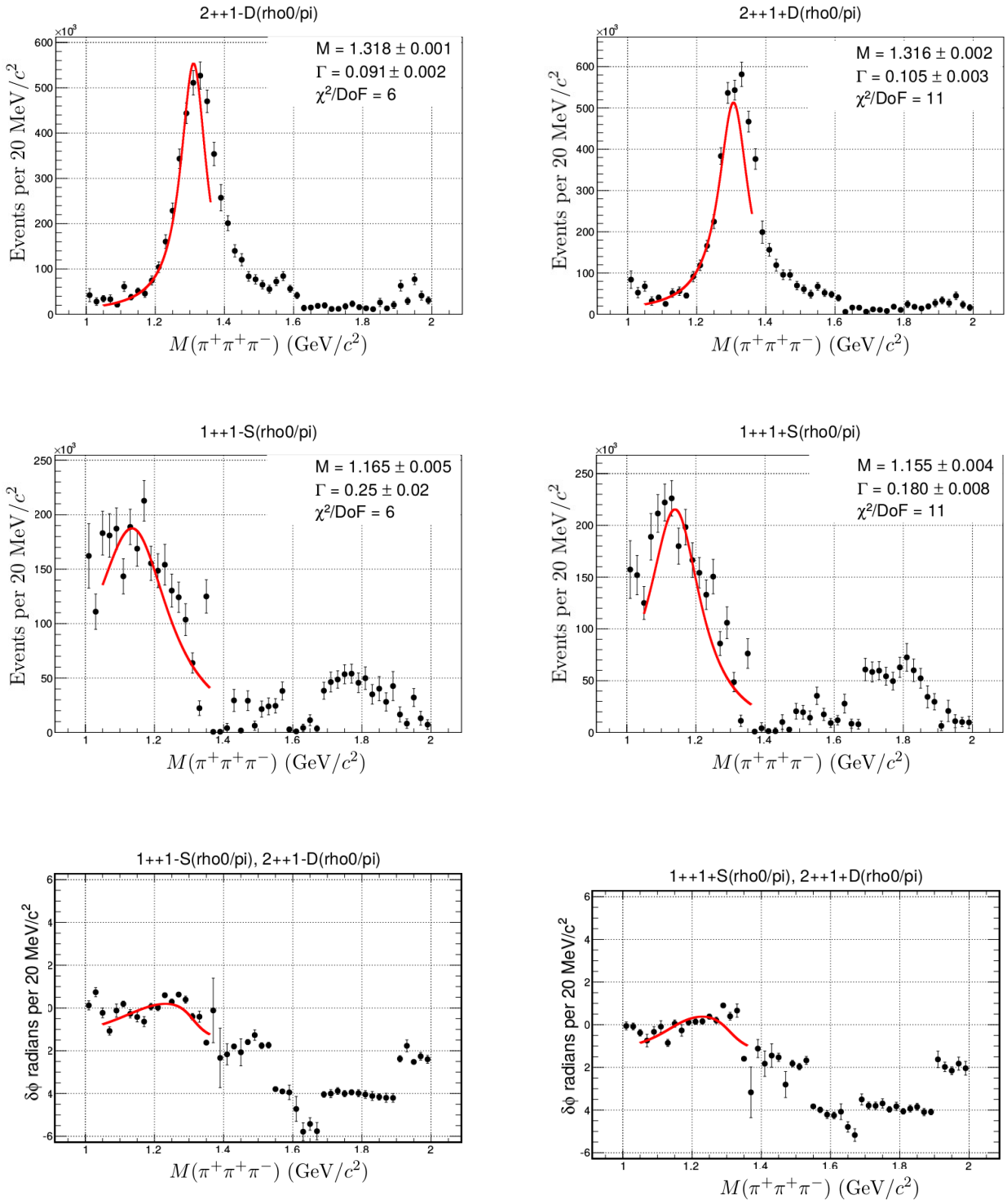

Figure 9.4: $\gamma p \to n\pi^+\pi^+\pi^-$: This Figure shows a simultaneously mass dependent fit of the $1^{++}[\rho(770)\pi]_S$ and $2^{++}[\rho(770)\pi]_D$ partial wave intensity distributions along with their phase difference. The **first column** shows the fit results for $M^\epsilon = 1^-$ and the **second column** for $M^\epsilon = 1^+$.

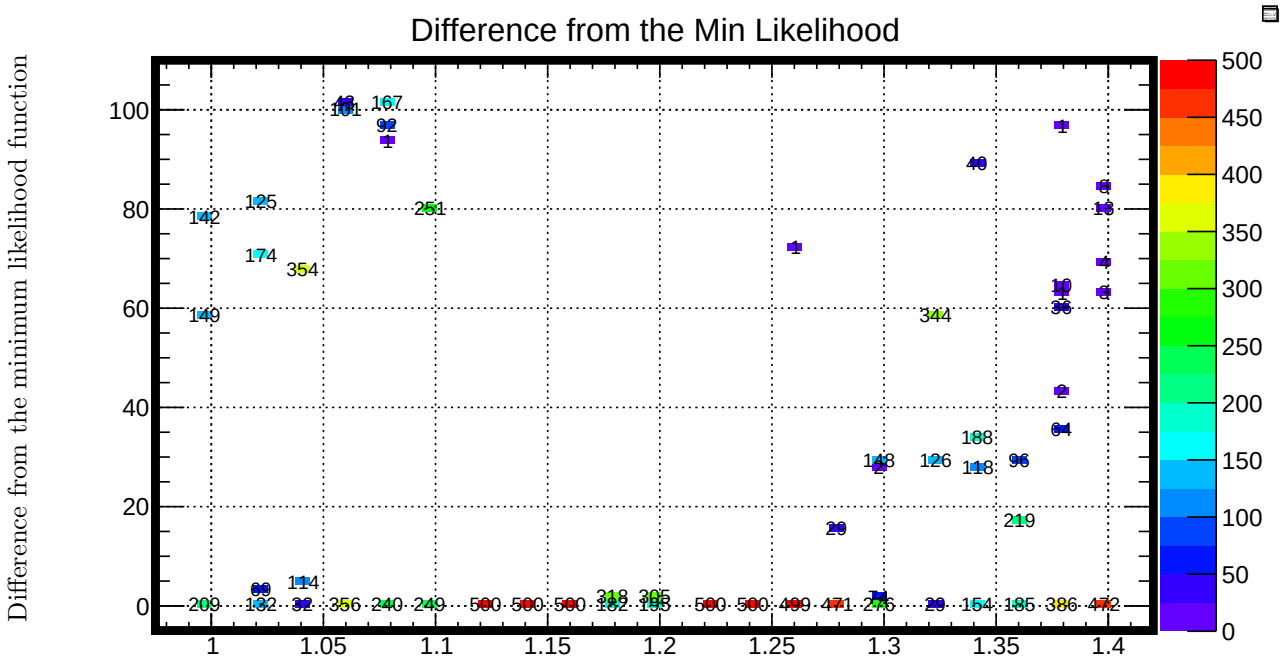

Figure 9.5: $\gamma p \to n\pi^+\pi^+\pi^-$: Difference between the final likelihood values in each mass bin and the minimum likelihood value seen among them for 500 PWA fits with the random starting values of the fitted parameters.

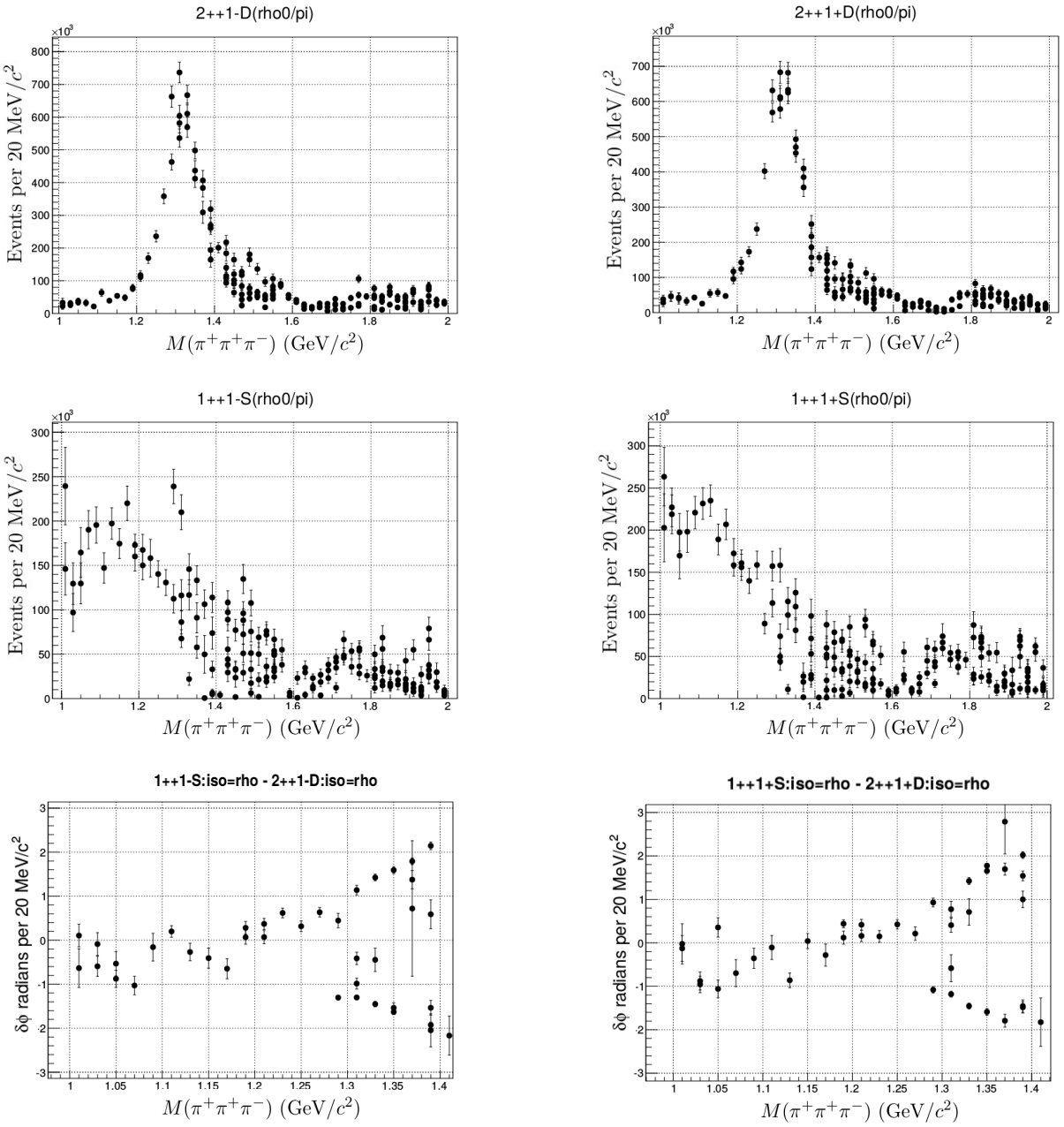

Figure 9.6: $\gamma p \to n\pi^+\pi^+\pi^-$: Results of multiple random fits after selection of only fits with final likelihood within 60 counts from the minimum value found. The **top and middle** plots show the intensities for the $1^{++}1^{\pm}[\rho(770)\pi]_S$ and $2^{++}1^{\pm}[\rho(770)\pi]_D$ waves. The **bottom left** plot shows the phase difference between the $1^{++}1^{-}[\rho(770)\pi]_S$ and $2^{++}1^{-}[\rho(770)\pi]_D$ wave. The **bottom right** plot shows the phase difference between the $1^{++}1^{+}[\rho(770)\pi]_S$ and $2^{++}1^{+}[\rho(770)\pi]_D$ wave.

a mass of $M = 1.169 \pm 0.004$ GeV and a width of $\Gamma = 0.29 \pm 0.02$ GeV which is consistent with the known PDG values for the $a_1(1260)$ meson. The phase difference between the $1^{++}S$ and $2^{++}D$ waves for $M^{\epsilon} = 1^{+}$ and $M^{\epsilon} = 1^{-}$ is also shown in Figure 9.7. The curve shows the Breit Wigner phase difference between the $a_1(1260)$ and $a_2(1320)$ with the parameters obtained from the mass dependent fit.

9.2.5 $2^{-+}[f_2(1270)\pi]$

In the high 3π mass region above the $f_2(1270)\pi$ mass threshold, the dominant wave is the $2^{-+}1^{\pm}[f_2(1270)\pi]_S$ wave. Figure 9.8 shows the $2^{-+}1^{\pm}[f_2(1270)\pi]_S$ and the $2^{-+}1^{\pm}[f_2(1270)\pi]_D$ partial wave intensity distributions for the two reflectivities. All four partial waves share a peak above 1.6 GeV, consistent with the production of the $\pi_2(1670)$ meson. Also the dominant behavior of the $2^{-+}1^{\pm}[f_2(1270)\pi]_S$ partial wave in this mass region is consistent with previous observations [53]. Again, the shape of the partial wave intensities for opposite reflectivities is consistent with the expectations of an un-polirized beam. The $2^{-+}1^{\pm}[f_2(1270)\pi]_D$ partial wave can serve as a second reference wave to search for possible phase motion against the $\pi_1(1600)$. The primary reference wave for the search of the exotic $J^{PC} = 1^{-+}$ state is going to be the well establish $2^{-+}1^{\pm}[f_2(1270)\pi]_S$ resonance and a mass dependent fit will follow.

9.2.6 $2^{-+}[\rho(770)\pi]$

Figure 9.9 shows the $2^{-+}1^{\pm}[\rho(770)\pi]_P$ partial wave intensity distribution for the two reflectivities. An enhancement is shown in the same region as the $2^{-+}[f_2(1270)\pi]$ partial waves, consistent with the production of the $\pi_2(1670)$ meson. It seems that the yield of the $2^{-+}[\rho(770)\pi]$ partial wave is almost half the yield of the $2^{-+}[f_2(1270)\pi]$ partial waves, where the PDG branching ratio of $\Gamma(\rho\pi)/\Gamma(f_2(1270)\pi)$ is 0.565. Also noticeable is the peak around 1.3 GeV in the partial wave intensity spectrum, where most likely it is a leakage from the dominant $a_2(1320)$ meson into the $2^{-+}1^{\pm}[\rho(770)\pi]_P$ partial wave.

9.2.7 The Exotic $J^{PC} = 1^{-+}$ Wave

As it was discussed before one of the main motivations for analyzing this channel is the study of the exotic $J^{PC} = 1^{-+}$ state. This state was previously claimed at 1.6 GeV decaying into $\rho\pi$ mode. For a resonance to be claimed, both a resonant intensity structure and a resonance phase

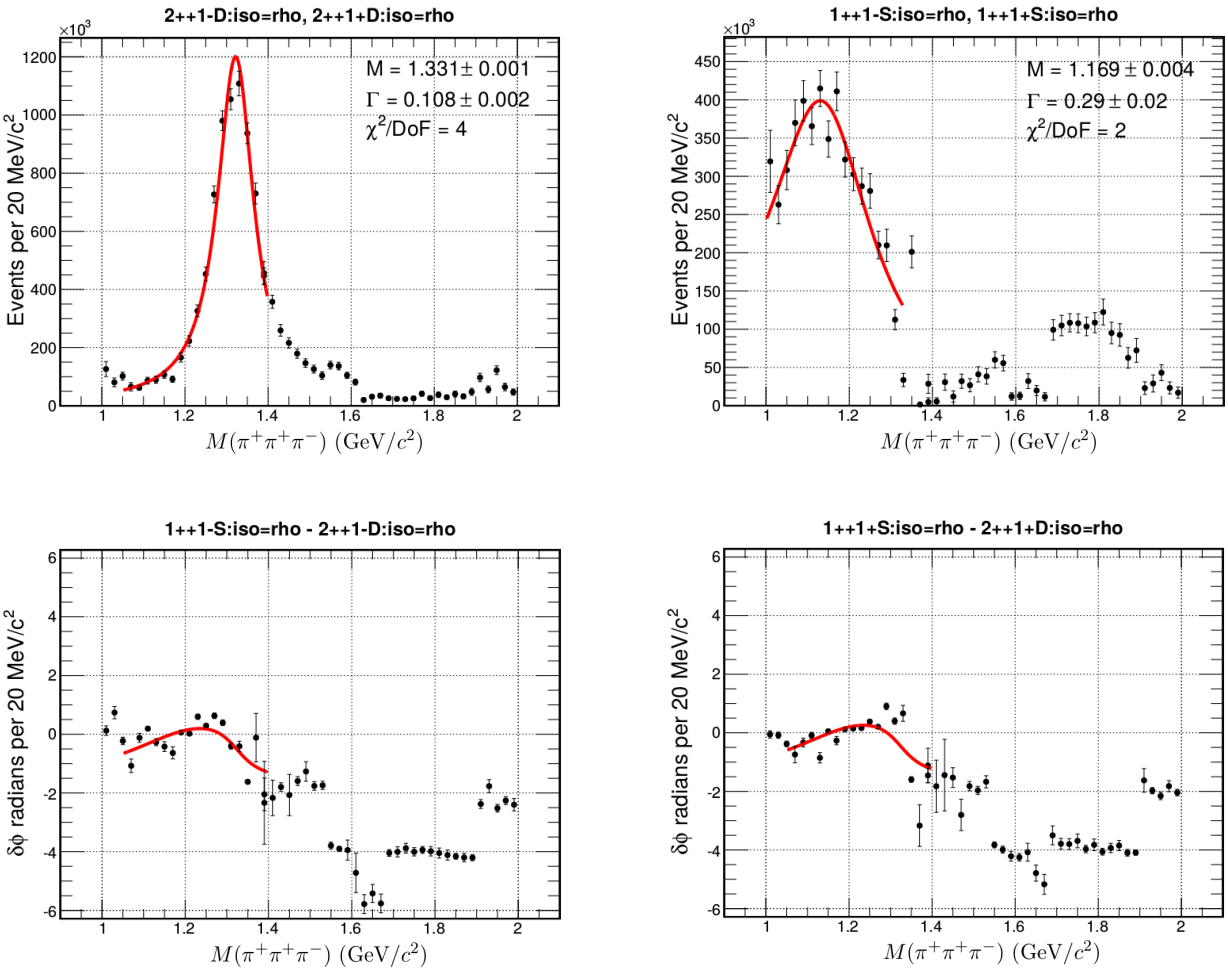

Figure 9.7: For the $\gamma p \to n\pi^+\pi^+\pi^-$ reaction: on the **top row** is the combined intensity for the two reflectivities $M^\epsilon = 1^\pm$ for the partial waves: $2^{++}1^\pm[\rho(770)\pi]_D$ and $1^{++}1^\pm[\rho(770)\pi]_S$. The two intensities have been fitted with a mass dependent BW function. The **bottom row** shows the the phase difference of the $2^{++}[\rho(770)\pi]_D$ wave against $1^{++}[\rho(770)\pi]_S$ wave for the two different reflectivities. The red curve is a plot of BW phase difference with the parameters obtained by fitting the intensities.

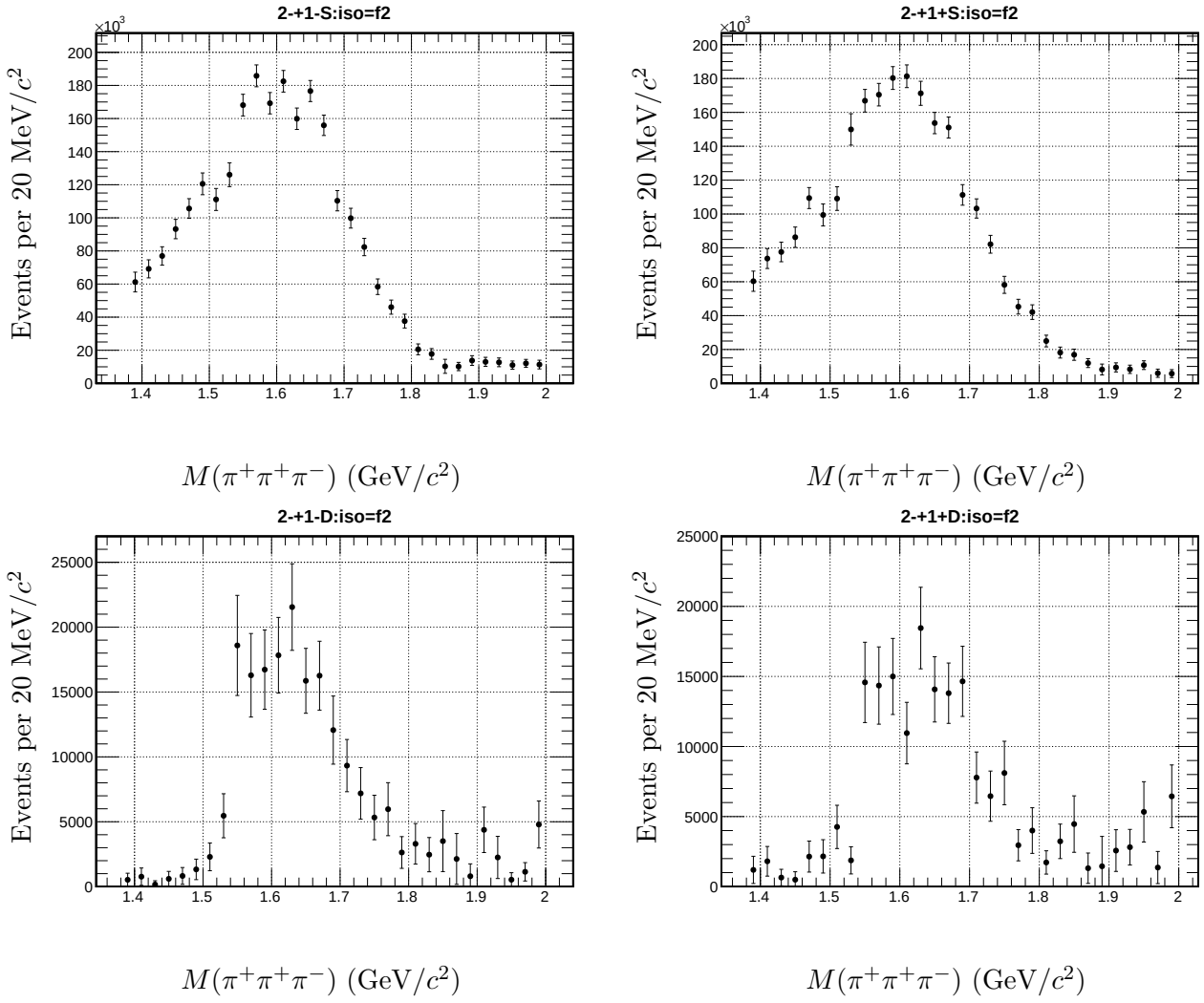

Figure 9.8: $\gamma p \to n\pi^+\pi^+\pi^-$: The partial wave intensity spectra of the $2^{-+}1^-[f_2(1270)\pi]_S$ (**top left**), $2^{-+}1^+[f_2(1270)\pi]_S$ (**top right**), $2^{-+}1^-[f_2(1270)\pi]_D$ and $2^{-+}1^+[f_2(1270)\pi]_D$ (**bottom left and right respectively**) partial waves.

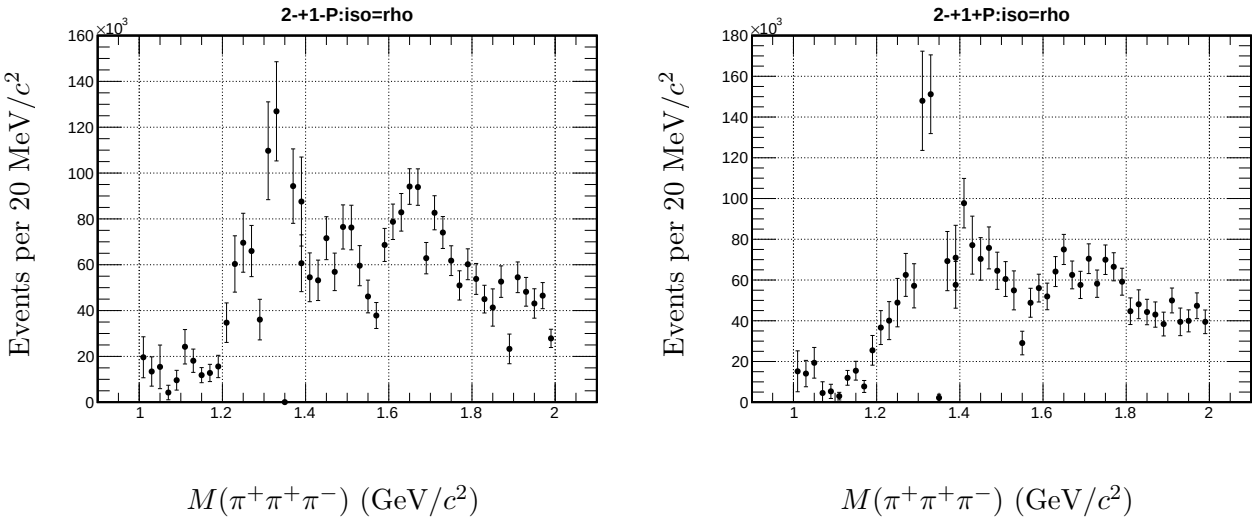

Figure 9.9: $\gamma p \to n\pi^+\pi^+\pi^-$: The partial wave intensity spectra of the $2^{-+}1^-[\rho(770)\pi]_P$ and $2^{-+}1^+[\rho(770)\pi]_P$ partial waves.

motion should exist. Since experimentally one measures relative phase motions, the 1^{-+} wave is studied relative to the dominant $2^{-+}[f_2(1270)\pi]$ wave.

Figure 9.10 shows the $1^{-+}1^\pm[\rho(770)\pi]_P$ partial wave intensity distribution. No structure exists that is consistent with an exotic resonance at 1.6 GeV. Also the $1^{-+}1^\pm[\rho(770)\pi]_P$ wave is comparatively weak as exhibits a depletion of events at 1.6 GeV.

A simultaneously BW mass dependent fit was performed of the $1^{-+}[\rho(770)\pi]_P$ and $2^{-+}[f_2(1270)\pi]_S$ partial wave intensities along with their phase difference, using the full error matrix. The fit was performed for the two reflectivities separately and results from this fit are shown in Figure 9.11. By considering the $1^{-+}[\rho(770)\pi]_P$ partial wave as a resonant in the fit, the resulting parameters show a non-resonating $1^{-+}[\rho(770)\pi]_P$ partial wave. Specifically, the fit yields for both reflectivities $M^\epsilon = 1^\pm$, a mass of $M = 0.9$ GeV and a width of $\Gamma = 3$ GeV for the 1^{-+} state.

Additionally, Figure 9.12 shows the combined intensity of the $2^{-+}1^\pm[f_2(1270)\pi]_S$ waves. By fitting this intensity with a mass dependent BW yields a mass of $M = 1.634 \pm 0.002$ GeV and a width of $\Gamma = 0.252 \pm 0.005$ GeV, which is consistent with a $\pi_2(1670)$ meson. The same Figure shows the combined intensity of the $1^{-+}1^\pm[\rho(770)\pi]_P$ waves along with the phase difference between $2^{-+}[f_2(1270)\pi]_S$ and $1^{-+}[\rho(770)\pi]_P$ waves for both $M^\epsilon = 1^+$ and $M^\epsilon = 1^-$. The red curve is a plot of a pure $2^{-+}[f_2(1270)\pi]_S$ phase motion with a non-resonating $1^{-+}[\rho(770)\pi]_P$. The parameters for

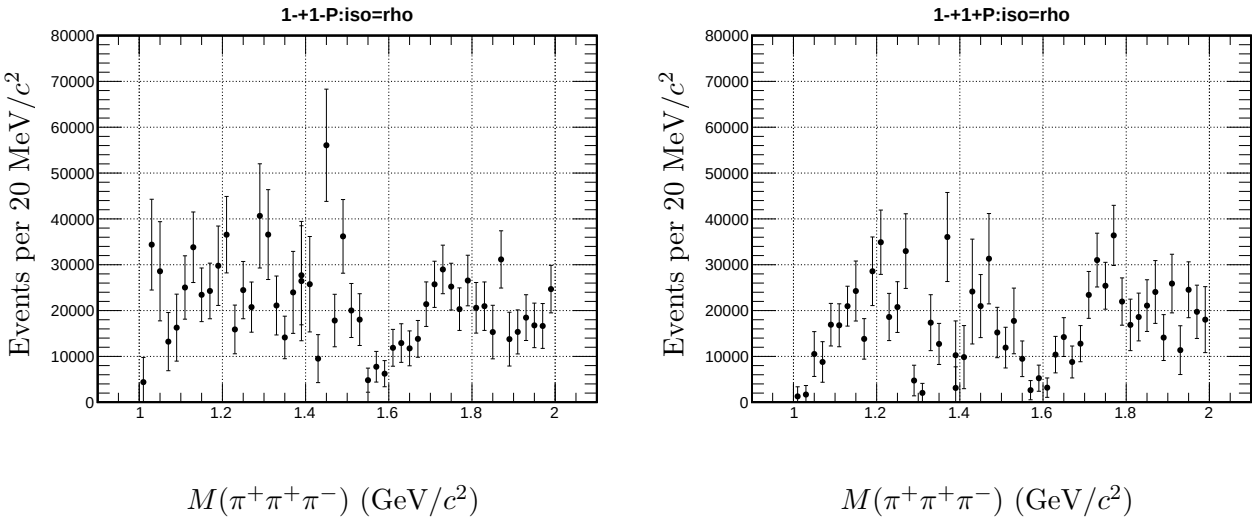

Figure 9.10: $\gamma p \to n\pi^+\pi^+\pi^-$: The partial wave intensity spectra of the $1^{-+}1^-[\rho(770)\pi]_P$ and $1^{-+}1^+[\rho(770)\pi]_P$ partial waves.

the BW curve were obtained from BW fit of $2^{-+}[f_2(1270)\pi]_S$ intensity. The dashed blue curve is the phase difference between a resonating $2^{-+}[f_2(1270)\pi]_S$ against a resonating $1^{-+}[\rho(770)\pi]_P$ with mass and width parameters reported by E852 decaying to 3π [53]. The solid blue curve is the phase difference between a resonating $2^{-+}[f_2(1270)\pi]_S$ against a resonating $1^{-+}[\rho(770)\pi]_P$ with mass and width parameters reported by E852 decaying to $\eta\pi$ [56]. The phase difference strongly favors a non-resonant $1^{-+}[\rho(770)\pi]_P$. Figure 9.13 shows the phase difference between the $1^{-+}[\rho(770)\pi]_P$ exotic wave and $2^{-+}[f_2(1270)\pi]_D$ wave for both $M^\epsilon = 1^+$ and $M^\epsilon = 1^-$. The behavior of phase motion is also consistent with a non-resonant $J^{PC} = 1^{-+}$ exotic wave and a resonating $\pi_2(1670)$ in both S and D wave amplitudes.

9.2.8 Predicted Angular Distributions

The "goodness" of the PWA fit results was determined by comparing the data distribution with predicted distributions using the PWA fit results. A description of how the predicted distributions obtained can be find in section 7.2.2. Discrepancies between the data and the predicted distributions would be an indication of a poor description of the data. Figures 9.14, 9.15, 9.16 show a comparison between the two distributions. There is a good agreement between the data and the predicted distributions, indicating that the selected wave-set describes well the measured by the CLAS spectrometer data.

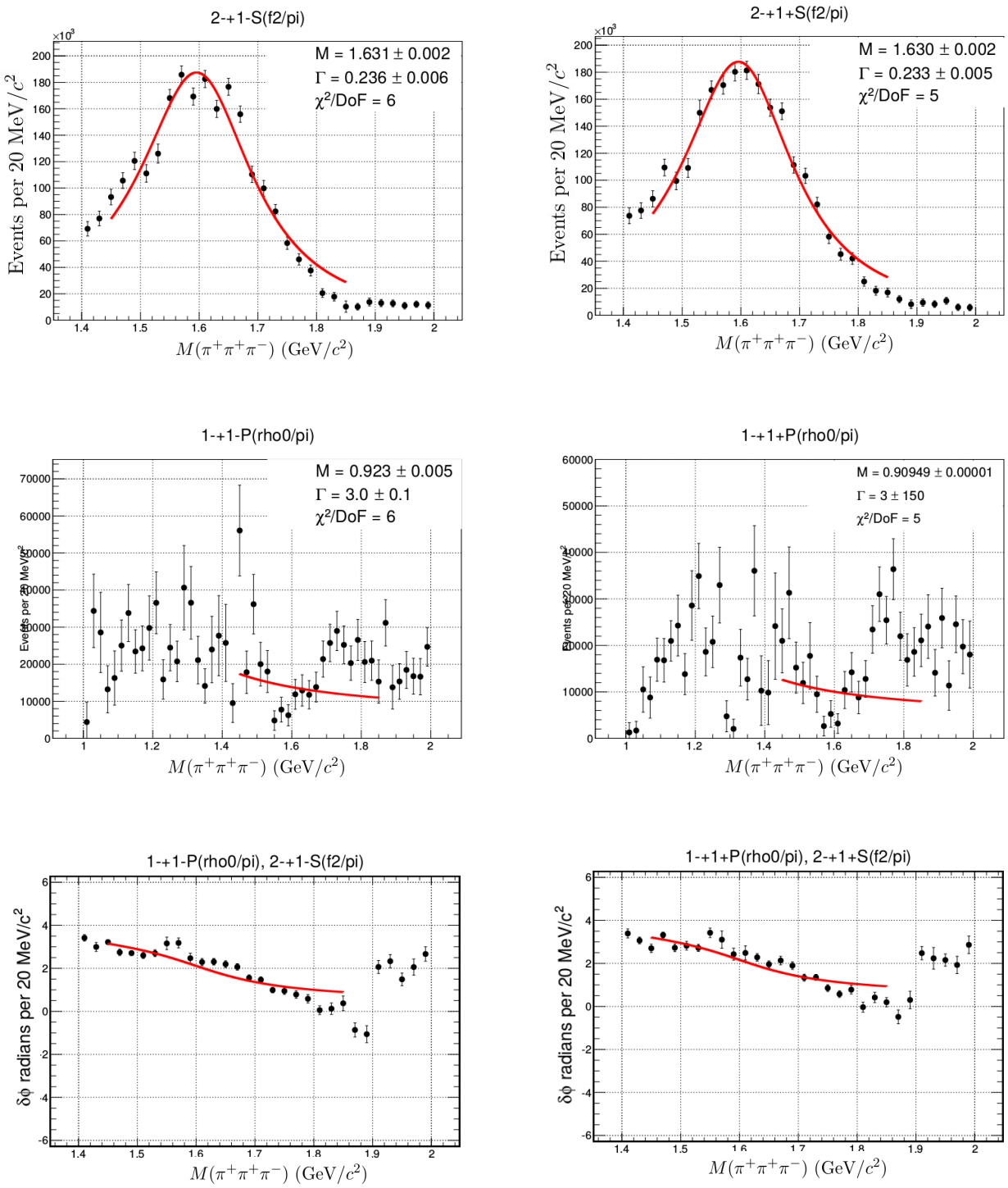

Figure 9.11: $\gamma p \to n\pi^+\pi^+\pi^-$: This Figure shows a simultaneously mass dependent fit of the $1^{-+}[\rho(770)\pi]_P$ and $2^{-+}[f_2(1270)\pi]_S$ partial wave intensity distributions along with their phase difference. The **first column** shows the fit results for $M^\epsilon = 1^-$ and the **second column** for $M^\epsilon = 1^+$. For the two different values of reflectively the $J^{PC} = 1^{-+}$ state exhibits a non-resonant behavior.

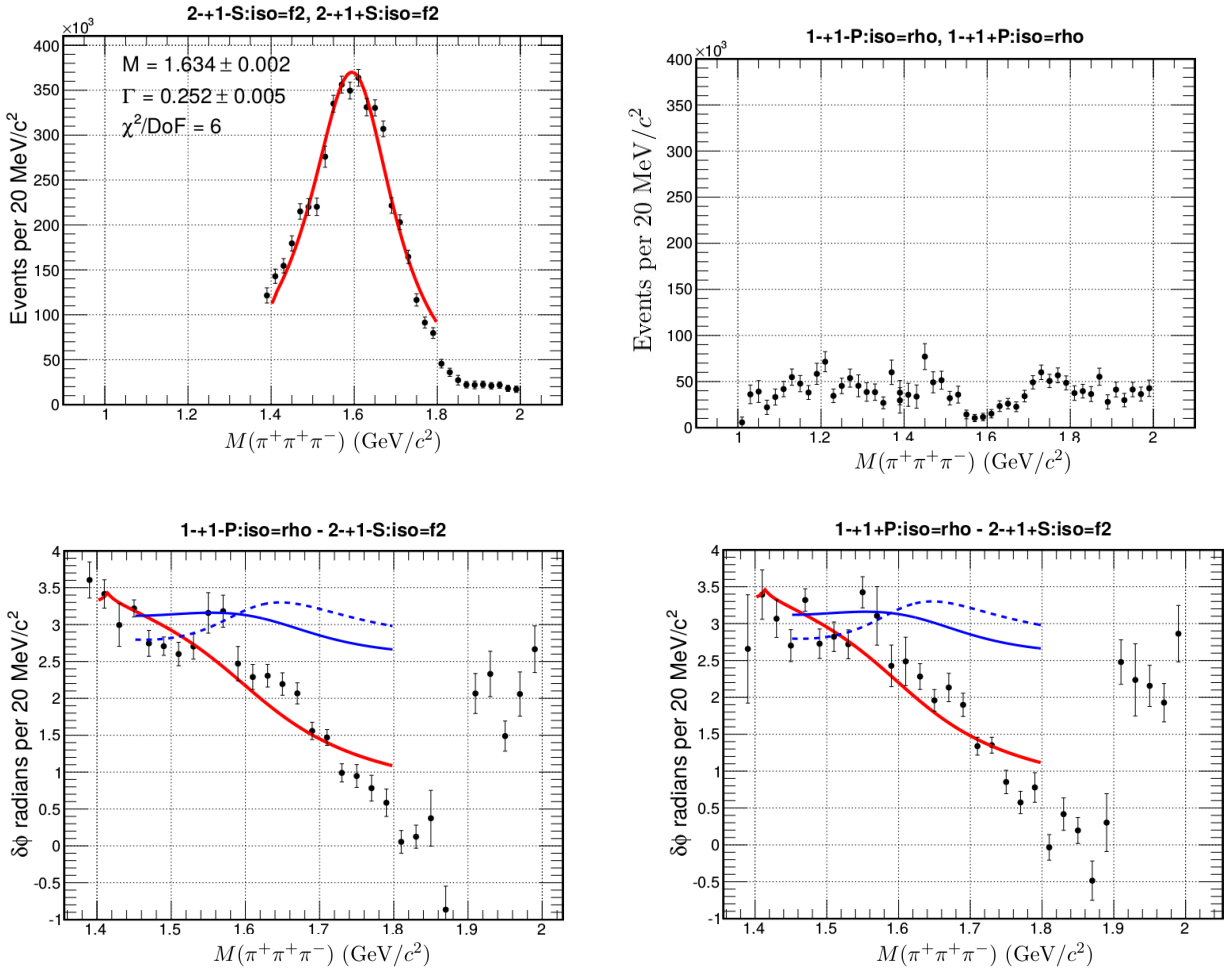

Figure 9.12: $\gamma p \to n\pi^+\pi^+\pi^-$: For the $\gamma p \to n\pi^+\pi^+\pi^-$ reaction: The **top row** shows the partial wave intensities for $2^{-+}1^{\pm}[f_2(1270)\pi]_S$ and $1^{-+}1^{\pm}[\rho(770)\pi]_P$. The $2^{-+}S$ intensity was fitted with a mass dependent BW amplitude and along with the parameters the resulting red curve has been plotted. The **bottom row** shows the phase difference between $2^{-+}S$ and $1^{-+}P$ waves for both $M^{\epsilon} = 1^+$ and $M^{\epsilon} = 1^-$. The red curve is a plot of a pure $2^{-+}S$ phase motion with a non-resonating $1^{-+}P$. The parameters for the BW curve were obtained from BW fit of $2^{-+}S$ intensity. The dashed blue curve is the phase difference between a resonating $2^{-+}S$ against a resonating $1^{-+}P$ with mass and width parameters reported by E852 decaying to 3π. The solid blue curve is the phase difference between a resonating $2^{-+}S$ against a resonating $1^{-+}P$ with mass and width parameters reported by E852 decaying to $\eta\pi$.

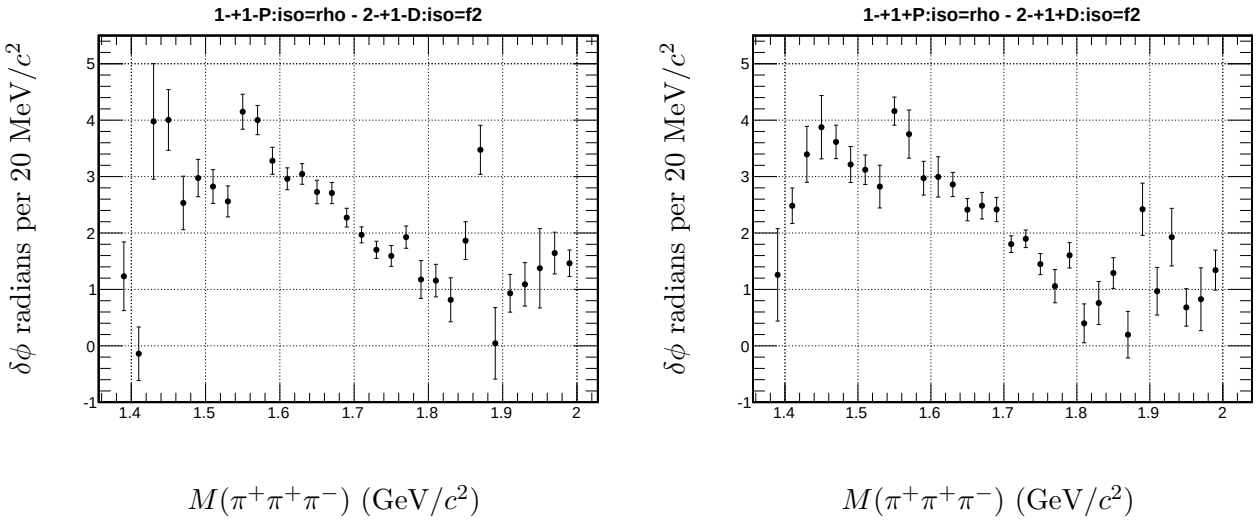

Figure 9.13: $\gamma p \to n\pi^+\pi^+\pi^-$: Phase difference for the two reflectivities between the $1^{-+}[\rho(770)\pi]_P$ wave and the $2^{-+}[f_2(1270)\pi]_D$ wave.

9.2.9 Systematic Dependencies of the Fit Results

On the whole, the presented results are stable against different values of the selection criteria and for different mass bin widths used in the PWA. The main selection criteria were tested, i.e. the θ_{lab} cut, the t' selection and the nominal fiducial cuts (as described here [54]). The non-observation of the $J^{PC} = 1^{-+}$ exotic state, as well as the observations of the a_1, a_2 and π_2 mesons did not change. As cuts are relaxed some signal leakage increases.

Specifically, by relaxing the angular cut the $2^{-+}P$ partial wave showed a small dependence by this cut. Also the enhancement in the high 3π mass region for the $1^{++}S$ partial wave was shifted from 1.8 to 1.5 GeV. The fit results obtained with the fiducial cuts do not different from the main fit results. By relaxing the t' cut the results were stable up to 1.0 GeV$^2/c^4$. Finally, the isotopic background shows stable behavior for the minimum selections, θ_{lab} cut and fiducial cuts. It shows an increment in the high 3π mass region as the t' selection cut is relaxed. This is another indication that the low t' selection helps to reduce the background in the high 3π mass region. Finally, the PWA fit results do not show any dependence for different values of the mass bin width.

In Appendix D a detailed description of the systematic studies due to the selection criteria can be find, and in Appendix B PWA fit results are shown for different mass bin widths.

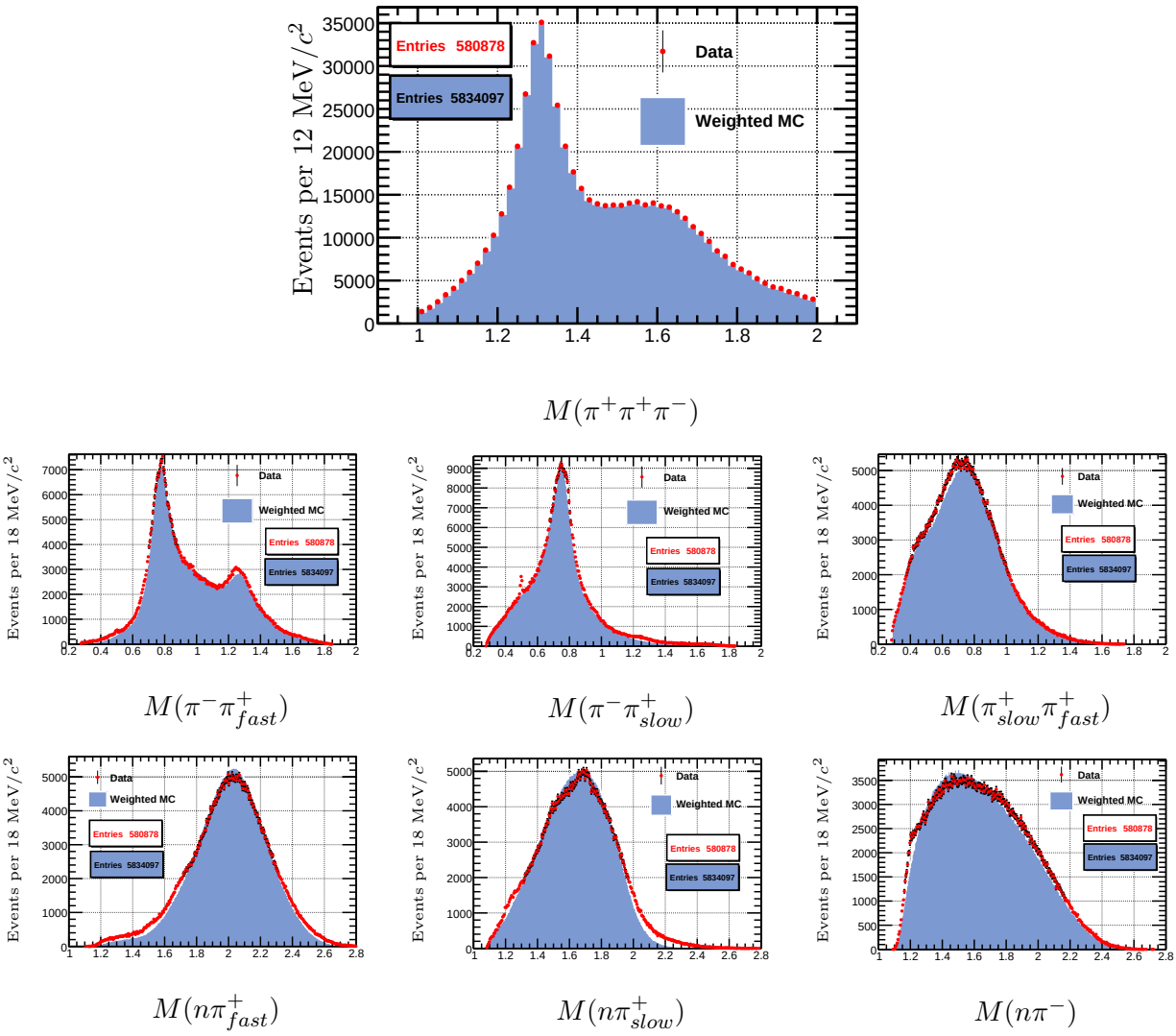

Figure 9.14: $\gamma p \to n\pi^+\pi^+\pi^-$: The measured (points) and the predicted (blue histograms) distributions for the 3π, $n\pi$ and $\pi\pi$ invariant mass distributions.

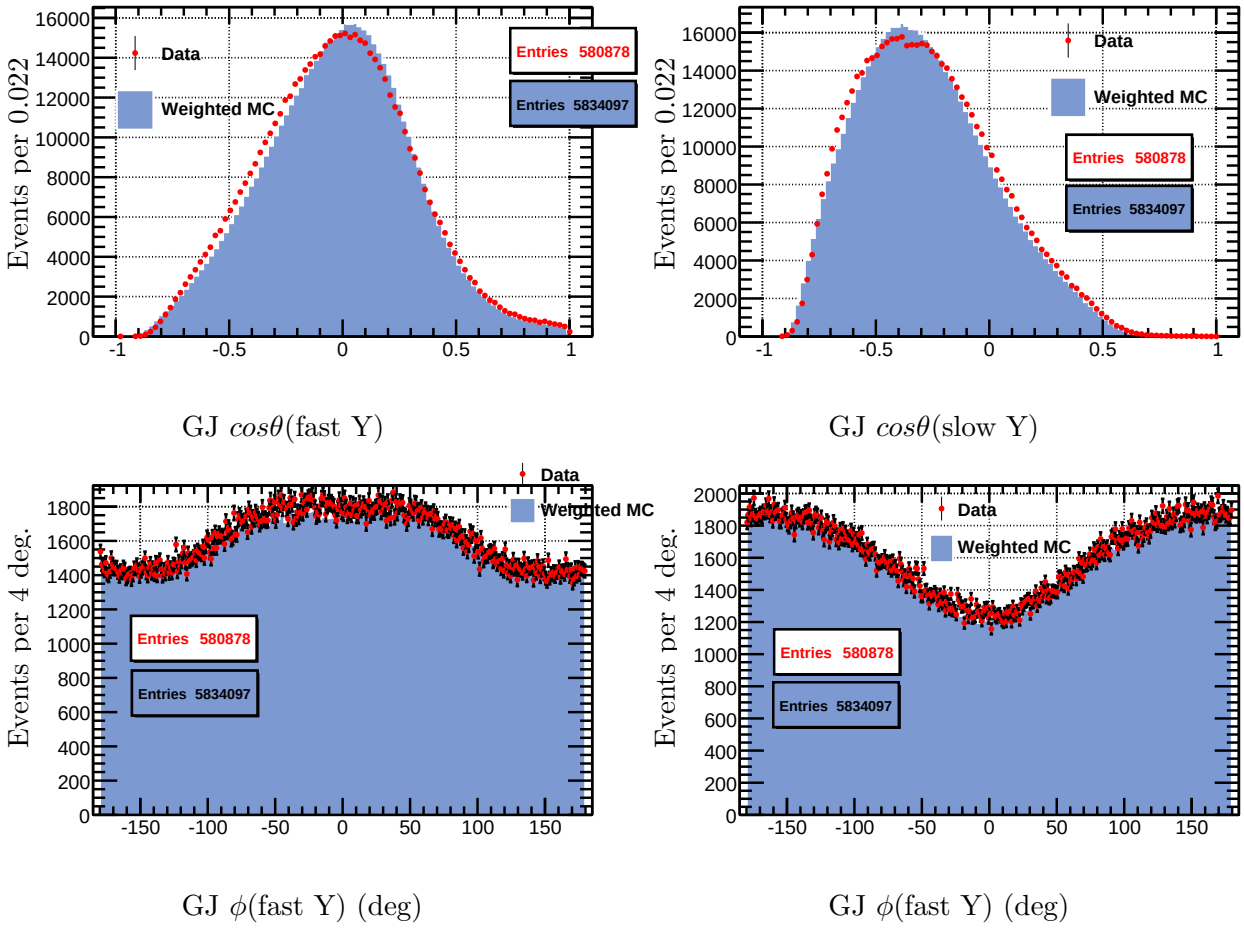

Figure 9.15: $\gamma p \to n\pi^+\pi^+\pi^-$: The measured (points) and the predicted (blue histograms) distributions in the Gottfried-Jackson rest frame for $cos\theta$ and ϕ.

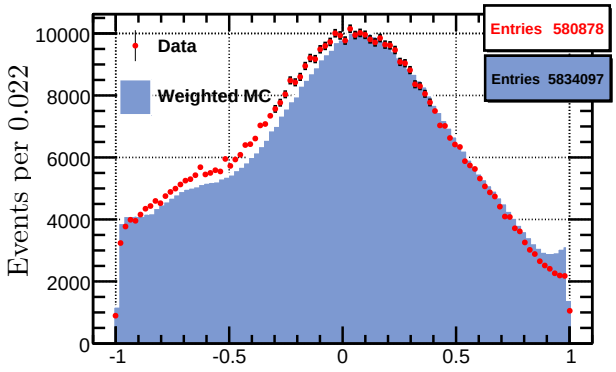

Helicity $cos\theta$(fast Y)

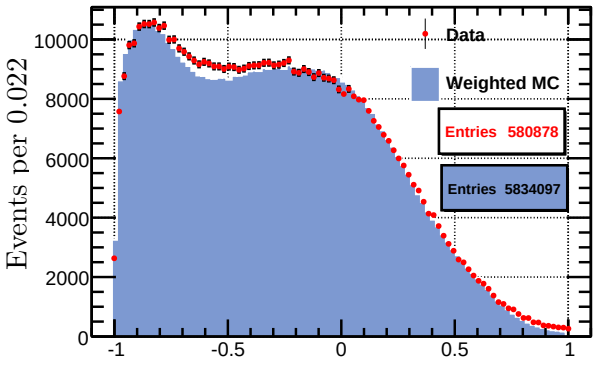

Helicity $cos\theta$(slow Y)

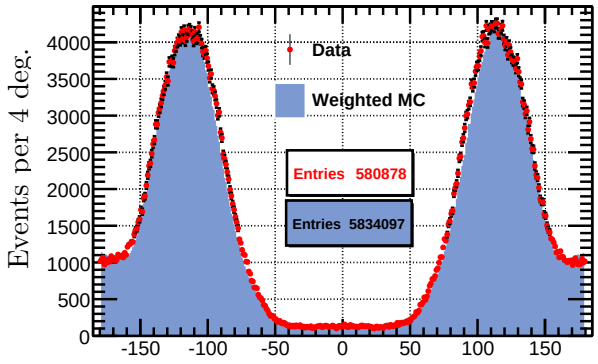

Helicity ϕ(fast Y) (deg)

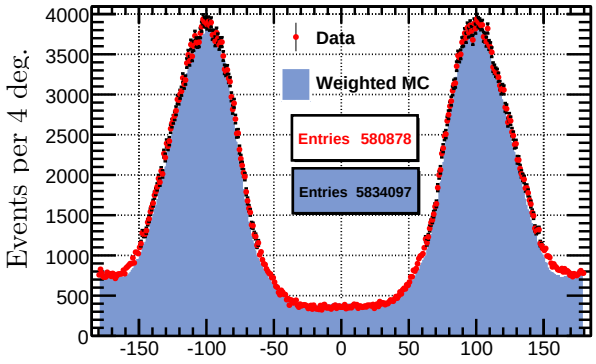

Helicity ϕ(slow Y) (deg)

Figure 9.16: $\gamma p \to n\pi^+\pi^+\pi^-$: The measured (points) and the predicted (blue histograms) distributions in the helicity rest frame for $cos\theta$ and ϕ.

9.3 Summary

The photoproduction of mesons decaying to 3π was studied using the $\gamma p \to n\pi^+\pi^+\pi^-$ reaction channel. Around 600k events were acquired resulting in the largest 3π photoproduction data-set to date. A mass independent partial wave analysis was performed. The $a_1(1260)$, $a_2(1320)$, and the $\pi_2(1670)$ mesons were observed. We subscript for the first time, observation of $a1(1260)$ photoproduction. The exotic $J^{PC} = 1^{-+}$ partial wave does not show resonant behavior and more so it is strongly consistent with a non-resonant non-interfering wave relative to a resonant $\pi_2(1670)$.

CHAPTER 10

INTERPRETATION OF RESULTS AND FUTURE WORK

A mass independent partial wave analysis was performed on 580K events for the $\gamma p \to n\pi^+\pi^+\pi^-$ reaction. The $a_2(1320)$ and $a_1(1260)$ mesons were observed in the $2^{++}[\rho(770)\pi]_D$ and $1^{++}[\rho(770)\pi]_S$ partial waves respectively. The $\pi_2(1670)$ meson was also observed in the $J^{PC} = 2^{-+}$ partial waves through the $f_2(1270)\pi$ and $\rho(770)\pi$ decay modes. It was found that M = 0 waves were not required. This is consistent with a spinless one pion exchange production in a photon beam. In addition, since the photon beam was unpolarized, the resonant states were expected and were indeed observed to equally populate the partial waves of opposite reflectivities (i.e., which differ only by $M^\epsilon = 1^+$ and $M^\epsilon = 1^-$) regardless of the naturality of the exchange particles [57].

The $a_1(1260)$ meson has never been seen before in charge-exchange photoproduction, including the previous $\gamma p \to n\pi^+\pi^+\pi^-$ CLAS analysis [25]. It was confirmed that the exotic $J^{PC} = 1^{-+}$ partial wave is not produced in equal amounts with the ordinary mesons as had been proposed before in [23]. To study the nature of the exotic wave, the Breit-Wigner mass dependent fits of the intensities and phase difference of the $1^{-+}[\rho(770)\pi]_P$ and $2^{-+}[f_2(1260)\pi]_S$ partial waves were performed. From the phase difference between the 1^{-+} and 2^{-+} partial waves it was found that the $J^{PC} = 1^{-+}$ partial wave does not show the resonant behavior in contrast to the resonant $\pi_2(1670)$ state. This behavior was consistent in both the positive and negative reflectivities when studied against either the $2^{-+}[f_2(1270)\pi]_S$ or the $2^{-+}[f_2(1270)\pi]_D$ partial waves.

One of the main motivations to study the 3π final state is a possible production of the $\pi_1(1600)$ state. As was mentioned in Chapter 1, the E852 [14] and COMPASS [16] experiments have published the analyses of the 3π final state showing the presence of the $\pi_1(1600)$ resonance in both the intensity and the phase. In both cases, this state was produced in the $\pi^- p \to p\pi^+\pi^-\pi^-$ reaction, which is a neutral exchange process. The $\gamma p \to n\pi^+\pi^+\pi^-$ reaction is a charge exchange process and, therefore, a Pomeron or glueball exchange is not allowed. If the $\pi_1(1600)$ is a hybrid state then a glue-rich exchange may be necessary for its production.

For the very first time a mass independent partial wave analysis was performed on the $\gamma p \to \pi^-\pi^-\pi^+\Delta^{++}$ reaction. The 345K events were split into two data-sets for $M_{3\pi} < 1.425$ GeV (the low mass region) and for $M_{3\pi} > 1.425$ GeV (the high mass region). The $a_2(1320)$ was observed in the $2^{++}[\rho(770)\pi]_D$ partial wave. The photoproduction of the $a_1(1260)$ meson was confirmed in this channel as well. The $a_1(1260)$ was observed in both the $1^{++}[\rho(770)\pi]_S$ and the $1^{++}[\rho(770)\pi]_D$ partial waves. In the high mass region, the $\pi_2(1670)$ meson was seeing in the $J^{PC} = 2^{-+}$ partial waves through the $f_2(1270)\pi$ and $\rho(770)\pi$ decay modes. Unfortunately, the results in this region were unstable due to the presence of the $\gamma p \to p4\pi$ background. It was not possible to eliminate such background due to a very low acceptance for backward-going pions (for which the kinematic difference between the main and background channels are the largest). This was caused by the specific configuration of the g12 run in which the target was moved upstream to increase the acceptance for the forward-going particles for other reactions.

At the beginning of 2016, the new GlueX detector in Hall D at Jefferson has started taking data. This detector has been design specifically for this kind of physics and, most likely, it will overcome the limitations of the CLAS detector that were mentioned earlier. Also, higher beam energy of 9 GeV should suppress the background contribution of the s-channel reactions in GlueX. In addition, the polarization of the photon beam will select a particular naturality of the exchange particle. Such additional information should help in the determination of the quantum numbers of the produced states. Another advantage of GlueX over CLAS is the presence of two calorimeters which should make it ideal for the neutral 3π analysis, such as $\gamma p \to p\pi^+\pi^-\pi^0$. A comparison of the neutral and charged exchanges in the photoproduction of 3π states should provide a further insight on the nature of the exotic $J^{PC} = 1^{-+}$ signal.

APPENDIX A

COMPARISON BETWEEN DATA AND MC FOR THE $\gamma p \to \pi^- \pi^- \pi^+ \Delta^{++}$ REACTION

In this Appendix, a comparison between data and Monte-Carlo events is shown. Figures A.1, A.2 show various invariant mass distributions for data and simulated events. Figure A.3 shows the angular distributions in the GJ and the helicity frame. The black curve in the plots is data for the exclusive $\gamma p \to \pi^- \pi^- \pi^+ \Delta^{++}$ reaction by selecting the Δ^{++} but without the baryon reduction cuts. The red curve represents data with all the selection criteria applied, while the blue curve has the same selection cuts applied for the accepted Monte-Carlo events.

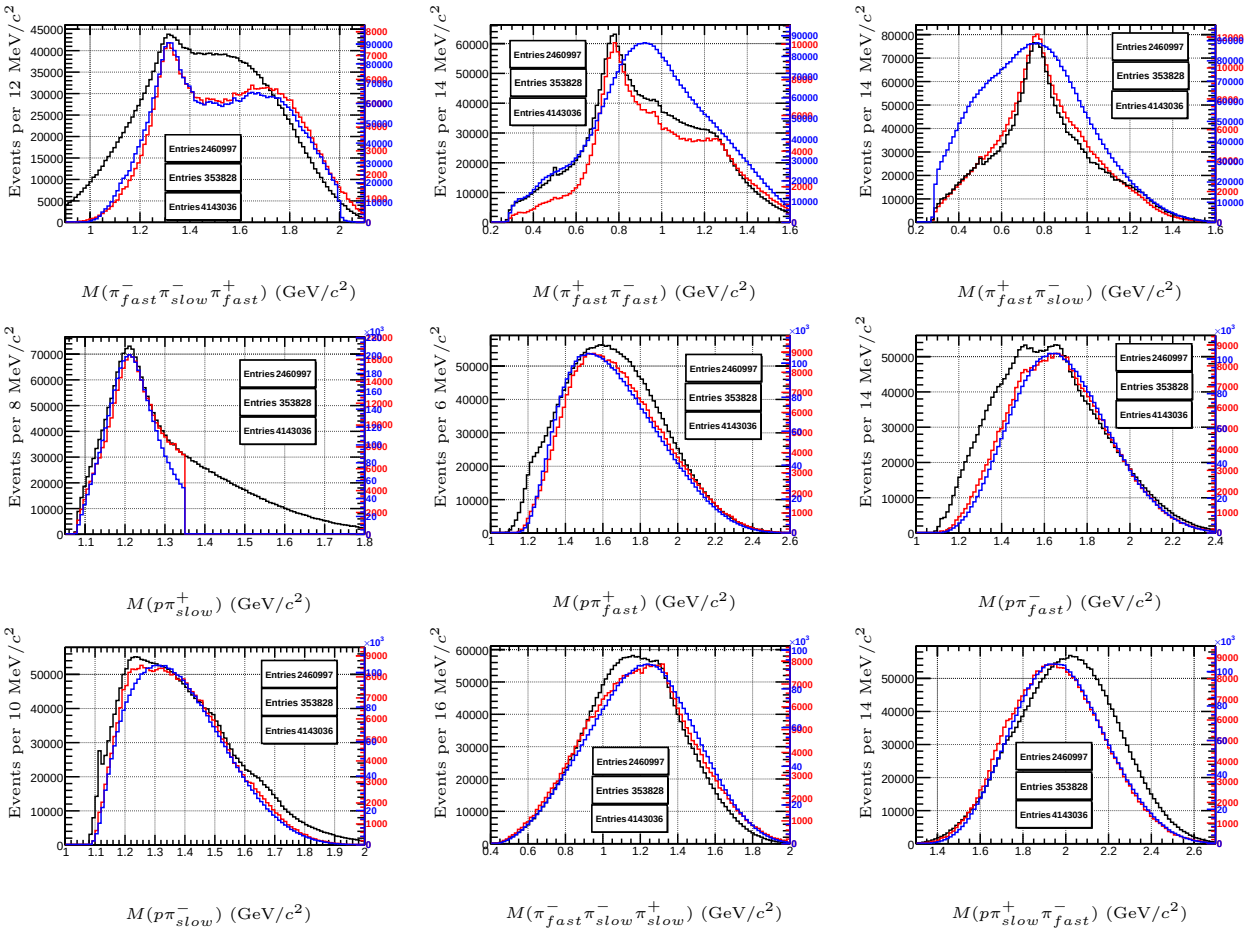

Figure A.1: $\gamma p \to \pi^-\pi^-\pi^+\Delta^{++}$: Various invariant masses. **Black line** is for data without baryon reduction. **Red line** is for data with baryon reduction background cuts. **Blue line** is for Monte-Carlo with baryon reduction background cuts.

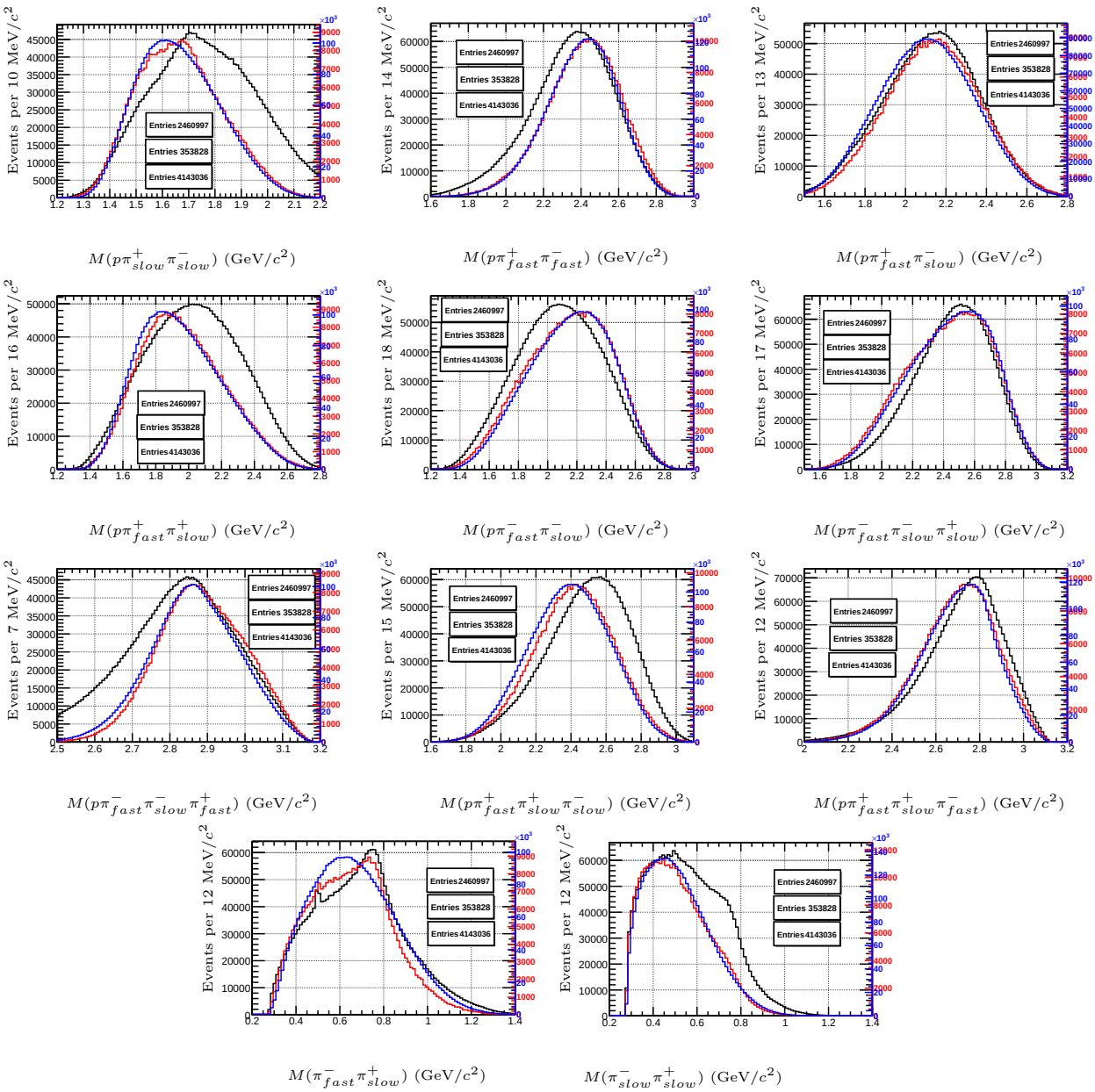

Figure A.2: $\gamma p \to \pi^-\pi^-\pi^+\Delta^{++}$: Various invariant masses. **Black line** is for data without baryon reduction. **Red line** is for data with baryon reduction background cuts. **Blue line** is for Monte-Carlo with baryon reduction background cuts.

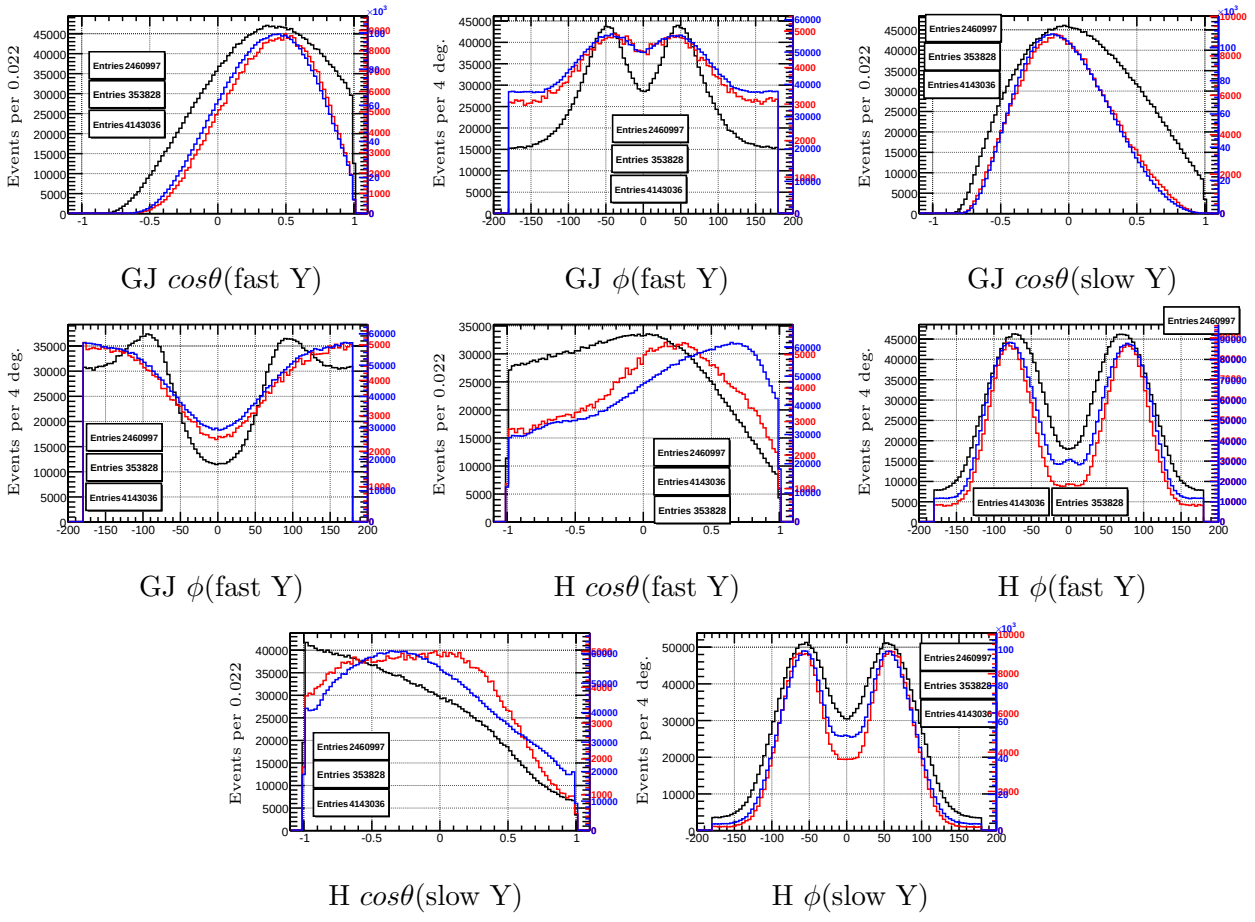

Figure A.3: $\gamma p \rightarrow \pi^-\pi^-\pi^+\Delta^{++}$: Rest frame angles. **Black line** is for data without baryon reduction. **Red line** is for data with baryon reduction background cuts. **Blue line** is for Monte-Carlo with baryon reduction background cuts.

APPENDIX B

SYSTEMATIC EFFECTS DUE TO BIN SIZE FOR THE $\gamma p \to n\pi^+\pi^+\pi^-$ REACTION

In order to test the systematic dependence of the results, two fits have been performed with different bin sizes. All the fits that have been presented so far for the $\gamma p \to n\pi^+\pi^+\pi^-$ reaction are with 20 MeV bin size. The results below are with 10 MeV and 50 MeV bin size. The results show stable behavior, within the statistical fluctuations, for the different bin sizes.

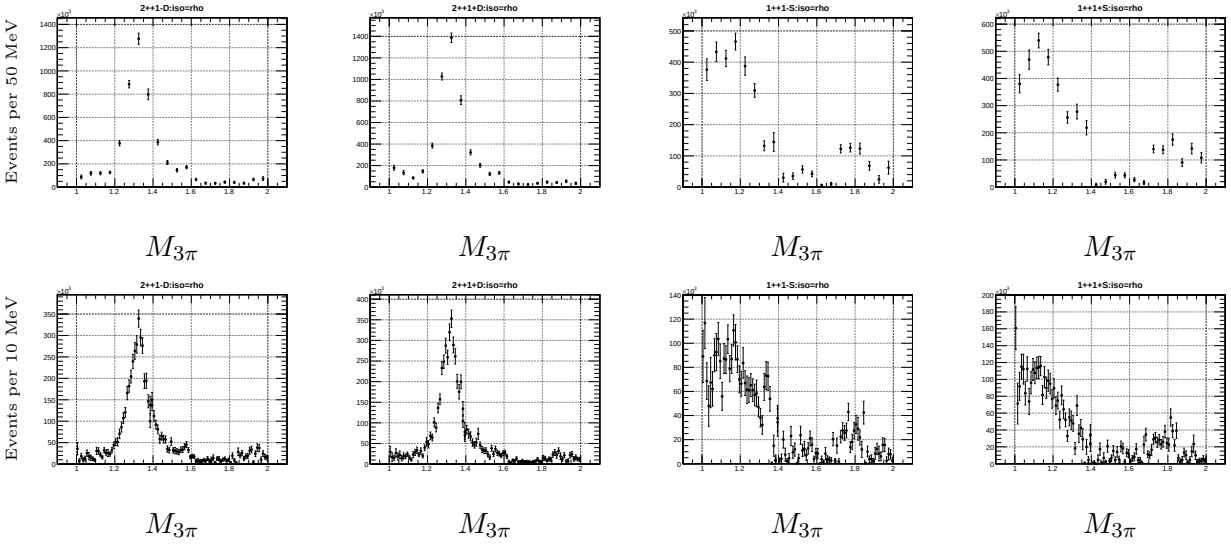

Figure B.1: $\gamma p \to n\pi^+\pi^+\pi^-$: 50 MeV mass bin size was used for the **top** plots and 10 MeV mass bin size for the **bottom** plots. The first two plots show the intensity of the $2^{++}D$ waves and the last two plots show the intensity of the $1^{++}S$ waves.

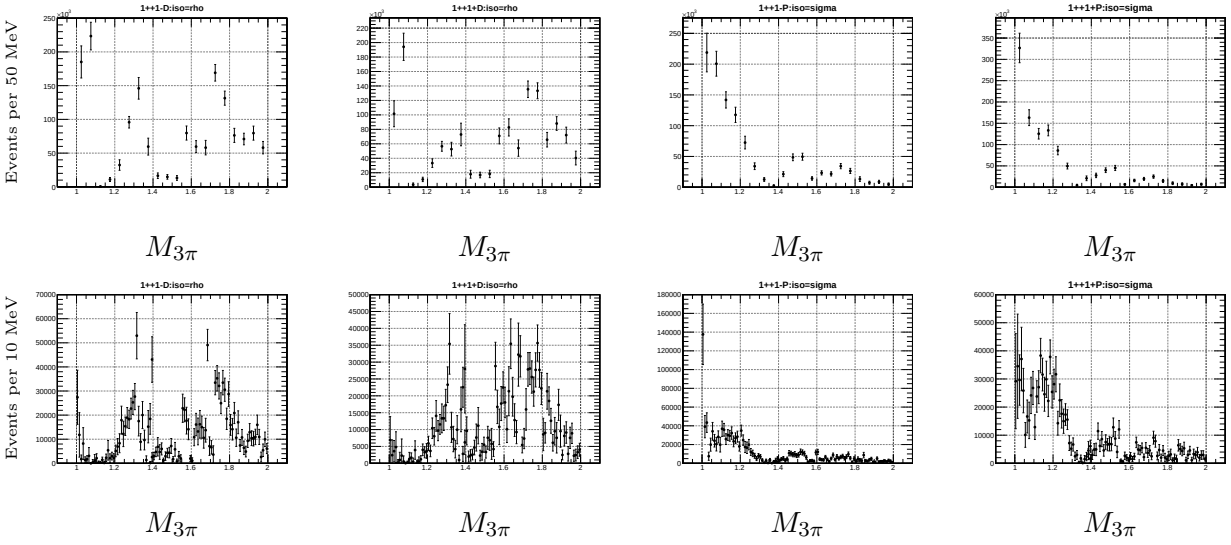

Figure B.2: $\gamma p \to n\pi^+\pi^+\pi^-$: 50 MeV mass bin size was used for the **top** plots and 10 MeV mass bin size for the **bottom** plots. The first two plots show the intensity of the $1^{++}D$ waves and the last two plots show the intensity of the $1^{++}P$ waves.

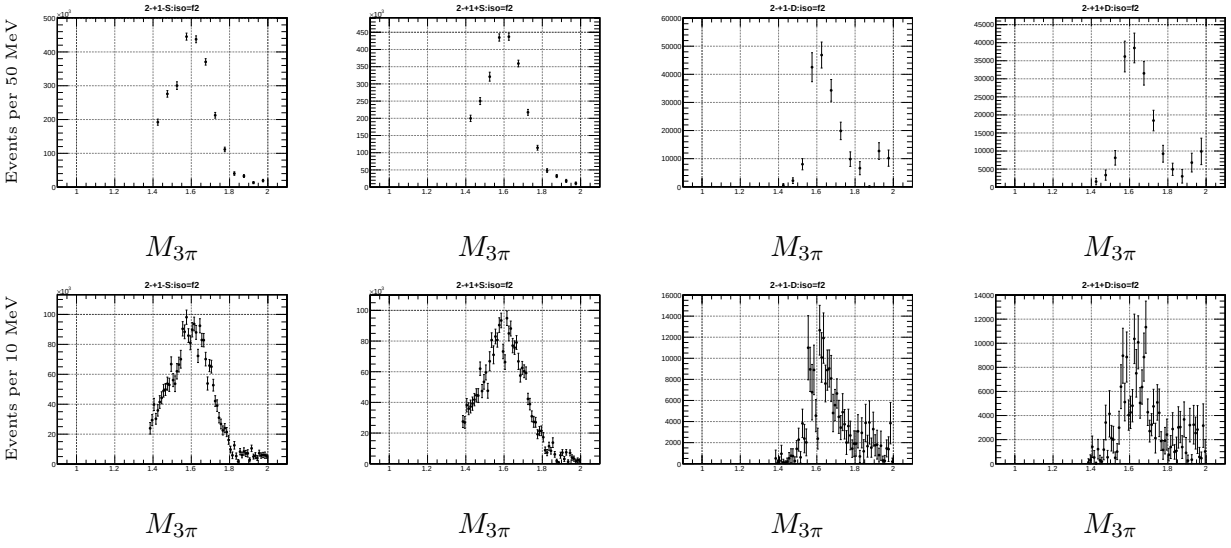

Figure B.3: $\gamma p \to n\pi^+\pi^+\pi^-$: 50 MeV mass bin size was used for the **top** plots and 10 MeV mass bin size for the **bottom** plots. The first two plots show the intensity of the $2^{-+}S$ waves and the last two plots show the intensity of the $2^{-+}D$ waves.

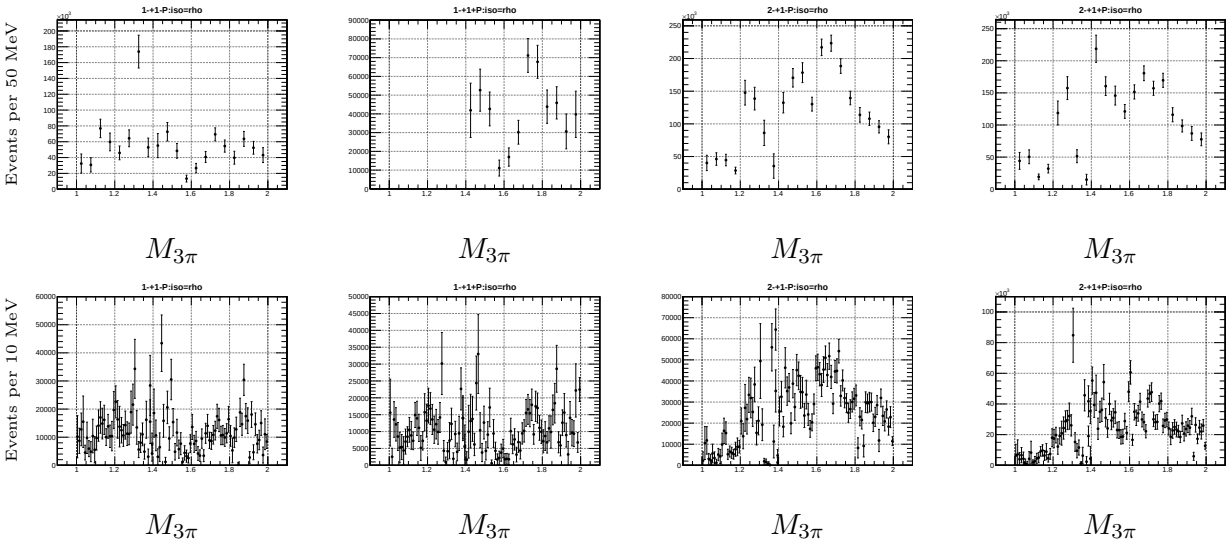

Figure B.4: $\gamma p \to n\pi^+\pi^+\pi^-$: 50 MeV mass bin size was used for the **top** plots and 10 MeV mass bin size for the **bottom** plots. The first two plots show the intensity of the $1^{-+}P$ waves and the last two plots show the intensity of the $2^{-+}P$ waves.

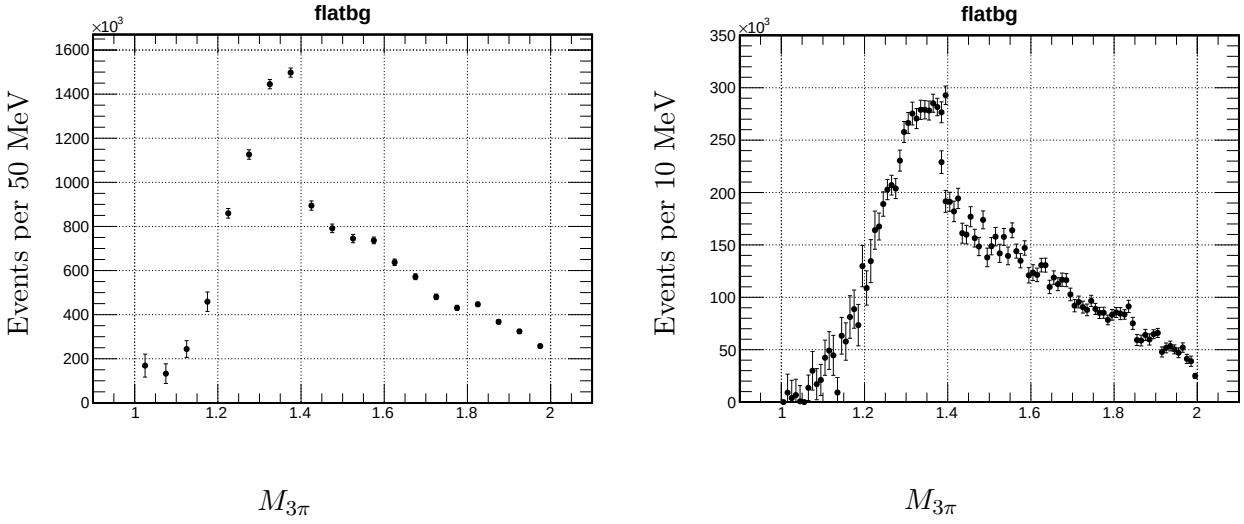

Figure B.5: $\gamma p \to n\pi^+\pi^+\pi^-$: 50 MeV mass bin size was used for the **left** plot and 10 MeV mass bin size for the **right** plot. The plots show the intensity of the isotropic background.

APPENDIX C

FIT RESULTS FOR THE $\gamma p \to n\pi^+\pi^+\pi^-$ REACTION INCLUDING M=2 WAVES.

In this Appendix fit results are shown by adding $2^{++}2D$ waves into the minimum wave-set. As it was discussed before, the better χ^2/DOF values (see Figure C.3) that are shown for this wave-set, compare to the minimum wave-set, is due to better mathematical description rather than better physical description of the data. The $\alpha_2(1320)$ meson decaying into $\omega\rho$ around 10% and into $\rho\pi$ around 70%. This means that we should expect a value between the $2^{++}1D$ and $2^{++}2D$ around 15%. Also since the photon beam composed 10% from ω and our selection criteria enhance one pion exchange we should actually expect a number lesser than 15%. The current fit results show 45% value between the two.

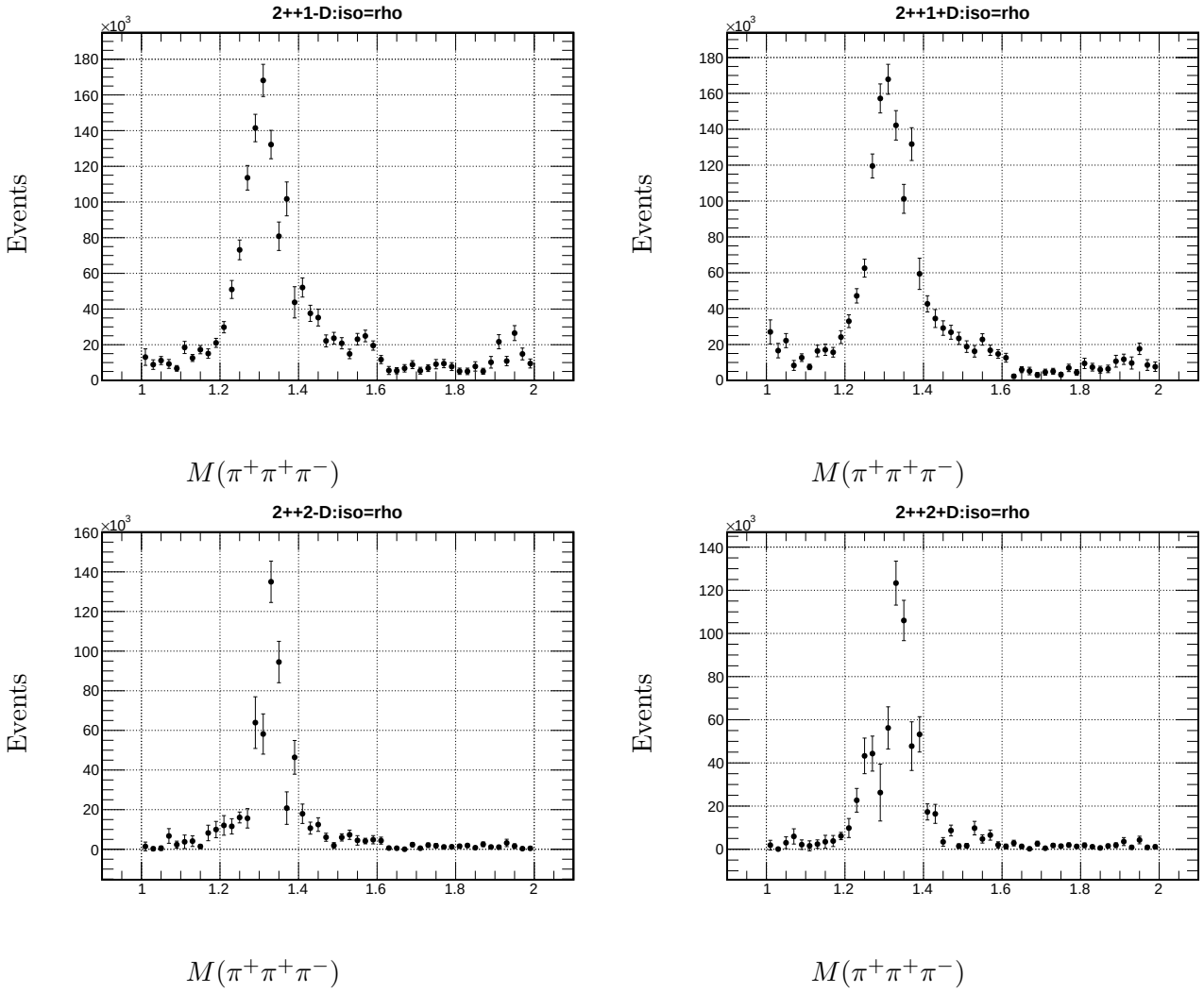

Figure C.1: $\gamma p \to n\pi^+\pi^+\pi^-$: The intensity spectrum of the $2^{++}1^-D[Y = \rho(770)]$ (**top left**), $2^{++}1^+D[Y = \rho(770)]$ (**top right**), $2^{++}2^-D[Y = \rho(770)]$ (**bottom left**) and $2^{++}2^+D[Y = \rho(770)]$ (**bottom right**) partial waves.

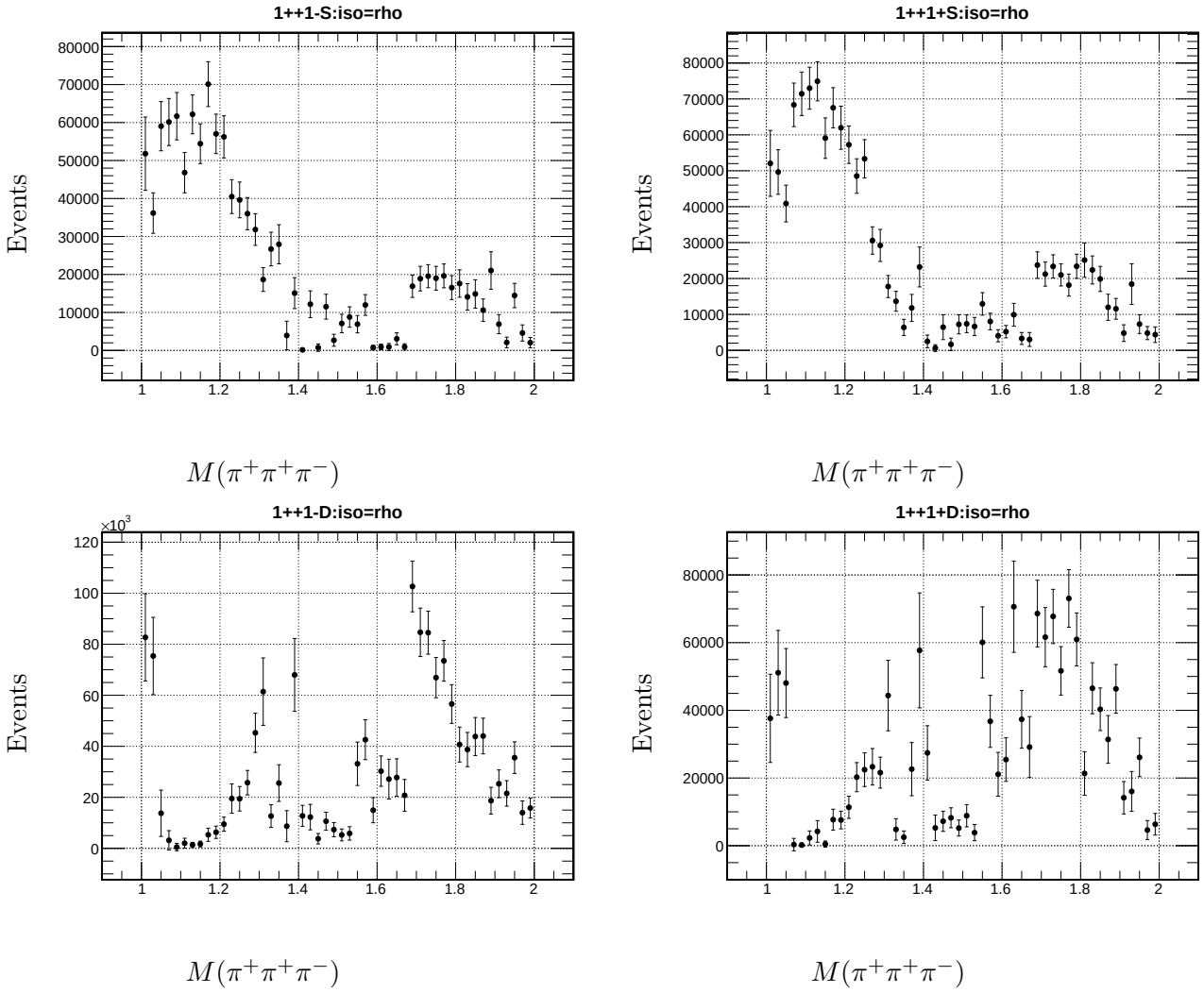

Figure C.2: $\gamma p \to n\pi^+\pi^+\pi^-$: The intensity spectrum of the $1^{++}1^-S[Y = \rho(770)]$ (**top left**), $1^{++}1^+S[Y = \rho(770)]$ (**top right**), $1^{++}1^-D[Y = \rho(770)]$ (**bottom left**) and $1^{++}1^+D[Y = \rho(770)]$ (**bottom right**) partial waves.

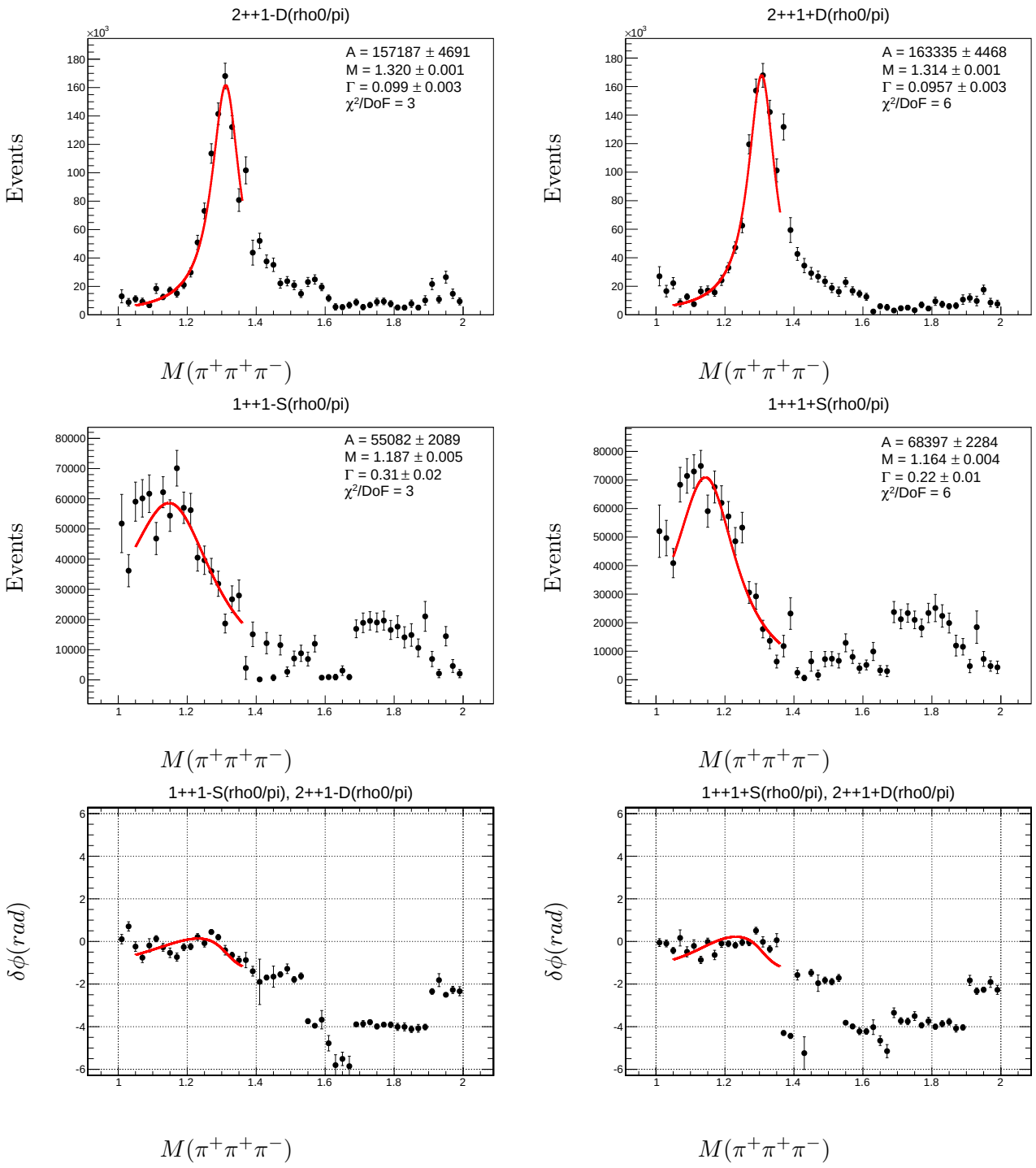

Figure C.3: $\gamma p \rightarrow n\pi^+\pi^+\pi^-$: The **first column** is a mass-dependent fit of the $1^{++}1^-S[Y = \rho(770)]$ intensity, $2^{++}1^-D[Y = \rho(770)]$ intensity and their phase difference.. The **second column** is a mass-dependent fit of the $1^{++}1^+S[Y = \rho(770)]$ intensity, $2^{++}1^+D[Y = \rho(770)]$ intensity and their phase difference.

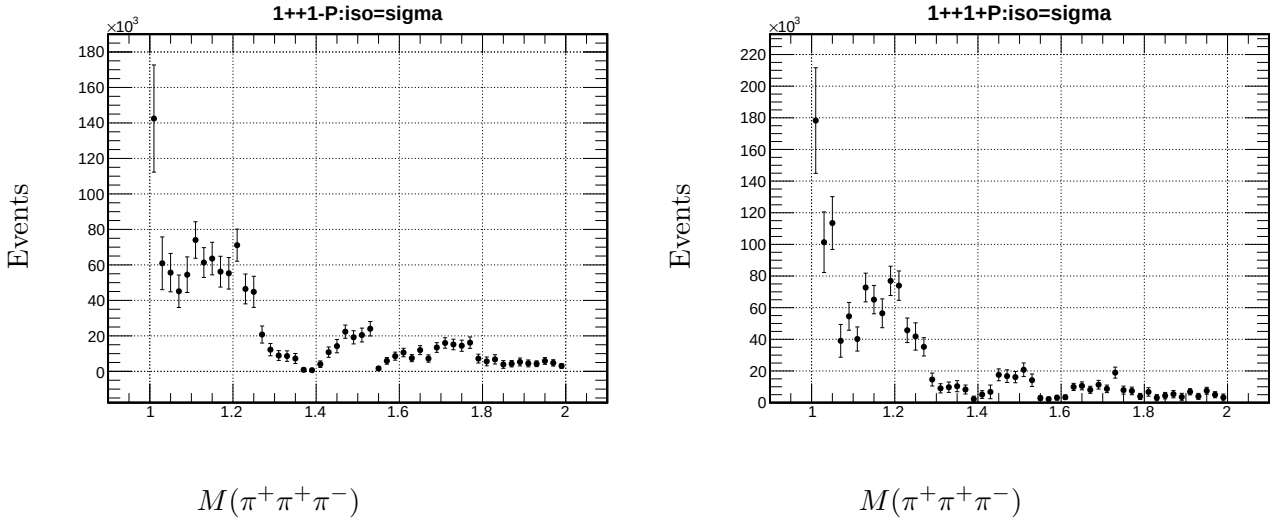

Figure C.4: $\gamma p \to n\pi^+\pi^+\pi^-$: The intensity spectrum of the $1^{++}1^-P[Y=\sigma]$ (**left**) and $1^{++}1^+P[Y=\sigma]$ (**right**) partial waves.

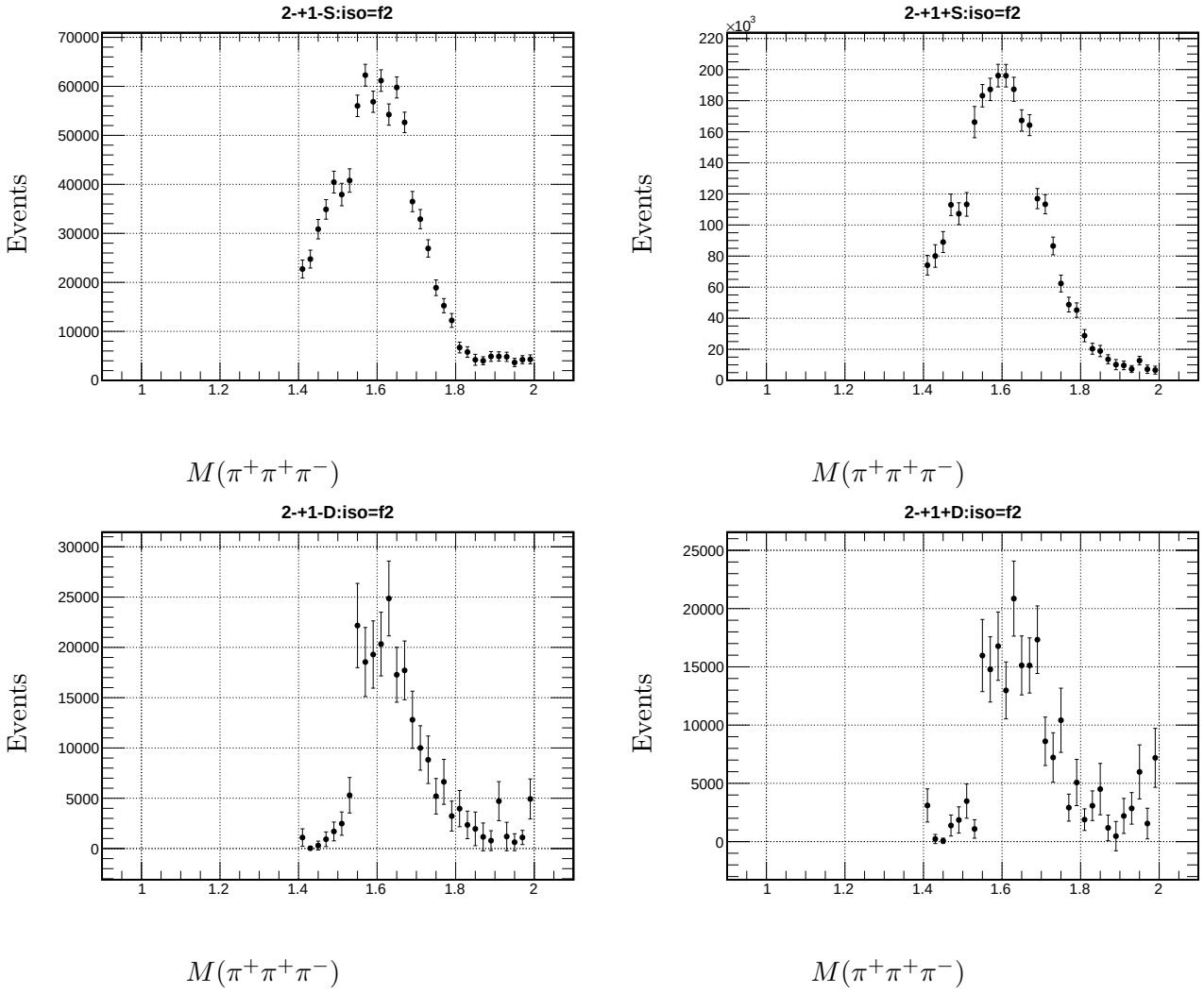

Figure C.5: $\gamma p \to n\pi^+\pi^+\pi^-$: The intensity spectrum of the $2^{-+}1^-S[Y = f_2(1270)]$ (**top left**), $2^{-+}1^+S[Y = f_2(1270)]$ (**top right**), $2^{-+}1^-D[Y = f_2(1270)]$ (**bottom left**) and $2^{-+}1^+D[Y = f_2(1270)]$ (**bottom right**) partial waves.

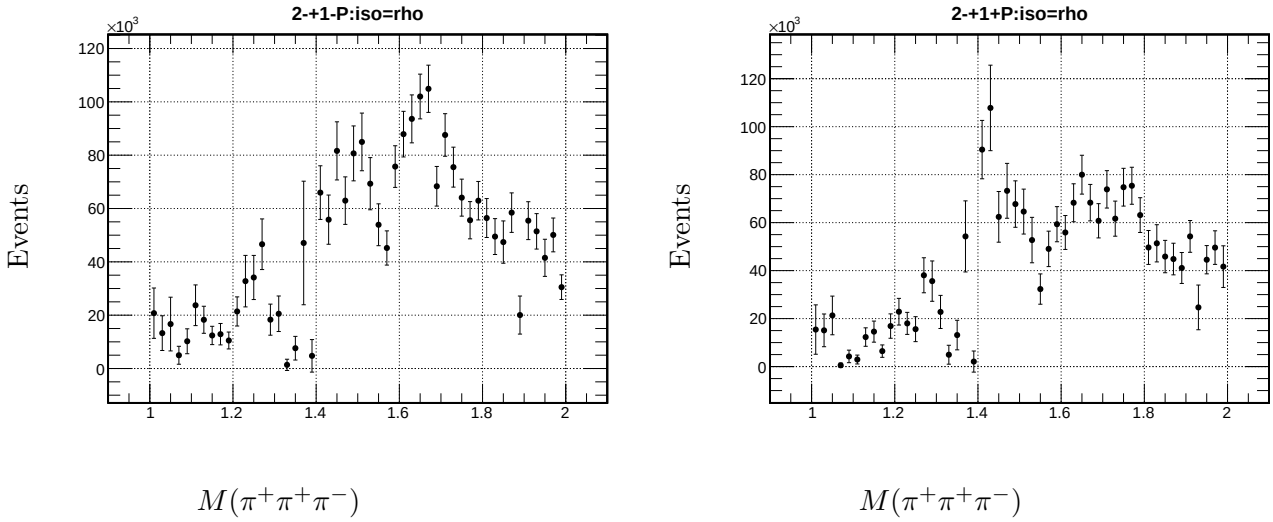

Figure C.6: $\gamma p \to n\pi^+\pi^+\pi^-$: The intensity spectrum of the $2^{-+}1^-P[Y = \rho(770)]$ and $2^{-+}1^+P[Y = \rho(770)]$ partial waves.

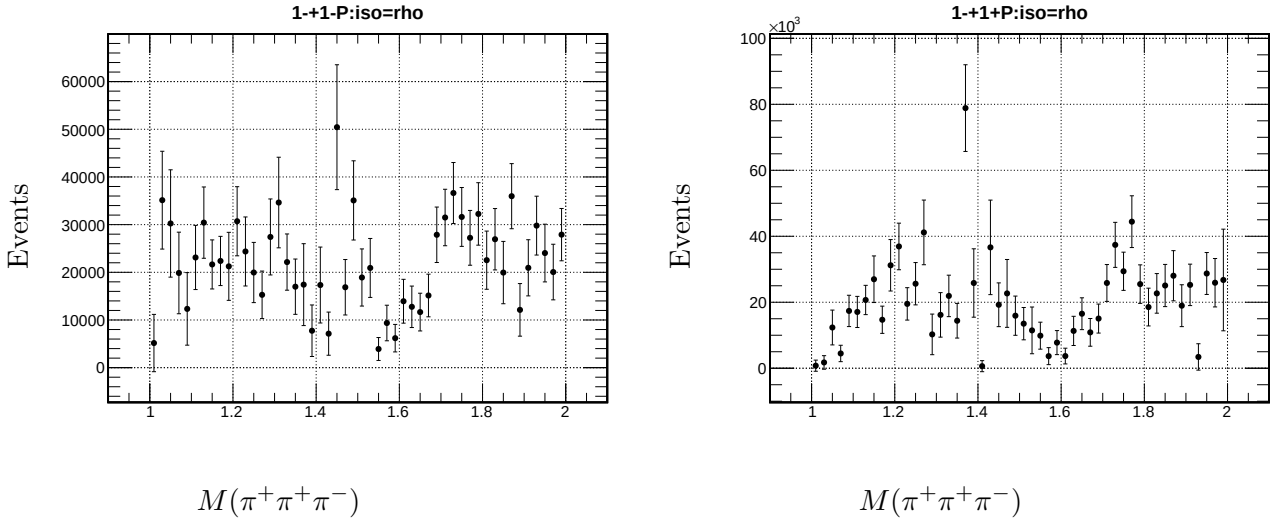

Figure C.7: $\gamma p \to n\pi^+\pi^+\pi^-$: The intensity spectrum of the $1^{-+}1^-P[Y = \rho(770)]$ and $1^{-+}1^+P[Y = \rho(770)]$ partial waves.

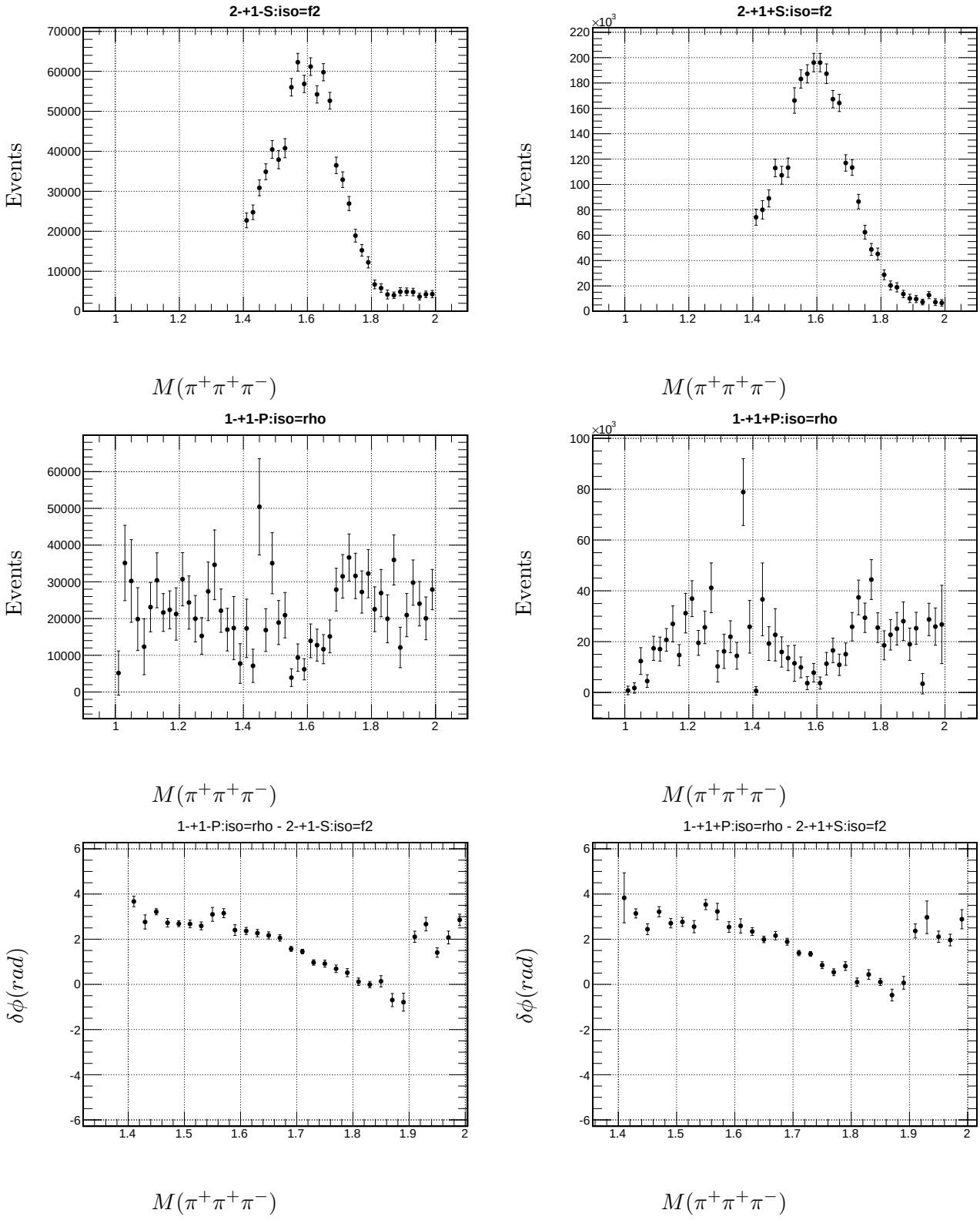

Figure C.8: $\gamma p \to n\pi^+\pi^+\pi^-$:

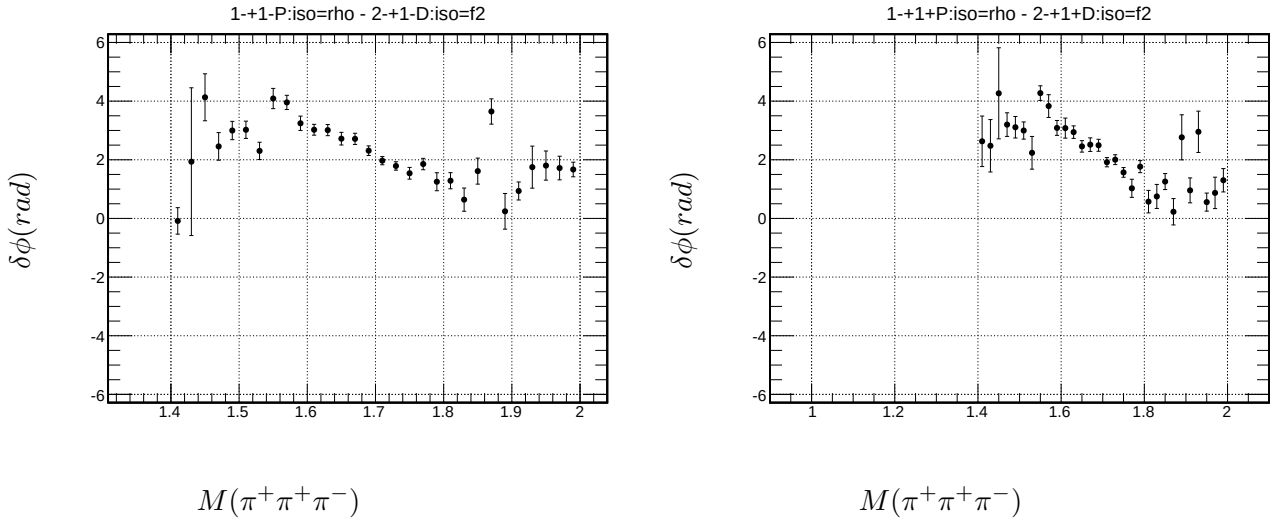

Figure C.9: $\gamma p \to n\pi^+\pi^+\pi^-$: Phase difference between the $1^{-+}1^-P[Y = \rho(770)]$ wave and the $2^{-+}1^-D[Y = f_2(1270)]$ wave for negative (**left**) and positive (**right**) reflectivity.

APPENDIX D

SYSTEMATIC EFFECTS FROM THE SELECTION CRITERIA FOR THE $\gamma p \to n\pi^+\pi^+\pi^-$ REACTION

We examine the dependence of our fit results by varying the range of the t' and $\theta_{lab}[\pi^+]$ selection. Specifically, the values 35^0, 55^0, 90^0 where tested for the $\theta_{lab}[\pi^+_{slow}]$ cut. For the t' cut the values 1.0, 0.5. 0.25 and 1.175 GeV^2/c^4 were tested as well as a fit was done without any t' selection. Finally, the nominal fiducial cuts were tested as described in [54]. The GPP program appears to have better efficiency than the data for some regions of the detector and with the fiducial cuts those regions are rejected.

D.1 $1^{-+}[\rho(770)\pi]_P$

In Figures D.1 and D.2 one can see the intensity spectrum for the exotic $1^{-+}P$ wave. By opening the θ_{lab} cut there is no significant difference for this wave. By opening the t' cut also there is no major discrepancy up to 1.0 GeV^2/c^4. After this value, as it was showed in the event selection Chapter, a lot of baryon background is leaking in and so it is unlikely this peak to be due to meson resonance. Also the fit with the nominal fiducial cut so similar results for the minimum fit.

D.2 $1^{++}[\rho(770)\pi]_D$

In Figures D.3 and D.4 one can see the intensity spectrum for the $1^{++}D$ wave. In all selection the leakage from the $\alpha_2(1320)$ meson is always present. Also as we open the θ_{lab} cut the peak at 1.8 GeV is been reduced. As we open the t' cut we do not see much difference, from the minimum selections, up to 1.0 GeV^2/c^4 where significant baryon resonances are leaking in. Also there is no significant difference for the fiducial-cut-fit, for this wave.

D.3 $1^{++}[\sigma\pi]_P$

In Figures D.5 and D.6 one can see the intensity spectrum for the $1^{++}P$ wave. There is no difference by opening the θ_{lab} cut. Furthermore, as we open the t' cut up to 1.0 GeV^2/c^4, there is

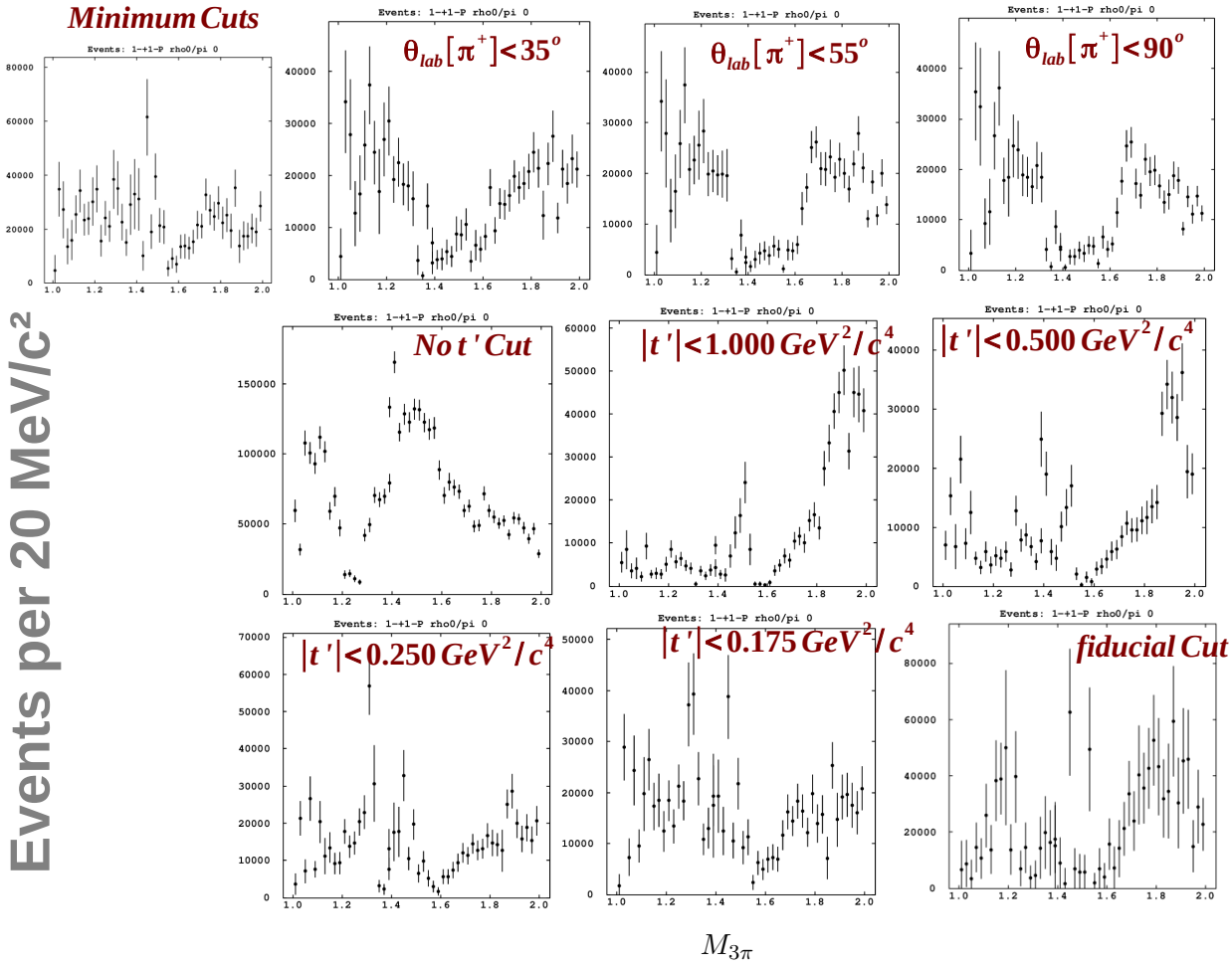

Figure D.1: $\gamma p \rightarrow n\pi^+\pi^+\pi^-$: $1^{-+}1^-P$ intensities for various selection criteria. The specific selection that is applied is labeled in each plot separately. The minimum represents the cuts that are in the PWA results Chapter.

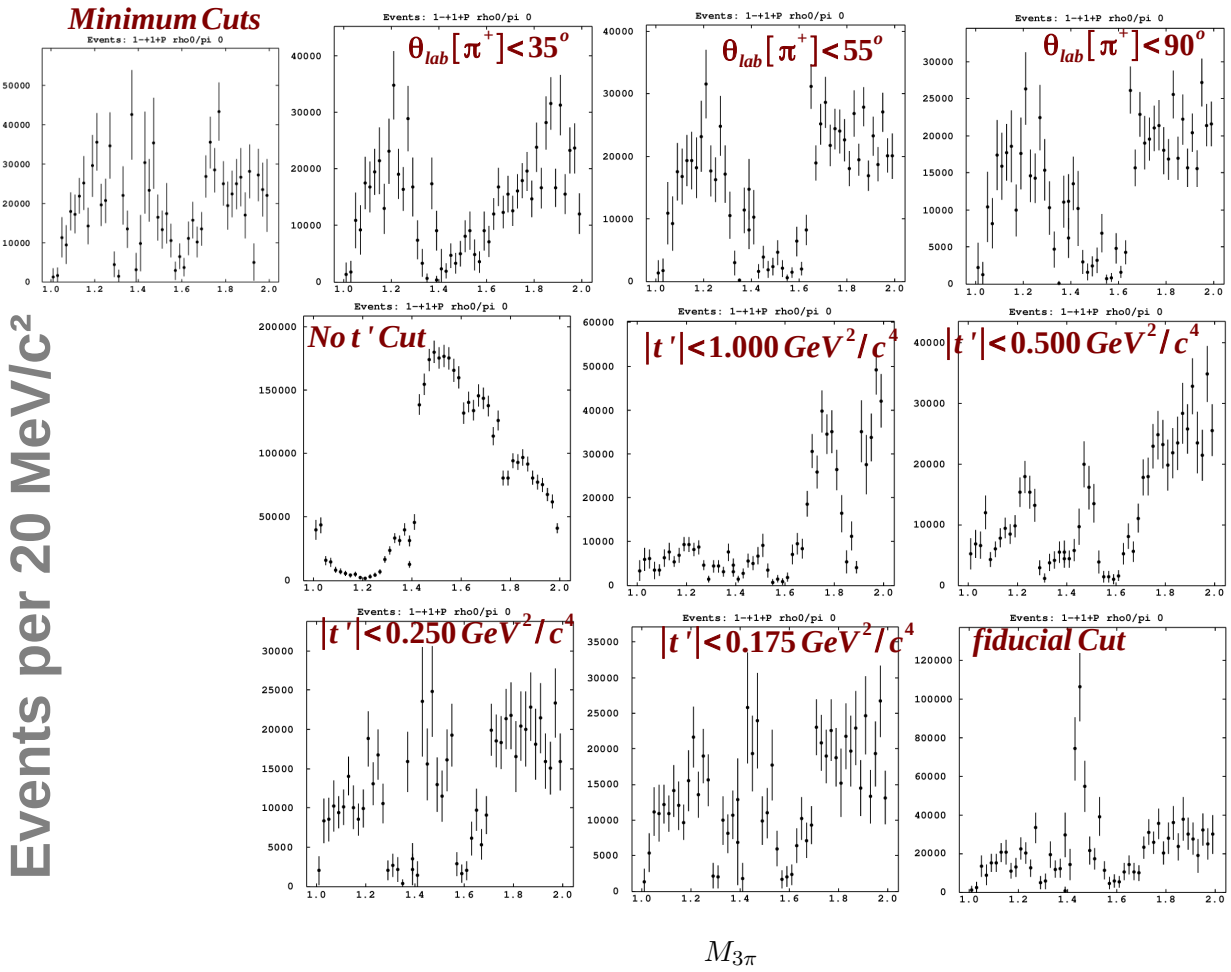

Figure D.2: $\gamma p \to n\pi^+\pi^+\pi^-$: $1^{-+}1^+P$ intensities for various selection criteria. The specific selection is labeled in each plot separately.

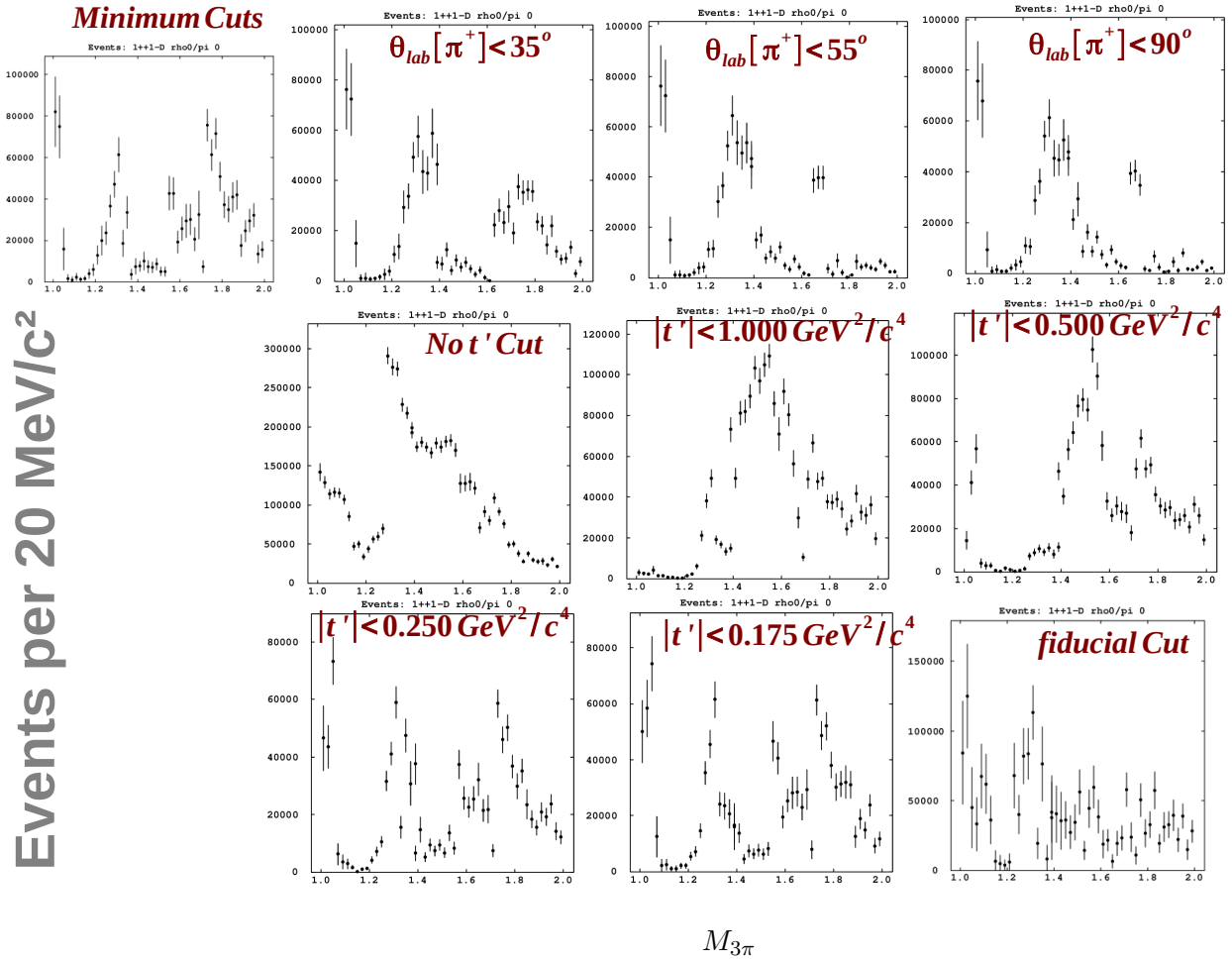

Figure D.3: $\gamma p \rightarrow n\pi^+\pi^+\pi^-$: $1^{++}1^-D$ intensities for various selection criteria. The specific selection that is applied is labeled in each plot separately. The minimum represents the cuts that are in the PWA results Chapter.

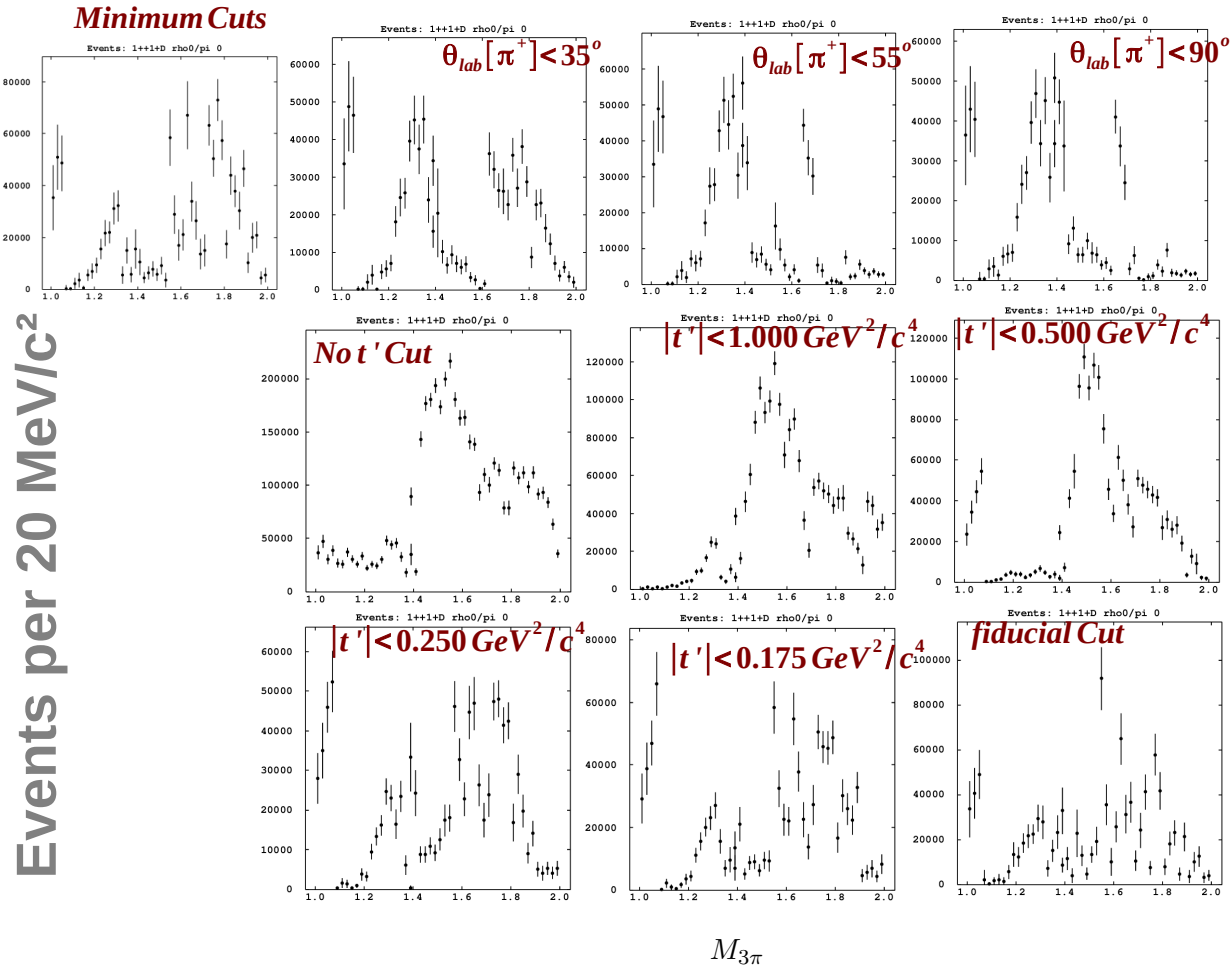

Figure D.4: $\gamma p \rightarrow n\pi^+\pi^+\pi^-$: $1^{++}1^+D$ intensities for various selection criteria. The specific selection that is applied is labeled in each plot separately. The minimum represents the cuts that are in the PWA results Chapter.

no significant difference. Above that region baryon background is leaking in and the difference is significant. Also there is no difference for this wave between the minimum cuts and adding fiducial cut.

D.4 $1^{++}[\rho(770)\pi]_S$

In Figures D.7 and D.8 one can see the intensity spectrum for the $1^{++}S$ wave. We do not see much difference between minimum and fiducian-cut fit. On the other hand when we open the θ_{lab} cut the major peak at 1.2 GeV remains the same, but a peak starts to appear at 1.5 GeV as events from backward angles are coming in. Also no major difference by opening the t' cut, up to 1.0 GeV^2/c^4 where at that region the $1^{++}S$ seems to take all the 3π mass spectrum.

D.5 $2^{-+}[f_2(1270)\pi]_D$

In Figures D.9 and D.10 one can see the intensity spectrum for the $2^{-+}D$ wave. As we open the θ_{lab} cut apart from the peak at 1.65 GeV there is another peak that is coming in at 1.9 GeV. Also more significant, it can be seen that the intensity of the $2^{-+}D$ wave is not as strong as in the minimum selection. This is consistent in both reflectivities and it might be an indication that the 3π mass is not as clean as it is in the tight θ_{lab} cut, and events are pushed more likely in the background. Also, we do see small difference between the fiducial cut fit and the minimum selection. Specifically, even though both intensity spectrum's seem to be similar strong, the resonance appears to be narrower and it is fluctuated more. The fluctuations are more likely because the number of events is smaller, but we kept the same bin size, 20 MeV. Also the t' selection seems to give wider resonance from 0.5 GeV^2/c^4 and above.

D.6 $2^{-+}[\rho(770)\pi]_P$

In Figures D.11 and D.12 one can see the intensity spectrum for the $2^{-+}P$ wave. Between the fit from the fiducial selection and the minimum selection, we do not see difference in the shapes that are present in the spectrum, but we it seems that for the former the $2^{-+}P$ wave appears to be stronger. Also as we open the θ_{lab} cut the leakage from the $\alpha_2(1320)$ meson seem to be reduced. The difference in the t' selection region does not show any significant difference from the minimum selection.

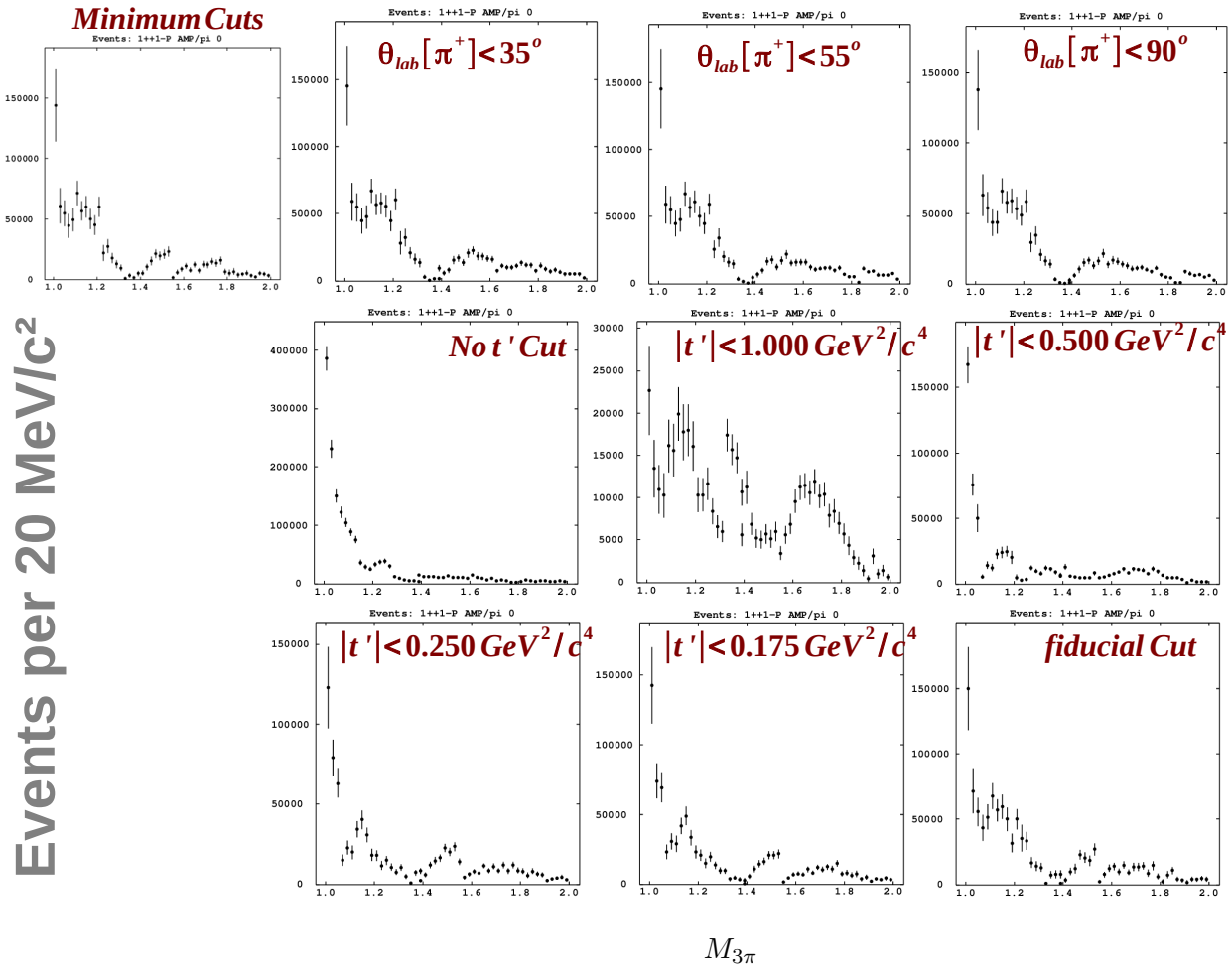

Figure D.5: $\gamma p \to n\pi^+\pi^+\pi^-$: $1^{++}1^-P$ intensities for various selection criteria. The specific selection that is applied is labeled in each plot separately. The minimum represents the cuts that are in the PWA results Chapter.

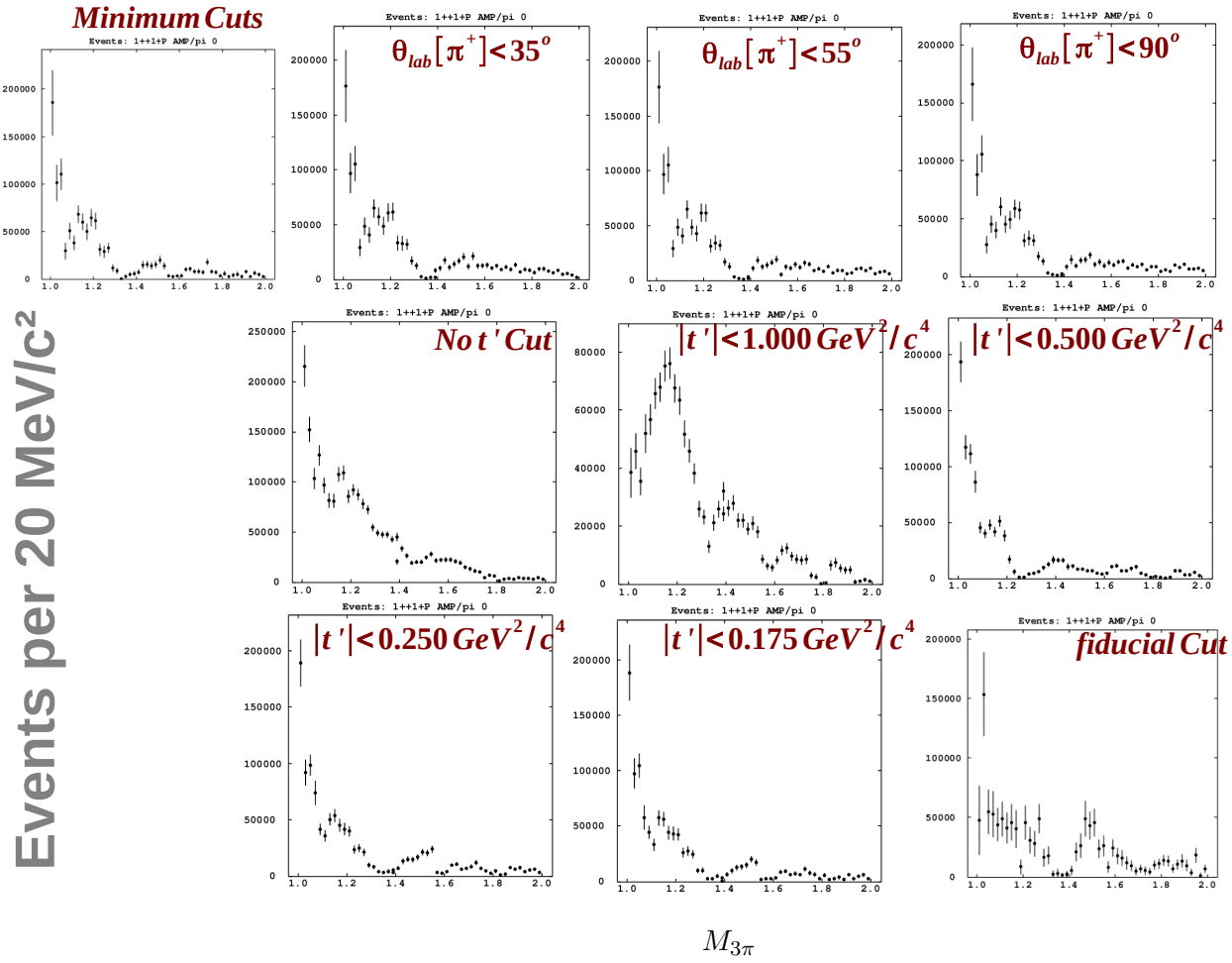

Figure D.6: $\gamma p \rightarrow n\pi^+\pi^+\pi^-$: $1^{++}1^+P$ intensities for various selection criteria. The specific selection that is applied is labeled in each plot separately. The minimum represents the cuts that are in the PWA results Chapter.

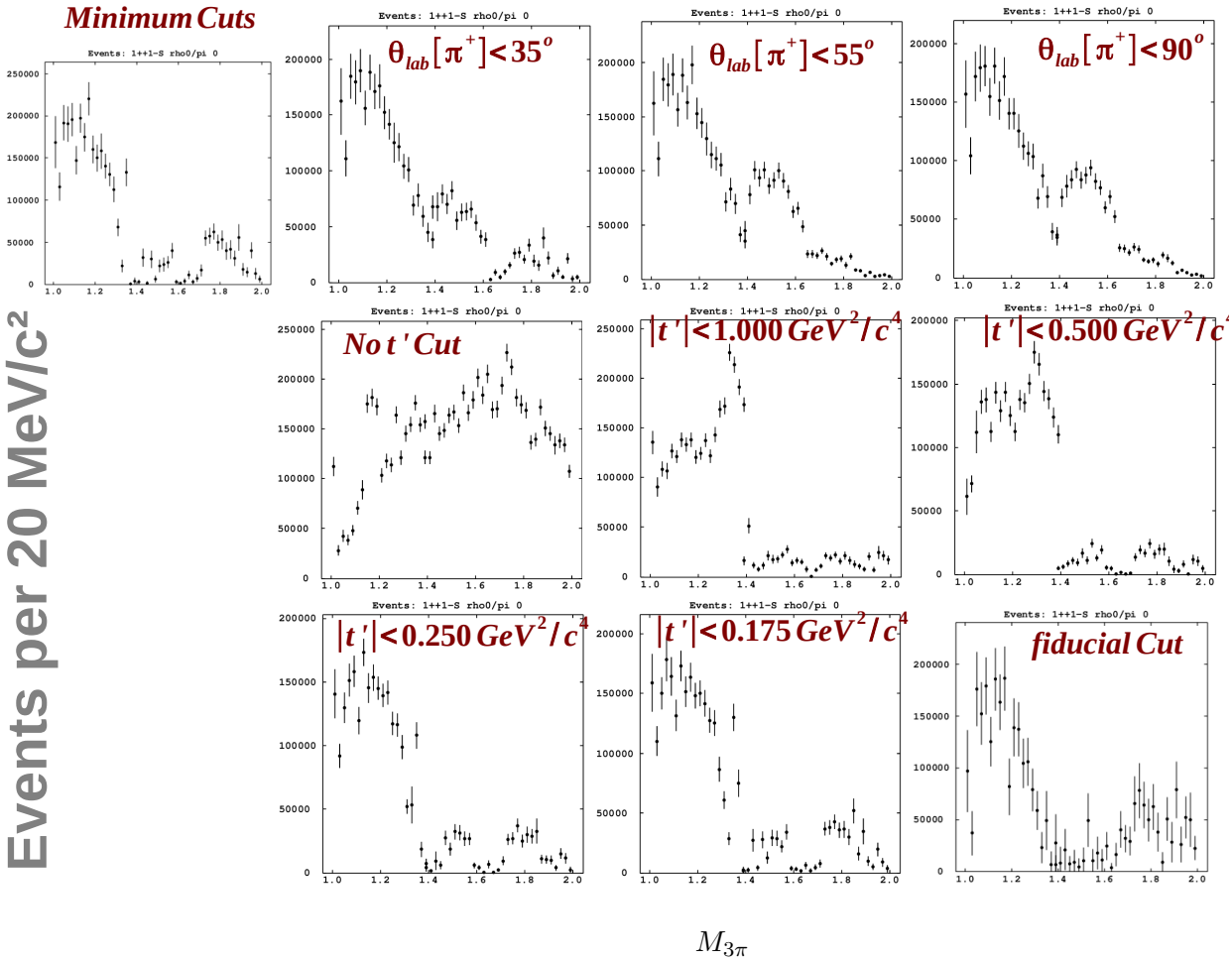

Figure D.7: $\gamma p \to n\pi^+\pi^+\pi^-$: $1^{++}1^-S$ intensities for various selection criteria. The specific selection that is applied is labeled in each plot separately. The minimum represents the cuts that are in the PWA results Chapter.

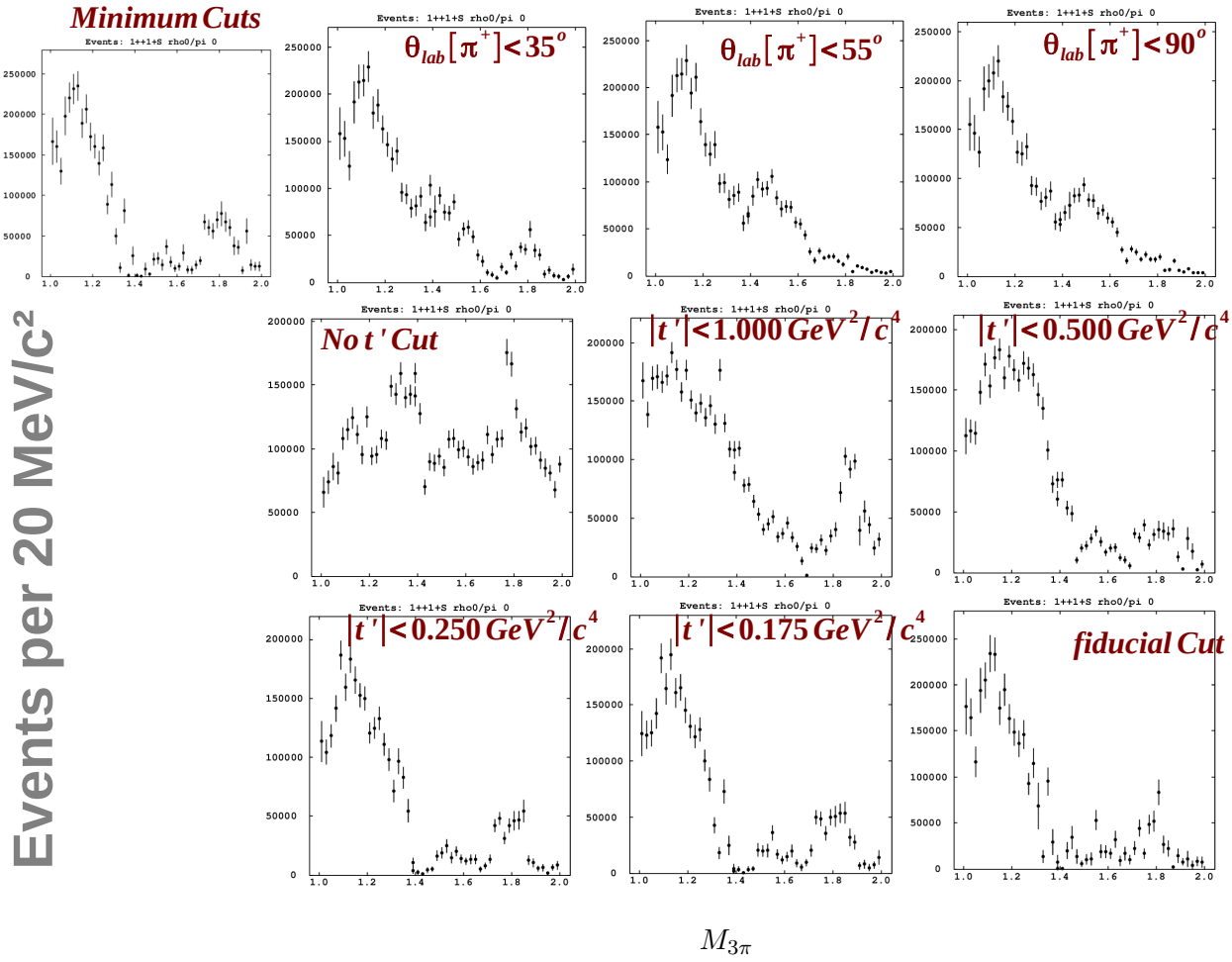

Figure D.8: $\gamma p \to n\pi^+\pi^+\pi^-$: $1^{++}1^+S$ intensities for various selection criteria. The specific selection that is applied is labeled in each plot separately. The minimum represents the cuts that are in the PWA results Chapter.

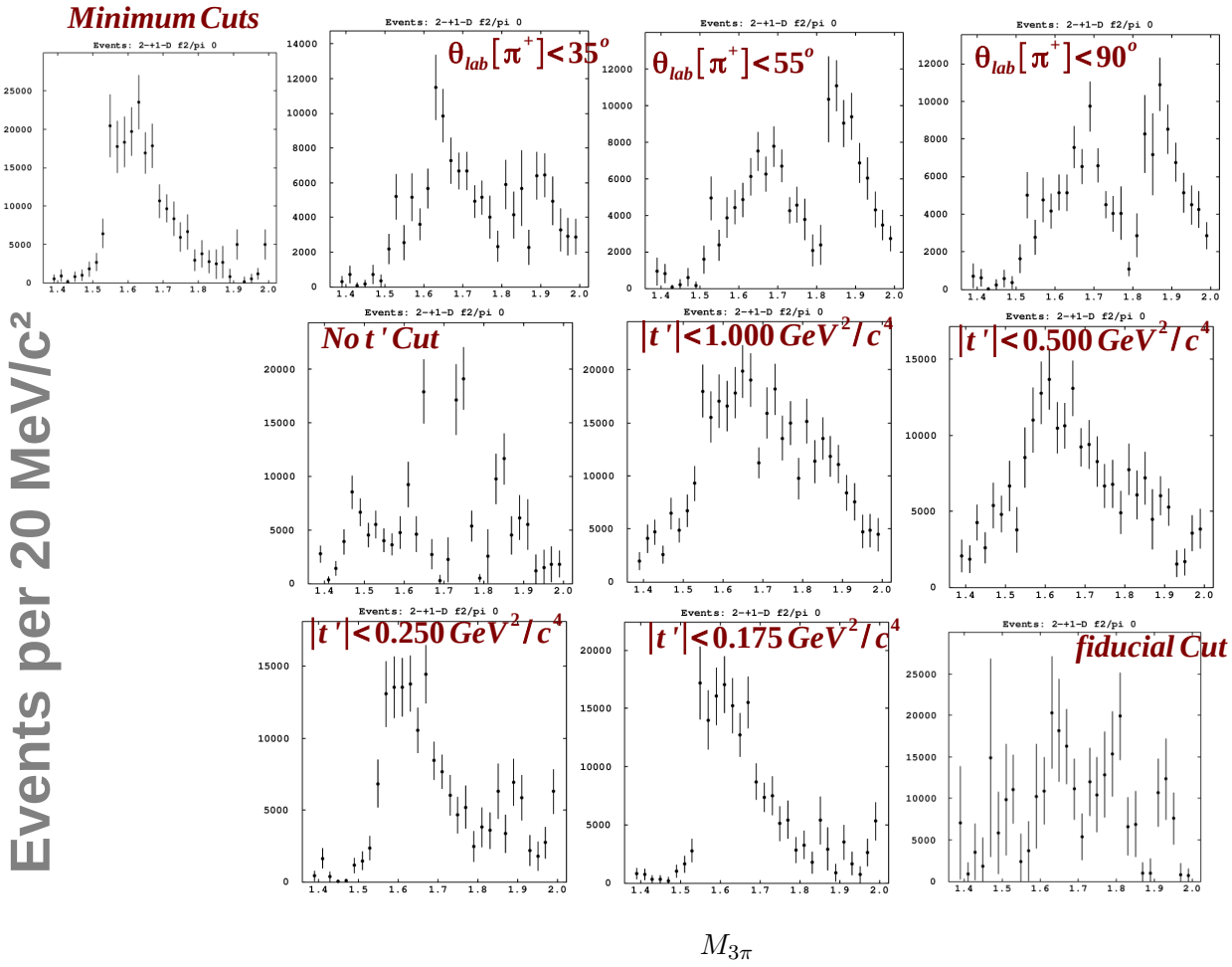

Figure D.9: $\gamma p \rightarrow n\pi^+\pi^+\pi^-$: $2^{-+}1^-D$ intensities for various selection criteria. The specific selection that is applied is labeled in each plot separately. The minimum represents the cuts that are in the PWA results Chapter.

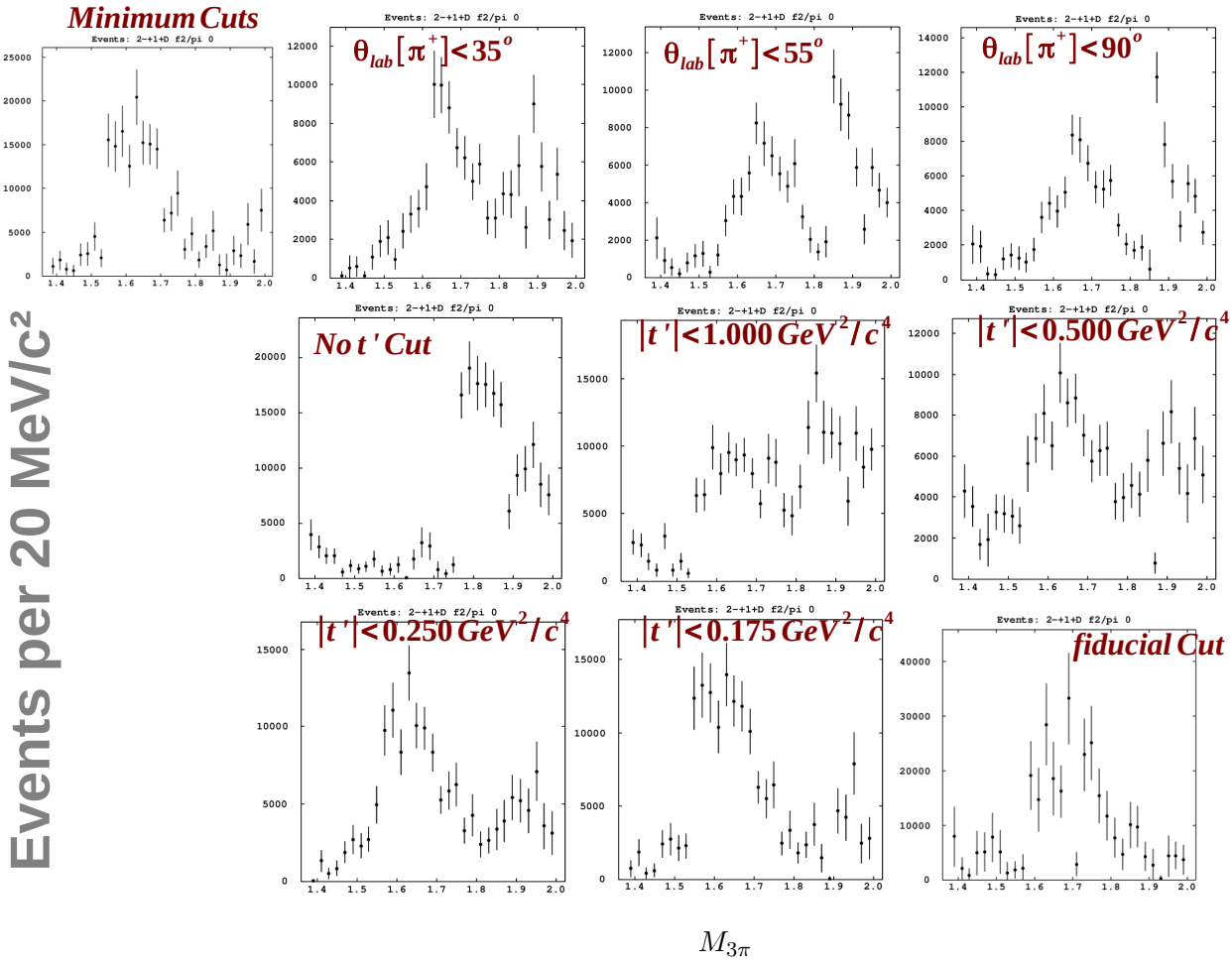

Figure D.10: $\gamma p \to n\pi^+\pi^+\pi^-$: $2^{-+}1^+D$ intensities for various selection criteria. The specific selection that is applied is labeled in each plot separately. The minimum represents the cuts that are in the PWA results Chapter.

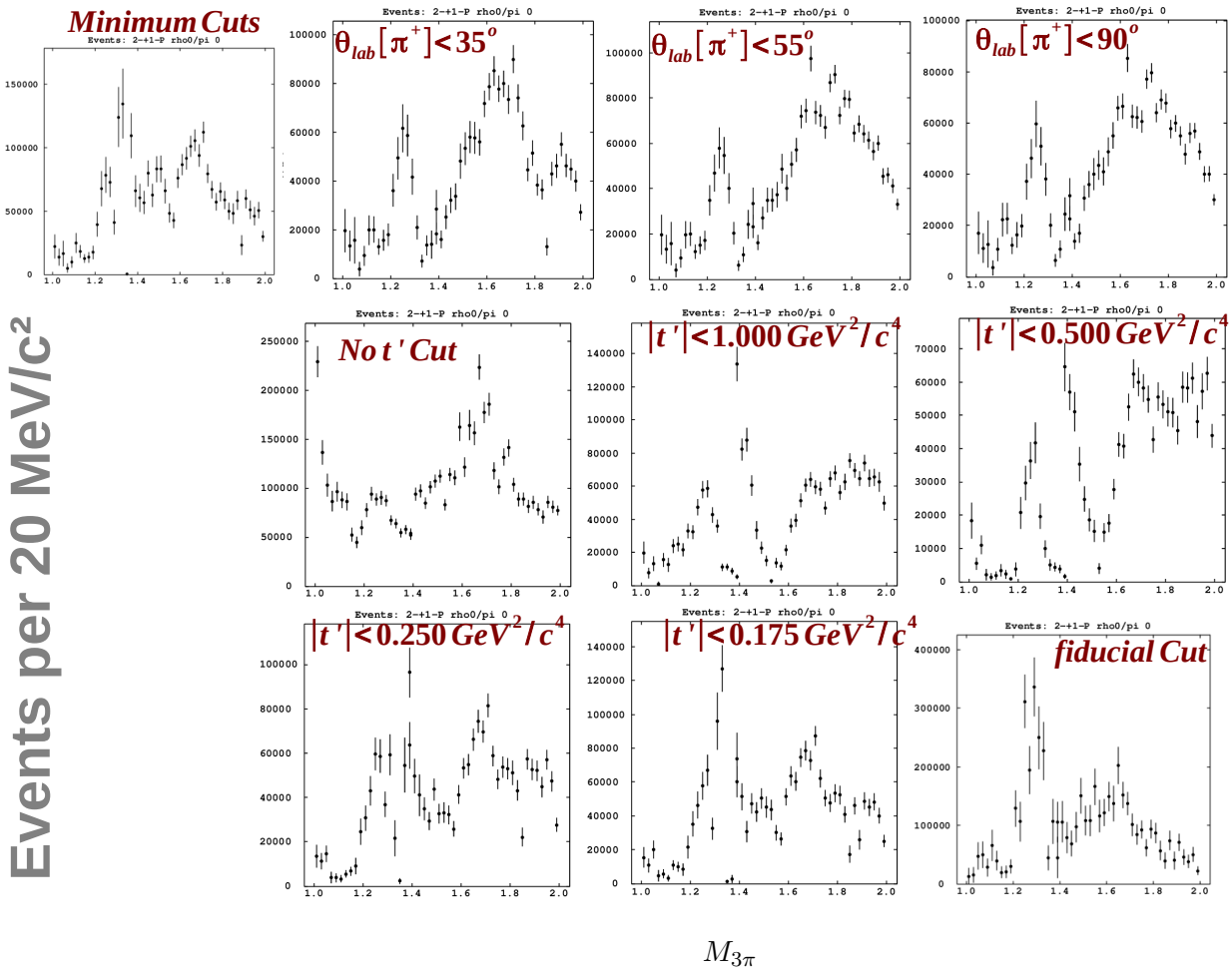

Figure D.11: $\gamma p \to n\pi^+\pi^+\pi^-$: $2^{-+}1^-P$ intensities for various selection criteria. The specific selection that is applied is labeled in each plot separately. The minimum represents the cuts that are in the PWA results Chapter.

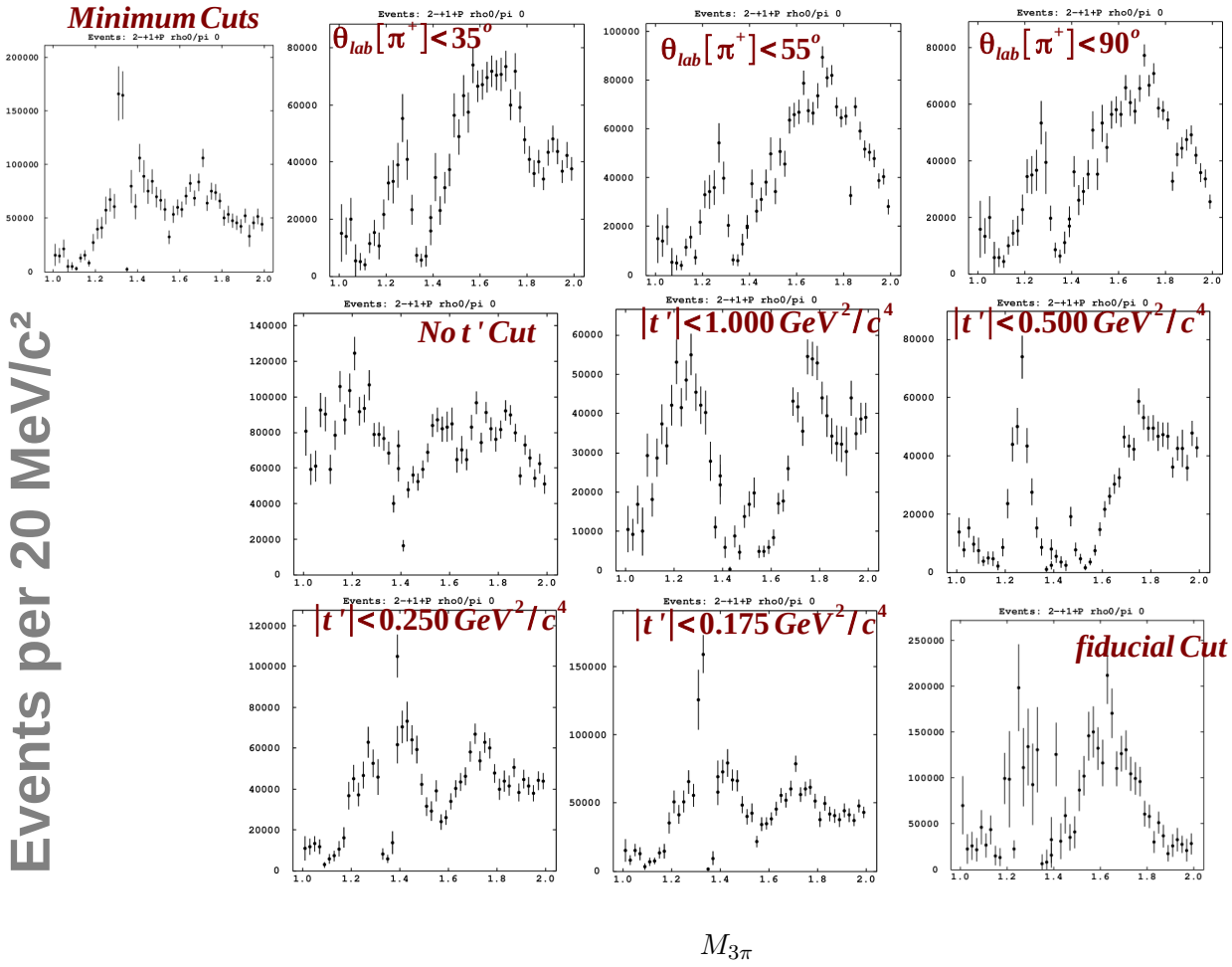

Figure D.12: $\gamma p \to n\pi^+\pi^+\pi^-$: $2^{-+}1^+P$ intensities for various selection criteria. The specific selection that is applied is labeled in each plot separately. The minimum represents the cuts that are in the PWA results Chapter.

D.7 $2^{-+}[f_2(1270)\pi]_S$

In Figures D.13 and D.13 one can see the intensity spectrum for the $2^{-+}S$ wave. For this major wave in the region there is no significant difference among different selections apart when there is no t' cut at all. Even the number of events in intensity spectrum among different selections seems to be similar.

D.8 $2^{++}[\rho(770)\pi]_D$

In Figures D.15 and D.15 one can see the intensity spectrum for the $2^{++}D$ wave. There is no difference in the fit results between the minimum selection and the fiducial cuts. Also, by opening the θ_{lab} cut the major peak stays the same, but the small peaks at 1.5 and 1.9 GeV disappear. By opening the t' cut the number of events in the intensity spectrum seems to be dropping and the $2^{++}D$ resonance is becoming wider.

D.9 Isotropic Background

In Figure D.17 one can see the intensity spectrum for the isotropic wave. We do not see any difference in the intensity spectrum's between the minimum selection, fiducial cut, or by opening the θ_{lab} cut. On the other hand, as the we open the t' selection, we see that the intensity of the isotropic background to be increased for the high 3π mass region. This is another indication that with the t' selection actually cut background events in the high 3π mass region.

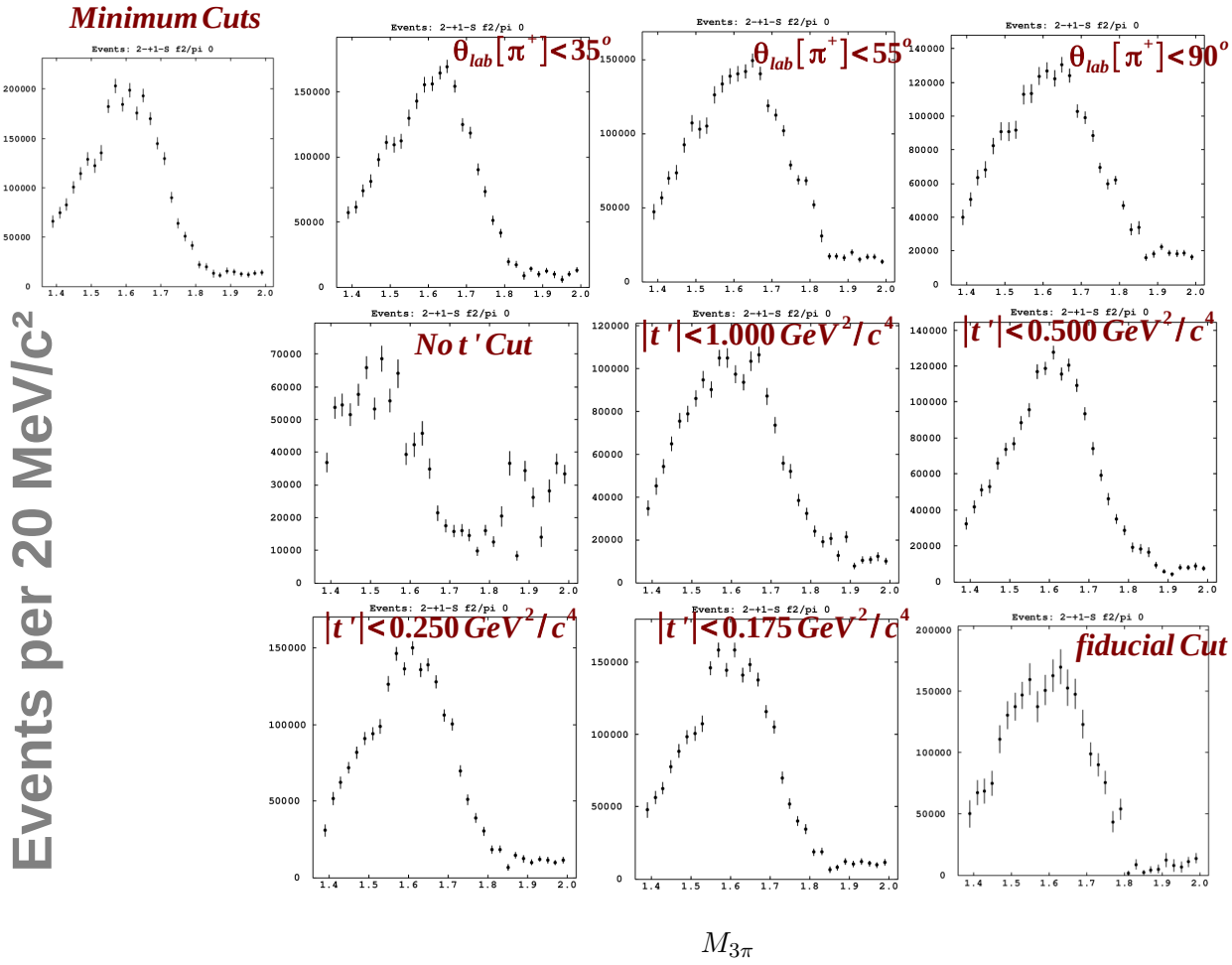

Figure D.13: $\gamma p \to n\pi^+\pi^+\pi^-$: $2^{-+}1^-S$ intensities for various selection criteria. The specific selection that is applied is labeled in each plot separately. The minimum represents the cuts that are in the PWA results Chapter.

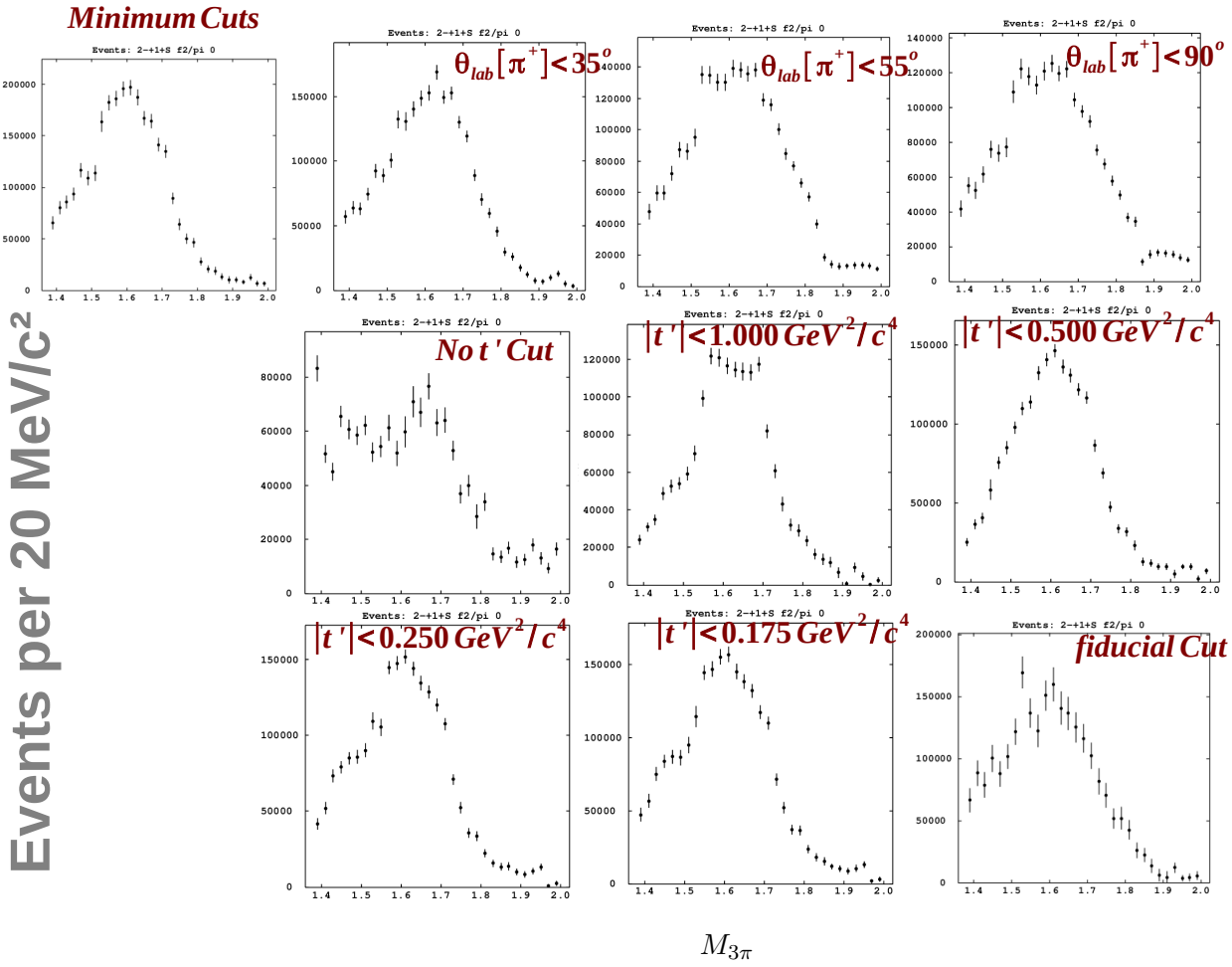

Figure D.14: $\gamma p \to n\pi^+\pi^+\pi^-$: $2^{-+}1^+S$ intensities for various selection criteria. The specific selection that is applied is labeled in each plot separately. The minimum represents the cuts that are in the PWA results Chapter.

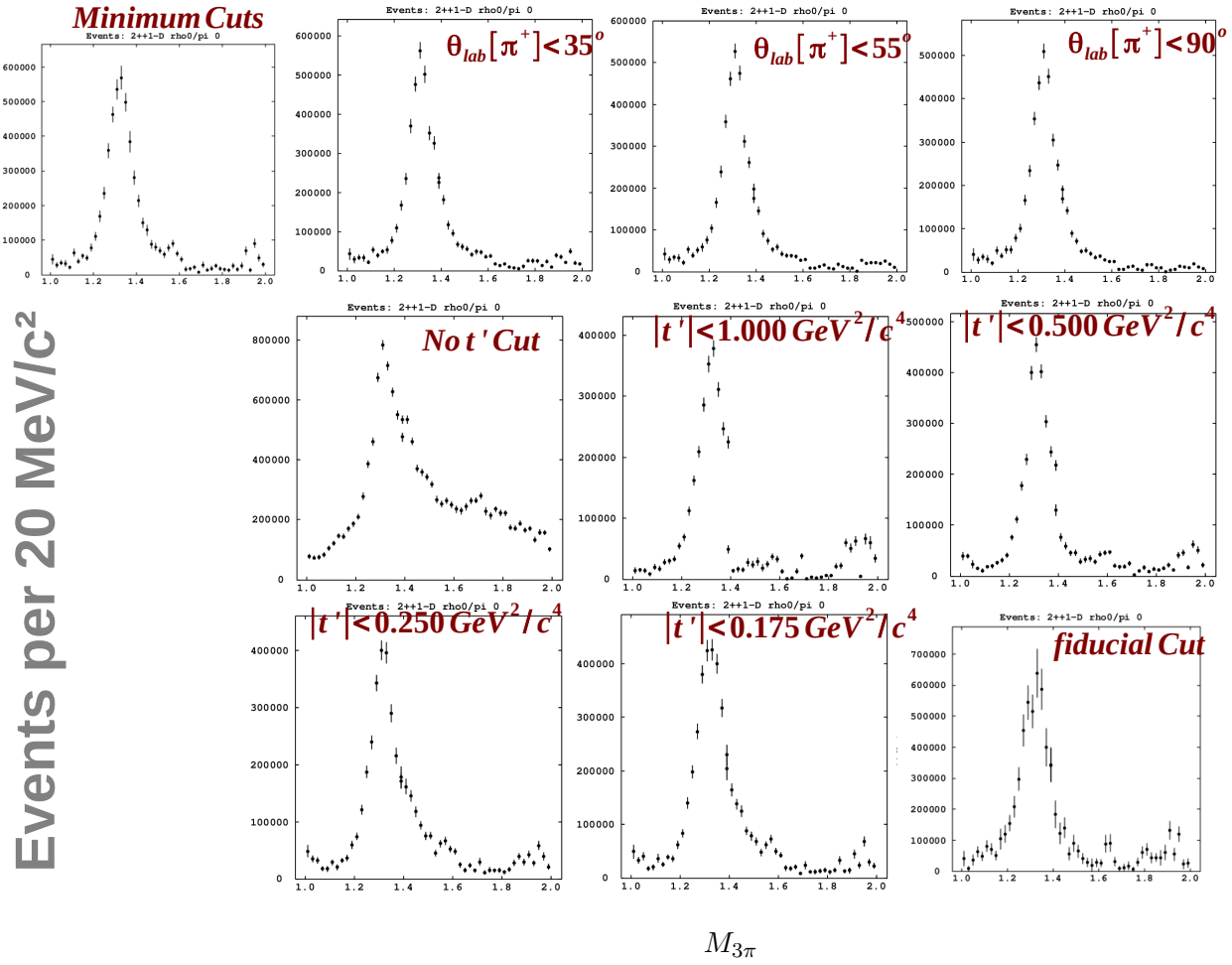

Figure D.15: $\gamma p \to n\pi^+\pi^+\pi^-$: $2^{++}1^-D$ intensities for various selection criteria. The specific selection that is applied is labeled in each plot separately. The minimum represents the cuts that are in the PWA results Chapter.

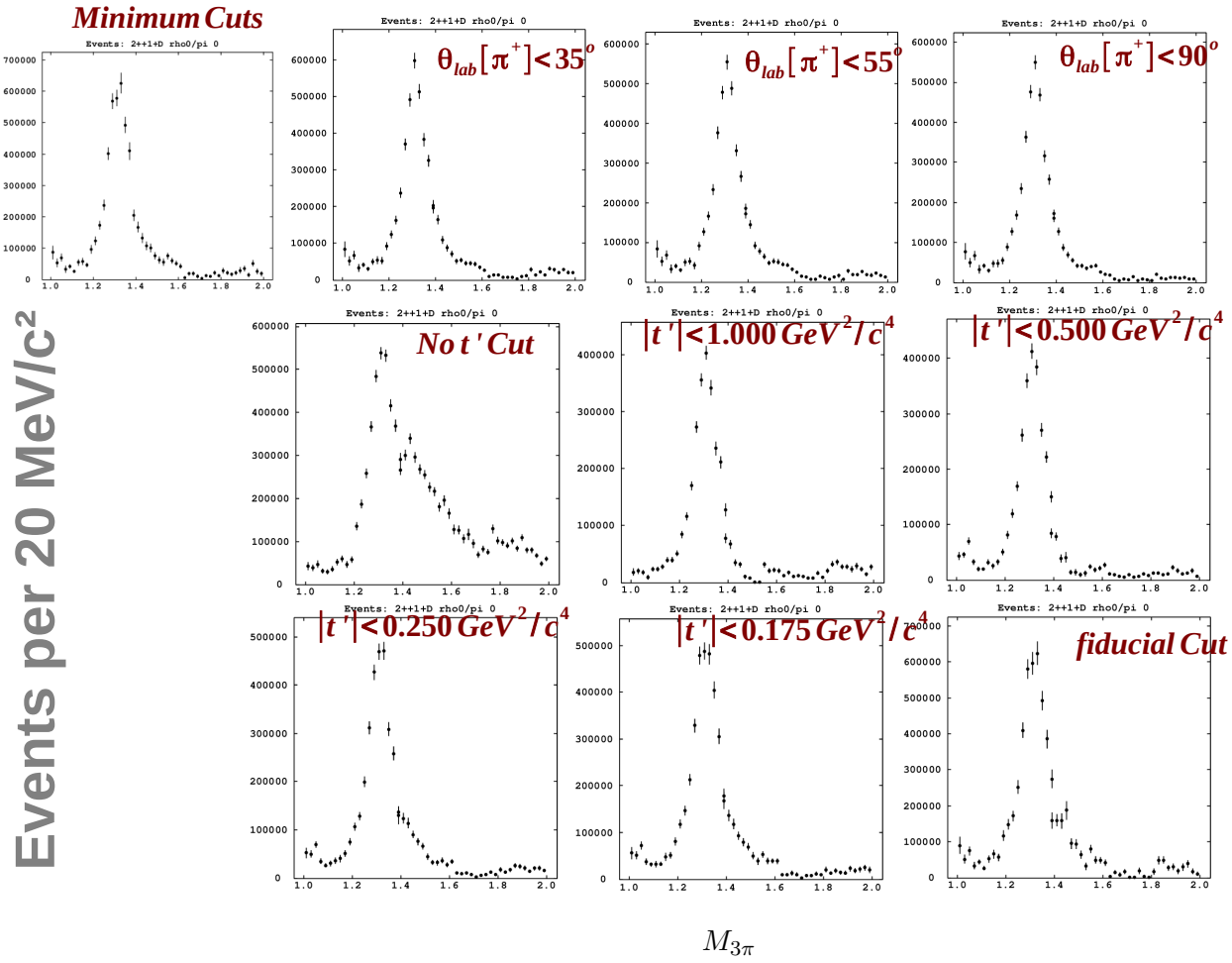

Figure D.16: $\gamma p \to n\pi^+\pi^+\pi^-$: $2^{++}1^+D$ intensities for various selection criteria. The specific selection that is applied is labeled in each plot separately. The minimum represents the cuts that are in the PWA results Chapter.

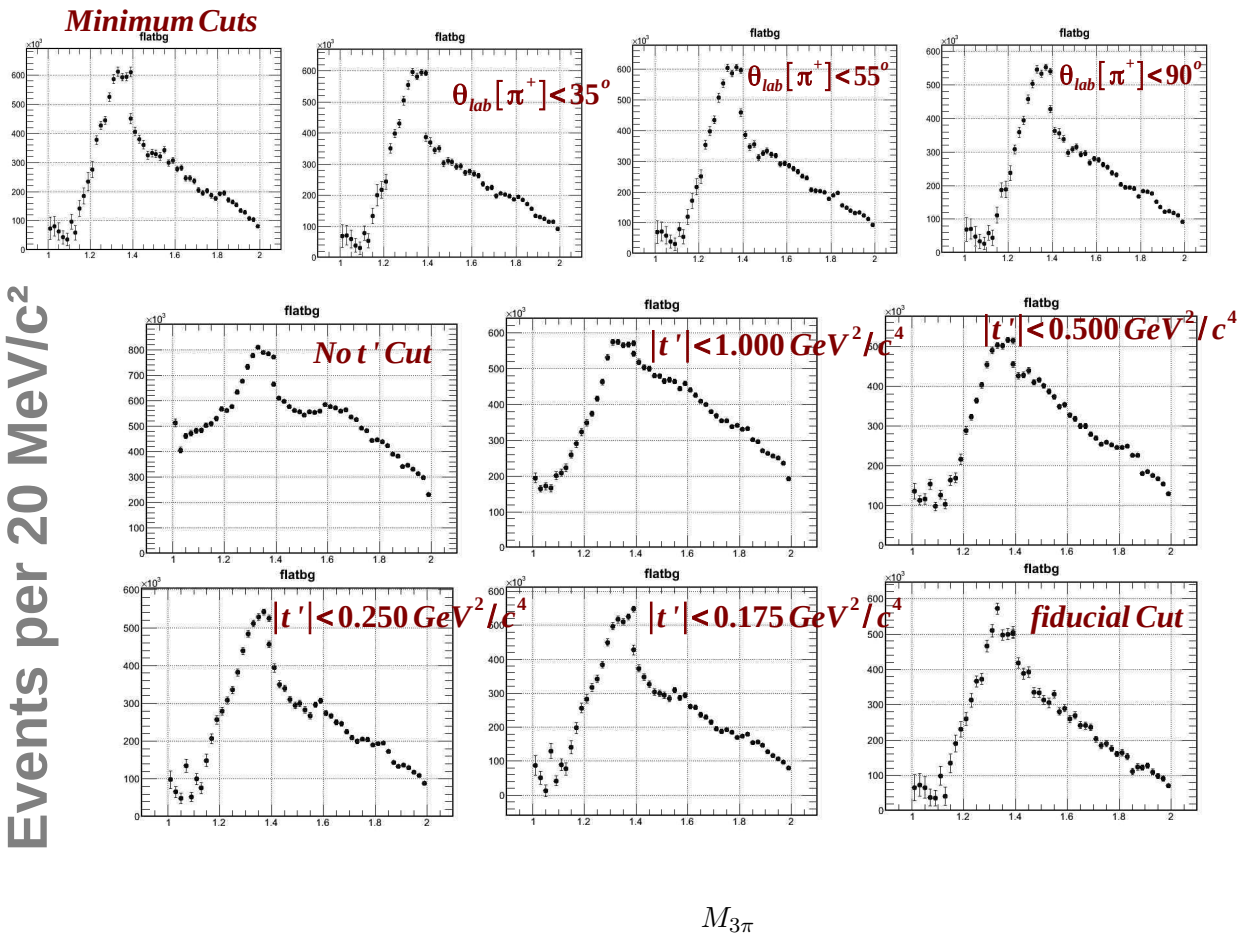

Figure D.17: $\gamma p \to n\pi^+\pi^+\pi^-$: Isotropic background intensities for various selection criteria. The specific selection that is applied is labeled in each plot separately. The minimum represents the cuts that are in the PWA results Chapter.

APPENDIX E

SYSTEMATIC EFFECTS DUE TO BIN SIZE FOR THE $\gamma p \to \pi^-\pi^-\pi^+\Delta^{++}$ REACTION

In order to test the systematic dependence of the results, two fits have been performed with different bin sizes. All the fits that have been presented so far for the $\gamma p \to \pi^-\pi^-\pi^+\Delta^{++}$ reaction are with 25 MeV bin size. The results below are with 10 MeV and 50 MeV bin size. There might be some small discrepancies for the $2^{-+}P$ wave. As a whole the results are stable for the different mass bin sizes, within the statistical fluctuations.

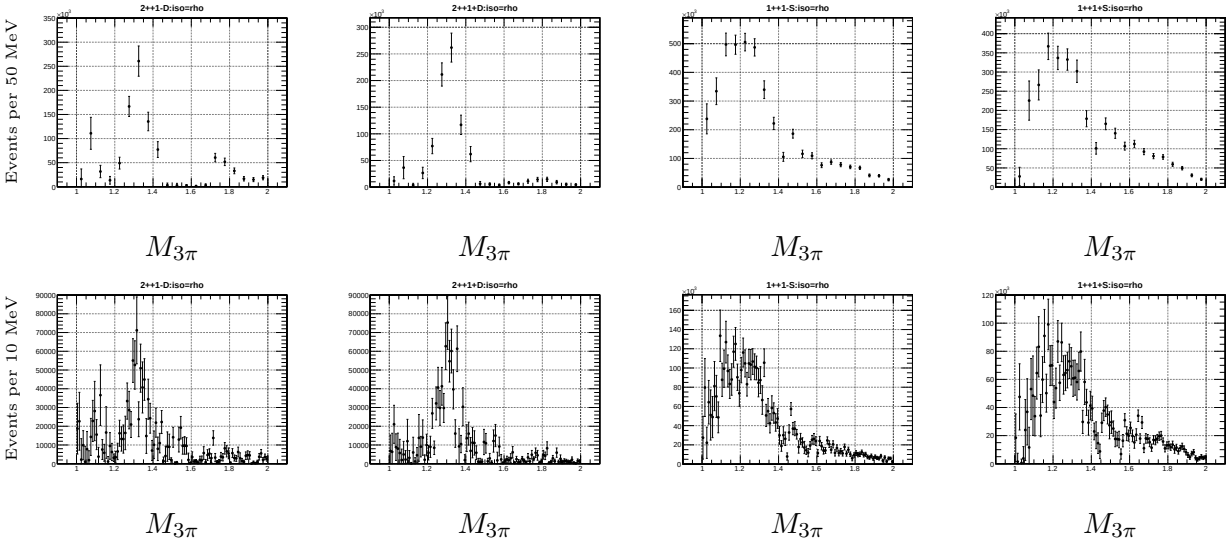

Figure E.1: $\gamma p \to \pi^-\pi^-\pi^+\Delta^{++}$: 50 MeV mass bin size was used for the **top** plots and 10 MeV mass bin size for the **bottom** plots. The first two plots show the intensity of the $2^{++}D$ waves and the last two plots show the intensity of the $1^{++}S$ waves.

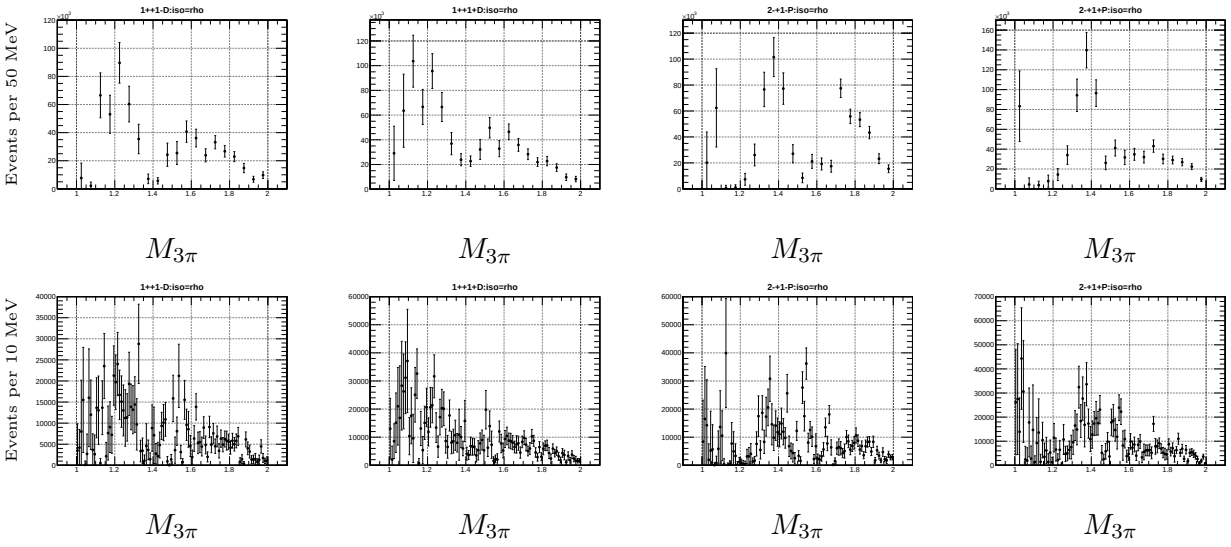

Figure E.2: $\gamma p \to \pi^-\pi^-\pi^+\Delta^{++}$: 50 MeV mass bin size was used for the **top** plots and 10 MeV mass bin size for the **bottom** plots. The first two plots show the intensity of the $1^{++}D$ waves and the last two plots show the intensity of the $2^{-+}P$ waves.

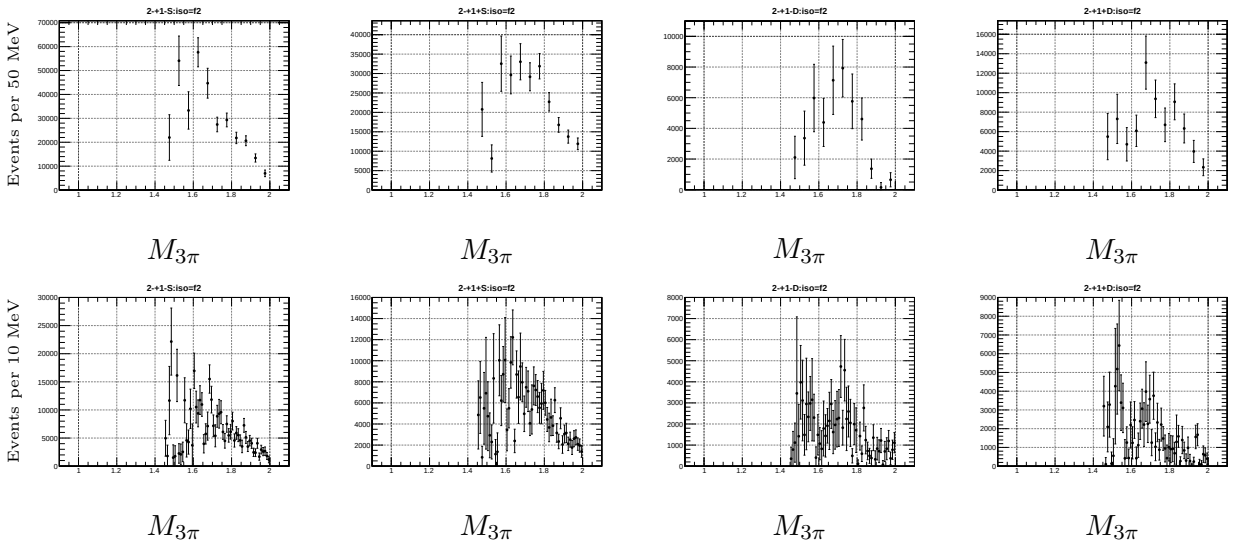

Figure E.3: $\gamma p \to \pi^-\pi^-\pi^+\Delta^{++}$: 50 MeV mass bin size was used for the **top** plots and 10 MeV mass bin size for the **bottom** plots. The first two plots show the intensity of the $2^{-+}S$ waves and the last two plots show the intensity of the $2^{-+}D$ waves.

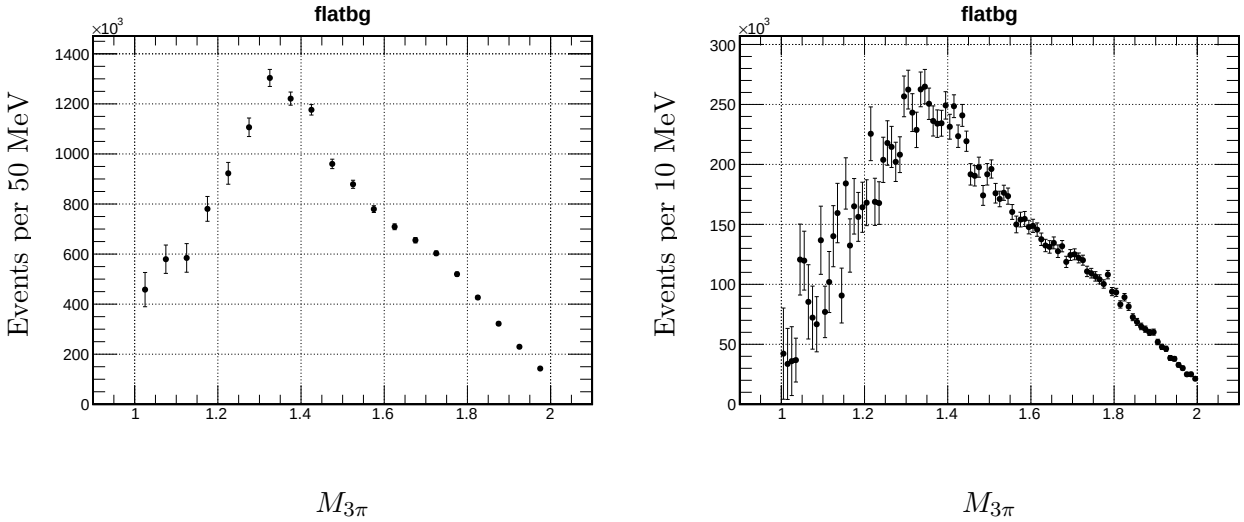

Figure E.4: $\gamma p \to \pi^-\pi^-\pi^+\Delta^{++}$: 50 MeV mass bin size was used for the **left** plot and 10 MeV mass bin size for the **right** plot. The plots show the intensity of the isotropic background.

APPENDIX F

SYSTEMATIC EFFECTS FROM THE SELECTION CRITERIA FOR THE $\gamma p \to \pi^-\pi^-\pi^+\Delta^{++}$ REACTION

The study of the dependence of the fit results is shown in this Appendix. Specifically, various fits were performed with t' threshold to be 0.1, 0.2, 0.4 and 1.0 GeV^2/c^4. Additionally, the values 0.25, 0.45, 0.65 and 1.0 GeV/c for the difference in momentum between the π^+ selection were tested. Fits were also performed with no t' selection and no difference in momentum cut. Nominal fiducial cuts were also tested. Finally, a fit was performed with the invariant mass of the $p\pi^+_{fast}$ bigger than 1.6 GeV. As it was discussed in the events selection Chapter, with this cut the $\pi^+_{slow}\pi^-_{fast}$ peak that is formed around the ρ mass is removed and the statistics are reduced by half.

F.1 $2^{-+}[f_2(1270)\pi]_S$

The intensity of $2^{-+}S$ wave is shown in figures F.1 and F.2. The $2^{-+}S$ wave, in general, appears to be stable. The intensity of the shoulder at 1.4 GeV seems to change, but the peak at 1.7 GeV can be seen in all selection apart from the no t' selection. The latter selection will have a major leakage from baryon background and we will not consider it's results as trustworthy. As the cuts become tighter, as expected, the statistical fluctuations become stronger. Finally, the results seem to be similar for both reflectivities.

F.2 $2^{-+}[\rho(770)\pi]_P$

The intensity of $2^{-+}S$ wave is shown in figures F.3 and F.4. The $2^{-+}P$ wave is not as stable as the $2^{-+}S$ wave. By tightening the selections, this partial wave seems to disappear. Also the ratio between the $2^{-+}P$ wave and the leakage from the $\alpha_2(1320)$ meson does not have strong dependence on the selection criteria.

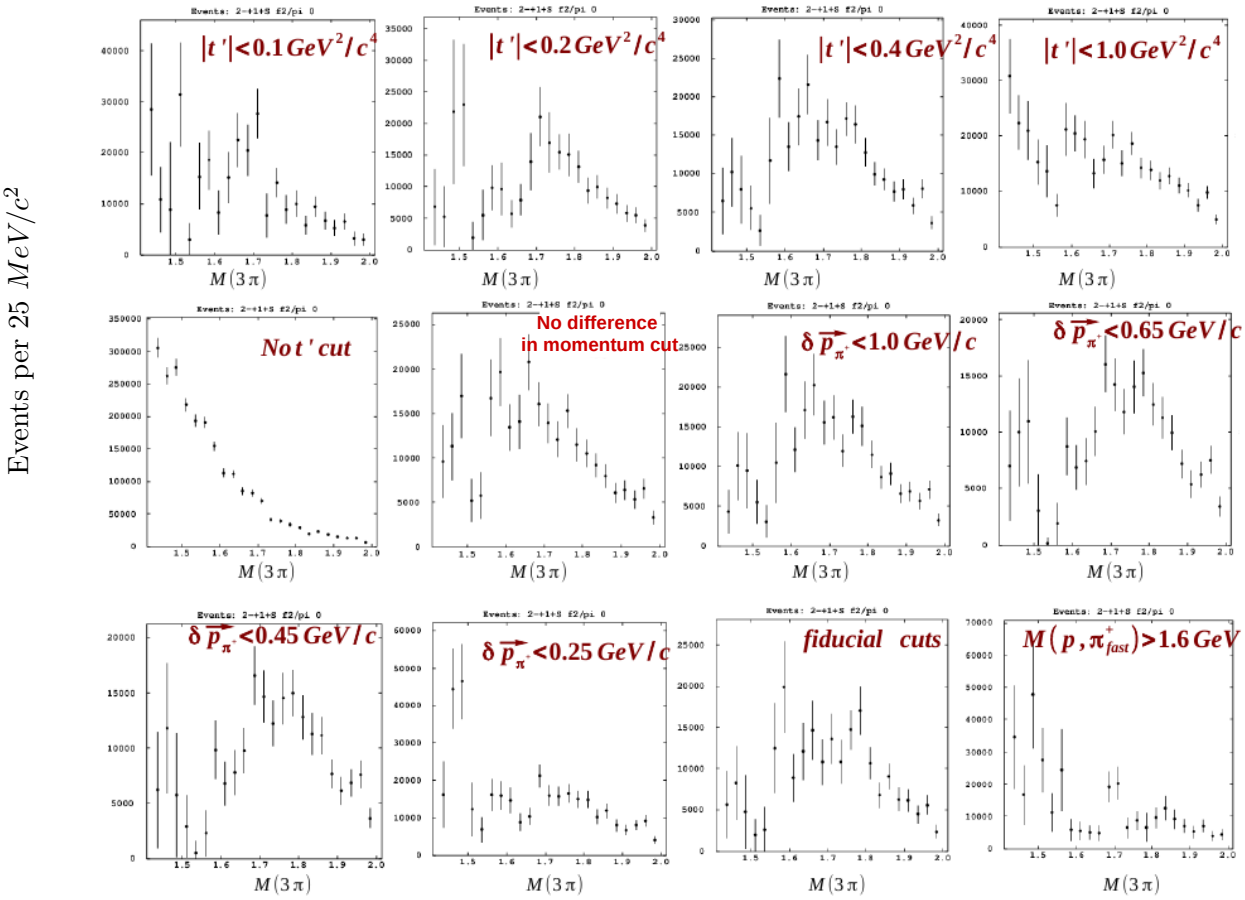

Figure F.1: $\gamma p \to \pi^-\pi^-\pi^+\Delta^{++}$: $2^{-+}1^-S$ intensities for various selection criteria. The specific selection that is applied is labeled in each plot separately. The fit-results with $|t'| < 0.4\ GeV^2/c^4$ represents the cuts that were used in the PWA results Chapter

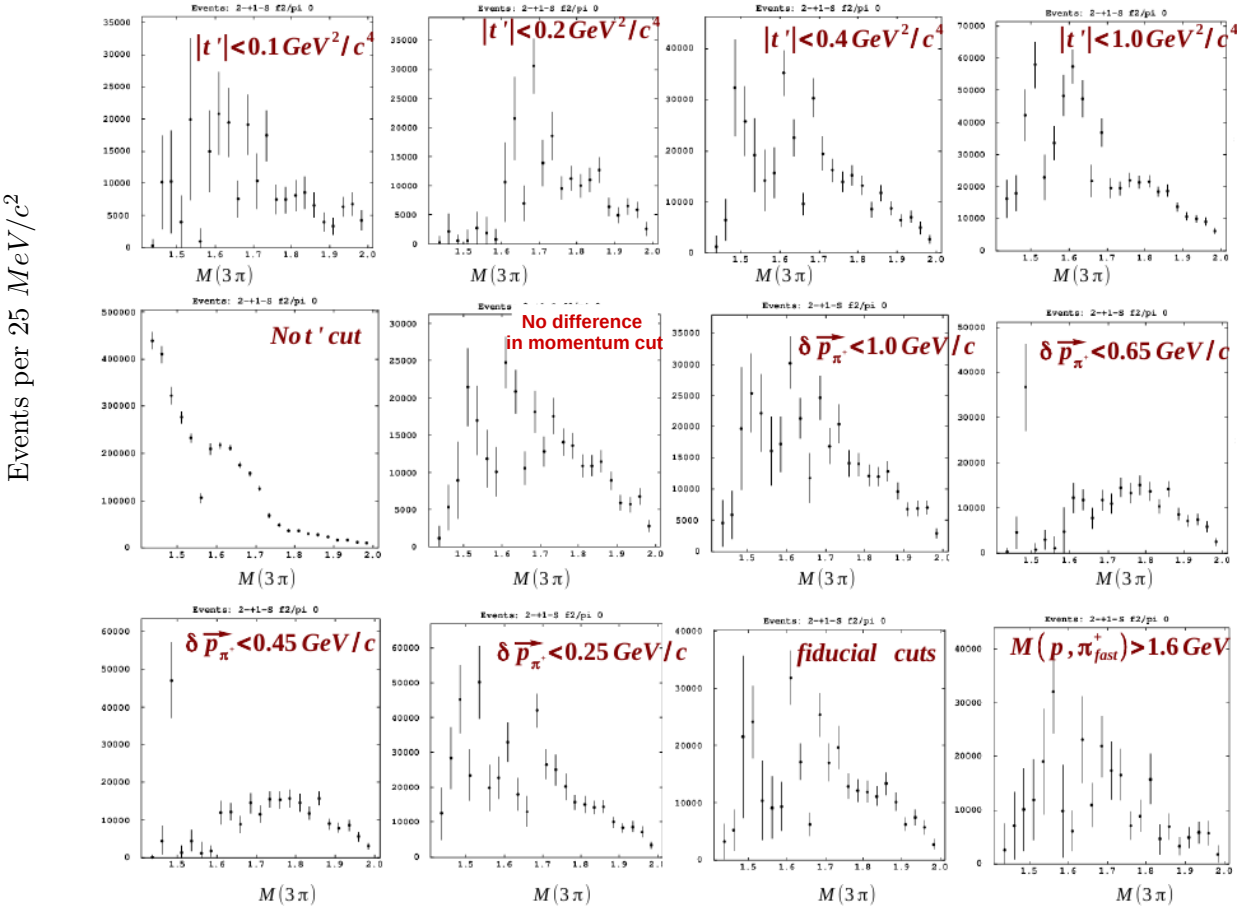

Figure F.2: $\gamma p \to \pi^-\pi^-\pi^+\Delta^{++}$: $2^{-+}1^+S$ intensities for various selection criteria. The specific selection that is applied is labeled in each plot separately. The fit-results with $|t'| < 0.4\ GeV^2/c^4$ represents the cuts that were used in the PWA results Chapter

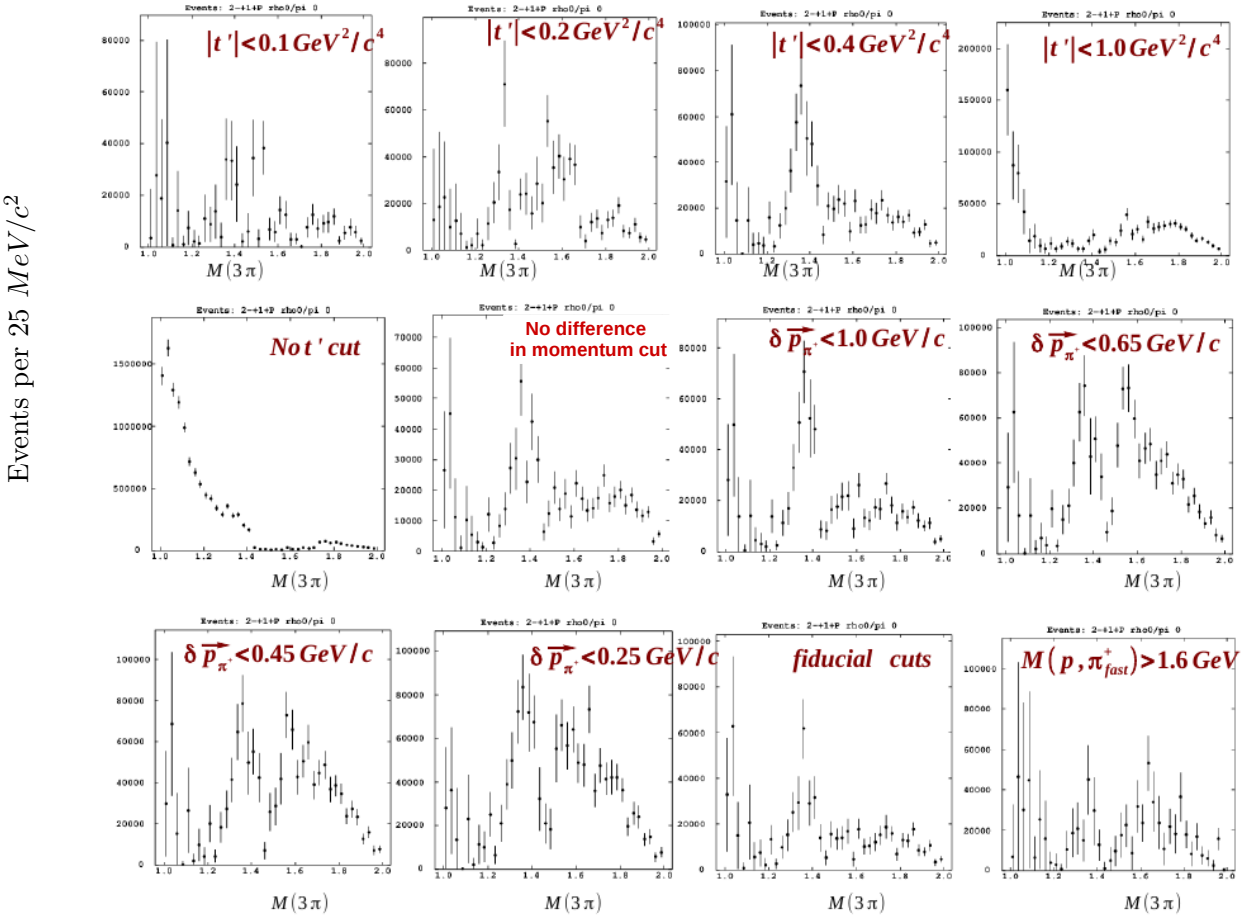

Figure F.3: $\gamma p \to \pi^-\pi^-\pi^+\Delta^{++}$: $2^{-+}1^-P$ intensities for various selection criteria. The specific selection that is applied is labeled in each plot separately. The fit-results with $|t'| < 0.4\ GeV^2/c^4$ represents the cuts that were used in the PWA results Chapter

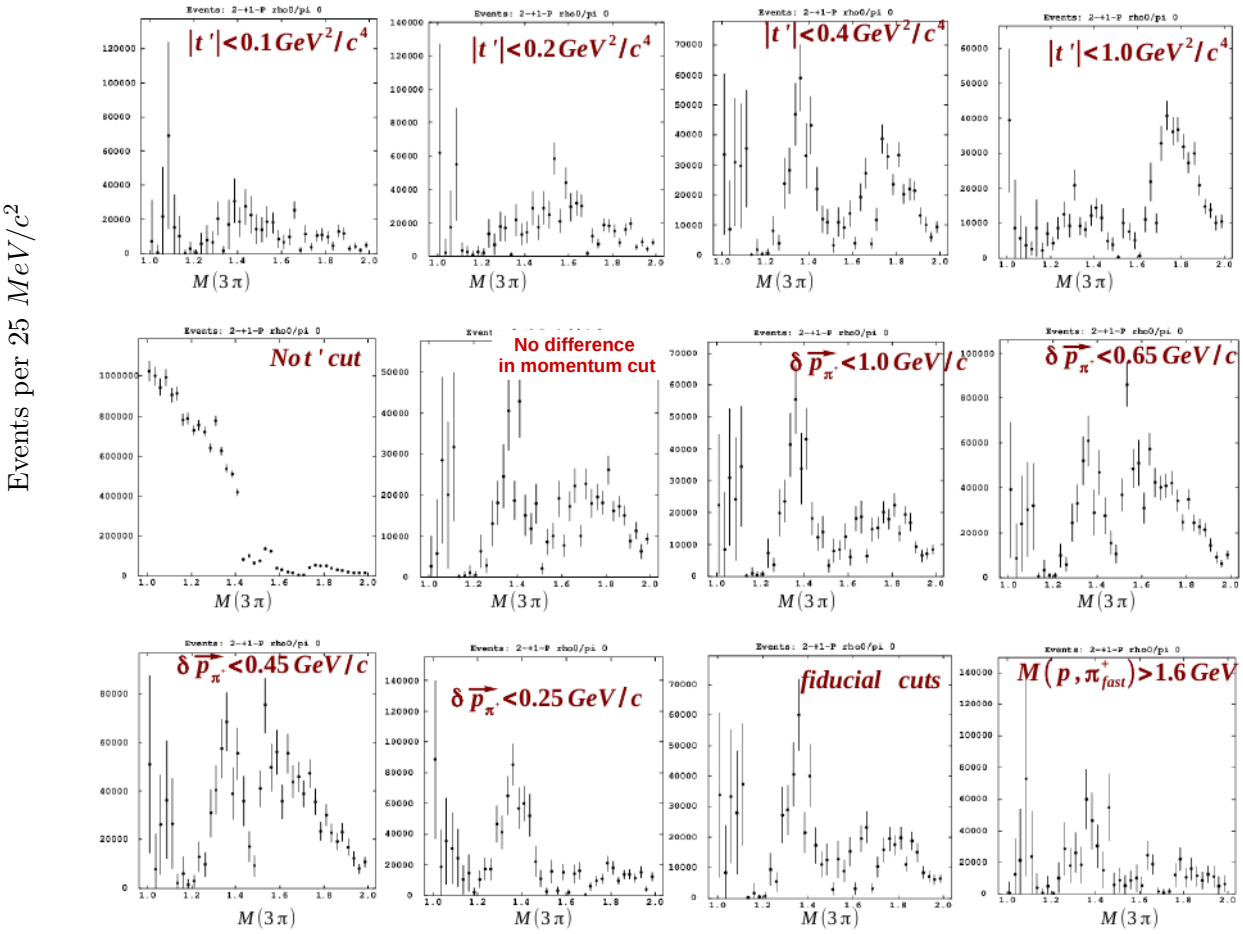

Figure F.4: $\gamma p \to \pi^-\pi^-\pi^+\Delta^{++}$: $2^{-+}1^+P$ intensities for various selection criteria. The specific selection that is applied is labeled in each plot separately. The fit-results with $|t'| < 0.4\ GeV^2/c^4$ represents the cuts that were used in the PWA results Chapter

F.3 $2^{-+}[f_2(1270)\pi]_D$

The intensity of $2^{-+}S$ wave is shown in figures F.5 and F.6. The peak at 1.7 GeV for the $2^{-+}D$ wave is present among all different selections. Similar with the $2^{-+}S$ wave, what seems to change with different selections is the intensity of the shoulder around 1.4 GeV.

F.4 $2^{++}[\rho(770)\pi]_D$

The intensity of $2^{-+}S$ wave is shown in figures F.7 and F.8. The $2^{++}D$ wave appears to be stable for the low 3π mass region and small differences from the main fit arise in the high region. Also the width of the resonance seems to have some small dependence from the selection criteria.

F.5 $1^{++}[\rho(770)\pi]_S$

The intensity of $2^{-+}S$ wave is shown in figures F.9 and F.10. The $1^{++}S$ wave seems to be stable for the low 3π mass region. For the height 3π mass region, it is interesting that as the cuts are tighten a peak starts appear at 1.7 GeV, as we were seeing for the $1^{++}D$ wave.

F.6 $1^{++}[\rho(770)\pi]_D$

The intensity of $2^{-+}S$ wave is shown in figures F.11 and F.12. Since the $1^{++}D$ is a small wave, the statistical fluctuations seem to be significant as the selections are tighter. The general features of this partial wave seems to be stable as a whole.

F.7 Isotropic Background

The intensity of the isotropic wave is being shown in figure F.13. The isotropic background is peaking around 1.3 GeV. It seems that the tighter the cuts are the narrower this structure is. When the t' selection is being relaxed, the intensity for the high mass region seems to be rising, which is an indication that the rejected events from the t' are most likely associated with the high mass region.

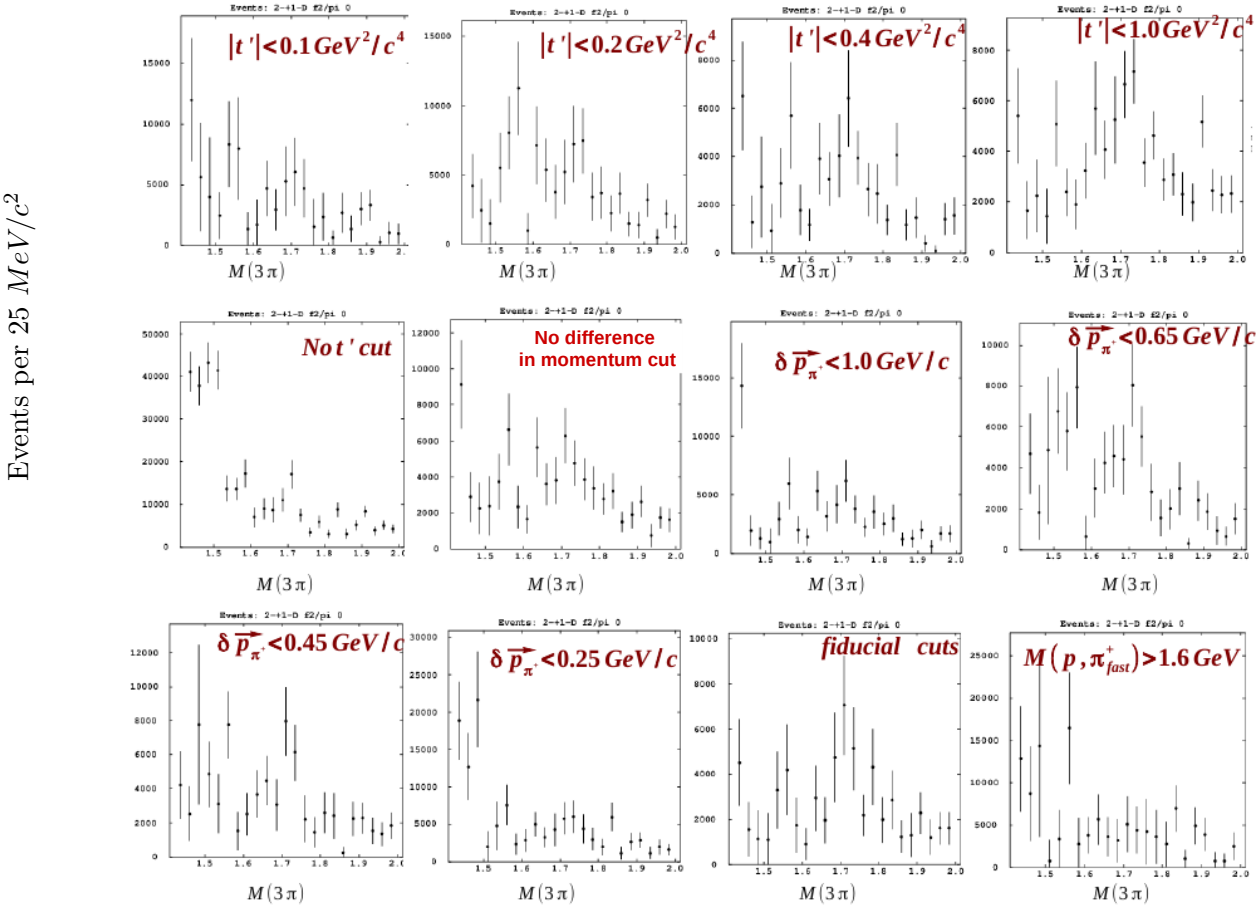

Figure F.5: $\gamma p \to \pi^-\pi^-\pi^+\Delta^{++}$: $2^{-+}1^-D$ intensities for various selection criteria. The specific selection that is applied is labeled in each plot separately. The fit-results with $|t'| < 0.4\ GeV^2/c^4$ represents the cuts that were used in the PWA results Chapter

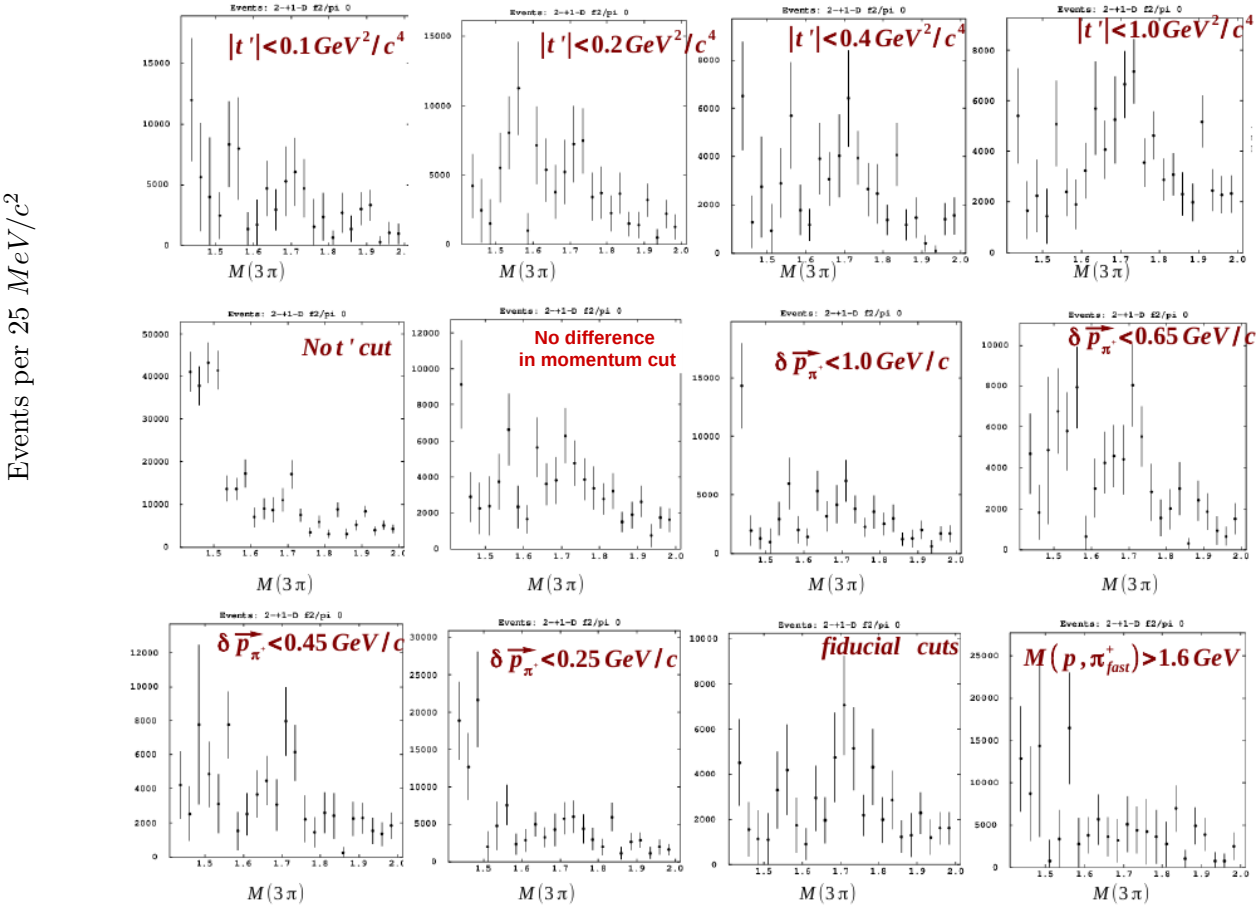

Figure F.6: $\gamma p \to \pi^-\pi^-\pi^+\Delta^{++}$: $2^{-+}1^+D$ intensities for various selection criteria. The specific selection that is applied is labeled in each plot separately. The fit-results with $|t'| < 0.4\ GeV^2/c^4$ represents the cuts that were used in the PWA results Chapter

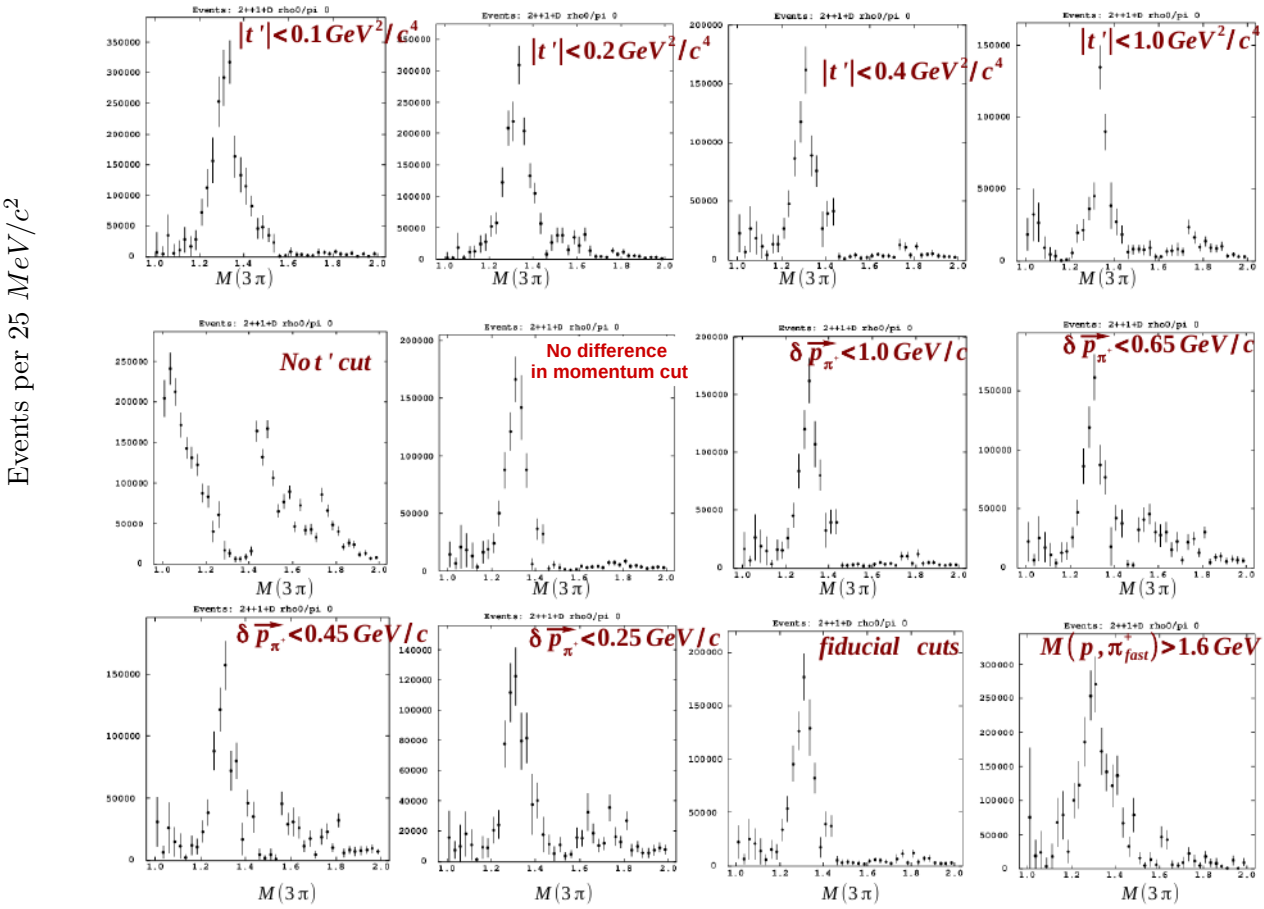

Figure F.7: $\gamma p \to \pi^-\pi^-\pi^+\Delta^{++}$: $2^{++}1^-D$ intensities for various selection criteria. The specific selection that is applied is labeled in each plot separately. The fit-results with $|t'| < 0.4\ GeV^2/c^4$ represents the cuts that were used in the PWA results Chapter

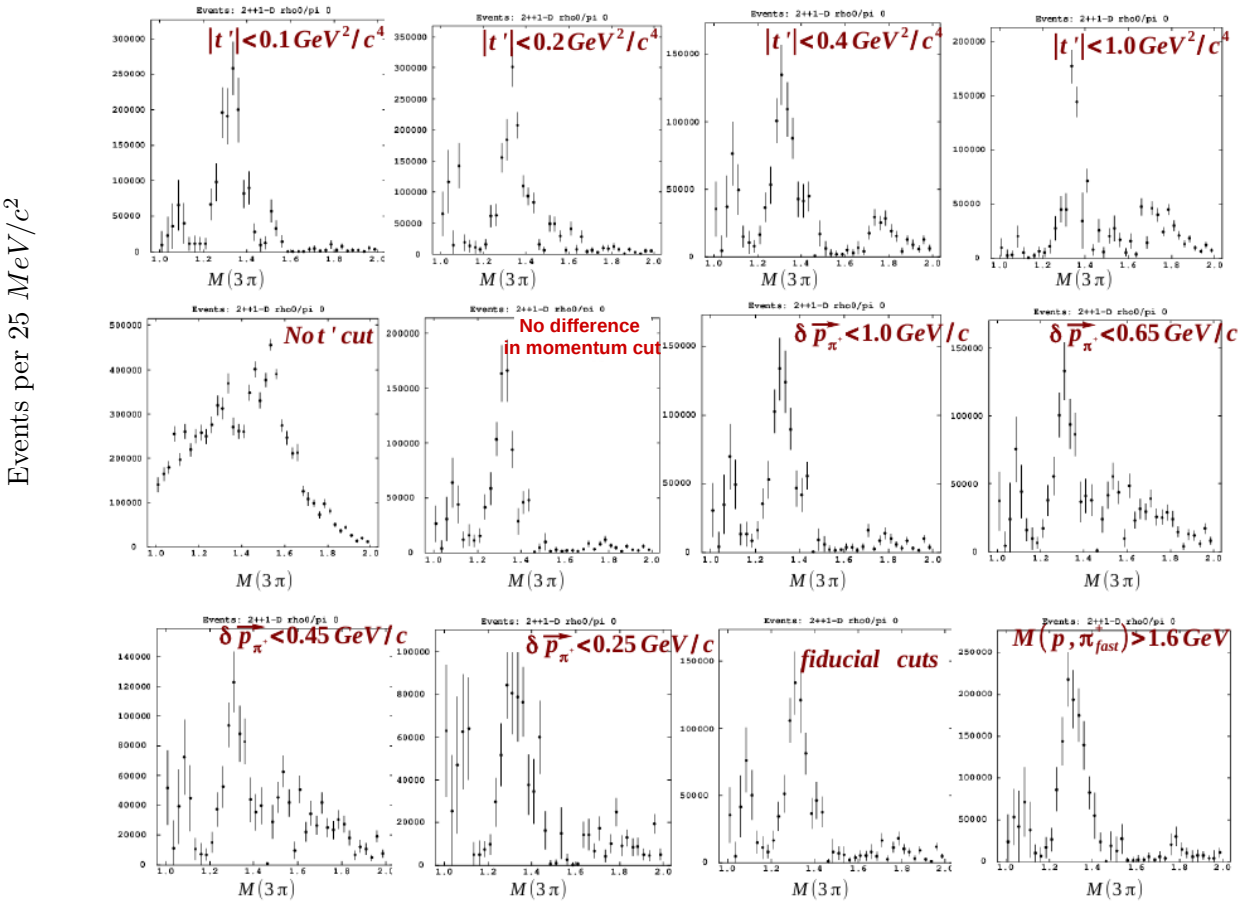

Figure F.8: $\gamma p \to \pi^-\pi^-\pi^+\Delta^{++}$: $2^{++}1^+D$ intensities for various selection criteria. The specific selection that is applied is labeled in each plot separately. The fit-results with $|t'| < 0.4\ GeV^2/c^4$ represents the cuts that were used in the PWA results Chapter

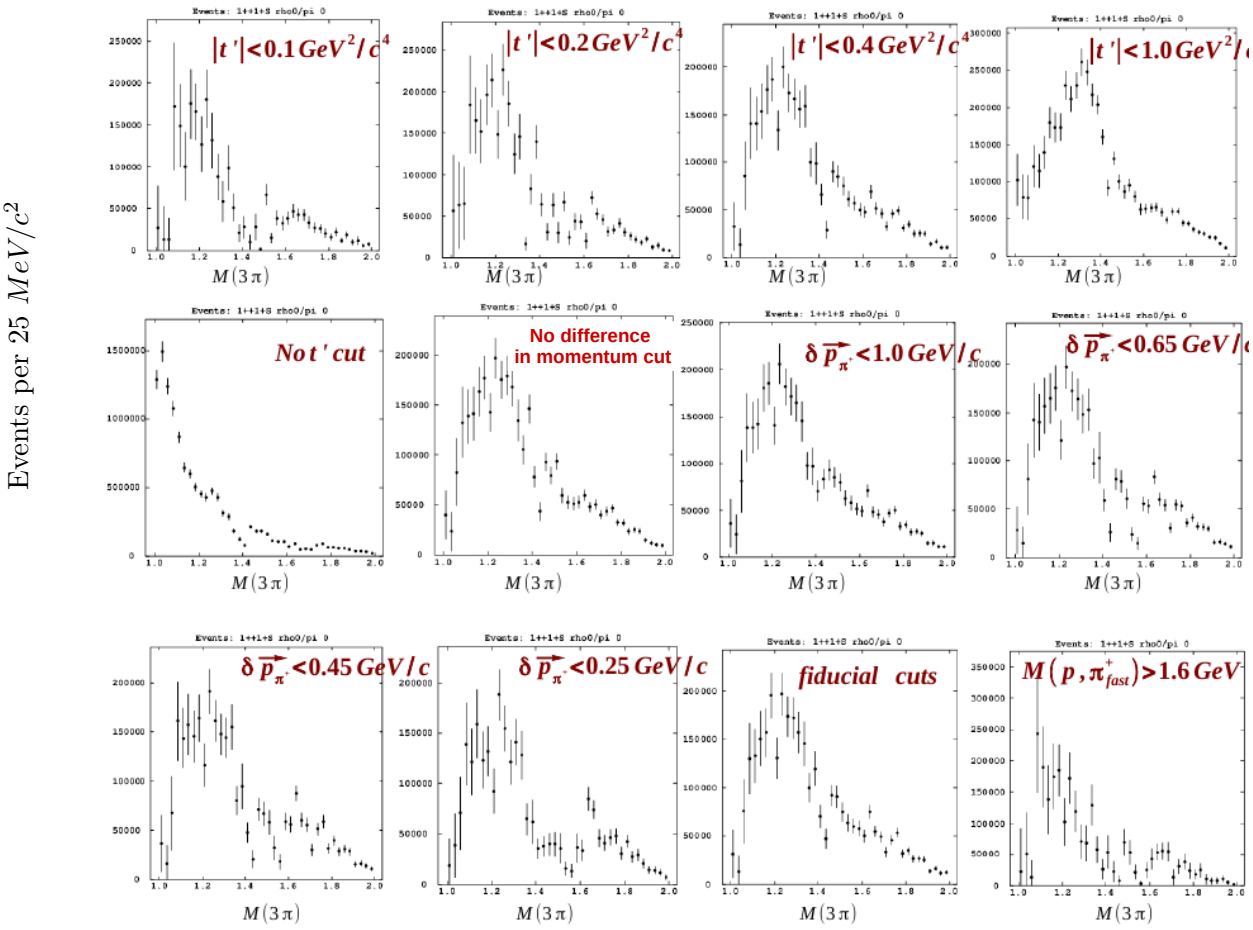

Figure F.9: $\gamma p \to \pi^-\pi^-\pi^+\Delta^{++}$: $1^{++}1^-S$ intensities for various selection criteria. The specific selection that is applied is labeled in each plot separately. The fit-results with $|t'| < 0.4\ GeV^2/c^4$ represents the cuts that were used in the PWA results Chapter

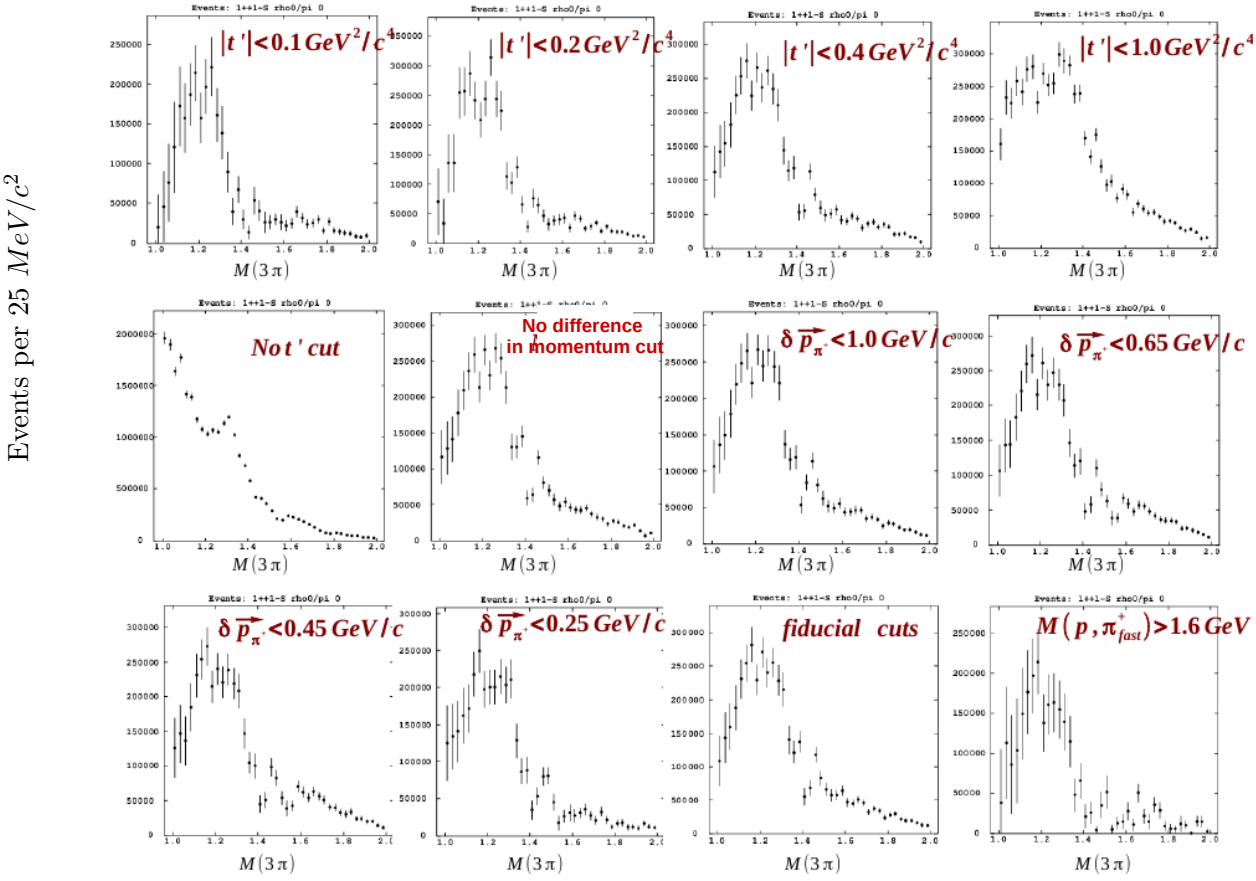

Figure F.10: $\gamma p \to \pi^-\pi^-\pi^+\Delta^{++}$: $1^{++}1^+S$ intensities for various selection criteria. The specific selection that is applied is labeled in each plot separately. The fit-results with $|t'| < 0.4\ GeV^2/c^4$ represents the cuts that were used in the PWA results Chapter

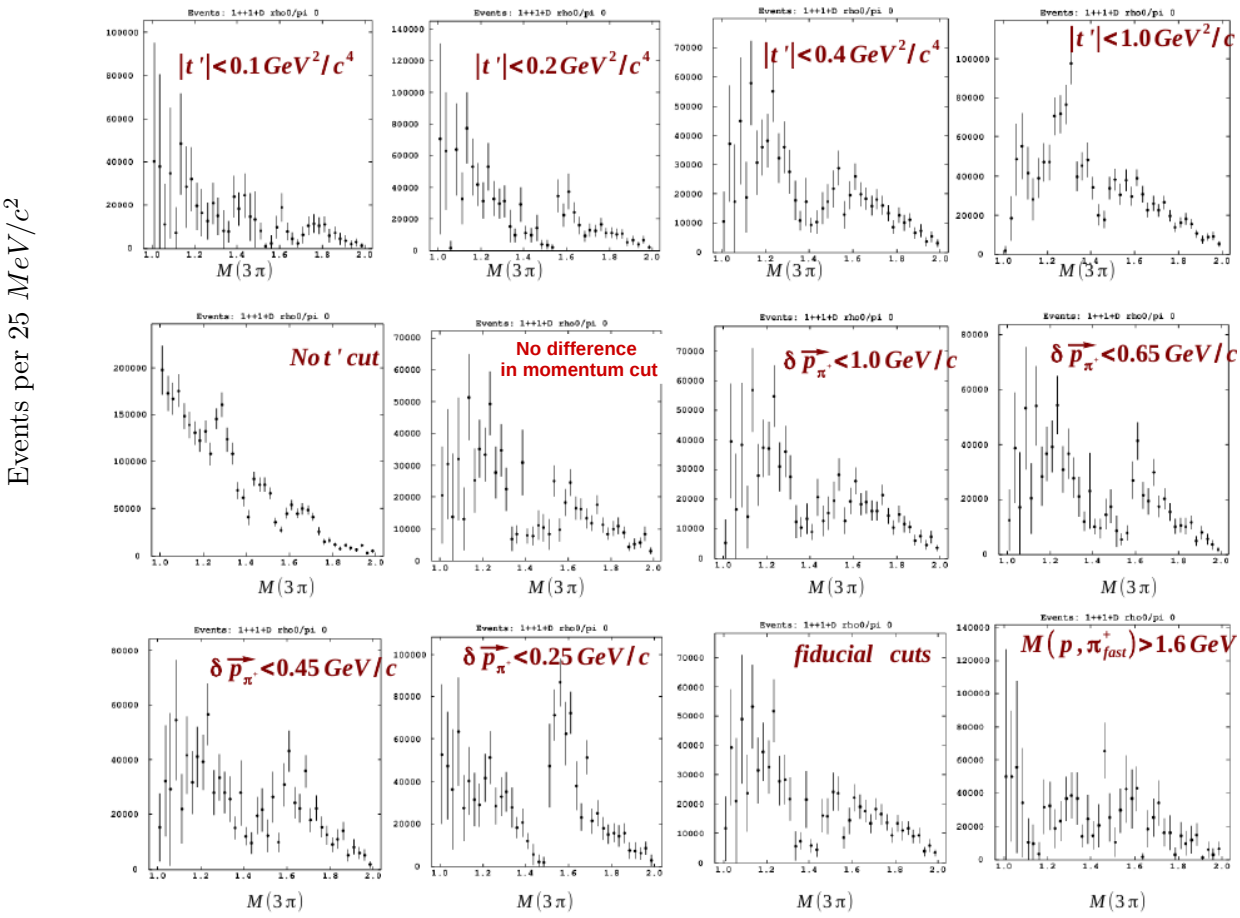

Figure F.11: $\gamma p \to \pi^-\pi^-\pi^+\Delta^{++}$: $1^{++}1^-D$ intensities for various selection criteria. The specific selection that is applied is labeled in each plot separately. The fit-results with $|t'| < 0.4\ GeV^2/c^4$ represents the cuts that were used in the PWA results Chapter

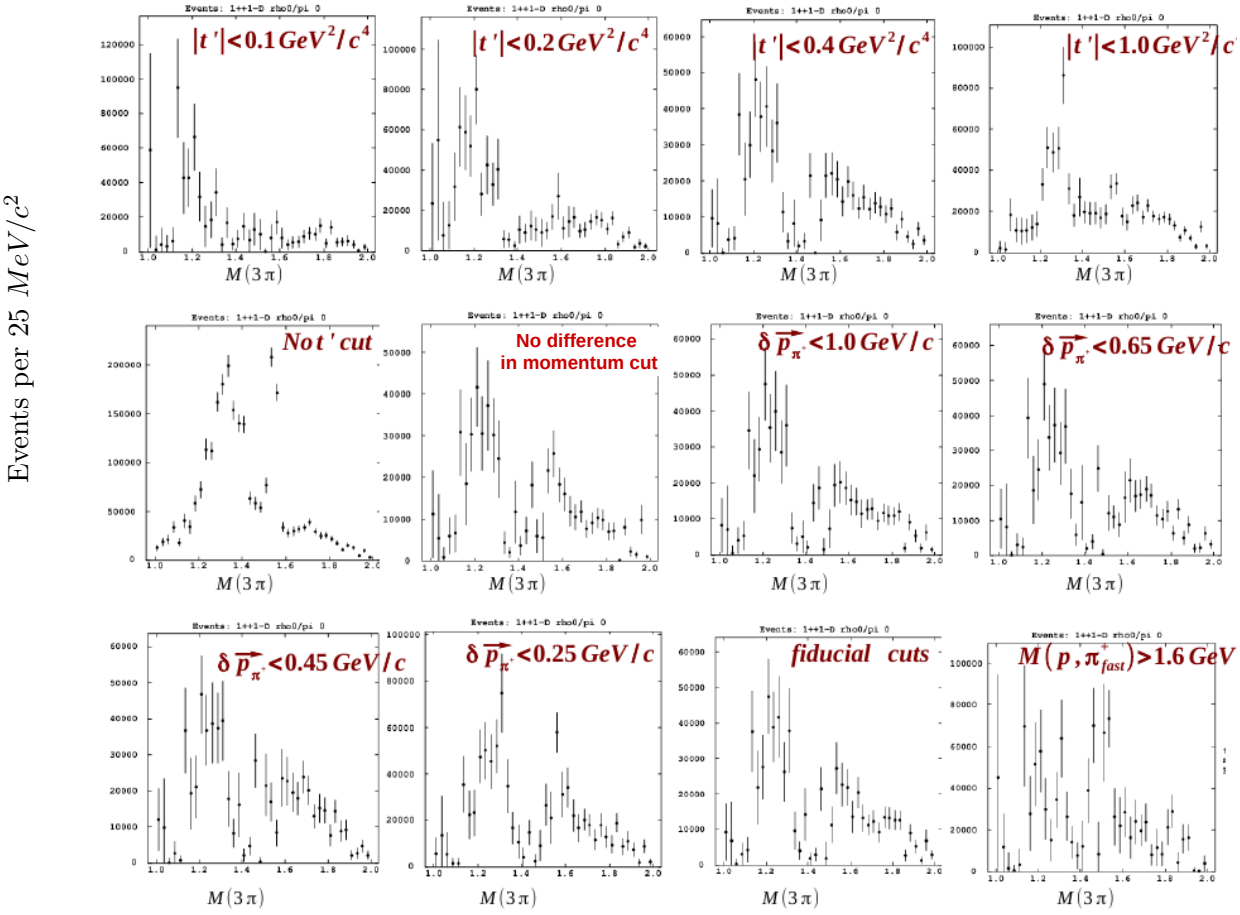

Figure F.12: $\gamma p \to \pi^-\pi^-\pi^+\Delta^{++}$: $1^{++}1^+D$ intensities for various selection criteria. The specific selection that is applied is labeled in each plot separately. The fit-results with $|t'| < 0.4\ GeV^2/c^4$ represents the cuts that were used in the PWA results Chapter

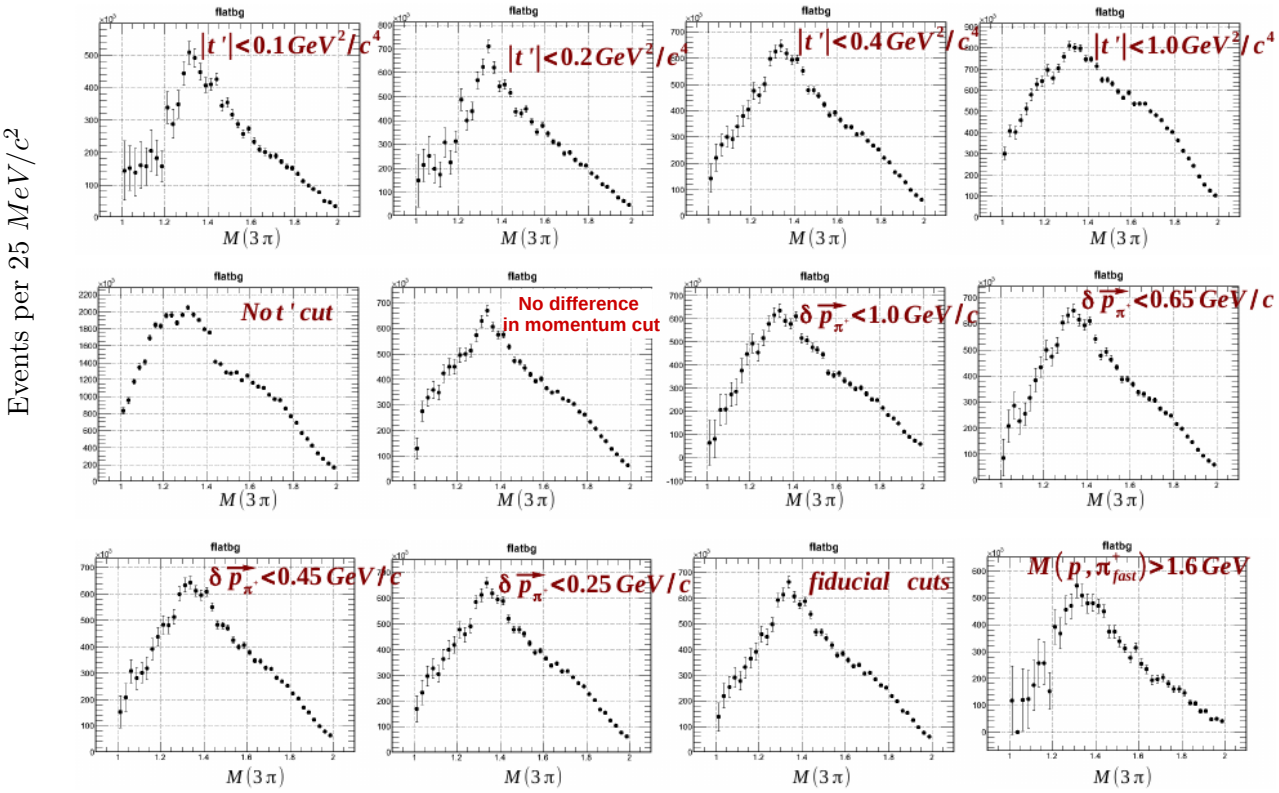

Figure F.13: $\gamma p \to \pi^-\pi^-\pi^+\Delta^{++}$: Isotropic Background intensity for various selection criteria. The specific selection that is applied is labeled in each plot separately. The fit-results with $|t'| < 0.4\ GeV^2/c^4$ represents the cuts that were used in the PWA results Chapter

APPENDIX G

REFERENCE FRAMES

The calculation of the decay amplitudes is done via the isobar model, i.e. a sequential decay of the meson resonance X into three pions. There are two decays, one of X into the isobar Y and a single pion (bachelor π) and then the decay of Y into $\pi^+\pi^-$. A schematic picture for the two reaction channels is shown in Figure G.1.

The decay amplitudes are primarly depending on the polar and azimuthial angles in the meson X rest frame and in the isobar rest frame. The former will be described as $\Omega = (\theta, \phi)$ and the latter as $\Omega_h = (\theta_h, \phi_h)$. The coordinate system in the meson rest frame is chosen to be that of Gottfried-Jackson (GJ) frame, i.e. the z-axis is along the beam direction and the y-axis is normal to the production plane. The latter is defined as $\hat{y} = \hat{beam} \times \hat{target}$. Then θ is defined as the angle between the $\vec{p}_Y$ and the $\hat{beam}$ and ϕ is defined as the angle between the $\vec{p}_Y$ and the $\hat{x}$ in the GJ frame.

The θ_h and ϕ_h are defined using the helicity convention. The z-axis in the isobar frame is defined as the $\vec{p}_Y$ in the GJ rest frame. After the boost into the Y rest frame, the y-axis in the isobar frame is defined as $\hat{z} \times \hat{z}_h$, where $\hat{z}$ is in the GJ frame. Then θ_h and ϕ_h are defined as in any spherical cooridinate system, with the π^+ to be the analyzer for the $\gamma p \to n\pi^+\pi^+\pi^-$ reaction and π^- is the analyzer for the $\gamma p \to \pi^-\pi^-\pi^+\Delta^{++}$ reaction. A sketch of the reference frames is shown is Figure G.2.

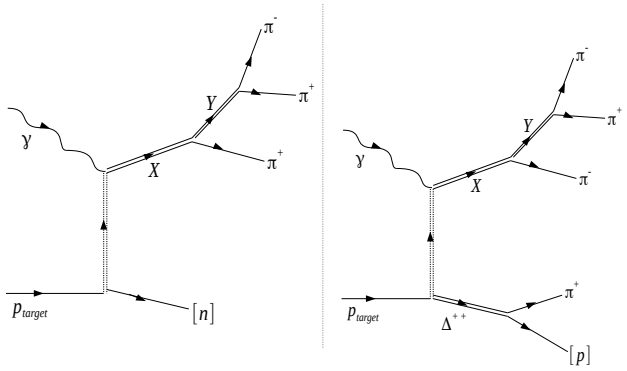

Figure G.1: The two diagrams show a diffractive reaction in the isobar model. The **left** shows a $\gamma p \to n\pi^+\pi^+\pi^-$ reaction and the **right** plot shows a $\gamma p \to \pi^-\pi^-\pi^+\Delta^{++}$ reaction.

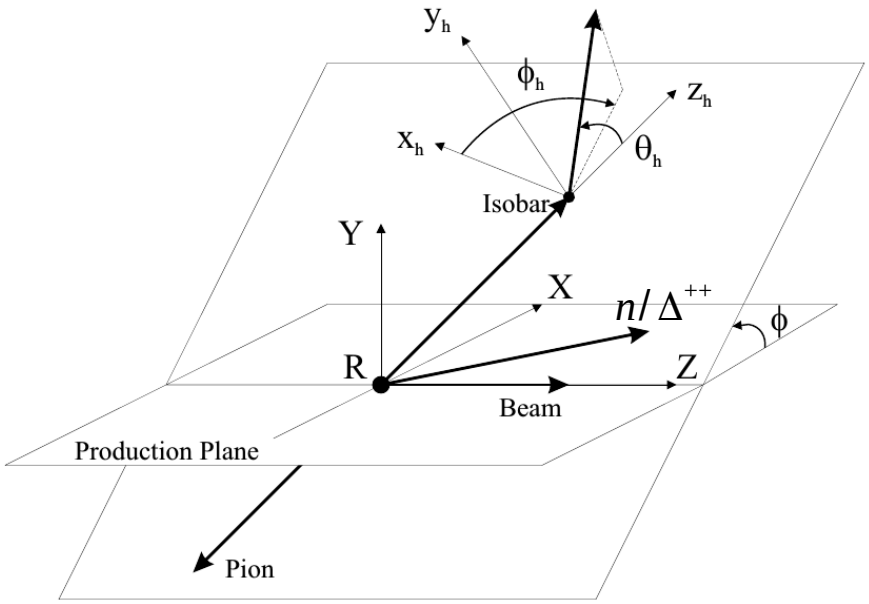

Figure G.2: The Gottfried-Jackson and helicity frames used to describe the sequential decay of the 3π meson resonance. The recoil particle lies in the XZ of the production plane and it is a neutron for the $\gamma p \to n\pi^+\pi^+\pi^-$ reaction and a Δ^{++} for the $\gamma p \to \pi^-\pi^-\pi^+\Delta^{++}$ reaction.

REFERENCES

[1] S. Bethke. *Experimental tests of asymptotic freedom.* Progress in Particle Nuclear Physics, 58(2):351-386, (2007).

[2] Alessandro Bettini. *Introduction to Elementary Particle Physics.* CAMBRIDGE UNIVERSITY PRESS, (2008).

[3] Jozef J. Dudek. *The lightest hybrid meson supermultiplet in QCD.* Phys.Rev., D84:074023, (2011).

[4] Jefferson lab picture exchange. *http://www.jlab.org.* website.

[5] M. Gell-Mann. Phys. Rev. 125, 1067, (1991).

[6] A. Chodos, R. L. Jaffe, K. Johnson, Charles B. Thorn, and V. F. Weisskopf. *A New Extended Model of Hadrons.* Phys. Rev. D9:34713495, (1974).

[7] K. Johnson Thomas A. DeGrand, R. L. Jaffe and J. E. Kiskis. *Masses and Other Parameters of the Light Hadrons.* Phys. Rev., D12:2060, (1975).

[8] F. de Viron Ted Barnes, F. E. Close and J. Weyers. *Q anti-Q G Hermaphrodite Mesons in the MIT Bag Model.* Nucl. Phys., B224:241, (1983).

[9] Michael S. Chanowitz and Stephen R. Sharpe. *Hybrids: Mixed States of Quarks and Gluons.* Nucl. Phys., B222:211, (1983).

[10] Nathan Isgur and Jack E. Paton. *A Flux Tube Model for Hadrons in QCD.* Phys. Rev., D31:2910, (1985).

[11] D. R. Thompson, G. S. Adams, and Adams. *Evidence for exotic meson production in the reaction $\pi^- p \to \eta\pi^- p$ at 18 GeV/c.* Phys. Rev. Lett., 79:16301633, (1997).

[12] D.V. et all Amelin. *Investigation of hybrid states in the ves experiment at the institute for high energy physics (protvino).* Physics of Atomic Nuclei, 68(3):359371.

[13] Claude Amsler. *Proton - anti-proton annihilation and meson spectroscopy with the crystal barrel.* Rev.Mod.Phys., 70:12931340, (1998).

[14] S.U. Chung, K. Danyo, R.W. Hackenburg, C. Olchanski, and et al J.S. Suh. *Exotic and q anti-q resonances in the pi+ pi- pi- system produced in pi- p collisions at 18-GeV/c.* Phys.Rev., D65:072001, (2002).

[15] A. Zaitsev. *Study of exotic resonances in diffractive reactions.* Nucl.Phys., A675:155C160C, (2000).

[16] M. G. Alekseev, V. Yu. Alexakhin, Yu. Alexandrov, G. D. Alexeev, A. Amoroso, A. Austregesilo, B. Badeek, and et al F. Balestra. *Observation of a $J^{PC} = 1^{-+}$ exotic resonance in diffractive dissociation of 190 gev/c π^- into $\pi^-\pi^-\pi^+$.* Phys. Rev. Lett., 104:241803, (2010).

[17] G.M. Beladidze et al. *Study of $\pi^- N \to \eta\pi^- N$ and $\pi^- N \to \eta'\pi^- N$ reactions at 37-GeV/c.* Phys.Lett., B313:276282, (1993).

[18] E.I. Ivanov et al. *Observation of exotic meson production in the reaction $\pi^- p \to \eta'\pi^- p$ at 18-GeV/c.* Phys.Rev.Lett., 86:39773980, (2001).

[19] Joachim Kuhn et al. *Exotic meson production in the f(1)(1285) pi- system observed in the reaction $\pi^- p \to \eta\pi^+\pi^-\pi^- p$ at 18-GeV/c.* Phys.Lett., B595:109117, (2004).

[20] M. Lu et al. *Exotic meson decay to $\omega\pi^0\pi^-$.* Phys. Rev. Lett., 94:032002, (2005).

[21] A.R. Dzierba, R. Mitchell, E. Scott, P. Smith, and et al M. Swat. *A Partial wave analysis of the $\pi^-\pi^-\pi^+$ and $\pi^-\pi^0\pi^0$ systems and the search for a $J^{PC} = 1^{-+}$ meson.* Phys.Rev., D73:072001, (2006).

[22] F. Close and P. Page. Phys. Rev. D52, 1706, (1995).

[23] A. Szczepaniak and M. Swat. Phys. Lett. B516, 72, (2001).

[24] N. Isgur and J. Paton. Phys. Rev. D31, 2910, (1985).

[25] M. Nozar et al. *Search for photo-excitation of exotic mesons in the $\pi^+\pi^+\pi^-$ system.* Phys. Rev. Lett. 102:102002, (2009).

[26] J. Beringer et al. *Review of Particle Physics (RPP).* Phys.Rev., D86:010001, (2012).

[27] Robert T. Deck. *Kinematical interpretation of the first pi - rho resonance.* Phys.Rev.Lett., 13:169173, (1964).

[28] G. Ascoli, L.M. Jones, B. Weinstein, and H.W. Wyld. *Partial-wave analysis of the deck amplitude for $\pi n \to \pi\pi\pi n$.* Phys.Rev., D8:38943919, (1973).

[29] G. Ascoli, R. Cutler, L.M. Jones, U. Kruse, and et al T. Roberts. *Deck-model calculation of $\pi^- p \to \pi^-\pi^+\pi^- p$.* Phys.Rev., D9:19631979, (1974).

[30] W.-M. et al. Yao. *Review of Particle Physics.* Journal of Physics G, 33, (2006).

[31] C. Daum et al. *DIFFRACTIVE PRODUCTION OF 3 pi STATES AT 63-GeV AND 94-GeV.* Nucl.Phys., B182:269, (1981).

[32] D.V. Amelin, E.B. Berdnikov, S.I. Bityukov, G.V. Borisov, and et al Yu.P. Gouz. *Study of diffractive reaction $\pi^- A \to \eta\eta\pi^- A$ at the momentum P(pi-) = 37-GeV/c.* Phys.Atom.Nucl., 59:976981, (1996).

[33] A.V. Anisovich, C.A. Baker, C.J. Batty, D.V. Bugg, V.A. Nikonov, A.V. Sarantsev, V.V. Sarantsev, , and B.S. Zou. *Study of $\bar{p}p \to \eta\eta\pi^0\pi^0$ in flight.* Physics Letters B, 500(34):222 231, (2001).

[34] Jozef Dudek and Adam Szczepaniak. *The deck effect in $\pi n \to \pi\pi\pi n$.* AIP Conference Proceedings, 814(1):587591, (2006).

[35] De-Min Li and Shan Zhou. *On the nature of the pi(2)(1880).* Phys.Rev., D79:014014, (2009).

[36] P. Eugenio et al. *Search for new forms of hadronic matter in photoproduction. Technical report.* CLAS Analysis Proposal PR04-005, (2003).

[37] D. Weygand et al. *Study of pentaquark states in photoproduction off protons. Technical report.* CLAS Analysis Proposal PR04-017, (2004).

[38] W. Chen et al. *The $\gamma p \to \pi^+ n$ single charged pion photoproduction. Technical report.* CLAS Analysis Proposal PR08-003, (2008).

[39] E. Pasyuk. *Energy loss corrections for charged particles in clas.* CLAS-NOTE, (2007).

[40] J. Goetz. *CLAS g12 analysis note.* CLAS-NOTE, (2012).

[41] H. Bichsel. *Passage of particles through matter*, (2006).

[42] Craig Bookwalter. *A search of exotic mesons in $\gamma p \to n\pi^+\pi^+\pi^-$ reaction with CLAS at Jefferson Lab.* PhD thesis, Florida State University, (2012).

[43] D. Keller. *Techiques in kinematic fitting.* CLAS-NOTE, (2010-015).

[44] R. Brun, F. Bruyant, M. Maire, M.C. McPherson, and P. Zanarini. *Geant3.* CERN.

[45] P. Landshoff S. Donnachie, G. Dosch and O. Nachtmann. *Pomeron Physics and QCD.* Cambridge Monographs on Particle Physics, 19, (2002).

[46] S. Chung. *Formulas for partial-wave analysis, note.* BNL, (1988).

[47] Dennis P. Weygand Carlos W. Salgado. *On the Partial-Wave Analysis of Mesonic Resonances Decaying to Multiparticle Final States Produced by Polarized Photons.* arXiv:1310.7498 [nucl-ex], (2013).

[48] Frank von Hippel and C. Quigg. Phys. Rev. 5, 624, (1972).

[49] John P. Cummings and Dennis P. Weygand. *An object-oriented approach to partial wave analysis.* eprint only, (2003).

[50] F. James and M. Roos. *Minuit A System for Function and Minimization and Analysis of the Parameter Errors and Correlations.* Comput Phys Commun, (1975).

[51] G. T. Condo et al. *Further results from charge exchange photoproduction.* Phys. Rev. D48:30453047, (1993).

[52] G.T. Condo. *Charge exchange photoproduction of the a2- (1320) in association with Delta++ at 19.3-GeV/c.* PhysRevD.41.3317, (1990).

[53] S. U. Chung et al. [BNL E852 Collab.]. *Exotic and qq resonances in the $\pi^+\pi^-\pi^-$ system produced in the π -p collisions at 18 GeV/c.* Phys. Rev. D65:072001, (2002).

[54] Michael C. Kunkel. *PHOTOPRODUCTION OF π^0 ON HYDROGEN WITH CLAS FROM 1.1 GEV - 5.45 GEV USING eeγ DECAY.* PhD thesis, Old Dominion University, (2014).

[55] G. T. Condo et al. *Further results from charge exchange photoproduction.* Phys. Rev., D48:3045-3047, (1993).

[56] E. I. Ivanov et al. [BNL E852 Collab.]. Phys. Rev. **86**, 3977, (2001).

[57] P. Eugenio. Int. Jour. of Mod. Phys. A Vol 18, No 3 (2003) 487.

BIOGRAPHICAL SKETCH

The author was born in Athens, Greece and graduated from Thrakomakedones High School in Attica. He studied at National Technical University of Athens where he received his 5 year bachelor degree of applied mathematical and physical science in 2010. In the same year the author came to Florida State University to pursue a Ph.D. in experimental hadronic physics.